

**THE EFFECTS OF ADVANCED FUELS AND ADDITIVES ON HOMOGENEOUS
CHARGE COMPRESSION IGNITION COMBUSTION AND DEPOSIT FORMATION**

by

Joshua S. Lacey

A dissertation submitted in partial fulfillment
of the requirements for the degree of
Doctor of Philosophy
(Mechanical Engineering)
in The University of Michigan
2013

Doctoral Committee:

Professor Zoran Filipi, Co-Chair, Clemson University
Associate Professor Angela Violi, Co-Chair
Professor James Driscoll
Research Scientist John Hoard
Professor Phillip Savage

New knowledge is the most valuable commodity on earth.

The more truth we have to work with, the richer we become.

- Kurt Vonnegut

© Joshua S. Lacey 2013
All Rights Reserved

ACKNOWLEDGEMENTS

I would first like to acknowledge my advisor Professor Zoran Filipi for giving me the opportunity to pursue this work. With this research effort I was able to oversee a project from its inception, from first establishing the experimental engine setup in the test cell, to a tangible conclusion, resulting in this dissertation. I also would like to acknowledge and thank Associate Professor Angela Violi for agreeing to come onto the project as a co-advisor here at the University of Michigan after Professor Filipi left for Clemson University, at the beginning of the 2012 calendar year. The remainder of the dissertation committee, comprised of Professor James Driscoll, Professor Phillip Savage and Research Scientist John Hoard, are recognized as well for their invaluable contributions and feedback in bolstering the quality of this scientific study.

Special thanks also go to the support staff in the W.E. Lay Auto lab as well. Melissa McGeorge, Laurie Stoianowski and Kathie Wolney were instrumental in helping with purchase requests and shipments, as well as booking rooms for meetings. Bill Kirkpatrick was in charge of retrieving gasoline from the fuel shed for experiments, and I greatly appreciate him accommodating my incessant need for test fuel. Also, I want to thank the technicians in the machine shop, including Kent Pruss, John Mears and Marv Cressey, who provided helpful guidance during the fabrication process for the experimental setup.

I want to specifically recognize the efforts of several students who have had significant impacts on the research project during my tenure here at the University of Michigan. Andrew Wong, now an employee at Chevron, helped in much of the test cell setup during his time as a Masters student, and Sakthish Sathasivam assisted in the remainder of the effort to get the engine system operational, as well as helping with data collection of the first phase of research. Karthik Kameshwaran helped run the engine and take data during the deposit collection phase of this research, and both Sakthish and Karthik contributed to the analysis presented in Chapter 9 of this document (Karthik and I have a working draft of a paper related to this material). It was a great pleasure to work alongside them and this project could not have been so fruitful without their assistance. I want to also thank Dr. Mark Hoffman, Ben Lawler and Dr. Orgun Gralp. Orgun, now an employee at GM, has been able to provide support for the engine setup, which initially came from GM. Mark, the de facto elder statesman of the W.E. Lay Automotive Laboratory, helped me to get my bearings when I was first starting in the lab, and provided vital advice throughout the experimental process. Ben has been a wonderful colleague to work alongside and was always available for useful discussions regarding my work. I'd also like to thank Dr. Joel Forman, who might have thought I looked busy at times...when in reality his visits to my office were much needed breaks, and ultimately helped to keep me focused more than he knows. There are more students than I can list here, all of whom have been more than just talented co-workers; rather, they have been great friends and made my time here at Michigan extremely worthwhile.

Finally, I would like to thank all my other colleagues, family, friends (both here in Ann Arbor and back in Dallas), and my loving fiancée, Jessica, for all the positive support I have received through the long, and oftentimes arduous graduate school process. Without this network of advocates, I believe the completion of my dissertation would have been significantly more intractable.

TABLE OF CONTENTS

ACKNOWLEDGEMENTS	ii
LIST OF FIGURES	x
LIST OF TABLES	xxxii
NOMENCLATURE	xxxiv
ABSTRACT	xxxix
CHAPTER 1 - PROJECT INTRODUCTION AND BACKGROUND	1
1.1 Project Introduction	1
1.2 HCCI Background	3
1.3 Fuel Chemistry Overview	11
1.4 Combustion Chamber Deposits	15
1.4.1 Deposits in Spark-Ignited Engines	16
1.4.2 Deposits in HCCI Engines	35
1.5 Motivation for the Research	48
1.6 Research Objectives and Projected Contributions	55
CHAPTER 2 – EXPERIMENTAL SETUP	59
2.1 Engine Specifications	59
2.2 Intake Air System	64
2.3 Exhaust System	66
2.4 Fuelling Hardware	67
2.5 Data Acquisition	71
2.5.1 Crank-Angle Resolved Measurements	72
2.5.2 Time Resolved Measurements	81

CHAPTER 3 – TECHNIQUES AND INSTRUMENTATION TO STUDY THE INTERPLAY OF FUELS, HCCI COMBUSTION AND DEPOSITS	86
3.1 Crank-Angle and Time-Resolved Measurements for Combustion Analysis	86
3.2 Heat Flux Probes	87
3.3 Heat Release Analysis	90
3.4 Fischer Dualscope	95
3.5 Thermal Diffusivity Measurements.....	97
3.6 Microscopic Instruments.....	99
3.6.1 SEM/ESEM	101
3.6.2 TEM	104
3.7 Spectroscopic Devices	107
3.7.1 XEDS.....	108
3.7.2 XPS	115
3.8 Small-Angle X-Ray Scattering (SAXS).....	120
CHAPTER 4 – EXPERIMENTAL UNCERTAINTY IN INSTRUMENTATION AND METHODS	131
4.1 Introduction to Sources of Uncertainty.....	131
4.2 Pressure Transducers and Crank-Angle Resolved Measurements.....	131
4.3 Temperatures, Mass Flows and other Time-Resolved Signals.....	133
4.4 Resolution Error Associated with Analog-to-Digital Data Acquisition Hardware	135
4.5 Propagation of Errors in Derived and Calculated Quantities.....	136
4.6 Precision Error and Uncertainty for Other Measurement Methods Employed	137
CHAPTER 5 – EXPERIMENTAL METHODS TO CHARACTERIZE THE EFFECTS OF FUELS ON HCCI COMBUSTION.....	139
5.1 Experimental Details	139
5.1.1 Compensated Load Sweep.....	145
5.1.2 HCCI Limits of Operability	145
5.1.3 Intake Air Temperature Sensitivity	146
5.2 Isolating the effects of Fuels from Deposit Growth	148

CHAPTER 6 – IMPACT OF REFINERY STREAM FUELS PROPERTY VARIATION ON LOAD SENSITIVITY OF HCCI COMBUSTION	152
6.1 Introduction	152
6.2 Sensitivity to Load	153
6.3 Fuel Efficiency Analysis	158
CHAPTER 7 – HCCI LIMITS OF OPERABILITY FOR REFINERY STREAM GASOLINE.....	170
7.1 Introduction	170
7.2 HCCI Operating Range	170
7.3 Variation in Limits with Engine Speed	176
7.4 Heat Release Analysis of HCCI Operating Limits.....	179
CHAPTER 8 – EFFECTS OF ETHANOL ADDITION ON HCCI COMBUSTION.....	186
8.1 Introduction	186
8.2 Load Sweeps with Matched Combustion Phasing.....	186
8.3 HCCI Limits of Operability	196
8.4 Sensitivity to Intake Air Temperature	204
CHAPTER 9 – INTAKE AIR TEMPERATURE SENSITIVITY AND THE OCTANE INDEX MODEL	210
9.1 Introduction	210
9.2 Octane Index Background	210
9.3 Octane Index analysis - Kalghatgi model	213
9.3.1 Calculation of 'K'	213
9.3.2 Calculation of Octane Index	214
9.4 Modifications to the Correlation	223
9.5 Comparison to Shibata-Urushihara model	230
9.6 Heat Release and the Modified Octane Index.....	235
CHAPTER 10 – EXPERIMENTAL METHODS FOR COMBUSTION CHAMBER DEPOSIT STUDIES.	238
10.1 Conditioning Sweeps	238
10.1.1 Tracking the Advance of Combustion Phasing and Equilibrium	241
10.1.2 Compensated Intake Temperature Points for Thermal Diffusivity	242

10.2	Testing in a Fully-Conditioned Combustion Chamber	244
10.2.1	“Dirty” Operating Limits.....	244
10.2.2	Intake Temperature Sweeps for a Fully-Conditioned Combustion Chamber	246
10.2.3	Coolant Temperature Studies for the CCD Coated Combustion Chamber.....	247
10.2.4	Thickness Mappings.....	247
CHAPTER 11 – EFFECT OF FUEL COMPOSITION ON HCCI COMBUSTION CHAMBER DEPOSITS		
.....		249
11.1	Introduction.....	249
11.2	Deposit Conditioning Sweeps.....	250
11.3	Advancement of Combustion Phasing and Characteristics of the Engine Performance as Deposits Accumulate	255
11.4	Cylinder Head Surface Temperature and Heat Flux.....	264
11.5	A Brief Note on Repeatability of Conditioning Results.....	276
CHAPTER 12 – THE ROLE OF ADDITIVE PACKAGES IN HCCI DEPOSIT ACCUMULATION		279
12.1	Introduction.....	279
12.2	Thickness Mappings for PBA and PEA Derived Deposits	279
12.3	In-Situ Engine Analysis during the Accumulation Process.....	286
12.4	Changes in Heat Flux at the Wall Surface and CCD Layer Interface.....	295
CHAPTER 13 – A STUDY OF THE PROPERTIES OF HCCI DEPOSITS FOR REFINERY STREAM FUELS		299
13.1	Introduction.....	299
13.2	Qualitative Microscopic Imaging	300
13.2.1	Scanning Electron Microscopy (SEM).....	301
13.2.2	Transmission Electron Microscopy (TEM).....	304
13.3	Spectroscopic Results.....	310
13.3.1	X-Ray Energy Dispersive Spectroscopy (XEDS).....	311
13.3.2	X-Ray Photoelectron Spectroscopy (XPS)	314
13.4	X-Ray Diffractometry.....	324

13.5	Thermal Diffusivity Studies	331
CHAPTER 14 – IMPACT OF A FULLY-CONDITIONED PISTON AND CYLINDER HEAD ON HCCI COMBUSTION.....		337
14.1	Introduction	337
14.2	Variation of Charge Temperature to Offset CCD Growth.....	337
14.2.1	Intake Air Temperature Adjustment.....	338
14.2.2	Coolant Temperature Adjustment	342
14.3	Impact of an Equilibrated CCD Layer on the HCCI Operating Range	347
CHAPTER 15 – CONCLUSIONS AND CONTRIBUTIONS TO INTERNAL COMBUSTION ENGINE RESEARCH		358
15.1	Introduction	358
15.2	Scientific Contributions	358
15.2.1	Fuels and HCCI Combustion	359
15.2.2	Fuels and Deposit Formation	361
15.3	Conclusions	363
15.3.1	Summary of Refinery Stream Fuels and Combustion Work.....	363
15.3.2	Summary of Fuels and Deposits Work	368
15.4	Suggestions for Continuing Efforts	373
REFERENCES.....		375

LIST OF FIGURES

Figure 1.1 - Comparison of spark ignition (SI), compression ignition (CI), and homogeneous charge compression ignition (HCCI); note that both SI and CI have a direct trigger in the form of a spark or fuel injection respectively, whereas HCCI does not	4
Figure 1.2 - Experimental data demonstrating the sensitivity of the HCCI combustion event to charge temperature; note that the Chemkin model envisions the entire combustion chamber as a single zone, thus the lengths of burn durations are under-predicted [6]	7
Figure 1.3 - HCCI sensitivity to intake charge temperature; notice that combustion phasing and burn duration correlate well with an increase in intake air temperature [5] .	8
Figure 1.4 - Effects of coolant temperature increase on HCCI; burn durations here do not seem to change in a manner consistent with only a change of phasing, as wall effects influence the HCCI combustion event [5].....	8
Figure 1.5 - A similar wall effect is seen with deposit growth as with coolant temperature increase, as burn duration changes do not correlate well with combustion phasing differences [5].....	9
Figure 1.6 - Chemical structure of 2,2,4 trimethylpentane, $(\text{CH}_3)_3\text{CCH}_2\text{CH}(\text{CH}_3)_2$, usually referred to as iso-octane, a common paraffin (alkane)	12
Figure 1.7 - Ethylene, C_2H_4 , the simplest olefin (also called alkenes)	12

Figure 1.8 - Toluene, C_7H_8 , an example of an aromatic molecule, composed of one benzene ring and one side methyl group; it is often added to gasoline to increase the octane rating 12

Figure 1.9 - Time to auto-ignite for propane, a paraffin, in a static reactor [9]; notice how in the intermediate temperature range, the time to autoignite increases with increasing temperature..... 13

Figure 1.10 - Intake temperature required to maintain the 50% mass fraction burned point at a range of equivalence ratios [10]..... 15

Figure 1.11 - Conceptual image of the auto-ignition process as experienced by a traditional spark-ignited gasoline engine 16

Figure 1.12 - A comparison of the relative combustion chamber deposits (CCD) formation tendencies of fuels at increasing boiling point; notice that at a given boiling point, aromatic structures tend to form more deposition [10]..... 19

Figure 1.13 - A closer look at primarily aromatic fuel structures and the difference in 1, 2, and 3-ring formation tendencies; 3-ring aromatics have very high boiling points and a commensurate level of CCD accumulation [10] 20

Figure 1.14 - Chemical structure of common aromatic molecules [3]..... 24

Figure 1.15 - The left plot shows deposit weight extracted from insertion coupons on a CFR engine as the surrogate fuel's concentration of toluene (an aromatic) increases; the right plot pictorially displays what had accumulated on the coupons and the weight of deposits buildup [15] 25

Figure 1.16 - Illustration of the importance of aromatic side chains on CCD formation; the right graphic shows the insertion coupons from the experiment and the weight of extracted deposits from the probe, as well as an average across all the coupons [15]. 26

Figure 1.17 - CA10 and CA10-90 burn duration curves shown over the course of passive conditioning [7]..... 36

Figure 1.18 - Emissions indices plotted against time as the deposit layer accumulates [7] 38

Figure 1.19 - Rate of net heat release in the engine as time progresses and the CCD layer builds [7] 38

Figure 1.20 - Progression of heat flux profiles as the combustion chamber is passively conditioned [7] 40

Figure 1.21 - Phasing of the surface temperature peak from a heat flux probe as the deposit layer grows with time [5] 41

Figure 1.22 - Changing thermal diffusivity of the deposit layer as the thickness increases [7] 43

Figure 1.23 - Shift in HCCI operating limits comparing a clean piston to one that is coated with an equilibrated layer of deposits (fully-conditioned) [5] 44

Figure 1.24 - Comparison of fuel efficiency for a speed sweep of an engine free of deposits as compared to one that has a deposit coating [5]..... 46

Figure 1.25 - Conceptual diagram of the effect of heat transfer and combustion phasing on Indicated Specific Fuel Consumption (ISFC) [74, 75]..... 47

Figure 1.26 - Comparison of combustion stability from a clean to a conditioned engine over a speed sweep [5] 47

Figure 1.27 - Example of how a few different fuel blends can influence heat release and pressure traces in an HCCI engine at the same operating condition [78]	50
Figure 1.28 - Aromatic concentrations of sampled pump gasoline throughout the United States [76]	51
Figure 1.29 - Olefin concentrations of sampled pump gasoline throughout the United States [76]	51
Figure 1.30 - Research Octane Number (RON) of sampled pump gasoline throughout the United States [76]	52
Figure 1.31 - Qualitative visual representation of the relative sizes of the HCCI and SI operating maps for naturally aspirated operation, adapted from [95]	53
Figure 2.1 - Picture of the engine setup highlighting some of the major components ...	59
Figure 2.2 - Cross-section of the single-cylinder HCCI Chevron fuels engine	60
Figure 2.3 - Valve profiles for the Chevron HCCI fuels engine highlighting the exhaust rebreathing event during the intake valve lift [7]	61
Figure 2.4 - The piston used in the single-cylinder GM HCCI fuels engine; this particular piston has a buildup of deposition clearly shown, with a notable clean spot centrally located where the fuel spray impinges upon the piston crown	63
Figure 2.5 - Schematic of the experimental engine cylinder head showing the fuel spray targeting in relation to the piston bowl (indicated by the dashed circle in the top image)	63
Figure 2.6 - Critical flow orifice system comprised of the orifices of known diameter to the left of the ball valves, and two manifolds to dampen any effects of pressure changes in the shop air	65

Figure 2.7 - Intake runner connecting the intake plenum to the engine; the slotted metal piece on the far side of the runner is for adjusting swirl (one of the ports in the runner can be blocked with a moveable plate)	65
Figure 2.8 - Exhaust system highlighting the major components	66
Figure 2.9 - Piston-style accumulator used to pressurize the fuel for direct injection	68
Figure 2.10 - The other portion of the fuel system located on the opposite side of the tower from the accumulator, with pneumatic valves to isolate the low and high pressure sides, as well as the fuel flow meter	69
Figure 2.11 - Data acquisition boom where the high speed and low speed measurement hardware is housed	71
Figure 2.12 - High level schematic outlining the connection of high-speed pressure signals to the high-speed data acquisition system	72
Figure 2.13 - Schematic showing the control signals and flow necessary for ignition and spark control on the HCCI fuels engine.....	75
Figure 2.14 - The 1PPC and 1PPR signals are used to determine the separation between cycles, as well as what portion of the cycle the engine is currently undergoing	75
Figure 2.15 - Schematic showing the location of high-speed heat flux probes in the HCCI fuels engine cylinder head.....	77
Figure 2.16 - Detailed schematic of the heat flux probe	78
Figure 2.17 - High level schematic outlining the connection of high-speed pressure signals to the high-speed data acquisition system	79

Figure 2.18 - Conceptual schematic of the heat flux probes with a CCD layer accumulated on the surface	80
Figure 2.19 - Indicom version 2.1 software used to capture crank-angle resolved measurements	81
Figure 2.20 - Low-speed, NI SCXI hardware with the chassis shown on the left, SCXI-1102 card on the top right, and SCXI-1300 isothermal block on the bottom right	82
Figure 2.21 - Screen capture of the interface for the low-speed system; the boxes in the upper left are fuel properties which are entered before each experiment and saved with the low-speed data so that the Matlab post-processing code has access to these properties during analysis	85
Figure 3.1 - A conceptual picture of the method used to calculate heat flux in the engine with the custom-made heat flux probes; reprinted from Overbye et al. [1].....	88
Figure 3.2 - Fischer Dualscope instrument used to measure the thickness of a layer over a substrate material.....	96
Figure 3.3 - Conceptual view of the Eddy current method [115].....	97
Figure 3.4 - A graphical example demonstrating how thermal diffusivity is calculated using the time difference in peak temperatures on a heat flux probe subjected to cyclic heating (in this case from a specialized laboratory oven, and not the HCCI engine); the red trace in the figure is the heat flux provided by the graphite element cut into square waves by the chopping wheel; reprinted from Hoffman [1].....	98
Figure 3.5 - A diagram showing the schematic of a scanning electron microscope [116]	101

Figure 3.6 – Standard Electron Microscope (SEM) mounting stub; samples are attached to this specimen pin, and loaded into the vacuum chamber 102

Figure 3.7 – Transmission Electron Microscope (TEM) grid storage device shown on the left with an individual grid for TEM study on the right 105

Figure 3.8 - A schematic of the lens system in a TEM (left) [119] and an example of bright-field imaging (right), the preferred technique that will be used to study engine deposits (right) [120]. In bright-field imaging, the optical and objective aperture axes are collinear so that only a direct beam is transmitted through the microscope; electrons scattered or diffracted at large angles are filtered out by the objective aperture and do not contribute to the image [119]. 106

Figure 3.9 - The electron-hole interaction that occurs during X-ray Energy Dispersive Spectroscopy (XEDS) analysis [116]. 109

Figure 3.10 - This schematic diagram of an Energy Dispersive Spectroscopy (EDS) mechanism shows how an incoming X-ray is received by the detector, and the corresponding voltage pulses which are seen as X-rays hit the detector are amplified for further processing by a field effect transistor (FET). Note that both the collector and the FET are kept at approximately 100K by the supply of liquid nitrogen, in order to minimize background noise and hinder Li atoms from drifting within the detector apparatus [120]. 110

Figure 3.11 - Engine deposits cold-mounted in epoxy and molding cup used for the mounting process 112

Figure 3.12 - An example of the spectrum collection from an XEDS device; the solid line represents the observed SEM spectrum, while the dashed line indicates background

continuum X-rays generated when electrons come close to an atomic nucleus and slow down; due to the loss in kinetic energy, the electron emits an X-ray, which can be at any wavelength and energy, unlike the characteristic X-rays [124]..... 114

Figure 3.13 - Here, the scenarios of electron emission when utilizing an X-ray Photoelectron Spectroscopy (XPS) analysis method are displayed..... 116

Figure 3.14 - A sample carbon scan of engine deposits (taken from another engine at UM) showing the 4-peak fit method; the experimental data is the more jagged curve 120

Figure 3.15 - Diagram of a position-sensitive SAXS instrument pictured with 1) the radiation source, 2) and 3) the collimation diaphragms for focusing the beam, 4) the sample, and 5) the 2-D detector surface [127] 122

Figure 3.16 - Classical manner to visualize the diffraction of X-rays by a single particle where 3 is the monochromating crystal, 6 is the sample, 8 is the detector and other numbered lines are collimating and guard slits in the apparatus; reprinted from Sinha [129] 124

Figure 3.17 - The black trace is an example of a scattering curve of measured intensity against the scattering vector q for carbon aerogel. The blue region highlighted in the bottom right corner of the plot is approaching the region of wide-angle SAXS which is not studied in this work; reprinted from Fairén-Jiménez et al. [132] 126

Figure 3.18 - Simplified visualization of the characteristic function for small-angle scattering. Note that the $\gamma(r)$ has been replaced with $g(r)$ using the notation of in this publication; reprinted from Kraus [133]..... 127

Figure 5.1 - Matrix of test fuels' properties showing the relative locations of the 10% ethanol blends..... 140

Figure 5.2 - Effect of the cleaning methodology on the location of net release rates, and ultimately on the location of the combustion event before and after cleaning for RD3-87 and RRA using the cleaning dose of Techron (1oz/gal fuel); bear in mind that the combustion chamber is never truly 'clean' using this method, but in fact, always contains some level of CCD growth..... 150

Figure 6.1 - Intake air temperature compensation required to maintain constant combustion phasing over a range of engine loads – high aromatic fuels 153

Figure 6.2 - Intake air temperature compensation required to maintain constant combustion phasing over a range of engine loads – high olefin fuels 155

Figure 6.3 - Comparison of the changing sensitivity of engine operation to fuelling rate for highly aromatic (left) and olefinic fuels (right)..... 156

Figure 6.4 - Indicated Mean Effective Pressure vs. Indicated Specific Fuel Consumption on a mass basis for high aromatic fuels; measured points and predicted trend lines.. 159

Figure 6.5 - Indicated Mean Effective Pressure vs. Indicated Specific Fuel Consumption for the high olefin fuels on a mass basis; measured points and predicted trend lines. 160

Figure 6.6 - Indicated Mean Effective Pressure vs. Indicated Specific Fuel Consumption on a volumetric basis for high aromatic fuels; this more accurately reflects “pump” efficiency as gasoline is sold on a volumetric and not a mass basis 161

Figure 6.7 - Indicated Mean Effective Pressure vs. Volumetric Indicated Specific Fuel Consumption for the high olefin fuels 162

Figure 6.8 - Indicated Mean Effective Pressure plotted vs. the total energy content of the injected fuel into the cylinder per cycle for the high aromatic fuels..... 163

Figure 6.9 - Indicated Mean Effective Pressure vs. the total energy content of the injected fuel for the high olefin fuels	163
Figure 6.10 - Indicated Thermal Efficiency for all the test fuels at the baseline condition	165
Figure 6.11 - Net Heat Release Rates for all the test fuels at their baseline operating point	167
Figure 6.12 - Combustion efficiency and CA10-CA90 burn duration determined at the baseline operating points for the complete range of fuels tested	167
Figure 7.1 - Limits of operability for high aromatic fuels in the test matrix.....	171
Figure 7.2 - Limits of operability for the test matrix high olefin fuels.....	172
Figure 7.3 - Comparing the overall operating map area for the test matrix fuels, normalized to the area for RD3-87 (not shown in previous figures)	175
Figure 7.4 - Differences between CA50 at the HLL and LLL for fuels with high aromatics	176
Figure 7.5 - Differences between the CA50 at the HLL and LLL for high olefin fuels ..	177
Figure 7.6 - CA50 for the lower and upper limits of the operating range sweep.....	180
Figure 7.7 - CA10-CA90 burn durations for the limits of operability sweep for all the test matrix fuels.....	181
Figure 7.8 - CA50 versus engine load for all the LLL and HLL points with each refinery stream fuel	182
Figure 7.9 - CA10-CA90 burn durations against engine load for the operating range sweep of all the test matrix fuels	182

Figure 7.10 - Net heat release rates in the instability limit for all test matrix fuels at 1600 RPM; the engine loads (BMEP) for each of these points is listed in the legend 184

Figure 7.11 - Net heat release rates in the ringing limit for all test matrix fuels at 1600 RPM; as with the previous figure, the BMEP for each point is given in the legend for each point..... 185

Figure 8.1 - Intake air temperature compensation required to maintain constant combustion phasing over a range of engine loads – 20% ethanol fuels..... 187

Figure 8.2 - Intake air temperature compensation required to maintain constant combustion phasing over a range of engine loads – 10% ethanol fuels..... 188

Figure 8.3 - Indicated Mean Effective Pressure vs. Indicated Specific Fuel Consumption on a mass basis for the 20% ethanol fuels; measured points and predicted trend lines 191

Figure 8.4 - Indicated Mean Effective Pressure vs. Indicated Specific Fuel Consumption on a mass basis for the 10% ethanol fuels; measured points and predicted trend lines 191

Figure 8.5 - Indicated Mean Effective Pressure vs. Indicated Specific Fuel Consumption on a volumetric basis; this is a better representation of a fuel efficiency that consumers would realize, because gasoline is sold by volume and not by mass. The arrows in the plot connect pairs of similar fuels that differ chiefly by ethanol content, e.g. B10 and B20 193

Figure 8.6 - Combustion efficiency and CA10-CA90 burn duration determined at the baseline operating points for the 20% ethanol fuels..... 195

Figure 8.7 - HCCI operating limits for the 20% ethanol fuels over the speed sweep... 196

Figure 8.8 - Comparison of the HCCI operating limits of B10 and B20 over a sweep of speed	197
Figure 8.9 – Comparison of the HCCI operating limits of C10 and C20 over a sweep of speed	198
Figure 8.10 – Comparison of the HCCI operating limits for F10 and F20 over a sweep of speed	198
Figure 8.11 - Comparison of the HCCI operating limits of G10 and G20 over a sweep of engine speeds.....	199
Figure 8.12 - Normalized HCCI operating range area of all the 10% and 20% ethanol fuels, where the previously calculated area of the baseline fuel RD3-87 is equivalent to 1 (not shown); essentially, this represents a percent improvement of each fuel's operating range over the range of RD3-87	201
Figure 8.13 - Differences in combustion phasing, given by CA50, between the HLL and LLL across the speed range for all 20% ethanol fuels.....	202
Figure 8.14 - Changes in combustion phasing over the speed sweep, given as the difference in CA50 at the HLL and LLL, for the 10% ethanol fuels.....	203
Figure 8.15 - CA50 against intake air temperature sweep at constant fuelling rate for the 20% ethanol fuels.....	205
Figure 8.16. CA50 against intake air temperature sweep at constant fuelling rate for the 10% ethanol fuels.....	205
Figure 8.17 - CA10-CA50 burn duration for 20% ethanol fuels over the sweep of intake air temperature	207

Figure 8.18 - CA10-CA50 burn duration for 10% ethanol fuels over the sweep of intake air temperature	208
Figure 9.1 - CA50 versus Octane Index (OI) at an intake air temperature of 81°C	215
Figure 9.2 - CA50 vs. OI at intake temperature 65°C for 10% and 20% ethanol fuels	217
Figure 9.3 - CA50 for 10% ethanol fuels at all intake temperatures	219
Figure 9.4 - CA50 for 20% ethanol fuels at all intake temperatures	219
Figure 9.5 - CA50 vs. OI at intake temperature 50°C; high aromatic and olefin fuels plotted separately	220
Figure 9.6 - CA50 for high aromatic fuels at all intake temperatures.....	222
Figure 9.7 - CA50 for high olefin fuels at all intake temperatures.....	223
Figure 9.8 - CA50 vs. OI at intake temperature 81°C; OI calculated with new correlation	226
Figure 9.9 - CA50 vs. OI at intake temperature 65°C with the new OI correlation; 10% and 20% ethanol fuels plotted separately.....	228
Figure 9.10 - CA50 vs. OI at intake temperature 65°C with new OI correlation; high aromatic and high olefin fuels plotted separately	229
Figure 9.11 - CA20 vs. HCCI Index at intake temperature 50°C; SU model using UM engine data	232
Figure 9.12 - CA20 vs. HCCI Index at intake temperature 50°C using the SU model; high aromatic and high olefin fuels plotted separately.....	233
Figure 9.13 - CA20 vs. HCCI Index at intake temperature 50°C; 10% and 20% ethanol fuels plotted separately	234

Figure 9.14 - Net heat release rate at 65°C intake temperature for a selection of fuels	236
Figure 9.15 - Zoomed in version of Figure 9.14 highlighting the relationship between the location of net heat release rate and OI	237
Figure 10.1 – Plot showing the changes the combustion event undergoes as the layer builds in an HCCI engine; these particular curves were generated from data taken in an engine of similar geometry using our baseline RD3-87 fuel, in a previous University of Michigan study [5]	241
Figure 10.2 - Evolution of cylinder head surface temperature profile with engine run-time as the CCD layer grows on the walls [7].....	243
Figure 10.3 - Effect of deposits on HCCI limits of operability; notice that the “clean” operating map is shifted down when the combustion chamber is fully-conditioned.....	245
Figure 11.1 - Deposit layer formed by D10 fuel on the piston; measurements given in μm	252
Figure 11.2 - CCD layer formed by CARBOB+10%EtOH on the piston; measurements given in μm	252
Figure 11.3. Deposit layer on the cylinder head resulting from the D10 fuel; measurements given in μm	254
Figure 11.4 - CCD layer on the cylinder head resulting from CARBOB+10%EtOH; measurements given in μm	255
Figure 11.5 - Change in combustion phasing given by CA50 as the deposit layer accumulates	256

Figure 11.6 - Ringing intensity increase as deposits build in-cylinder over the conditioning sweep.....	258
Figure 11.7 - Coefficient of variance (COV) percentage of indicated mean effective pressure (IMEP) during the conditioning sweeps of the two fuels	259
Figure 11.8 - Emissions index for NO _x (EINO _x) over the course of the conditioning sweep for each fuel	261
Figure 11.9 - Emissions index for hydrocarbons (EIHC) while deposits accumulate in-cylinder for each fuel	261
Figure 11.10 - Change in combustion efficiency calculated from emissions measurements as a function of engine run time.....	262
Figure 11.11 - Probe 1 surface temperature for the D10 blend while the deposit layer accumulates	266
Figure 11.12 - CARBOB+10%EtOH temperature at the interface between the surface of probe 1 and CCD interface, changing with engine run-time	266
Figure 11.13 - Surface temperatures for probe 2 located in the “anti-squish” region as deposits build over the surface of the thermocouple for D10 fuel.....	269
Figure 11.14 - The surface temperature for probe 2 (“anti-squish”) for CARBOB+10%EtOH at the CCD interface, changing with engine run-time	270
Figure 11.15 - D10 heat flux probes after engine disassembly from the fully-conditioned state; the probe from the “squish” region is on the left and the probe from the “anti-squish” region is on the right; the thermocouple junction partly visible is highlighted by the box in the picture	270

Figure 11.16 - Heat flux through the squish side probe in the cylinder head as the CCD layer evolves for D10 fuel.....	272
Figure 11.17 - CARBOB+10%EtOH heat flux at location 1 in the cylinder head as the CCD layer accumulates.....	272
Figure 11.18 - Cylinder head probe 2 heat flux during the deposit conditioning sweep for D10.....	273
Figure 11.19 - CARBOB+10%EtOH heat flux at cylinder head location 2 as the deposit layer builds over the probe.....	273
Figure 11.20 - In-cylinder net heat release rates for the D10 blend as deposits grow.	275
Figure 11.21 - CARBOB+10%EtOH net heat release rates in-cylinder with engine run-time.....	276
Figure 11.22 - Two conditioning sweeps for the base D10 fuel with no additive, showing CA50 against engine run time.....	277
Figure 12.1 - Deposits on the piston after a conditioning sweep with D10+PBA fuel ..	280
Figure 12.2 - CARBOB+10%EtOH+PBA piston deposits after a conditioning sweep .	281
Figure 12.3 - D10+PEA deposits on the piston top after conditioning	282
Figure 12.4 - CARBOB+10%EtOH+PEA piston deposits at the equilibrium thickness	283
Figure 12.5 - D10+10%EtOH+PBA cylinder head CCD layer at the equilibrium thickness	284
Figure 12.6 - CARBOB+10%EtOH+PBA cylinder head deposits at the equilibrium thickness	284
Figure 12.7 - Cylinder head deposit layer thicknesses for the D10+PEA fuel after conditioning	285

Figure 12.8 - CARBOB+10%EtOH+PEA deposits on the cylinder head after a conditioning sweep; the asterisks for the exhaust valve measurements refer to the fact that the layer was so thin a measurement could not be taken with the Dualscope	285
Figure 12.9 - Change in combustion phasing (CA50) over the course of a conditioning sweep for D10+PBA and D10+PEA	287
Figure 12.10 - CA50 advance during a deposit accumulation sweep for CARBOB+10%EtOH+PBA and CARBOB+10%EtOH+PEA.....	289
Figure 12.11 - Emissions index for NO _x (EINO _x) species in the exhaust as deposits accumulate in-cylinder; from the D10+PBA and D10+PEA tests	292
Figure 12.12 - Emissions index of NO _x (EINO _x) in the exhaust as the CCD layer builds for the CARBOB+10%EtOH+PBA and CARBOB+10%EtOH+PEA fuels	292
Figure 12.13 - D10+PBA and D10+PEA evolution of the emissions index of hydrocarbon species as the deposit layer accumulates	293
Figure 12.14 - CARBOB+10%EtOH+PBA and CARBOB+10%EtOH+PEA hydrocarbon emissions index (EIHC) as the CCD builds over a conditioning sweep.....	294
Figure 12.15 - D10+PBA head probe location 1 heat flux change during deposit buildup	295
Figure 12.16 - CARBOB+10%EtOH+PBA change in heat flux at probe location 1 during deposit accumulation.....	296
Figure 12.17 - Heat flux evolution during deposit buildup for D10+PEA at head probe location 1	297
Figure 12.18 - Heat flux evolution during deposit buildup for CARBOB+10%EtOH+PEA at head probe location 1	298

Figure 13.1 - General area over which deposits were collected for ex-situ analysis ...	300
Figure 13.2 - Deposits from the D10 base fuel on the left side (1000 times magnification) and CARBOB+10%EtOH on the right side image (2000 times magnification) with fissure type structures in the flakes.....	301
Figure 13.3 - D10+PBA derived deposits on the left image (1500 times magnification) and CARBOB+10%EtOH deposits on the right side (1500 times magnification)	303
Figure 13.4 - Deposits samples from PEA additized fuels; D10 on the left (2500 times magnification) and CARBOB+10%EtOH on the right (1500 times magnification)	304
Figure 13.5 - Deposit sample from D10+PBA (at 300k magnification) showing features of amorphous carbon	305
Figure 13.6 - An example of soot particles taken from diesel exhaust [172]	306
Figure 13.7 - Deposit flake from the CCD layer formed by D10 base fuel with soot features marked by circles, 300k magnification.....	307
Figure 13.8 - CARBOB+10%EtOH+PBA derived deposit flake showing some signs of soot-like behavior as marked with circles; 300k magnification	308
Figure 13.9 - Proposed mechanism for in-cylinder CCD formation [33]	309
Figure 13.10 - D10 derived deposit XEDS spectrum.....	312
Figure 13.11 - D10+PBA derived deposit XEDS spectrum	312
Figure 13.12 - D10+PEA derived deposit XEDS spectrum	313
Figure 13.13 - Spectra for the unadditized D10 and CARBOB+10%EtOH deposit samples scanned by XPS (D10 on the top, CARBOB on the bottom); here the dominant elements, C and O, are highlighted	316

Figure 13.14 - Carbon scan for the unadditized D10 and CARBOB+10%EtOH deposits (D10 on the top, CARBOB on the bottom)	317
Figure 13.15 - Core scan for deposits from both base fuel types dosed with a PBA additive package; carbon and oxygen peaks are highlighted along with atomic composition (D10+PBA on the top, CARBOB+PBA on the bottom).....	318
Figure 13.16 - Carbon scan for deposits samples from both fuel types dosed with the PBA additive package (D10 on the top, CARBOB on the bottom)	319
Figure 13.17 - PEA additized deposit samples core scan with carbon and oxygen peaks highlighted (D10 on the top and CARBOB on the bottom)	320
Figure 13.18 - Carbon scan for deposit samples from PEA additized fuels (D10 on the top, CARBOB on the bottom)	321
Figure 13.19 - Scattering curves for deposits derived from D10 blends showing the collected intensity against the scattering vector \mathbf{q}	325
Figure 13.20 - CARBOB+10%EtOH deposit sample scattering curves with intensity plotted against the scattering vector \mathbf{q}	326
Figure 13.21 - Characteristic function for the D10 deposit samples against the translation length r , measured in angstroms	327
Figure 13.22 - Characteristic function for the CARBOB+10%EtOH deposit samples against the translation length r , measured in angstroms	328
Figure 13.23 - Thermal diffusivity for deposits samples of all tested fuels against thickness measured on the coaxial heat flux probe.....	332

Figure 14.1 - CA50 combustion phasing over a sweep of intake air temperature for all the test fuels and additive packages; D10 blends are on the left and CARBOB+10%EtOH blends are on the right 339

Figure 14.2 - Burn length (CA10-CA90) for all the test fuels over a sweep of intake air temperature; D10 blends are on the left and CARBOB+10%EtOH on the right 340

Figure 14.3 - Combustion efficiency for the test fuels run in a fully-conditioned combustion chamber with D10 blends on the left and CARBOB+10%EtOH on the right 341

Figure 14.4 - CA50 combustion phasing for a sweep of coolant temperature in a fully-conditioned combustion chamber for all fuels and additive packages 343

Figure 14.5 - Burn durations from CA10-CA90 over a sweep of coolant temperature in the fully-conditioned combustion chamber for all test fuel blends 344

Figure 14.6 - Coolant temperature sweeps and the resulting combustion efficiencies in a conditioned combustion chamber 345

Figure 14.7 - ISFC against coolant temperature for the conditioned combustion chambers with D10 on the left and CARBOB+10%EtOH on the right 347

Figure 14.8 - HCCI limits of operability for all the CCD layers formed with D10 fuel blends compared to the limits test where the deposit chamber was not fully-conditioned 349

Figure 14.9 - Comparison of the operating limits for the CARBOB+10%EtOH blends with a fully-conditioned combustion chamber and the “clean” case 349

Figure 14.10 - HCCI operating map areas for D10 blends normalized to RD3-87 on the left and the amount that conditioned operating maps overlap with the “clean” range on the left 351

Figure 14.11 - CARBOB+10%EtOH normalized operating areas on the left and overlap areas on the right; note that the fuel designation has been shortened for space considerations 352

Figure 14.12 - CA50 of the load limits for the D10 and CARBOB+10%EtOH blends shown against engine load (BMEP) 354

Figure 14.13 - CA10-90 burn duration at the limits against engine load (BMEP) for the both the D10 and CARBOB+10%EtOH blends 355

Figure 14.14 - Combustion efficiency of the D10 and CARBOB+10%EtOH blends for the operating limits sweep against speed; D10 blends are pictured on the left, CARBOB blends are on the right..... 356

LIST OF TABLES

Table 1.1 - Rules for determining the number of oxygen additions to a hydrocarbon molecule ($C_x \rightarrow C_xO_z$) dependent on its structure where z is the number of oxygen atoms that can be added during oxidation.....	22
Table 1.2 - Oxidation of polycyclic aromatic hydrocarbons [3]	23
Table 1.3 - Summary of factors effecting CCD formation [4]	23
Table 2.1 - Valve Timings.....	61
Table 2.2 - Engine Specifications	62
Table 2.3 - Summary of Low-Speed Signals	83
Table 4.1 – Uncertainties for Important Derived Quantities.....	137
Table 5.1 – Fuels Specifications	141
Table 5.2 - Baseline Operating Conditions*	142
Table 5.3 - Fuelling Rates for Temperature Sensitivity Studies.....	147
Table 8.1 - A summary of the rates of intake temperature compensation from Figures 8.1 and 8.2; here, the “dominant” chemical component is bolded, whether the fuel was a high aromatic fuel, or a high olefin fuel.....	189
Table 8.2: Change in density between 10% and 20% ethanol fuel pairs.....	194
Table 8.3 - Differences between the maximum and minimum ΔCA_{50} for a given fuel in Figures 8.13 and 8.14	204
Table 9.1 - Values of K for different intake air temperature conditions	214

Table 9.2 - Strength of correlation between CA50 and OI for all the intake temperature conditions given by R ² value of the best fit line	215
Table 9.3 - Strength of correlation with fuel blends of 10% and 20% ethanol as determined from a best fit line	217
Table 9.4 - Strength of the OI correlation with high aromatics and high olefins separated as given by the best fit line	221
Table 9.5 - K, κ and ε values at different intake temperature conditions	225
Table 9.6 - Strength of correlation with new OI model for tested intake air temperatures from the best fit line	226
Table 9.7 - New OI correlation strength at several intake air temperature conditions using a best fit line; 10% and 20% ethanol fuels are separated from one another	229
Table 9.8 - Strength of correlation with new OI model using a best fit line; high aromatic and high olefin fuels are separated out	230
Table 9.9 - Strength of SU HCCI Index correlation with all fuels using a best fit line ..	233
Table 9.10 - Strength of the HCCI Index correlation from the SU model against CA20 using a best fit line; high aromatic and high olefin fuels are separated	234
Table 9.11 - Fit for the HCCI Index of the SU model to CA20 using a best fit line; 10% and 20% ethanol fuels are separated	235
Table 10.1 - Fuel Properties for the Deposit Studies Test Matrix	239
Table 10.2 - Reference Conditions for Test Matrix Fuels	240
Table 10.3 - Equivalent Fuelling Rates for Intake Air Temperature Sweeps	246
Table 13.1 - Summary of XEDS composition results with C:O ratio included	313

Table 13.2 - Carbon to oxygen ratios for all tested deposit samples from XPS analysis
..... 323

Table 13.3 - Summary of the molecular structure for all the deposit samples tested with
XPS; molecules given as a % area from the 4-peak analysis of the carbon scans 323

Table 13.4 - SAXS results summary for all tested deposit samples 329

NOMENCLATURE

A	Aromatics
ASTM	American Society for Testing and Materials
BMEP	Brake Mean Effective Pressure
BSFC	Brake Specific Fuel Consumption
CA10	Crank angle position of 10% mass fraction burned
CA20	Crank angle position of 20% mass fraction burned
CA50	Crank angle position of 50% mass fraction burned
CA90	Crank angle position of 90% mass fraction burned
CARBOB	California Reformulated Blendstock for Oxygenate Blending
CAD	Crank Angle Degree
CAFE	Corporate Average Fuel Economy
CCD	Combustion Chamber Deposits
CI	Compression Ignition
CJC	Cold Junction Compensation
COV%	Coefficient of Variance percentage
DAQ	Data Acquisition
EDS	Energy Dispersive Spectroscopy
EGR	Exhaust Gas Recirculation
EIHC	Emissions Index of Hydrocarbons

EINO _x	Emissions Index for Oxides of Nitrogen
EMAL	Electron Microbeam Analysis Laboratory
EPA	Environmental Protection Agency
ESEM	Environmental Scanning Electron Microscopy
EtOH	Ethanol
EVC	Exhaust Valve Close
EVO	Exhaust Valve Open
FET	Field Effect Transistor
GHG	Greenhouse Gas
GM	General Motors
GSG	Gaseous Secondary Atom
HC	Hydrocarbons
HCCI	Homogeneous Charge Compression Ignition
HTHR	High Temperature Heat Release
HTHR CA20	Crank angle position of 20% mass fraction burned point for HTHR
HLL	High Load Limit
KLSA	Knock-Limited Spark Advance
NHRR	Net Heat Release Rate
IMEP	Indicated Mean Effective Pressure
ISFC	Indicated Specific Fuel Consumption
IVC	Intake Valve Close
IVD	Intake Valve Deposit
IVO	Intake Valve Open

LFD	Large Field Detector
LHV	Lower Heating Value
LLL	Low Load Limit
LPP	Location of Peak Pressure
LTHR	Low Temperature Heat Release
MFB10	Crank Angle Location of 10% Mass Fraction Burned
MON	Motor Octane Number
MPRR	Maximum Pressure Rise Rate
N	Engine Speed (RPM)
NDIR	Nondispersive Infrared Sensor
NI	National Instruments
NO _x	Oxides of Nitrogen
NTC	Negative Temperature Coefficient
NVO	Negative Valve Overlap
O	Olefins
OEM	Original Equipment Manufacturer
OI	Octane Index
ON	Octane Number
ORI	Octane Requirement Increase
PAH	Polycyclic Aromatic Hydrocarbons
PBA	Polybutene Amine
PEA	Polyether Amine
POA	Polyolefin Amine

PP	Peak Pressure
PRF	Primary Reference Fuel
RI	Ringing Intensity
RON	Research Octane Number
RPM	Revolutions Per Minute
S	Sensitivity
Sat	Saturates
SAXS	Small-angle X-ray Scattering
SE	Secondary Electron
SEM	Scanning Electron Microscopy
SI	Spark Ignition
SU	Shibata-Urushihara HCCI index model
TDC	Top Dead Center
TDCE	Top Dead Center Exhaust
TDCF	Top Dead Center Firing
TEM	Transmission Electron Microscopy
THC	Total Hydrocarbons
UM	University of Michigan
V	Volume
VI	Virtual Instrument (LabVIEW designation for a program)
XEDS	X-ray Energy Dispersive Spectroscopy
XPS	X-ray Photoelectron Spectroscopy
ZAF	Z Atomic Correction Factor

aTDC	After Top Dead Center
bTDC	Before Top Dead Center
\dot{m}	mass flow rate
nm	nanometers (1E-9 meters)
Å	Angstrom (1E-10 meters)
$\gamma(r)$	SAXS characteristic function
η_{comb}	Combustion Efficiency
μm	Micrometers (1E-6 meters)

ABSTRACT

HCCI combustion is highly dependent on in-cylinder thermal conditions and the chemical kinetics of the fuel. In addition to the impact on auto-ignition, the fuel properties will also affect the accumulation of deposits on the combustion chamber walls, and this in turn alters the in-cylinder thermal environment. Because the fuels available at the pump differ considerably in composition, strategies intended to bring the HCCI to market must account for the interplay between the fuel chemical components, the HCCI combustion event, and the deposit accumulation in the engine.

In an effort to quantify the impacts of fuel composition on HCCI combustion, a large test matrix of fuel blends was investigated in a single-cylinder HCCI engine with re-induction of residual. These fuels were blended from pure refinery streams in an effort to reproduce expected variations of pump gasoline, and were oxygenated with 10% of ethanol. The matrix has three dimensions, i.e. the fraction of Olefins (O), the fraction of Aromatics (A), and the Sensitivity (S), defined as the difference between the RON and MON (RON-MON). The experiments generated a complete picture about the auto-ignition phenomena over the range of speeds and load. The HCCI operability range was characterized too. The impact of fuel composition on performance and thermal efficiency was investigated in a systematic way, such that the obvious impact of the lower heating value is compensated for.

The insights gained during the HCCI combustion study were captured with a new model. Additional terms in the Octane Index model were developed to correlate the composition (O and A) as well as sensitivity (S) to the auto-ignition trends.

The effect of fuel composition and additive packages on HCCI combustion chamber deposit formation was investigated with a second set of refinery stream fuels. The equilibrium CCD thickness was shown to be on the order of 250 μm for a highly Aromatic fuel, which is three to five times more than in the case of low-Aromatic fuel. The heat release and burn durations at various operating points served to quantify the impact of the deposits on combustion. The subsequent part of deposit formation study considered two additive packages, namely the polybutene amine (PBA) and polyether amine (PEA). The PEA package helped to reduce in-cylinder thickness while the PBA package actually promoted growth.

Finally, microscopic, spectroscopic and diffractometric techniques were employed to quantify physical structure, morphology, chemical composition, and porosity of deposits formed with different fuels and/or additive packages. Thermal diffusivity was also determined. It is shown that the morphological and chemical dissimilarities among CCD formed with different fuels and additives are not as important to the HCCI combustion event as is the overall thickness.

CHAPTER 1

Project Introduction and Background

1.1 Project Introduction

Extensive research of the homogeneous charge compression ignition engine, or HCCI, strongly correlates combustion in the HCCI engine and the in-cylinder thermal environment with chemical kinetics. Because of this correlation, all strategies for HCCI operation revolve around creating favorable in-cylinder conditions which promote stable and controllable combustion for a given fuel and its respective properties. The variation of fuel properties impacts the auto-ignition event and is crucial in determining the level of intake temperature, or recirculated hot exhaust, required to achieve optimum phasing for any speed-load combination. In addition, fuel properties have an important influence on HCCI combustion's sensitivity to intake air temperature, and therefore play a significant role in developing robust control strategies. Furthermore, recent experimentation indicates that one of the major challenges to address in achieving this amenable in-cylinder environment is a thorough understanding of the combustion chamber deposit (CCD) layer that accumulates in the HCCI engine during operation. At present, it is known that the deposit layer has a profound effect on the auto-ignition and on HCCI combustion in its entirety. It has been hypothesized that the primary

mechanism by which the deposit layer affects HCCI combustion stems from the effect of CCD on near-wall conditions and thermal stratification in the combustion chamber [1]. However, to date no research has determined the exact physical and chemical characteristics of the layer formed in an HCCI engine, or correlated these parameters with combustion phenomena. Any control strategies developed for commercial HCCI engine packages must account for CCD buildup, and thus, a thorough knowledge of the deposits will be necessary for the viability of all HCCI engines.

Another facet of the HCCI deposit building process that requires more attention is the impact of fuel and additive composition upon CCD formation. While this mechanism is relatively well established in spark-ignited (SI) engines, the same cannot be said of engines using low temperature compression ignition, such as HCCI. It is well established that deviations of fuel composition can result in vastly different rates of deposit growth, and potentially different CCD structures. Considering that pump gasoline from different regions of the country can be comprised of various constituents depending on the refinery where it was blended, it is imperative to advance our understanding of the interaction between a fuel's chemical composition and HCCI deposit growth.

Moreover, it is likely that fuels of dissimilar composition will result in the growth of deposit layers with varying properties. It is possible that the way a CCD layer impact the HCCI combustion event is a function of the physical structure of the deposits, as well as their chemical composition. Therefore, a study is needed to accurately characterize the physical and chemical properties of the layer and to link distinct CCD layer traits back to observed in-cylinder combustion phenomena.

In an effort to answer the aforementioned scientific quandaries, an experimental engine test cell was constructed to study of the complex interplay of fuels, HCCI operation and deposits. In addition, a measurement methodology for a more fundamental chemical and physical investigation of the deposition was considered and implemented. Thus, the available, relevant engine hardware was utilized to grow the deposits and study them in-situ, as well as harvest samples for ex-situ characterization of properties and structure.

1.2 HCCI Background

The impetus for investigation novel forms of internal combustion stems from geopolitical concerns about energy security and the environmental impact of vehicles that burn hydrocarbon based fuels, such as the effects of greenhouse gas (GHG) emissions. These concerns are captured by the U.S. Environmental Protection Agency (EPA) exhaust emissions regulations and by pending Corporate Average Fuel Economy (CAFE) regulations, which are intended to address both fuel economy and GHG emissions. The OEM's (Original Equipment Manufacturer) need to meet consumers' demands for increased fuel economy within these constraints, as well as market pressure for reduced cost, is driving intense research efforts which seek all possible avenues to increase the efficiency of the internal combustion, or IC, engine and create in-cylinder strategies to lower emissions levels. It is necessary to meet this need because it is likely that liquid fueled IC engines will dominate the transportation sector for a significant time to come [2]. The HCCI concept which has been around nearly three decades [3], is an attractive option because it holds the promise of achieving

diesel-like efficiency, with only trace levels of nitrogen oxide (NO_x) or soot in the exhaust [4]. Although the concept of HCCI is decades old, thorough research of HCCI only began within the last 10 years. These intensified research efforts were spurred by the realization that advances in engine technology might enable control of this formerly defined “uncontrollable engine”, and the development of implementable solutions. A brief summary of the features of HCCI as compared with other more conventional forms of IC combustion is presented in Figure 1.1.

HCCI combustion is typically very lean, and the engine load can be controlled by varying the amount of fuel injected. Therefore, the HCCI engine runs unthrottled even at low loads. In addition, the combustion process occurs over a relatively short period of time, and thus more closely approaches the ideal of constant volume combustion than a conventional spark-ignited (SI) flame propagation. Finally, because HCCI relies in part upon compression ignition, it is run at higher compression ratios than SI engines.

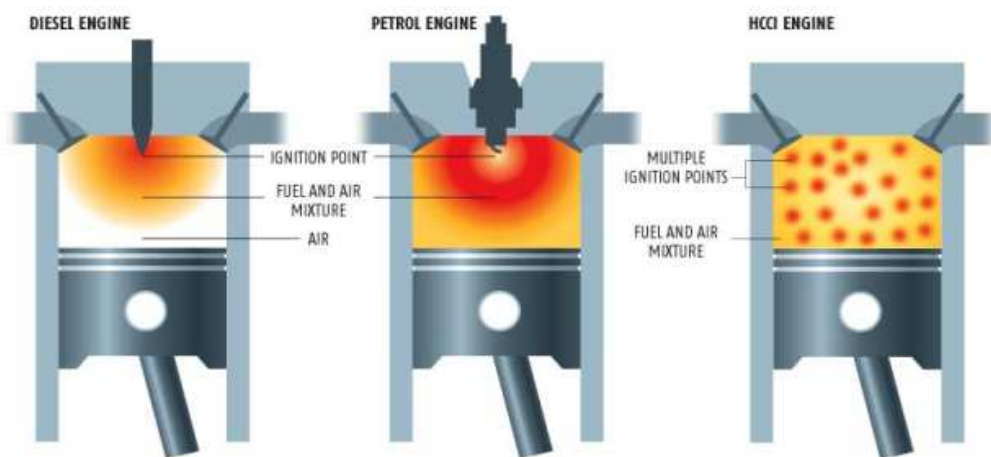


Figure 1.1 - Comparison of spark ignition (SI), compression ignition (CI), and homogeneous charge compression ignition (HCCI); note that both SI and CI have a direct trigger in the form of a spark or fuel injection respectively, whereas HCCI does not

These factors contribute to a higher thermal efficiency, and translate into an engine that runs on gasoline but exhibits higher specific fuel efficiency than conventional SI engines. Moreover, because combustion chamber temperatures are relatively low during the engine cycle as a consequence of lean homogeneous operation, the NO_x emissions are greatly reduced from those of orthodox SI operation. Because of the nearly homogeneous mixture of air and fuel present when combustion occurs, there is no soot and particulate matter formation in HCCI. Therefore, HCCI engines do not suffer from the NO_x/soot dilemma that exists in diesel engines.

While there are numerous merits to running in HCCI mode, there are also a number of challenges related to this type of combustion strategy. HCCI has no direct trigger for combustion, such as the spark in an SI engine or fuel injection in a diesel compression ignition motor, and instead relies on reaching a favorable thermal environment in-cylinder for auto-ignition to occur. This lack of a combustion trigger presents a significant obstacle in terms of control. Also, the range of operating points for HCCI is limited compared with the range of a standard SI gasoline engine. At the low load range, there is not enough enthalpy in-cylinder for combustion to occur, and thus, misfires plague the engine. At high loads, the pressure rise rates cause excessive ringing and possible mechanical failure. In addition to these dilemmas, because of the lean combustion and low equivalence ratio, the combustion efficiency is less than that of an SI engine. The loss of combustion efficiency is directly correlated with an increase in hydrocarbon and carbon monoxide emissions because these byproducts arise as a result of the incomplete combustion of injected fuel.

As there is no direct control of HCCI combustion, as opposed to the spark of SI and the fuel injection event of compression ignition (CI), the process is primarily a product of two indirect drivers; in-cylinder thermal environment and chemical kinetics. HCCI combustion will occur when favorable thermal surroundings are achieved in-cylinder, and it is extremely sensitive to any factors that can affect in-cylinder conditions. One such example is shown in Figure 1.2, which displays the effect of intake temperature on the combustion phasing in an HCCI regime. As intake temperature is decreased (actual temperature values are not pictured in the plot) the temperature of the incoming charge is consequently lowered, and the combustion phasing is retarded, shown by the 10% mass fraction burned point shifting to crank angle values farther away from top dead center (TDC) in the cylinder. As this phasing goes to larger crank angles away from TDC the burn duration, given as the crank angle when 10% of the mass of fuel was burned (CA10) to the crank angle where 90% of the mass of fuel was combusted (CA90), increases accordingly. This effect is indicative of the sensitivity of HCCI combustion to changes in the thermal surroundings, in this case intake charge temperature. The intake air temperature effect is confirmed by experiments conducted on a single-cylinder HCCI engine at the University of Michigan [5], shown in Figure 1.3.

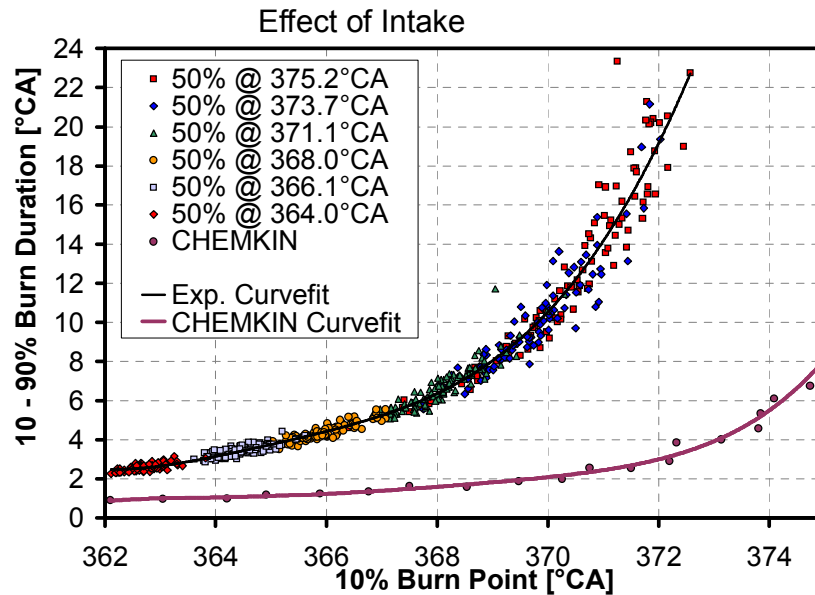


Figure 1.2 - Experimental data demonstrating the sensitivity of the HCCI combustion event to charge temperature; note that the Chemkin model envisions the entire combustion chamber as a single zone, thus the lengths of burn durations are under-predicted [6]

Continuing, adjustment of intake air temperature is not the only manner to influence the thermal in-cylinder environment of an HCCI engine; wall temperature effects resulting from coolant temperature and the accumulation of deposits also play an integral role. In Figure 1.4 and Figure 1.5 examples of these wall phenomena are displayed, as coolant temperature and deposit layer thickness are increased. As either of these is raised (shown as higher hours in the case of deposit buildup in Figure 1.5), the in-cylinder temperatures increase, and consequently combustion phasing is advanced closer to TDC (values closer to 0). However, the correlation between combustion phasing, again given by the crank angle where 10% of the fuel mass has

been burned, and 10%-90% burn duration is not as strong as with intake air temperature.

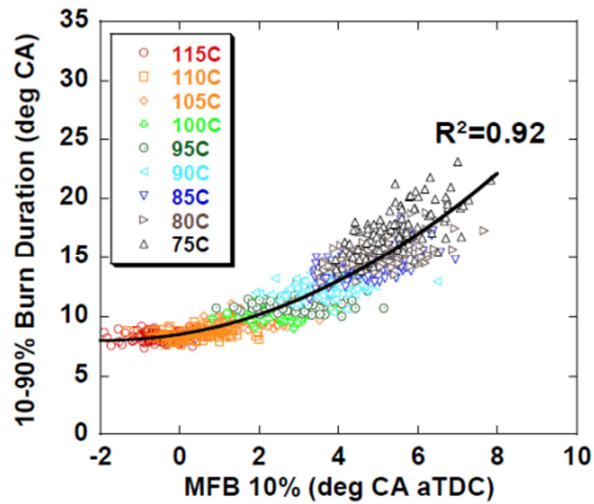


Figure 1.3 - HCCI sensitivity to intake charge temperature; notice that combustion phasing and burn duration correlate well with an increase in intake air temperature [5]

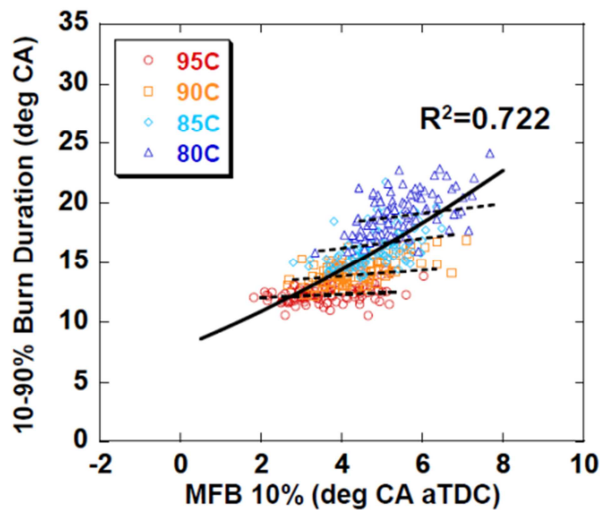


Figure 1.4 - Effects of coolant temperature increase on HCCI; burn durations here do not seem to change in a manner consistent with only a change of phasing, as wall effects influence the HCCI combustion event [5]

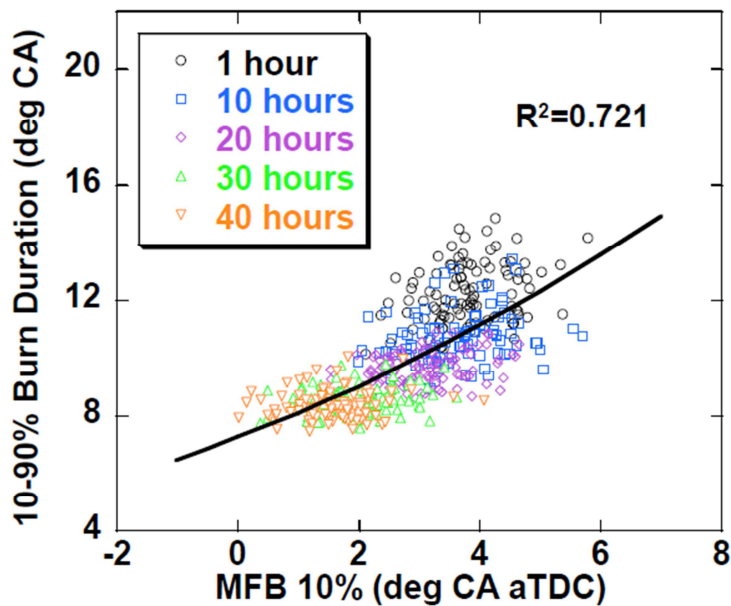


Figure 1.5 - A similar wall effect is seen with deposit growth as with coolant temperature increase, as burn duration changes do not correlate well with combustion phasing differences [5]

These two plots speak to the fact that the wall effects from either coolant temperature changes or deposit buildup have an additional effect on the in-cylinder conditions, primarily through the thermal stratification.

The potential, practical applications of HCCI hinge upon our ability to address the challenges related to achieving desired combustion phasing through indirect measures, such as intake charge temperature or variations of the residual fraction, and to understand the variability that can occur in real-world situations, and adapt accordingly. Two significant sources of variability experienced by engines in real vehicles are fuel properties and the accumulation of combustion chamber deposits. Commercially available, pump gasoline can vary greatly in composition, as demonstrated in the

following section. Variations in composition obviously lead to variations in chemical kinetics, therefore the ignition and burn rates will differ for any in-cylinder thermal conditions depending on the fuel. Additionally, the presence of CCD, which form as the engine is run, creates a thermal barrier on the combustion chamber wall which changes the thermal environment in-cylinder. The substantial impact of the CCD layer on combustion was documented by Guralp et al [7]. These issues provide a primary motivation for the research pursued in this document. There are several aspects of the CCD effects that deserve attention. HCCI operation can be thought of as “controlled knock”, because the entire range of the combustion process is dictated by the auto-ignition quality of the fuel, and by the octane requirement of the engine operating condition. Previous efforts in spark-ignited engines have shown that combustion chamber deposition can impact the onset of knock and detonation; deposits act as a thermal barrier increasing in-cylinder temperatures, and thus, decreasing the time for a fuel to auto-ignite. In an SI engine, the octane requirement increase primarily affects operations at high loads and low speeds, and is therefore a factor only when considering these extreme conditions. A spark retard is typically used to mitigate the operational extremes, and the vast majority of the operating conditions that dominate everyday driving are not affected. However, for HCCI, where the entire spectrum of operating conditions is determined by the auto-ignition chemistry of fuel, the deposit layer takes on a substantially more integral role over the entire combustion range. For this reason, it is critical to firmly establish an understanding of the layer and precisely what influence it exerts over HCCI combustion.

Furthermore, it is important to determine the fashion in which the layer forms and how the deposition properties change in regards to the type of fuel used to run the engine. This is relevant in the context of future production vehicles, as they will need to be able to run pump gasoline from any region of the U.S. or around the world. The properties of refinery fuels available at the pump have a significant variance based on the refinery the fuel originated from and the additive package used. Differing fuel compositions lead to differing growth rates of deposition, and alterations in the chemical composition and physical structure of the layer. Because variations in the thickness, morphology and composition between distinctive layers affect HCCI combustion in a significant, but not yet fully understood fashion, it is of the utmost importance to determine the interplay between the fuel's composition, the formation and properties of the deposit layer and the features of HCCI combustion process.

1.3 Fuel Chemistry Overview

Pump gasoline available in the United States is composed of hundreds of compounds of vastly different chemistry, and a working knowledge of these fuel components and their structure is necessary to carry out this research program. There are three main classes of molecules present in the refinery streams which create pump gasoline as it is recognized in the United States; aromatics, olefins (also known as alkenes) and paraffins (sometimes referred to as saturates). The underlying structure of these chemicals is substantially varied. Figures 1.6, 1.7 and 1.8 highlight some of these disparities.

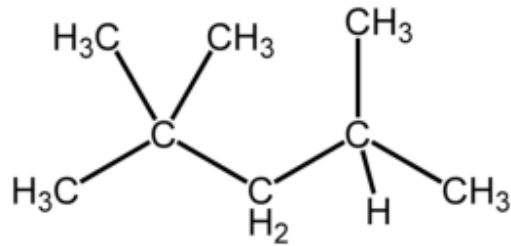


Figure 1.6 - Chemical structure of 2,2,4 trimethylpentane, $(\text{CH}_3)_3\text{CCH}_2\text{CH}(\text{CH}_3)_2$, usually referred to as iso-octane, a common paraffin (alkane)

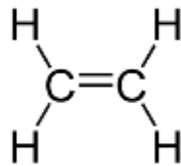


Figure 1.7 - Ethylene, C_2H_4 , the simplest olefin (also called alkenes)

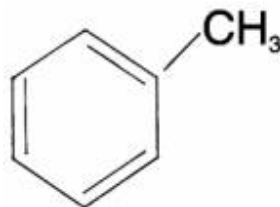


Figure 1.8 - Toluene, C_7H_8 , an example of an aromatic molecule, composed of one benzene ring and one side methyl group; it is often added to gasoline to increase the octane rating

A fuel called iso-octane (C_8H_{18}), a paraffin characterized by single bonds between carbon atoms and a carbon and a chemical formula of the form $\text{C}_n\text{H}_{2n+2}$, is pictured in Figure 1.6. Paraffin fuels are often dubbed saturates, as they are saturated hydrocarbon compounds, meaning they do not contain any double or triple bonds and

they have bound as many hydrogen atoms as the carbon can support. Paraffins such as iso-octane and n-heptane belong to a group of fuels known as primary reference fuels (PRFs), which are used in octane testing procedures for IC engines. These fuels do not show any sensitivity to octane tests (the research octane number, RON and motor octane number, MON, are equal) and have a negative temperature coefficient (NTC) region in an auto-ignition regime [8]. This means that the time for auto-ignition does not monotonically decrease with increasing in-cylinder temperature, rather, there is a temperature region where the time to auto-ignite actually increases as the temperature ramps up, as shown in Figure 1.9. These fuel constituents account for the majority of what comprises pump gasoline, with saturates typically comprising a dominant fraction, by volume.

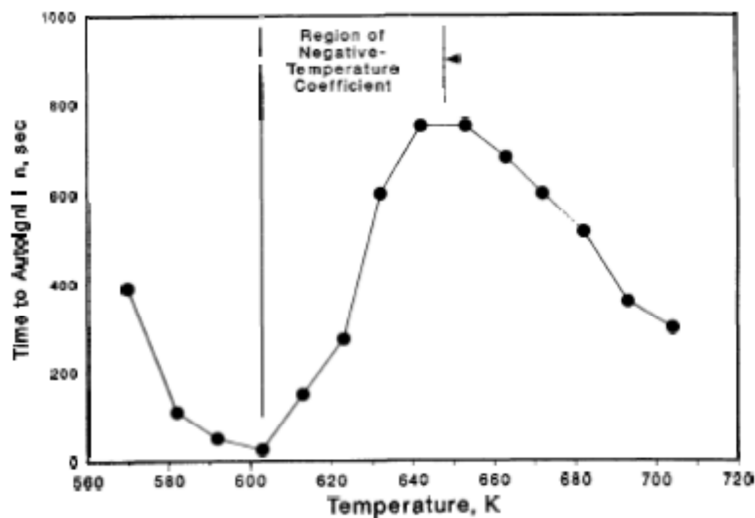


Figure 1.9 - Time to auto-ignite for propane, a paraffin, in a static reactor [9]; notice how in the intermediate temperature range, the time to autoignite increases with increasing temperature

The simplest olefin, ethylene, shown in Figure 1.7, is readily identifiable by its double carbon bond (these types of molecules are often referred to as alkenes). The auto-ignition chemistry of olefins is a significant departure from that of saturates, as these fuels do exhibit a difference between the RON and MON octane tests and there is no NTC region.

The last primary fuel component in gasoline which warrants discussion is aromatics (denoted as "A"); a simple example of these is toluene, shown in Figure 1.8. Aromatic molecules are composed of chains of benzene rings (6 carbon atoms bonded together by alternating single and double bonds in a ring) with possible hydrocarbon side chains bound to these rings. Similar to olefin fuels, aromatics do not display an NTC behavior in auto-ignition and show sensitivity in octane rating tests, having a higher RON than MON. Aromatics are commonly utilized in refinery streams to increase the octane rating of pump gasoline.

Previous experiments have shown that fuel composition has an exceedingly important impact on HCCI combustion. Figure 1.10 shows blends of iso-octane and n-heptane against unoxygenated (no ethanol) gasoline. Here, equivalence ratio, or mixture strength, is varied and the intake temperature is adjusted to maintain the same 50% of the mass fraction of fuel burned crank angle point. It is apparent that all the fuels require not only different intake temperatures to keep combustion phasing constant, given as their relative position on the plot, but also different rates of temperature compensation over the equivalence ratio range, represented by the slopes of the lines in Figure 1.10.

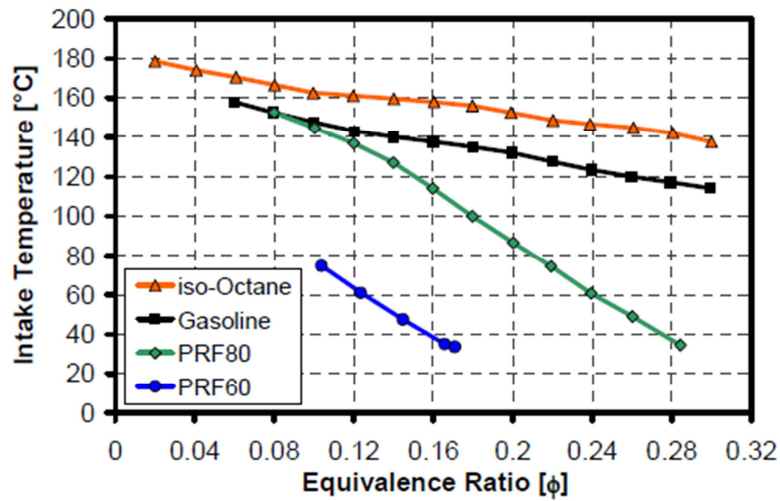


Figure 1.10 - Intake temperature required to maintain the 50% mass fraction burned point at a range of equivalence ratios [10]

For this reason, a portion of this research effort is focused on determining the effects of fuel properties on the HCCI combustion event and the influence these properties have on engine performance parameters.

1.4 Combustion Chamber Deposits

The body of knowledge accumulated over multiple decades of engine research demonstrates that CCD growth in SI engines is strongly tied with fuel properties and in-cylinder conditions, and how this accumulated deposition affects the SI combustion regime. The effect of deposits in the SI engine is briefly summarized in Figure 1.11. While there is vast experimental insight into such phenomena, the understanding of the CCD layer as it relates to HCCI combustion is limited. Groundbreaking efforts at the University of Michigan reveal intriguing data uncovering the direct effect CCD has on HCCI burn rates [7]. This pioneering study was performed using a single fuel, an 87

octane gasoline of controlled composition. The major findings of this endeavor is reviewed in more detail later in this document. First, however, we must review the deposition formation in SI engines, and the role of a fuel's chemical composition in this process.

1.4.1 Deposits in Spark-Ignited Engines

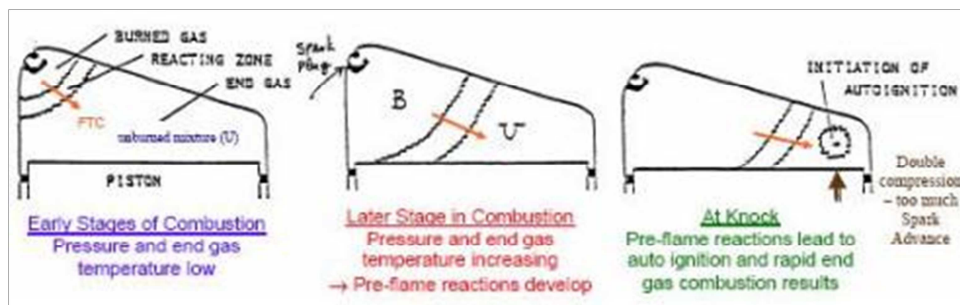
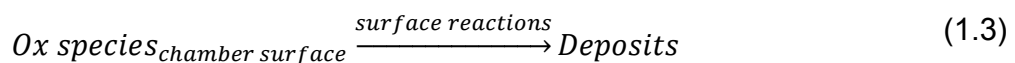
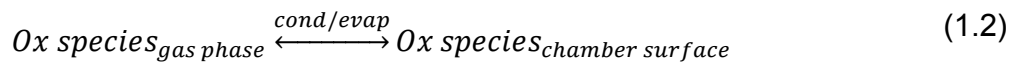
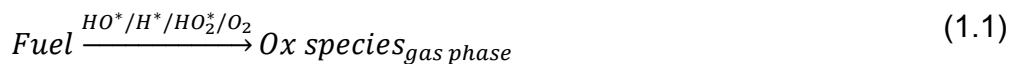


Figure 1.11 - Conceptual image of the auto-ignition process as experienced by a traditional spark-ignited gasoline engine

Because testing throughout the last half century has shown that the buildup of CCD is primarily attributable to the condensation of fuel, the study of various fuels in an engine is of paramount importance when attempting to gain insight into deposit formation. For instance, Spilners and Hedenburg [11] concluded that partially unburned hydrocarbon fuel was the primary source of CCD for the range of temperatures found in engine operation. When retrieved from the cylinder walls and scrutinized, these combustion deposits tend to be fairly heterogeneous in nature, containing refractory polymeric carbon, physisorbed aromatic hydrocarbons from the fuel, inorganic material from lubricating oil and trace amounts of metal from the engine, and tend to be about

65% carbon by weight [12]. Crucial to an understanding of the deposit formation mechanism is an analysis of the process involved in creating these deposits, as well as an analysis of deposit precursors. Intuitively, the combustion process is critical in the process of deposit formation [13], as tests run on a motored gasoline engine with the spark plugs turned off produced no measurable level of deposits. In regards to deposits derived from fuel, the substance which precedes CCD is partially-oxidized fuel in the gas phase [14, 15]. The beginning of the deposit formation process occurs as this gaseous fuel condenses on a relatively cooler combustion chamber surface, in this case, the piston top and cylinder head walls. This in-cylinder phenomenon is followed by either the decomposition of the fuel into its constituents via pyrolysis, or addition polymerization of the fuel molecules as they incur reactions with themselves. It is important to note that both processes occur at some point during the deposit formation process; the high oxygen content can only be accounted for via the polymerization, because pyrolysis occurs in absence of oxygen [16]. As oxidation reactions begin to occur, more reaction sites are available on the condensed gases, leading to a higher level of deposit formation. This phenomenon is observed because raising the level of oxidation reduces the volatility of the fuel [17], and a more involatile fuel has a higher tendency to form CCD. These reaction sites occur in the fuels as substituent chains. Based upon their quantity and length the chains influence fuel properties, such as boiling point, which is an instrumental factor in determining a fuel's ability to produce CCD [18]. Previous research has further characterized the chemical reaction phenomena occurring in the engine that causes the fuels to produce combustion deposits. Hydrocarbon based fuels lose hydrogen atoms during pre-combustion

reactions, and in this process, the hydrocarbon radicals that form experience a thermal decomposition. The carbon-carbon bonds are broken and other hydrogen atoms are removed by present oxygen, thereby yielding olefins (organic molecules containing at least one double carbon bond in the chain). Continuing reactions in the cylinder can also lead to aldehydes, ketones and smaller olefins. However, aromatic fuels, such as toluene, benzene and xylene cannot form olefins during combustion, because they do not contain sufficient hydrogen during the period when the carbon bonds are being cleaved [11]. The mechanism for CCD creation can be summarized by a few basic reaction equations [17, 19]:



Other early experiments involving fuels and their effect on combustion deposits uncovered a number of salient points regarding the effects of fuel composition on CCD buildup, as in tests performed by Shore and Ockert [20, 21] using leaded fuels. Their experimentation determined that the deposit-forming tendency of hydrocarbon based fuels has a significant correlation to the boiling point of the fuel; the tendency increases

as boiling point rises. Furthermore, at any established boiling point level, fuels with a higher concentration of aromatics are more prone to create deposits in the engine. These aromatic compounds are constructed primarily from one and two benzene ring structures [22], which are composed of cyclic chains of alternating carbon single and double bonds with possible substituent chains attached to these rings (often referred to as polycyclic aromatic hydrocarbons). Among hydrocarbon based fuels, the tendency to form deposits in increasing order begins with paraffins, such as methane, olefins, like ethylene and aromatics, such as toluene. A comprehensive study conducted by Price [19], presenting the boiling point effect for different fuel compositions, is shown below in Figure 1.12 and Figure 1.13.

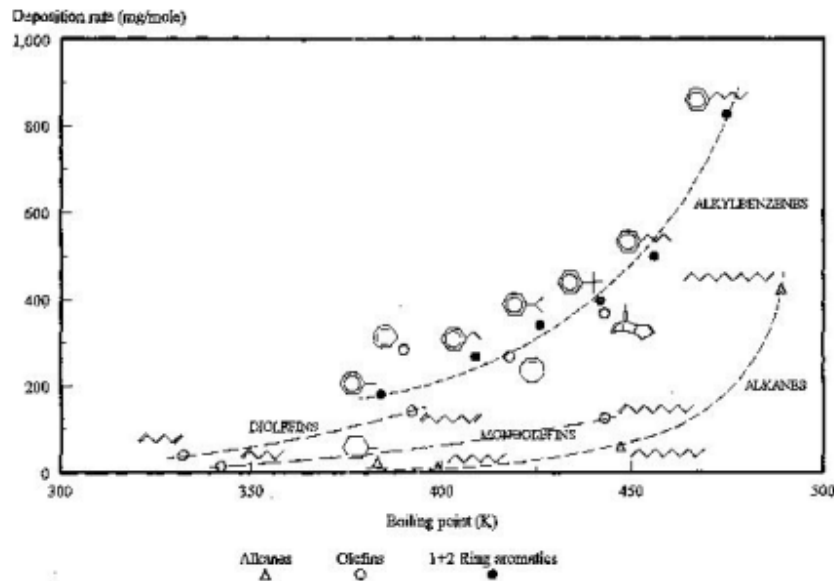


Figure 1.12 - A comparison of the relative combustion chamber deposits (CCD) formation tendencies of fuels at increasing boiling point; notice that at a given boiling point, aromatic structures tend to form more deposition [10]

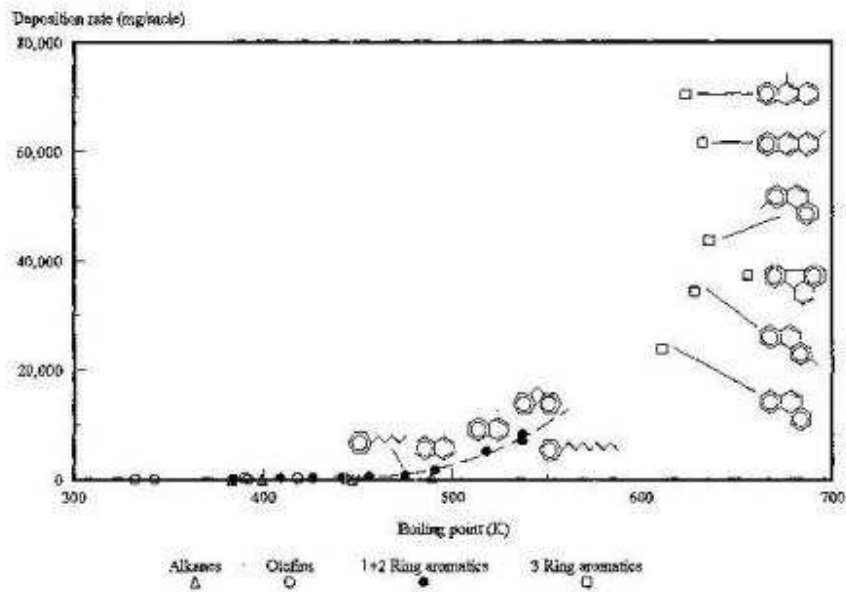


Figure 1.13 - A closer look at primarily aromatic fuel structures and the difference in 1, 2, and 3-ring formation tendencies; 3-ring aromatics have very high boiling points and a commensurate level of CCD accumulation [10]

In the case of aromatics, the proclivity to form deposits can be predicted based primarily on boiling point as all carbon atoms within the molecule are equally likely to form CCD. Myers et al. postulated [23] that combustion chamber deposits resulting from unburned fuel were predominantly derived from the last remnant fractions of high boiling point fuels (e.g. aromatic fuels), further substantiating the correlation between fuel boiling point and deposit formation tendency. The proclivity of aromatics to form CCD was further confirmed by Lauer and Friel [24], who studied several different fuel types on an L-head Lauson engine, and found that a toluene fuel, a well-known aromatic, produced the highest overall deposit weight. Bittner et al [16] constructed an informative experiment in which benzene fuel, the backbone of every aromatic fuel, was burned at two different equivalence ratios, 1.0 and 1.8, along with an acetylene fuel

(C₂H₂, a simple aliphatic, alkyne) at stoichiometry. As the fuels were burned, the flames were quenched on a specially designed copper plate to simulate flame quenching against combustion chamber walls. The deposits resulting from these flames were measured and recorded. During the course of testing, both benzene flames produced an appreciable deposit weight on the plate, with more produced via the sooting 1.8 equivalence ratio flame. In contrast, the acetylene flame produced no measurable levels of deposit. Therefore, Bittner concluded that aromatics are vital precursors in the formation of CCD. These results are not unexpected, as aromatic substances exhibit a stronger stabilization that is characteristic of their conjugated ring of carbon bonds (benzene ring), and thus, fuels with these molecules require more energy to be fully combusted. The inherent stability of these benzene rings makes the chemical bonds more difficult to break. Therefore higher aromaticity translates to higher boiling points and more CCD forming tendency for a given fuel. In addition, the substituent chains branching from the benzene ring structures that are available for oxidation engender the adhesion of the rings [25], as previously mentioned, and further augment a fuel's boiling point. Olefin-rich fuels exhibit some similar characteristics; the double-bonded carbons in their chains lead to higher boiling points, and more energy is needed for their complete combustion. Their chemical composition also leads to a higher tendency to form deposits, although olefins are a more intermediate contributor than aromatics [17, 26]. To further characterize these polycyclic aromatic hydrocarbons (PAH) and their relation to CCD formation, consider the oxidation reactions of such substances. The general chemical reaction that occurs during combustion for an aromatic molecule is given by the proceeding equation.



In this equation, the aromatic in question is oxidized by the oxygen present during the combustion process, forming aromatic cations responsible for CCD buildup [12]. These aromatic cations can react with other aromatic molecules, and the resulting conglomeration can be oxidized yielding a product of higher molecular weight, which requires more energy to completely burn, and in turn yields a higher level of CCD. Oligomerization of aromatic cations, from a chemical standpoint, is considered to be one of the primary reaction mechanisms which promotes deposit growth [12]. Table 1.1 illustrates the relationship between carbon bonds and the number of oxygen additions that can occur, for various fuel structures. Structures that permit more oxidation generally induce more deposit formation, and as is expected, fuel structures incorporating an aromatic ring allow for the most oxidation, and thus, have the highest deposit forming predilection.

Table 1.1 - Rules for determining the number of oxygen additions to a hydrocarbon molecule ($\text{C}_x \rightarrow \text{C}_x\text{O}_z$) dependent on its structure where z is the number of oxygen atoms that can be added during oxidation

Structure	Z
Alkane or alkyl side chain	1
Naphthene	2
Double bond	3
Aromatic ring	4

Continuing along this line, Table 1.2 illustrates the tendency of certain PAH to oxidize based upon their electrochemical oxidation potential, measured in electron volts. Analyzing the chemical structures in Figure 1.14 shows that the likelihood of an aromatic to be oxidized generally increases with molecular size, further substantiating the previous point that larger, and hence more molecularly heavy and involatile aromatics, produce more CCD.

Table 1.2 - Oxidation of polycyclic aromatic hydrocarbons [3]

Molecule	E_{ox} (eV)
Anthracene	+1.37
Phenanthrene	+1.83
Tetracene	+1.1
1,2 Benzanthracene	+1.44
Chrysene	+1.64
Perylene	+1.06
Pyrene	+1.36
Triphenylene	+1.88

Table 1.3 - Summary of factors effecting CCD formation [4]

Fuel Properties	CCD
Olefin content	
Aromatic content	+
Boiling point	+
Mean molecular weight	+
Fuel Additives	
Antioxidants	
Detergents	+

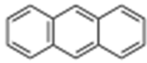
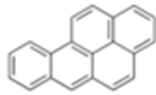
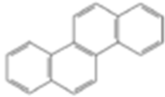

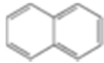



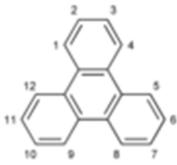
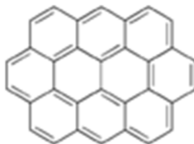
Anthracene		Benzo[a]pyrene	
Chrysene		Coronene	
Naphthalene		Pentacene	
Phenanthrene		Pyrene	
Triphenylene		Ovalene	

Figure 1.14 - Chemical structure of common aromatic molecules [3]

Table 1.3 provides a brief compilation of factors shown to influence the growth of deposits in gasoline engines, including a brief mention of additives and detergents. The correlation between boiling point and molecular structure was also shown by Cheng [15] who performed tests using various unleaded fuels, with a focus on alkylaromatics, such as toluene and ethylbenzene.

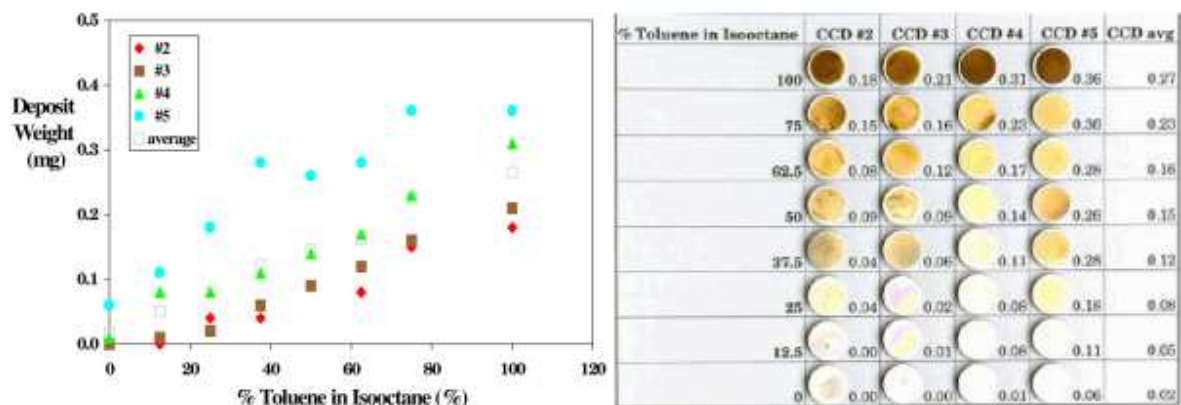


Figure 1.15 - The left plot shows deposit weight extracted from insertion coupons on a CFR engine as the surrogate fuel's concentration of toluene (an aromatic) increases; the right plot pictorially displays what had accumulated on the coupons and the weight of deposits buildup [15]

Cheng found that these aromatics produced a higher average deposit weight than fuels such as isooctane, and was able to extend analysis further on several fronts. First, as detailed in Figure 1.15, Cheng discovered that mixing an aromatic with another fuel does not inhibit its tendency to create deposits; as an increasing proportion of toluene is mixed with isooctane the deposit weight increased linearly with the concentration of toluene, suggesting that the two fuels do not affect one another. Testing also showed another trend regarding aromatic fuels; increasing molecular size, and consequently the boiling point, is responsible for producing more deposits. Comparing the deposit forming tendencies of toluene, ethylbenzene, cumene and propylbenzene, which all possess similar chemical structures, shows that fuels with longer substituents of alkyl groups (CH_3) attached to the benzene ring of the fuel, and the resulting larger molecular size, create more deposits. An additional set of aromatics was considered, this time comprised of toluene, p-xylene, o-xylene and mesitylene,

whose structures differ from one another based on the location and length of methyl chains bonded to a single benzene ring. Again, a more complex chemical composition, this time in the form of increasing substituent chain length, leads to a higher fuel boiling point and hence more CCD formation during testing. One interesting note is that the second set of fuels tested show a higher predilection towards CCD production, leading to the supposition that a higher quantity of substituent chains attached to the benzene ring of the fuel is more important for deposit forming tendency than adding length onto a side chain. These results are summarized in Figure 1.16.

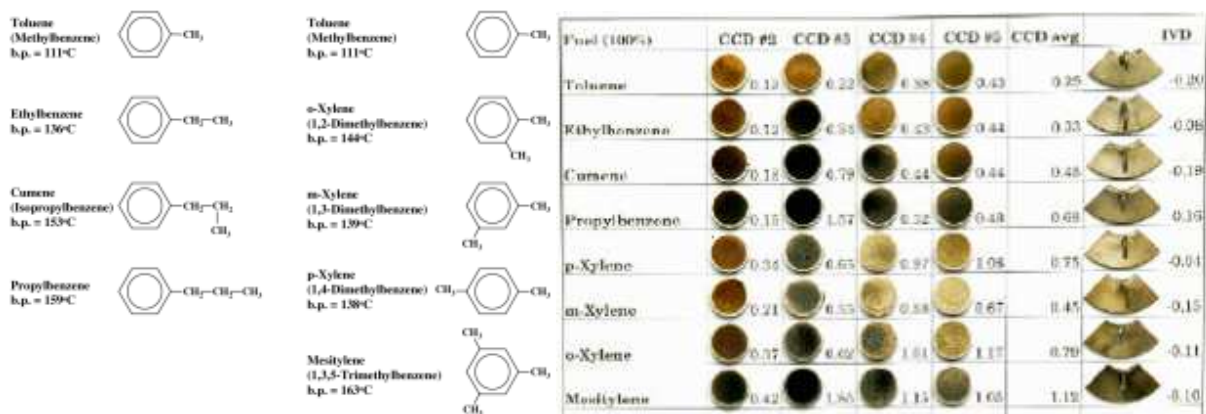


Figure 1.16 - Illustration of the importance of aromatic side chains on CCD formation; the right graphic shows the insertion coupons from the experiment and the weight of extracted deposits from the probe, as well as an average across all the coupons [15]

Cheng also determined that the boiling point of the fuel plays a substantial role in the deposit formation process, though he theorized that the correlation was only strong when the boiling point was beyond a certain threshold temperature. Experimentalists have been able to conclude that the primary mechanism of deposit formation is a function of the condensation of high boiling point substances, particularly those of high

aromaticity, as they adsorb to the combustion chamber surface and are subsequently subject to carbonization [21]. This phenomenon arises as a result of the underlying structure of aromatic substances, which possess chains of molecularly stable benzene rings that are bound to the cylinder chamber surface via the oxidation of substituent chains attached to those rings. Fuels with a higher quantity of these sub-groups connected to the benzene ring structure will exhibit increased ability to form deposits.

With regard to fuels, it is also imperative to consider how these different substances affect deposit morphology during the combustion process, and to explore the nature of the CCD they engender. The initial creation of deposits coats the combustion chamber with a glassy, liquid-like material [14, 27, 28]. Further deposit accumulation over this initial layer takes on the form of insoluble carbonaceous structures. A cursory analysis of the deposits shows that they are primarily composed of highly oxygenated, carbonaceous material, hence consisting primarily of carbon and oxygen [29], though nitrogen, hydrogen and trace amounts of other elements can be found in CCD [22, 28-30]. During the beginning stages of their formation the deposits rapidly accumulate [22], however, this growth eventually reaches a steady state thickness when enough deposits have been created. As shown during experimentation [31], a critical temperature occurs when the surface temperature of the deposition layer reaches approximately 310 degrees Celsius, at which point deposits no longer form. The existence of this critical temperature is a direct product of several characteristics of the deposits closely coupled with the nature of these in-cylinder deposits. Chiefly, due to their elemental composition, these deposits possess an extremely low thermal conductivity [31, 32] as compared to the engine's other metal components, thus CCD is

an exceedingly effective insulator of heat. Because of this trait, the evolution of CCD growth over time occurs in distinct stages, rather than at a constant rate, and the physical structure of the CCD is significantly impacted by the fuel composition used while running the engine.

As discussed previously, fuel-derived deposit precursors come in the form of partially-oxidized fuel in the gas phase, as is substantiated by analysis of the underlying CCD structure. In his testing, Cheng [14] used toluene fuel which initially produced a liquid layer of deposition, and from this he concluded that this initial buildup is not the toluene itself. Because the boiling point of the toluene, at 110°C, is well below the temperature of the hotter cylinder walls, the fuel would be vaporized upon contact with the metal and thus the fuel alone cannot account for the CCD. Furthermore, Cheng shows that impurities of the fuel are not a factor, as chemical grade toluene of nearly unblemished purity and industrial grade toluene produced the same levels of deposition. The liquid layer also exhibits a high level of surface tension, as evidenced by ball-like protrusions on its surface at 180°C, characteristic of substances with a polar molecular structure. All these empirical observations indicate that while CCD is not the fuel itself, it must somehow be derived from the fuel, and are thus constituted of molecular components of said fuel.

To reiterate a previous point, fuel-derived deposition is initiated by the gas phase condensation of fuel as it adsorbs onto cylinder walls. However, this is not the entire sequence of the deposition process, as there is a further evolution which occurs once the initial, liquid-like film has become established on the cylinder walls. Depending on if this reaction involves oxidation or not, as progressively more of the deposit precursor

condenses, it will either undergo a pyrolyzation process or polymerize. For a certain temperature range, the ball-like protuberances mentioned previously will begin to form on the surface, while at lower temperatures liquid droplets begin to coalesce. For temperatures outside the range small bubbles appear [14]. The process of either polymerization or pyrolyzation occurs at a slower rate than the initial film layer buildup, further accentuating the point that the deposit growth occurs in stages [14, 33]. The nature of this two-phase growth results in distinct deposition zones, which, as intuition indicates, possess two distinct chemical compositions. The lacquer-like layer attached to the cylinder wall has a significant aliphatic construction, which is defined by chains of hydrogen and carbon bonds that lack benzene rings, similar to that of coal, while the zone which builds atop the initial layer resembles graphite or soot, a material that possesses a high degree of aromaticity [33]. As this top layer accumulates further, it is exposed to increasing temperatures caused by the thermal insulating property of the deposition and the significant temperature gradient found in the thermal boundary layer corresponding to the CCD surface [14]. As a result the top zone becomes solid deposits, while the viscous, liquid structure underneath remains, shielded from much of the high combustion chamber temperatures by the insulating zone above it. This two layer construction explains why the deposition layer on top is prone to cracking; liquid materials experience more thermal expansion than solid materials, therefore as the cylinder undergoes successive cycles of heating and cooling, the relatively larger expansion and contraction of the liquid under-layer causes the top more solid layer to experience some instability, which leads to cracking. It is important to note that if significant amounts of the top solid layer are lost to cracking and the subsequent

process of flaking, revealing the liquid layer below, the CCD process will begin anew, with the liquid zone already intact.

While to this point the discussion has focused solely on fuel composition and its relation to CCD buildup, another important factor to consider is the introduction of fuel additives, which can contribute to CCD formation. Though these fuel additives are generally considered for use in intake valve deposit (IVD) control and minimization, experimentation shows that some additives will actually contribute to the overall deposit growth [14]. Using gel permeation chromatography to measure the fractions of CCD soluble in chloroform, scientists have been able to aver that indeed, a greater amount of CCD (higher soluble fraction) is measured when using an IVD control in combination with a base fuel, as opposed to the soluble fraction of CCD with just the base fuel [34]. Fuel additives tend to have a high molecular weight and a commensurate boiling point, and are therefore less volatile than fuel. Because of this quality, there is ample time for the additives to carbonize, or act as a binder for carbon, thus aiding in the deposition phenomenon.

An important note to consider is that while fuel-derived deposit precursors occur in the form of partially oxidized fuel in the gas phase, those deposits that arise from additives are a product of the additive itself, in the liquid phase [14]. As a certain critical concentration is reached, additive surfactants begin to form an aggregate structure known as a micelle, with a hydrophobic tail portion that is projected into the fuel, and a hydrophilic head section that is forced into contact with the associated metal surface, which in this case are combustion chamber walls. The primary category of fuel additives in use is detergents [35], which are surfactants that are comprised of a

hydrocarbon-soluble polymer attached to a polar head, a structure which plays a role in allowing the additive to adhere to the metal surface. There are a few types of common detergents, including polyether amines (PEA) and polybutene amines (PBA), as well as alkyl polyamino carbamates [35], which all function in a similar manner, operating in either a “keep-clean” or “clean up” mode. In the former of the two operating modes, the surfactant is introduced to a clean cylinder, and upon coating it, forms a film that precludes the adhesion of deposit precursors to the cylinder wall. In the latter [36], the detergent is added to an already conditioned cylinder that contains some level of combustion deposition, and the non-polar tail of the surfactant dissolves the soluble portions of the deposit, which are thought to bind the deposit to the metal surface. In the case of PEA and PBA, both of which are frequently used in the modern gasoline engine, the PEA additive is much less viscous than the PBA, so it breaks apart with more ease during engine operation and also requires a lower rate of treatment. Furthermore, because the chemical infrastructure of the polyether has less strength than that of the polybutene, the PEA breaks down more easily during combustion and, hence forms less deposits. This weakened strength is due to oxygen atoms contained in the PEA backbone which decompose more readily than the hydrocarbons which constitute the backbones of PBA [37]. Note that due to generally high boiling points, much of the additives will enter the combustion chamber in liquid form [15], so if the additive is not properly dispersed, the conditions are ideal for additive-derived deposit precursors.

During testing conducted by Cheng [14], he found that the accumulation of deposits using the PEA does indeed have a lower overall weight than deposit formation

from the more chemically complex PBA additive, though some of the addition is due to the fact that the PBA is used at a higher recommended treatment dosage. In addition, he demonstrated that increasing the concentration of fuel additive in the combustion chamber serves to increase combustion deposition as well. During the course of a number of experiments using a base fuel and PBA-based additive package (polyisobutylene amine), Zelemen et al. noticed an increase in deposit weight and thickness due to the inclusion of the additive [22]. In another study which utilized varying additives within the PEA and PBA families in testing, Zerda et al. [37] found that deposits resulting from polyether based additives have a lower mass than those that results from the polybutenes, though the overall surface area of the polybutene-based deposits is lower. Another interesting observation, related to the previously mentioned additive concentration phenomenon, is that while the additives are able to reduce the surface area of deposition, this reduction is accompanied by an increase of deposit mass. In another test using two different types of hydrocarbon amine additives (HC-1 and HC-2), which have a hydrocarbon backbone and a polyether amine as well [28], the first HC amine, of a lesser chemical complexity, produces approximately the same gross weight of CCD as the base fuel, while the second HC amine additive creates a significant amount of cylinder deposits. This amount is even more than the PEA tested, which was more prone to break up than the second HC amine and produces a level of deposits between HC-1 and HC-2. It is of importance to consider what exact property of the additive is causing the trend to produce more CCD. As opposed to relying on boiling point to determine the CCD production capability of fuel, gasoline additives deposit forming tendency is derived as a function of oxidative degradation pathways

[28]. In another test conducted using a polyether amine and polyolefin amine (POA) additive package [34], the POA produced an overall higher CCD thickness due to its more complex chemical structure. To summarize, the introduction of more structurally complex liquid IVD additive packages and the use of a higher concentration of these additives into the combustion chamber reduces the amount of deposits that accumulates on the intake valves, but also contributes to the growth of CCD.

To this point, fuel property and composition effects have been the primary consideration in the growth of CCD, however, other SI engine parameters do play a role in the production of deposits. In general, the temperatures of the metal walls plays a substantial role in the formation of SI deposits, therefore any engine operation that affects surface temperatures will impact deposits. Cooler walls promote growth of the deposit layer, while warmer regions exposed to combustion gases experience less deposit growth. Because there is a great deal of variance in the average surface temperature across various regions of an SI engine, the corresponding deposit weights and thicknesses differ accordingly [13, 38-42]. Increasing engine speeds and loads tends to decrease deposit growth [18, 34], as these raise in-cylinder temperatures and as a result those of the wall as well. In fact, operating an SI engine at relatively high loads and speeds is an effective method for removing accumulated deposits [43-45]. Consequently, the reduction of wall temperature that results from lowering the coolant temperature promotes the growth rate of CCD [31].

The final point to mention with respect to SI engine deposits is the manner in which they affect engine operation. While the combustion process itself is not significantly impacted by deposits, other performance characteristics are influenced,

such as the octane requirement increase (ORI), emissions and fuel economy. As deposits build up in an engine, there is an increased tendency to knock and its octane requirement increases. In general, fuels that promote deposit growth, such as those with a high boiling point, a high aromatic content or certain additives augment ORI [41, 46-51]. The chief reason for this ORI phenomenon is that the deposit layer stores thermal energy from one cycle and then transfers this heat to the next, thus raising end gas temperatures and exacerbating knock [52]. In addition, there is a possible chemical catalytic effect from the layer, as hydrogen peroxide molecules can be adsorbed during combustion and later released in the end gas to promote further knocking [53]. In addition to ORI, the concentration of a number of important species in the engine emissions changes as a result of deposit accumulation. NO_x levels are reduced whenever CCD is completely removed from the chamber [54-58]. This is attributed to the decrease of bulk gas temperature when deposits are not present in the cylinder. Comparatively, hydrocarbon (HC) emissions usually decrease with deposits in-cylinder [54-56, 59, 60], as the increase of gas temperatures served to burn up more of these species during the combustion process. Of further interest is a study that showed how surface temperature of the chamber walls has a noticeable impact on HC levels [56, 61-63], as hotter surfaces from increased coolant temperatures produces less HC. Because the deposits induce a similar thermal effect, it was thought that a deposit coating could be useful in suppressing some HC emissions. Thus far there is no conclusive evidence to support whether CO increases or decreases with deposit growth, although, CO_2 was lowered with increased deposition [54, 64]. These reductions were directly related to the increased fuel economy shown in engines with a

coating of CCD [64-69]. It was reasoned that fuel efficiency gains were realized because the deposit coating in the combustion chamber reduced the heat loss to the walls and coolant. This was more pronounced at lower speeds where time scales are larger and there is more time for heat transfer to occur.

1.4.2 Deposits in HCCI Engines

While there has clearly been a vast amount of combustion chamber deposit research in SI engines, there is far less research available in HCCI combustion to give any appreciable indication of how fuel compositions would affect the layer, and how this layer would then influence combustion. The only studies currently available are the result of previous and ongoing efforts at the University of Michigan, which consider steady-state operating points with one fuel, a research grade gasoline designated RD3-87. While at this point our knowledge is limited, these studies have been instrumental in conveying a critically important fact concerning deposits in an HCCI engine; their impact is significant across the entire spectrum of HCCI combustion. Furthermore, as the interaction between combustion and fuel properties is a complex and intricate interplay, it is insufficient to view the layer as a homogenous thermal wall boundary [70]. As mentioned previously, in SI operation the deposits' impact is seen primarily at the extremes of the load range, when there are more favorable conditions for knocking, but because auto-ignition is present over the course of the entire load range in HCCI, the deposits' effect is not limited to the extremes. Thus, a comprehensive understanding of the manner in which deposits influence combustion, with respect to the fuel constituents from which they originate, is crucial in further controls development for the HCCI engine.

As alluded to previously, there are a number of quantifiable effects seen in an HCCI engine as the CCD layer accumulates, and furthermore, the experiments at the University of Michigan thus far have confirmed an “extreme sensitivity of HCCI combustion to deposit formation on the surfaces of the combustion chamber” [71]. Beginning with the most fundamental of experimental measurements, we see that as the deposit layer accumulates in our test HCCI engine, the pressure trace is altered, chiefly as the location of peak pressure and the crank angle of 50% mass fraction fuel burned (CA50) advances. Moreover, for a given operating point, as the peak pressure location in the combustion process approaches TDC as a result of this continual advance, the ringing intensity also increases.

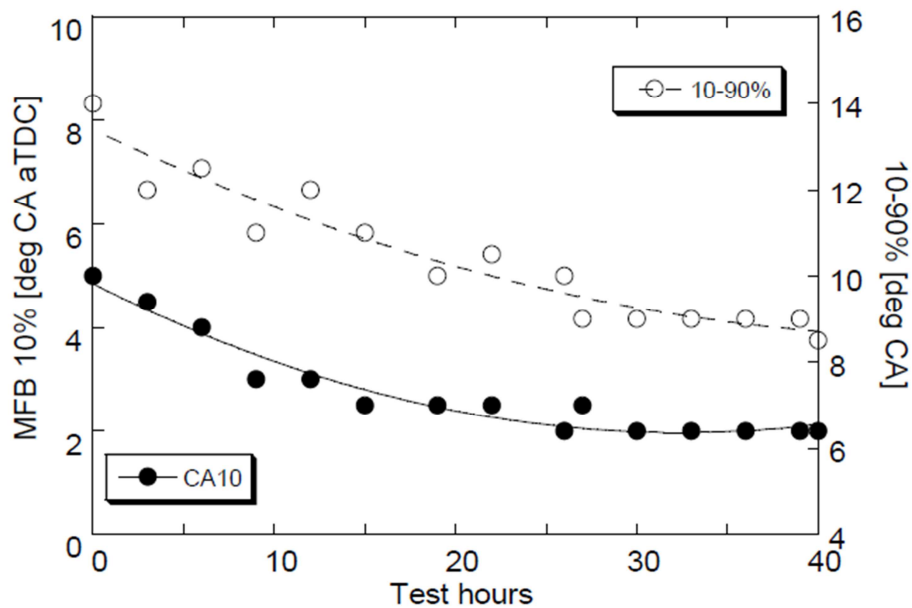


Figure 1.17 - CA10 and CA10-90 burn duration curves shown over the course of passive conditioning [7]

These changes in combustion phasing caused by the layer also have a profound effect on other in-cylinder phenomena, primarily burn duration and heat transfer. As the CCD layer accumulates and the combustion chamber is conditioned, there is a marked decrease in the time for combustion, as shown in Figure 1.17. Notice that over the 40 hour conditioning period, the CA10 and 10-90% mass fraction burn duration (CA10-90) steadily drop until they begin to asymptote to an equilibrium level. Eventually, the CCD layer reaches a state of full conditioning, at roughly 40 hours with the RD3-87 fuel, where the surface temperature of the layer is sufficiently high to prevent further deposit accumulation.

Due to the alterations in heat transfer and in-cylinder temperatures caused by the conditioning process, it is not surprising to learn that emissions output from the engine changes in accordance with the layer's growth. Figure 1.18 conveys how the emissions levels for hydrocarbons (HC) and oxides of nitrogen (NO_x) evolve as deposit growth progresses in the combustion chamber. Due to higher in-cylinder temperatures around the peak of combustion, there is an increase in NO_x emissions, the production of which is correlated strongly with increasing temperature. Conversely, the HC emissions decrease because they are more completely burned during combustion, which manifests itself as better combustion stability.

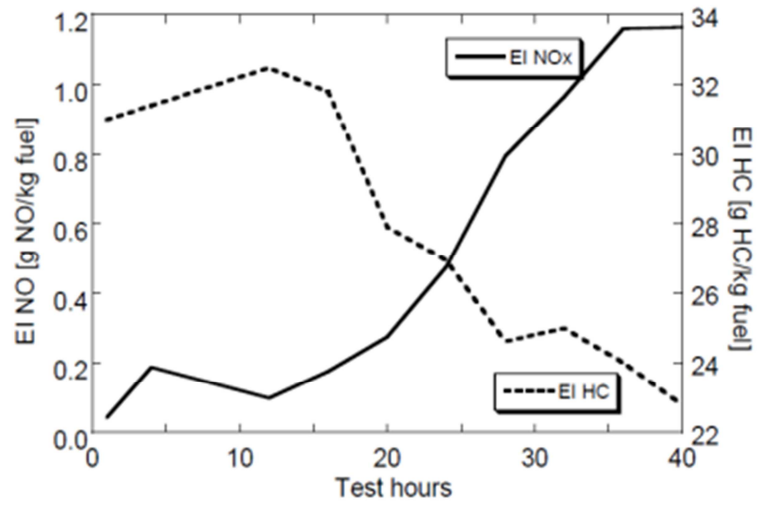


Figure 1.18 - Emissions indices plotted against time as the deposit layer accumulates [7]

Indeed, this stability is confirmed, by lower coefficient of variance of IMEP values as the combustion chamber becomes more conditioned.

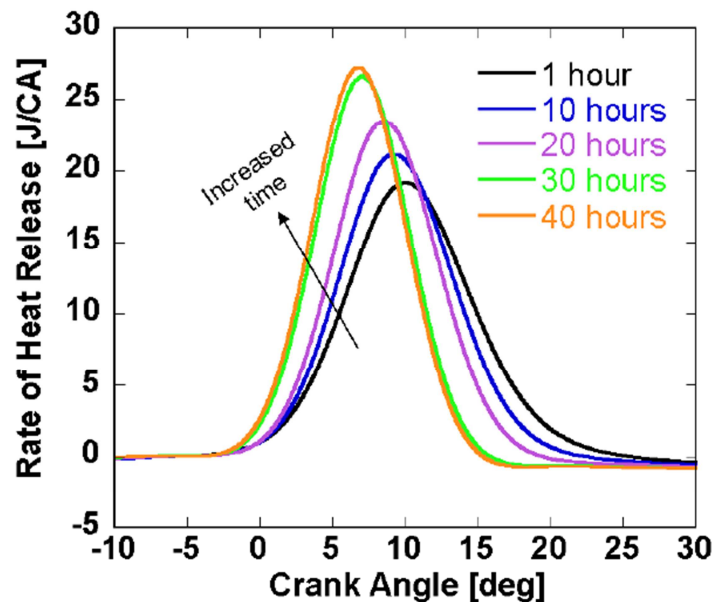


Figure 1.19 - Rate of net heat release in the engine as time progresses and the CCD layer builds [7]

In addition, as Figure 1.19 shows, heat release is changed dramatically over the course of the conditioning process. As the combustion chamber is subjected to thicker layers of deposition, the peak of the net heat release advances, a result that is consistent with previous observations regarding the advance of peak pressure and faster burn rates. Continuing, not only does the peak of net heat release advanced with increased growth of the deposit layer, but its peak magnitude also increases. Figure 1.19 also implicitly drives at another important phenomenon; there are distinct “phases” of growth, similar to those observed in the deposit formation process in SI engines. Initially, when starting from a completely clean metal piston, the layer will build rapidly during the first hour of operation making it difficult to collect data as in-cylinder conditions are constantly changing. After the initial accumulation, there is a period of growth over the next 10-20 hours where rates of deposition slow, but the layer continues to shows appreciable thickening. Finally, after 30 hours of operation, the surface temperature of the layer is sufficient enough to greatly reduce deposit growth rates, and the thickness of the layer begins to asymptote to an equilibrium state. The graph in Figure 1.20 was taken from heat flux probes mounted in the cylinder head of the HCCI test engine that were used in the previous deposits study. The specifics of these heat flux probes will be detailed in a future section, so, for now, it will suffice to say they consist of a pair of fast response thermocouple probes mounted at a known distance apart, so that one-dimensional heat flux can be measured with a known thermal conductivity of the probe. The heat flux is measured at the deposit layer and metal, probe surface interface, and it is immediately apparent that as time progresses and the layer builds on the probe’s surface, the heat flux normal to that surface retards

with regards to the crank angle location of the peak. Furthermore, the value of the peak heat flux at the interface decreases with increasing layer thickness. Such results indicate that the deposit layer acts to insulate 1-D heat transfer to the probe surface, leading to reduced and retarded heat flux peaks.

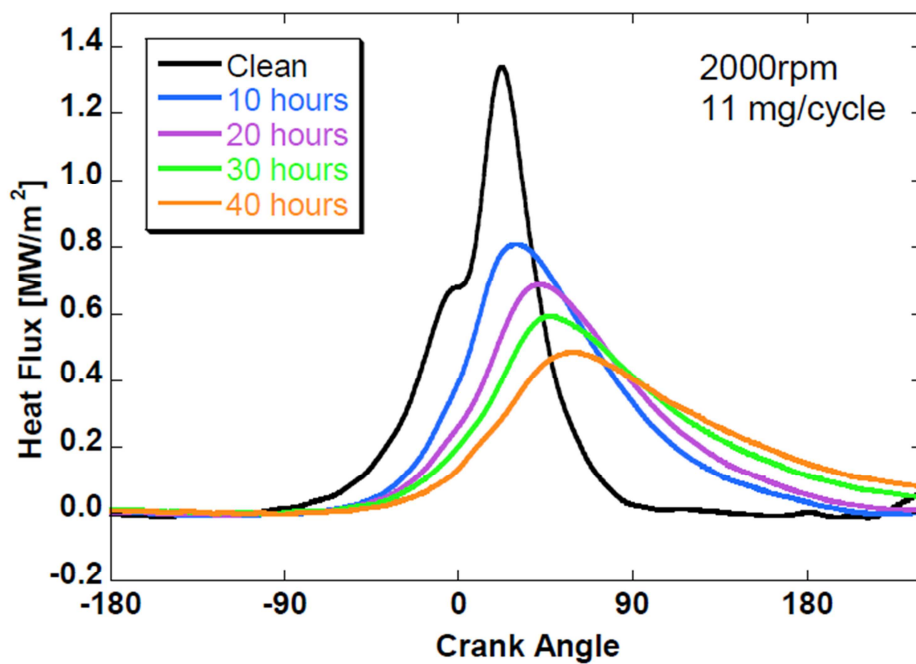


Figure 1.20 - Progression of heat flux profiles as the combustion chamber is passively conditioned [7]

Another characteristic worthy of mention is the redistribution of heat transfer throughout the combustion cycle. In other words, while there is diminished peak heat flux during combustion, the total heat transfer during the entirety of the combustion process does not change. Instead, there is a phase shift of heat transfer to the metal walls, with reduced values during the main part of the combustion event, and an extended tail that persists deeper in the expansion stroke. In Figure 1.20, as compared

to a nearly clean probe after 1 hour of operation, a conditioned probe covered with a significant CCD layer indicates a retarded heat flux profile, which extends to later stages of the cycle. Physically, this is because the deposit layer serves as an insulator during compression and subsequent combustion, causing more heat to be retained in-cylinder during the main stage of combustion than is with clean metal walls, which feature a higher thermal conductivity than the CCD layer (as evidenced by the reduced heat flux peaks and positive crank angle shift of that peak, when the metal surface with the thermocouple junction is covered with CCD). Because the engine does not continue to store excess heat from cycle to cycle, this increasing quantity of retained heat during compression and combustion must be rejected as a commensurate increase in heat flux, later in the cycle, shown quite clearly by the growth of the CCD layer which has substantially higher heat flux at later crank angles.

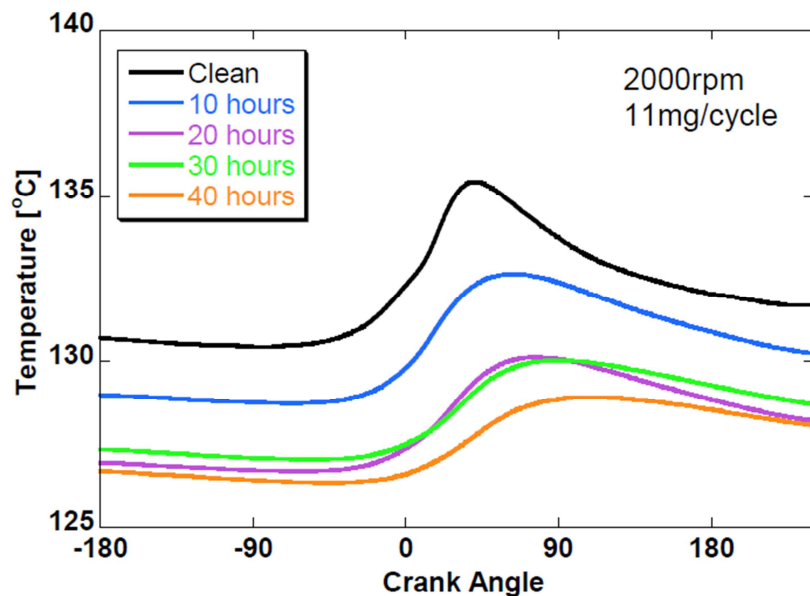


Figure 1.21 - Phasing of the surface temperature peak from a heat flux probe as the deposit layer grows with time [5]

Figure 1.21 displays yet another important trend provided by the heat flux probe analysis, chiefly, the ever changing surface temperature of the probe at the metal/deposit interface. The figure shows that as the combustion chamber becomes more conditioned with increasing run time, the surface temperature profile of the probe is altered drastically, as the peak surface temperature decreases and the location of the peak moves to larger crank angle degrees at later points in the cycle. Given previous discussion this outcome is logical, as the growing deposit layer insulates more heat energy in-cylinder and prevents heat from reaching the surface of the probe, and as a result the reduced surface temperature of the heat flux probes is reduced. However, a more important detail to glean from this analysis is the change in phasing of the surface temperature peak, denoted as $\Delta\theta_{T_{max}}$ in the figure. Using this measured shift of the surface temperature peak in crank angle degrees, it is possible to determine information regarding the thermal properties of the layer, most notably the thermal diffusivity [7, 72, 73] (the specifics of the heat flux probes and data interpretation are covered in chapter 3). Utilizing a trigonometric function as an approximation for the instantaneous surface temperature, a set of expressions for in-situ thermal diffusivity, shown by Equation 1.5 and Equation 1.6, is obtained. This derivation is further explained in Chapter 3.

$$t_{peak} = \Delta t = x \frac{(1 + \sqrt{2})}{6} \sqrt{\frac{t_o}{\pi\alpha}} \quad (1.5)$$

$$\alpha = \left(\frac{x (1 + \sqrt{2})}{\Delta t \cdot 6} \right)^2 \frac{t_o}{\pi} \quad (1.6)$$

These expressions allow for the observation of trends with increasing CCD layer thickness on the two cylinder head heat flux probes. The plot in Figure 1.22 summarizes these trends over the conditioning period of 40 hours, using the RD3-87 test fuel.

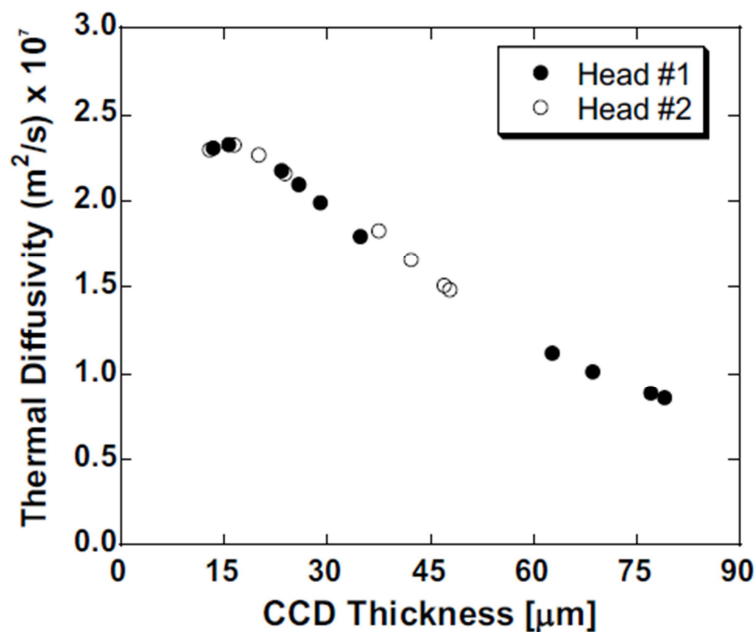


Figure 1.22 - Changing thermal diffusivity of the deposit layer as the thickness increases [7]

In short, as the layer collects on the cylinder head, the thermal diffusivity of the layer drops appreciably, and begins to asymptote as the layer reaches an equilibrium thickness. It is interesting to note that the thermal diffusivity of the layer is a strong function of layer thickness, and there is a great degree of similarity between the thermal diffusivity of the deposit layers in the two different head locations. This suggests that the properties of the layer at these two locations are comparable. The correlation between thermal diffusivity and thickness arises because the underlying morphology of

the CCD layer is constantly changing as it forms, which naturally affects the properties of the deposition.

Another crucial finding is the manner in which the deposit formation impacts the range of operability for HCCI combustion [2]. Consider Figure 1.23, which depicts the load range of HCCI operation over a 1200-2400 RPM speed sweep for a clean metal piston as opposed to a piston that is fully-conditioned with deposits.

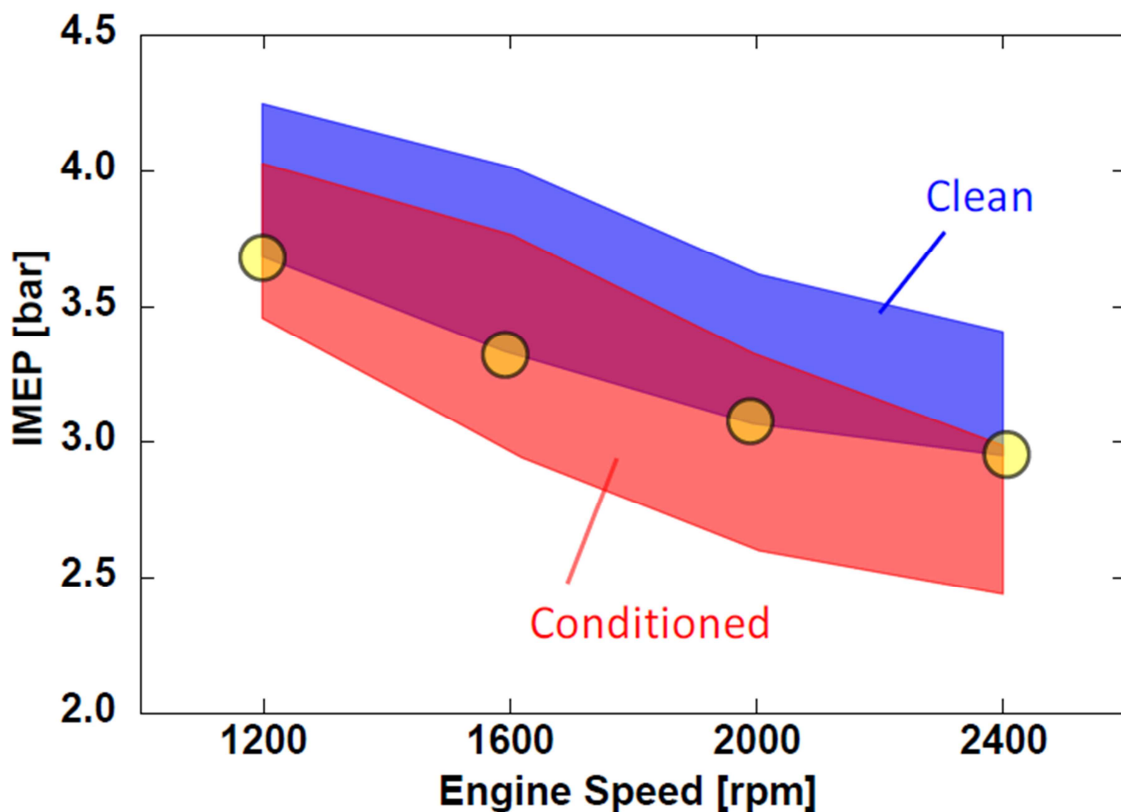


Figure 1.23 - Shift in HCCI operating limits comparing a clean piston to one that is coated with an equilibrated layer of deposits (fully-conditioned) [5]

The limits of operation were determined by a ringing intensity of 5 for the highest permitted load, and a coefficient of variance percentage (COV%) of indicated mean

effective pressure (IMEP) at 3% for the misfire limit. As shown in Figure 1.23, while the overall areas of operation encompassed in these two cases are similar, the position of the regions relative to IMEP are quite different, as the fully-conditioned piston shifts the entire range down in IMEP value. At the misfire limit, having a coating of deposits helps to retain additional heat in-cylinder, as the insulating CCD layer limits the amount of heat transfer to the walls. This, in turn, aids in the HCCI auto-ignition process, and allows the engine to run at lower load points than are possible with a clean engine. At the point of excessive knocking at high loads the deposits shift the limit down due to a similar physical reasons. More heat is retained during the compression stroke with an accumulated deposit layer, which causes higher temperatures and pressures in-cylinder, effectively advancing combustion from where it would occur in a clean engine. This brings about higher ringing intensities at the same IMEP level, and so with deposits the engine cannot safely reach the same height in load level as it does when it is free from CCD growth. While it does not necessarily expand the range of HCCI operation, it does shift it to a potentially more beneficial region in terms of fuel economy. The most inefficient region of the SI regime is at idling conditions and low loads where brake specific fuel consumption (BSFC) values are unfavorable. Here, the unthrottled, high-efficiency operation of HCCI is extremely desirable, so there are substantial fuel economy gains to be realized if the limit of HCCI can be shifted down into this low load regime.

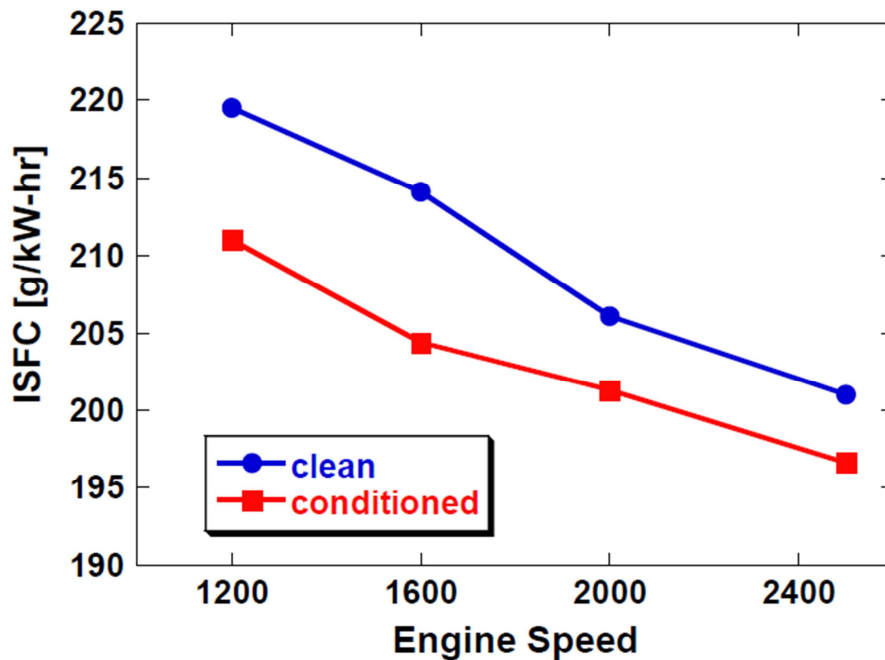


Figure 1.24 - Comparison of fuel efficiency for a speed sweep of an engine free of deposits as compared to one that has a deposit coating [5]

In fact, over the same speed range as is depicted in Figure 1.23, there is a perceived benefit to indicated specific fuel consumption (ISFC), shown in Figure 1.24. The points in Figure 1.24 were taken from the speed and load intersections highlighted in yellow in Figure 1.23. These operating points were found in both the clean and conditioned maps, which allows for a direct comparison between the two cases. In all the speed cases presented, the conditioned chamber always exhibits lower ISFC calculations, which is likely attributable to the reduced heat transfer to the walls provided by the insulating effect of the deposit layer. Figure 1.25 illustrates conceptually the ISFC benefit that could be realized with a deposit coating. As heat transfer is reduced and combustion phasing is advanced, both of which are characteristic of the CCD layer, ISFC lowers as long as combustion is not advanced too

close to TDC. This further substantiates the claim that a layer of deposits serves to benefit fuel economy performance at lower load operation.

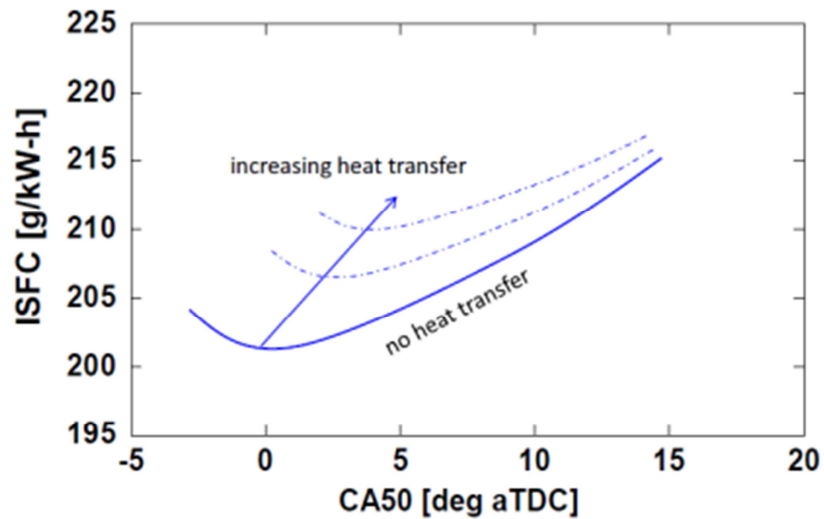


Figure 1.25 - Conceptual diagram of the effect of heat transfer and combustion phasing on Indicated Specific Fuel Consumption (ISFC) [74, 75]

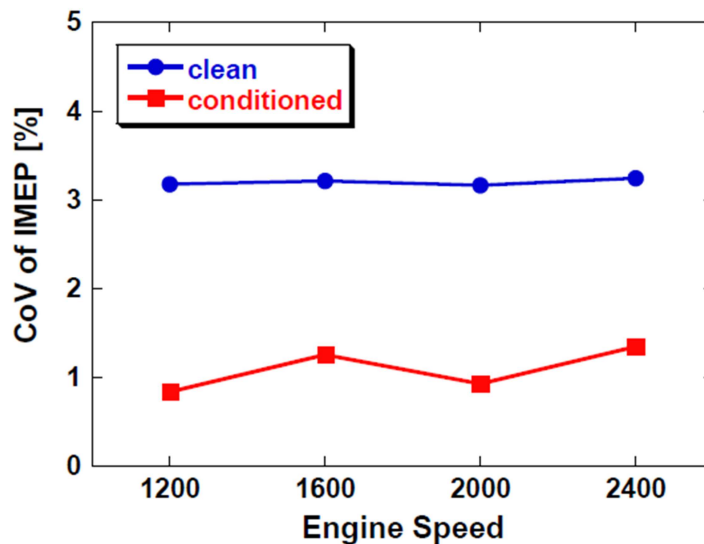


Figure 1.26 - Comparison of combustion stability from a clean to a conditioned engine over a speed sweep [5]

In addition to bolstering fuel economy, the deposit layer also aids in combustion stability when considering the COV% of IMEP at a given operating point. Figure 1.26 uses the same speed and load points as the plot of Figure 1.24, and while all the clean data occurred at the misfire limit of 3%, the conditioned points are located at more comfortable stability levels, near 1%. As previously alluded to, because the deposits diminish heat transfer during the compression stroke, they shift the temperatures and pressures in-cylinder up prior to the combustion event occurs. These increases result in an auto-ignition process that transpires earlier and burns faster, both of which contribute to a more stable combustion event.

In summary, though there is some understanding of how the CCD layer forms in regards to fuel properties and the role CCD plays on SI combustion, only a fraction of this knowledge base is directly applicable in a low-temperature combustion regime, such as HCCI. We do possess some insight as to the sensitivity of the HCCI process to a burgeoning layer from one fuel, but more testing must be conducted with additional fuels to best assess how HCCI combustion, fuel properties and the deposit layer are coupled.

1.5 Motivation for the Research

To this point, it is clear that combustion chamber deposits and fuel components have a prolific effect on the HCCI combustion event. However, it is not readily apparent how to design practical control strategies to compensate for fuel constituent variations and the subsequent accumulation of deposits. Because the HCCI combustion event

does not have the same type of direct triggers as in SI and CI, it presents a significant combustion controls challenge. The HCCI controls issue is further compounded by variability of performance parameters, intrinsic to the life-cycle of any engine used in a commercial passenger vehicle. Variations of ambient conditions, engine hardware, e.g. tolerances, sealing ability of piston rings, valve timing mechanism etc., can all create additional challenges in a practical application. One of the principal contributors to this issue is the vast array of refinery streams used to create the gasoline delivered to fuelling stations throughout various regions of the U.S. The histograms in Figure 1.28, Figure 1.29 and Figure 1.30 were taken from a 1999-2005 survey [76] that sampled all major U.S. brands. They illustrate the range in which the concentration of aromatics, concentration of olefins and the RON vary in pump gasolines sold in the United States [76]. The selection of fuel in an HCCI application has the potential to substantially influence design and control systems for an HCCI engine [77]. The principal components of gasoline, paraffins, olefins and aromatics, exhibit different heat release profiles (see Figure 1.27) in an HCCI engine, so varying proportions of these chemicals in refinery stream fuel could impact HCCI combustion.

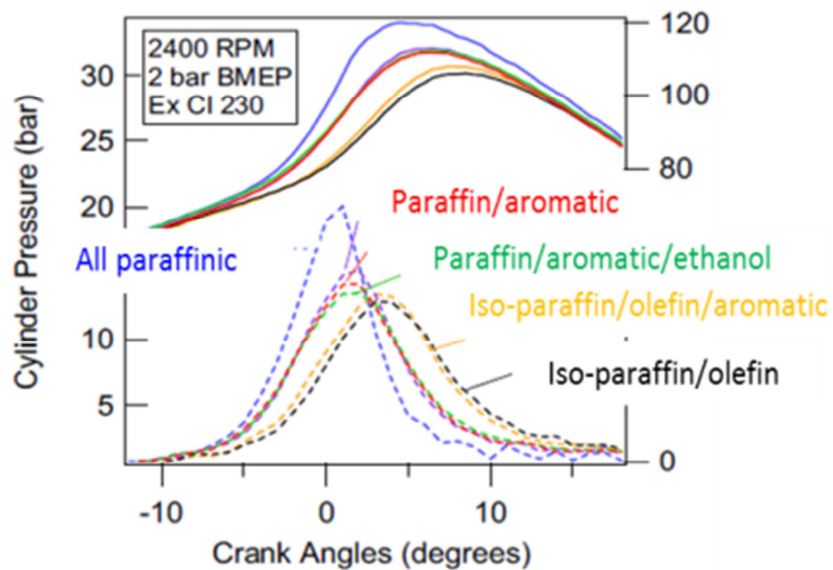


Figure 1.27 - Example of how a few different fuel blends can influence heat release and pressure traces in an HCCI engine at the same operating condition [78]

Moreover, a fuel blend created with ideal properties and composition could be instrumental in making the HCCI process more robust [79]. Multiple scientific experiments and modeling studies have concluded that the fuel composition impact on HCCI combustion manifests itself in ignition delay, combustion phasing and rate of heat release [8, 80-93]. However, most of these studies have focused on single-component fuels and fuel surrogates, which do not constitute a representative sample of the gasoline available at the pump. Examination of refinery stream gasoline, and determination of the range in which the key properties vary, is a crucial first step in understanding the potential impact of these factors on real-world HCCI engine applications.

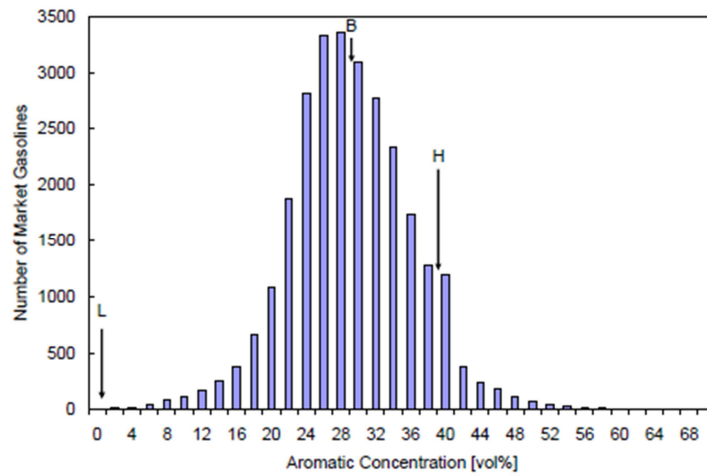


Figure 1.28 - Aromatic concentrations of sampled pump gasoline throughout the United States [76]

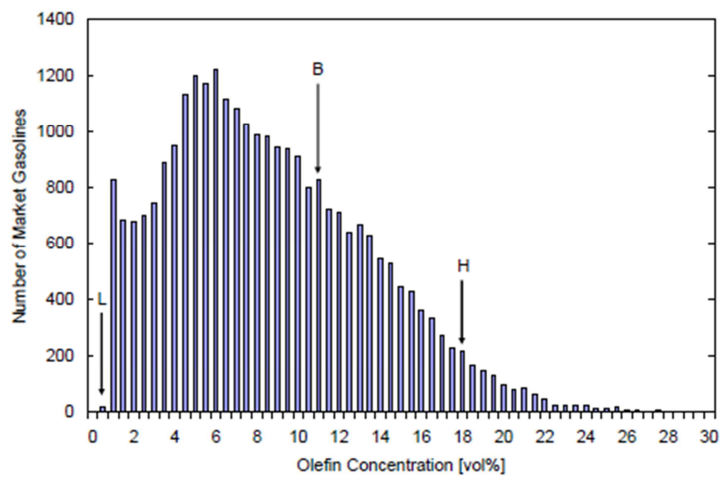


Figure 1.29 - Olefin concentrations of sampled pump gasoline throughout the United States [76]

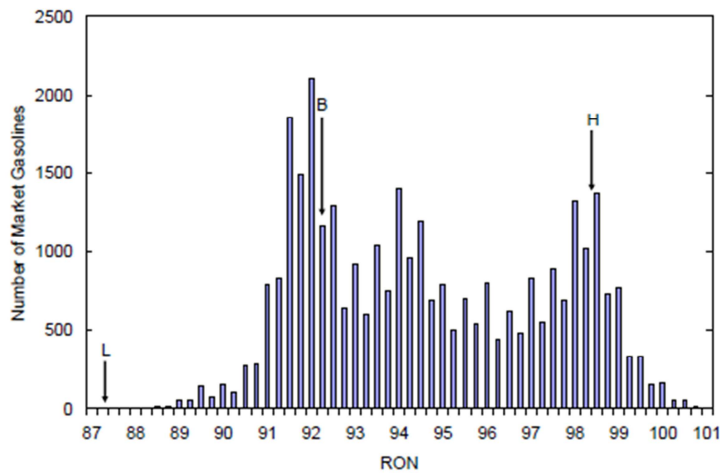


Figure 1.30 - Research Octane Number (RON) of sampled pump gasoline throughout the United States [76]

Adding to the controls challenge, the benefits of the HCCI engine in a vehicle depend on the attainable operating range. The first figure in a paper from Yang [94] summarizes the study of expanding the HCCI load range and the problems that hinder the limits of operability for HCCI. On the low load side, the instability limit is reached when there is insufficient thermal energy in-cylinder to initiate and sustain combustion. At the high load limit, the reaction rates accelerate to a point that causes ringing, or knocking conditions, characterized by very high pressure rise rates. This noise is unacceptable to consumers, and excessive pressure waves can lead to mechanical stresses that damage the engine.

Figure 1.31 provides an approximate visual illustration of the loads that are normally achieved by SI engines and the fraction of the load range that can typically be covered by naturally-aspirated HCCI operation, based on a previous study [95]. The more points that an engine can run in HCCI mode, particularly at the low load limit

where SI engines are highly throttled and have high brake specific fuel consumption (BSFC), the more fuel economy savings can be realized. To address the limited range of HCCI, much of the current research in advancing HCCI technology is driven by the need to expand the relatively limited load range of HCCI [94, 96-104]. Variation in fuel composition has the capability to alter the range over which HCCI can reliably operate [76], because as fuel composition changes, the auto-ignition properties of the fuel such as RON and MON are affected, and these changes have the potential to impact the low and high load limits of HCCI operation.

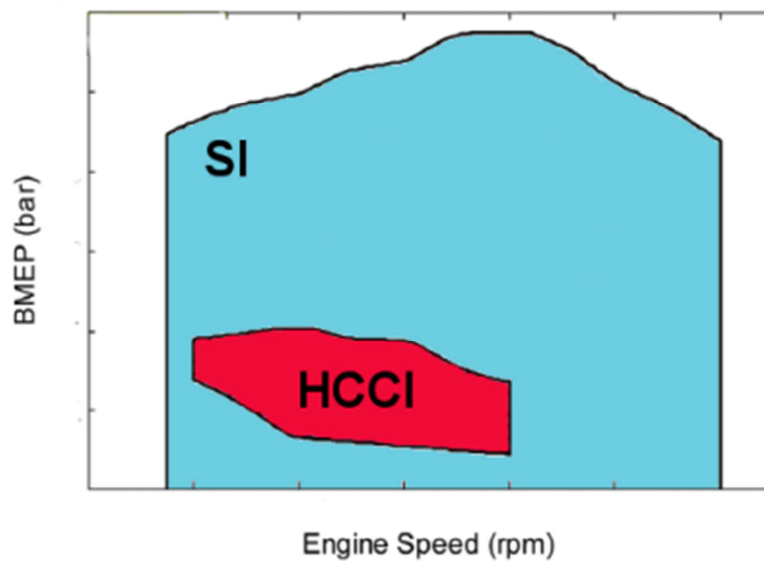


Figure 1.31 - Qualitative visual representation of the relative sizes of the HCCI and SI operating maps for naturally aspirated operation, adapted from [95]

The compositional variability in the fuel available at the pump also has significant implications as to how the deposit layer will develop in-cylinder in an HCCI engine. As mentioned in previous sections, SI experiments show that fuel composition plays an

integral role in the growth of combustion chamber deposits (CCD) and the overall quantity of deposition that will accumulate in an engine [15, 17, 19, 22, 28, 35, 105-110]. Essentially, gasoline that possesses more complex molecules, such as aromatics, and has a higher boiling point has a tendency to promote in-cylinder CCD buildup. CCDs will not accumulate indefinitely, but rather, will reach an equilibrium “fully-conditioned” state, at which the surface temperature of the layer (which increases as the layer accumulates) becomes high enough to prevent any further deposition [111]. This equilibrium state is highly dependent on the fuel composition responsible for the creation of the CCD layer [33]. Furthermore, the presence of deposits affects the entire operating range of an HCCI engine in substantial fashion [5, 7], and the extent of that effect is largely related to the state of the CCD layer.

In summary, because commercially available refinery stream fuels are likely to be the primary source of fuel for HCCI engines when they come to market, there is an appreciable need for this work. The chemical properties of fuel play an integral role in the HCCI combustion event, and they have an influence upon the buildup of deposits. As there is a wide array of chemical components in pump gasoline in the United States, it is critical that the CCD layer be fully characterized and that the interplay among fuels, deposits and HCCI thoroughly understood. Ultimately, this knowledge can lead to the development of practical strategies and technologies to cope with the variability of pump gasoline, and its impact on HCCI engine operation.

1.6 Research Objectives and Projected Contributions

Despite the pioneering efforts in HCCI deposits research at the University of Michigan, substantially more study is required to fully understand the complex interplay between fuels, HCCI combustion and combustion chamber deposits.

The first major research objective is to characterize the effect of fuel composition on HCCI engine's combustion performance and fuel efficiency. A comprehensive set of fuels will be investigated, which covers all of the relevant variations seen in refinery stream gasoline. The test matrix developed for this research has three dimensions: the fraction of olefins (O); the fraction of aromatics (A); and the sensitivity (S), defined as the difference between the RON and the MON (RON-MON). The goal is to correlate variations in auto-ignition and combustion phasing with either the fuel composition or octane rating. We say "either" because the previous research clearly emphasizes the importance of developing insights into fuel behavior, but did not produce sufficient knowledge to establish a correlation between fuel parameters and HCCI combustion. The first set of measurements taken during this endeavor will investigate auto-ignition phenomena, such as the intake charge temperature required to achieve the optimum combustion phasing at a given reference condition, and the sensitivity of HCCI combustion to changes in load. A deeper understanding will be pursued by correlating fuel properties to changes in the HCCI operability range and variations in combustion phasing that result under extreme conditions. The HCCI operability range has a strong relationship with practical engine design, due to its relationship with fuel economy.

The combustion studies will be performed in a manner which ensures no impact from CCD, i.e. the combustion trends will be monitored to ensure that there is no

appreciable deposit formation. In the event of deposit accumulation, tests will be stopped, and a cleaning procedure applied, in order to return the combustion chamber to a “clean” state. Eight fuels in the test matrix contain 10% ethanol by volume. In addition, a smaller matrix of fuels with 20% ethanol as well as pure ethanol will be tested to assess the effects of this molecule on overall trends.

The results of these fuels-combustion tests will provide meaningful guidance for future HCCI research that focuses on production-intent design and controls solutions. To this end, it would be valuable to capture the main trends with a model or correlation, which can subsequently be used for an array of HCCI studies. The direction adopted for this study is to investigate the usefulness of the existing Octane Index model, and based on the findings develop additional terms which correlate composition (A or O) and sensitivity (S) to auto-ignition trends.

In viewing performance and fuel economy, the examination of the direct effect of fuel on engine output will be carried out through the analysis of IMEP trends, combustion efficiency, thermal efficiency and specific fuel consumption. Of interest in this analysis are effects which extend beyond simple variations in fuel lower heating value. It is hypothesized that combustion efficiency and the thermodynamic effects that result from variations in the required intake air temperature will cause tangible changes in indicated specific fuel consumption, even when combustion phasing is maintained at an optimum level.

The second major objective is to investigate the effect of fuel composition and additive packages on HCCI deposit formation. In order to maximize relevance, the project will utilize custom multi-component fuel blends (made from actual refinery

streams) indicative of the variation in pump gasoline from different refineries. Refineries have available to them various components and methods for achieving a given octane rating in a fuel, and these varied chemistries will likely have a major impact on the formation of combustion chamber deposits. This diversity will be characterized based on variations in olefinic content, aromatic content, research octane number (RON) and sensitivity, much like the original matrix developed for the combustion study. However, the set of fuels for the deposit study is much smaller and the composition of these fuels will be altered to exacerbate the CCD formation effects. The amount of time required to reach an equilibrium thickness state, which is when the surface temperatures are sufficient to inhibit further layer growth, will be considered in light of varying fuel compositions and additive packages. The thickness of the equilibrated layer will be measured and compared among fuels. Two additive packages, polybutene amine (PBA) and polyether amine (PEA), will be included in this investigation. Their respective compositions and behaviors in SI engines vary greatly, and it will be important to discover their impact on the HCCI engine. The ultimate objectives differ depending on the combustion mode, as in the case of the HCCI engine we want to achieve control over the thickness of CCD, while in the case of the SI engine the focus is on removing deposits from the intake valve.

The second part of the deposits study will aim to discover and explain how the deposit layers formed from dissimilar fuel chemistries affect the HCCI combustion event. Specifically, it is desired to obtain data that can conclusively determine if the effect of deposits on HCCI combustion is purely that of a thermal insulating barrier, or if there is any secondary chemical or catalytic effect. An investigation of heat release and

burn durations at various operating points will serve as an indication of the impact of the deposits on combustion phenomena.

Finally, the properties of combustion chamber deposits will be investigated using a variety of techniques for physical and chemical characterization. In the interest of fully describing the structure of the CCD, certain microscopic, spectroscopic and diffractometric techniques will be employed to quantify physical structure, morphology, chemical composition and porosity. It is critical to capture thermal properties such as diffusivity, and advanced techniques will be utilized to achieve this. Physical structure and morphology of the deposits will be studied using low-vacuum scanning electron microscopy (SEM) and transmission electron microscopy (TEM) imaging methodologies. The detailed chemical composition is captured using both X-ray energy dispersive spectroscopy (XEDS) and X-ray photoelectron spectroscopy (XPS). Porosity and characteristic pore size is evaluated with small-angle X-ray scattering (SAXS).

CHAPTER 2

Experimental Setup

2.1 Engine Specifications

A significant part of developing the testing methodology for the study of HCCI deposits involved the implementation of the physical hardware which produces said deposition, in the form of our HCCI fuels engine in the W.E. Lay Automotive Laboratory, shown in Figure 2.1. A cross-sectional picture of the single-cylinder setup is given in Figure 2.2. The numerous layers of system design and integration necessary to bring the engine online, are detailed in this chapter.

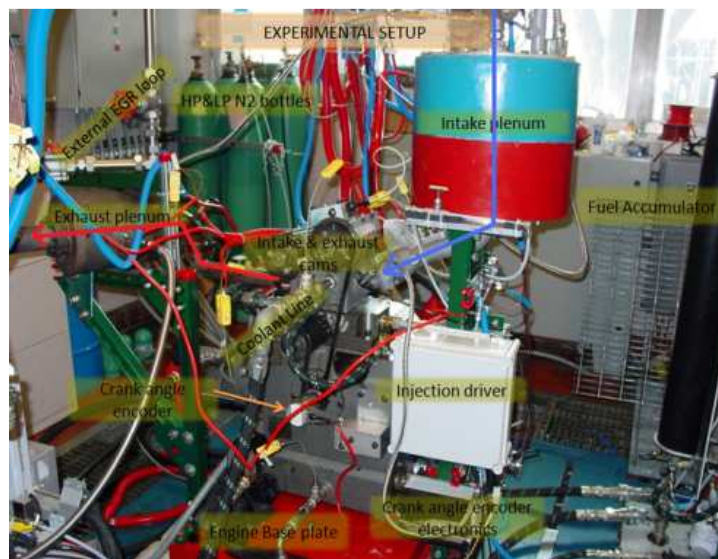


Figure 2.1 - Picture of the engine setup highlighting some of the major components

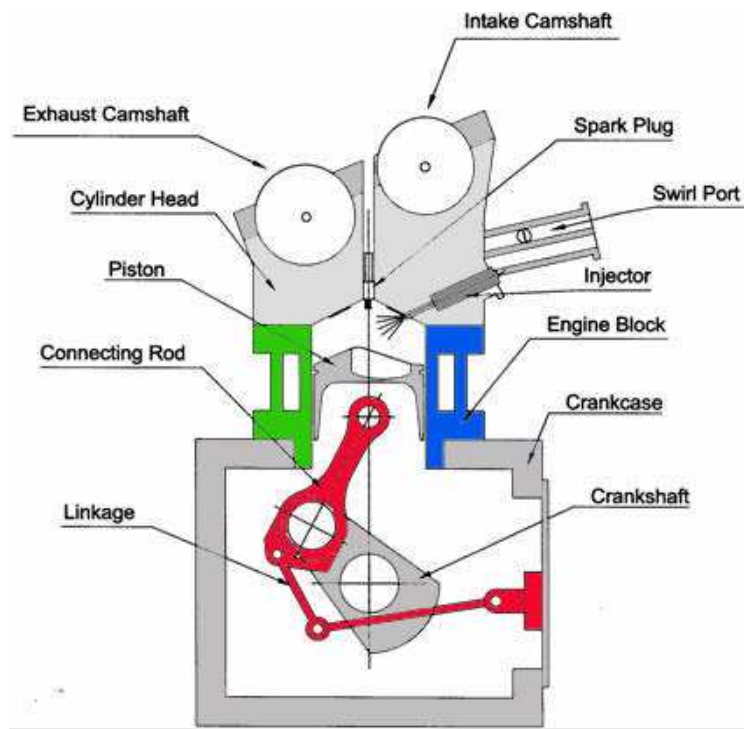


Figure 2.2 - Cross-section of the single-cylinder HCCI Chevron fuels engine

The engine used for the fuels and deposits experiments is composed of a Ricardo Hydra L850, single-cylinder crankcase, which is configured for a 4-stroke gasoline cycle. The cylinder head is a pent-roof, dual-overhead, fixed-cam prototype with two intake and two exhaust valves developed by General Motors. It has an exhaust rebreathing camshaft profile that consists of a main exhaust valve event, followed by a secondary exhaust event of reduced duration and lift, which occurs during the intake valve opening, as summarized in Figure 2.3, which depicts the valve timing profile. Table 2.1 gives the specific crank angles of the valve events.

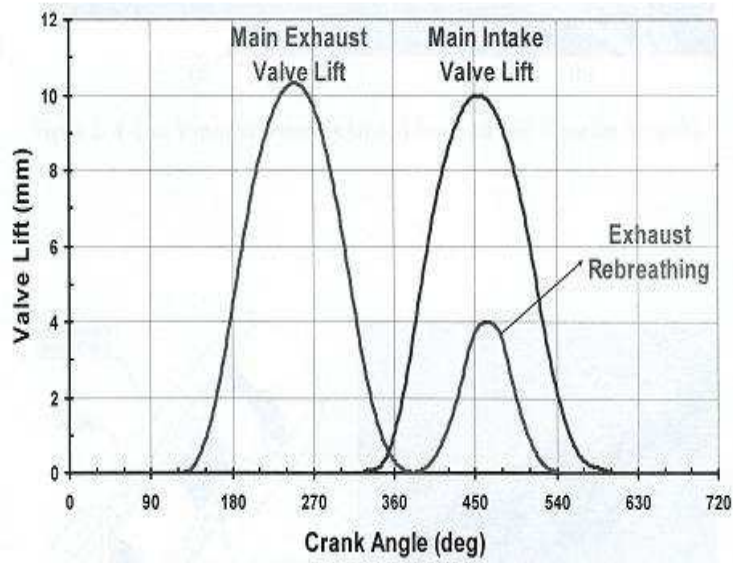


Figure 2.3 - Valve profiles for the Chevron HCCI fuels engine highlighting the exhaust rebreathing event during the intake valve lift [7]

Table 2.1 - Valve Timings

Valve Event Description	Crank Angle Degree
I/O/IVC	346 aTDC/128 bTDC
Main EVO/EVC	130 aTDC/352 bTDC
2nd EVO/EVC	326 bTDC/189 bTDC

The purpose of the rebreathing exhaust lobe on the camshaft is to re-induct hot residual gas from the exhaust runner as fresh charge is being inducted, to ensure that there is a sufficient amount of enthalpy in-cylinder for auto-ignition to occur. In addition to intake air heating, this is necessary for combustion to occur in the test engine. Several other pertinent specifications regarding the engine are summarized in Table 2.2.

Table 2.2 - Engine Specifications

Compression ratio	~12.5
Bore	86 mm
Stroke	94.6 mm
Displacement	0.549 liter
Connecting rod length	152.2 mm
Fuel Injection	333 CAD bTDC

Fuel is delivered directly in-cylinder via a GM 8-hole injector, which is angled toward the top of the piston so that the spray impinges upon the piston crown. The piston in Figure 2.4 is a shallow bowl design created to promote better spray break-up as it strikes the bowl, allowing a more homogeneous mixture of air and fuel to be achieved prior to the start of combustion. The piston's asymmetric surface geometry introduces a "squish" and "anti-squish" region in the clearance volume of the engine where the cylinder head heat flux probes are mounted, as detailed later in this chapter. In the "squish" region, pictured in the upper left portion of Figure 2.4 at the highest point on the piston surface, the clearance volume is smallest when the piston is at TDC. Likewise, clearance volume is larger in the "anti-squish" region located on the opposite side of the piston. Both of these areas are marked with arrows in the figure for easier reference. The implications of these regions and their impact on combustion are discussed primarily in Chapter 11 and 12. A schematic that illustrates the relative location of the piston bowl and the fuel spray is provided in Figure 2.5. In this image, the "squish" region is located at the top circle above the valves and the "anti-squish" region is on the opposite side.



Figure 2.4 - The piston used in the single-cylinder GM HCCI fuels engine; this particular piston has a buildup of deposition clearly shown, with a notable clean spot centrally located where the fuel spray impinges upon the piston crown

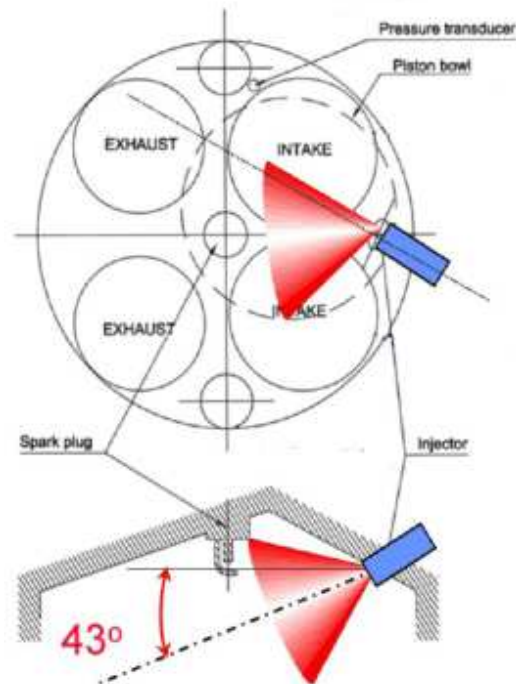


Figure 2.5 - Schematic of the experimental engine cylinder head showing the fuel spray targeting in relation to the piston bowl (indicated by the dashed circle in the top image)

2.2 Intake Air System

Air for the engine is provided via a connection to the lab's compressed air supply, located upstairs from the experimental floor, which is dried and filtered before reaching the test cell. This air flows through a critical orifice supply system, shown in Figure 2.6, wherein the compressed air is fed through a pressure regulator and into orifices of known diameter. Furthermore, these orifices connect to two manifolds, which are used to dampen out any pulsations in the shop air. Downstream of the outlet manifold is a mass air flow metering device, a Fox Instrument FT2. This flow meter device is a hot-wire anemometer, in which as air flows over a wire the flow meter provides a current to keep the temperature of the wire constant. There is a proportional relationship between the amount of current supplied and the flow of air over the wire, which is recorded by the NI DAQ. From there, the air flows through piping until it reaches the intake plenum, which is designed to have roughly forty times the displacement of the engine, in an effort to mitigate any air flow pulsations that might enter the engine. Because intake air heating is required to run the engine in HCCI mode, fin-style heaters are mounted inside the intake plenum canister perpendicular to the flow of air in order to accomplish the intake temperature control necessary during experimentation. The intake runner is attached from the bottom of the intake cylinder, which provides air supply directly to the engine. The runner also contains instrumentation for measuring intake pressure and temperature, shown in Figure 2.7.



Figure 2.6 - Critical flow orifice system comprised of the orifices of known diameter to the left of the ball valves, and two manifolds to dampen any effects of pressure changes in the shop air

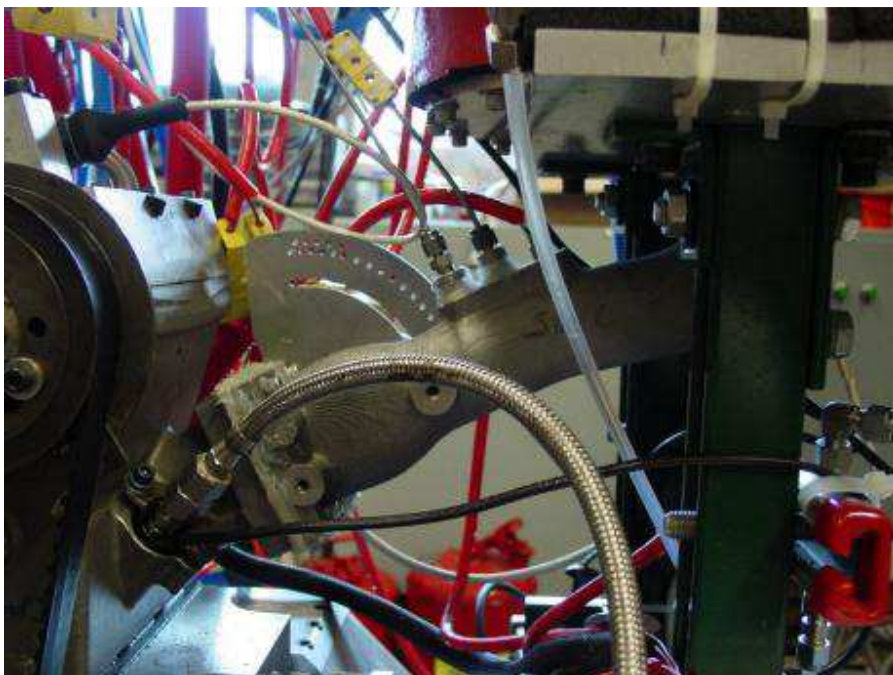


Figure 2.7 - Intake runner connecting the intake plenum to the engine; the slotted metal piece on the far side of the runner is for adjusting swirl (one of the ports in the runner can be blocked with a moveable plate)

2.3 Exhaust System

Some hot exhaust gas from the engine flows back into the combustion chamber via the re-breathing exhaust valve event. The remainder flows through the exhaust runner, which is instrumented in a manner similar to the intake runner, and into another smaller cylindrical plenum, as depicted in Figure 2.8.

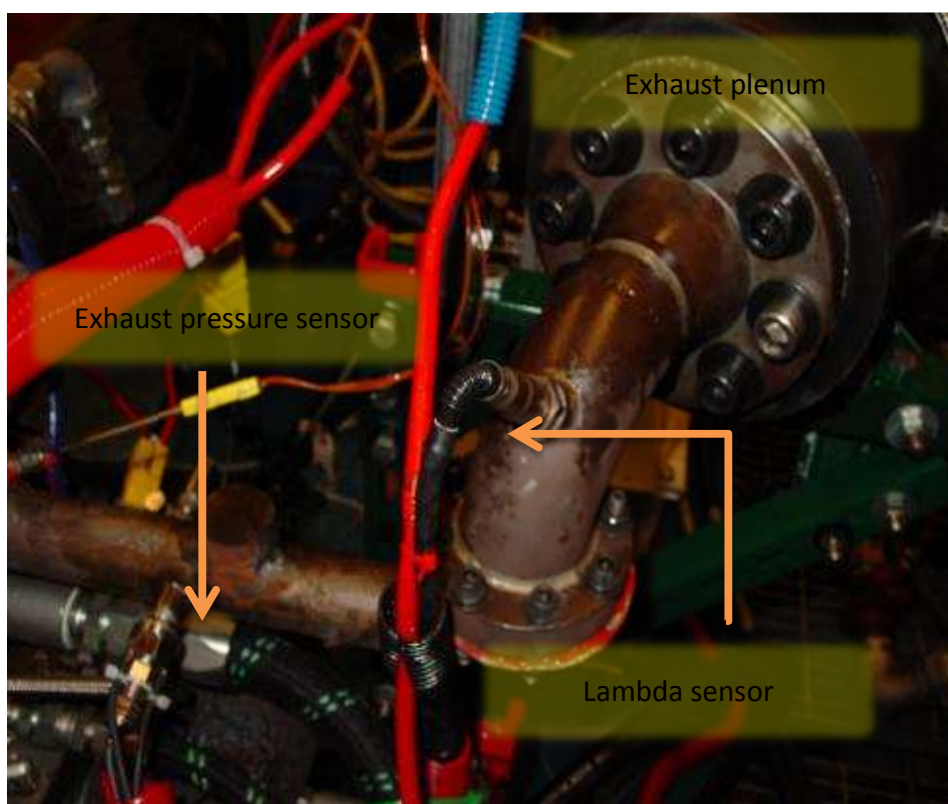


Figure 2.8 - Exhaust system highlighting the major components

Just upstream of this plenum is a Bosch LSU 4.9 wide-band lambda sensor used to determine the air/fuel ratio of the charge in the engine. This sensor is integrated with an ETAS LA4 lambda meter that conditions the signal, and is ultimately run to the low-

speed DAQ. Extending from the exhaust plenum is a small tube which feeds into an oven connected to a Horiba Mexa 7100D emissions bench system. Utilizing this bench, we are able to sample relevant engine emissions, including CO, CO₂, NO_x, O₂ and total hydrocarbons (THC), to aid in the tabulation of combustion efficiency and assessment of engine performance. Farther upstream from this sensor is an exhaust switching adapter, detailed in the next chapter, which houses the exhaust pressure transducer. The adapter receives water cooling from three lines, and takes a 2 to 5 bar air signal to open. Downstream of the exhaust plenum is a gate valve which can be opened or closed in order to adjust the exhaust backpressure experienced by the engine. The backpressure setting is extremely critical to HCCI operation, as slight backpressure alterations can result in substantial changes to internal gas residuals that engender significant changes in operation. In general, it is optimal to maintain backpressure at the nominal motoring condition of 2000 RPM and an intake air temperature of 90 degrees Celsius from day to day before the engine is fired, to ensure experimentation is running with similar residual conditions.

2.4 Fuelling Hardware

The HCCI fuels engine is a directly-injected gasoline engine, and in order to accomplish said injection, we required a highly-pressurized fuel system that was custom built for this setup, and is displayed in Figure 2.9. The key component of the fuel system is the storage and subsequent delivery unit; the piston-style accumulator which is the long cylindrical object in the picture. This unit has the capacity to store

approximately 2.5 gallons of fuel, ensuring a run time of nearly 6 hours between fill-ups, under normal operating conditions.



Figure 2.9 - Piston-style accumulator used to pressurize the fuel for direct injection

A free-moving piston inside the cylinder is pressurized from one end with inert nitrogen gas (shown at the bottom of the picture in Figure 2.9); a sufficient amount of energy can be stored in this manner as the gas is highly compressible. This provides the method for pressurizing the fuel, which is filled from the other end of the cylinder, and is nominally charged to 1600 psi (roughly 110 bar injection pressure). The system also contains a number of bleed valves, so that before the pressurization process, any

excess gas bubbles in the system can rise and then be removed from the fuel side of the system.

Several other components comprise the fuelling subsystem, including the fuel storage cans, which are located below the base plate in the trench of the test cell. There is one larger pressure vessel of 3 gallon capacity which acts to hold fuel until it is transferred into the piston accumulator for testing. This storage vessel is lightly pressurized to 60 psi using extra nitrogen in the lab, in order to pump the fuel into the accumulator. A smaller 1 gallon pressure vessel is connected to the bleed lines from the accumulator and the fuel injector to act as a catch can for excess fuel extracted during the bleeding process. Some measure of safety is also in place on the system, located on a metal plate on the fuel tower, as shown in Figure 2.10.

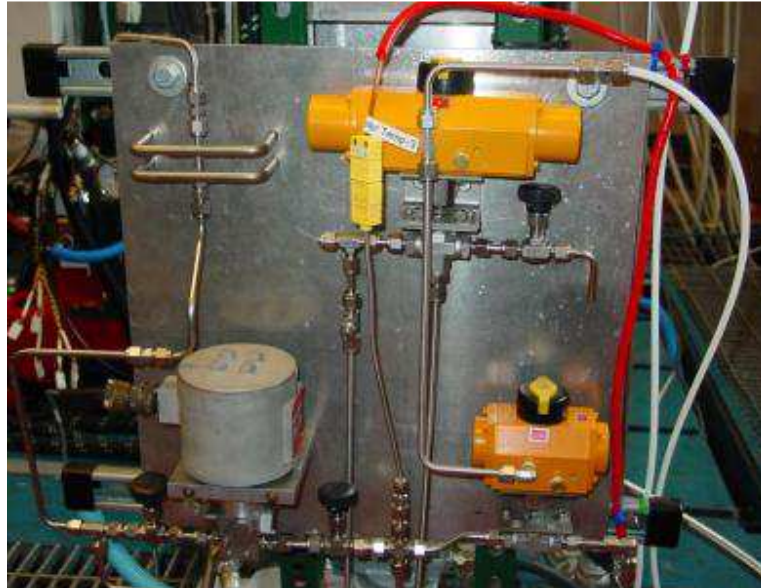


Figure 2.10 - The other portion of the fuel system located on the opposite side of the tower from the accumulator, with pneumatic valves to isolate the low and high pressure sides, as well as the fuel flow meter

The yellow, rectangular objects in Figure 2.10 are both pneumatically actuated valves, controlled by a separate nitrogen bottle and pressure regulator. The smaller of the two acts as a division between the high pressure and low pressure side of the fuel system, while the larger three-way valve permits nitrogen to charge the fuel accumulator. When necessary, the nitrogen supplying these pneumatic valves can be shut off, which both closes the flow of any fuel from the accumulator to the fuel injector, and stops nitrogen flow into the accumulator cylinder, to depressurize the fuel.

A flow meter, shown as the small cube connected to a larger cylinder, allows for accurate measurement of the mass flow of injected fuel. This particular unit is a Max Machinery 214 piston-style flow meter, with a 284-512 transmitter. The transmitter converts the rotation of the internal shaft, which four pistons attach to, into a frequency signal that is routed to the low-speed DAQ. There is a bypass loop built around this device using a manual valve, which facilitates possible diagnostic processes, but more importantly, allows fast flowing fuel another pathway around the sensitive flow meter during period of air bleeding or filling/purging.

Due to the nature of this project, frequent fuel changes are required, which necessitates that some of the system be designed to accommodate and facilitate rapid transitions. Purging the fuel lines is a relatively simple process, wherein, the accumulator is lightly charged to 50 psi, and the bleed valves are opened to allow any fuel remaining in the lines or the accumulator to be recollected in the catch can. A complete fuel system change, from draining one fuel to filling the accumulator with

another, can be conducted with relative ease in this manner, decreasing the amount of time between runs of different fuels.

2.5 Data Acquisition

All of the measurement equipment is centrally located in a data acquisition boom in the test cell, shown in Figure 2.11. The boom is located close to the engine in order to minimize the length of signal lines, and, ideally, to prevent any unnecessary signal attenuation. The arm of the boom is hollow, which allows lines to be run from the equipment in the cell into the control room (and vice versa) enabling connections between the high and low speed data acquisition systems and the data collection computer. In addition, because the test cell is prone to high temperatures during engine operation, four cooling fans are installed on the top of the boom enclosure to help exhaust hot air and maintain safe temperature levels for the electronics housed within.

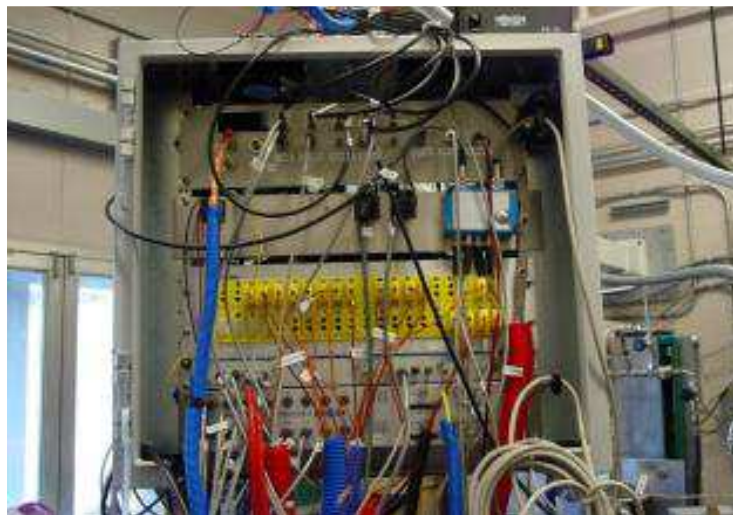


Figure 2.11 - Data acquisition boom where the high speed and low speed measurement hardware is housed

2.5.1 Crank-Angle Resolved Measurements

The block diagram in Figure 2.12 displays most of the major components and pathways used in the high-speed system, more specifically the location of the three pressure transducers critical to combustion analysis.

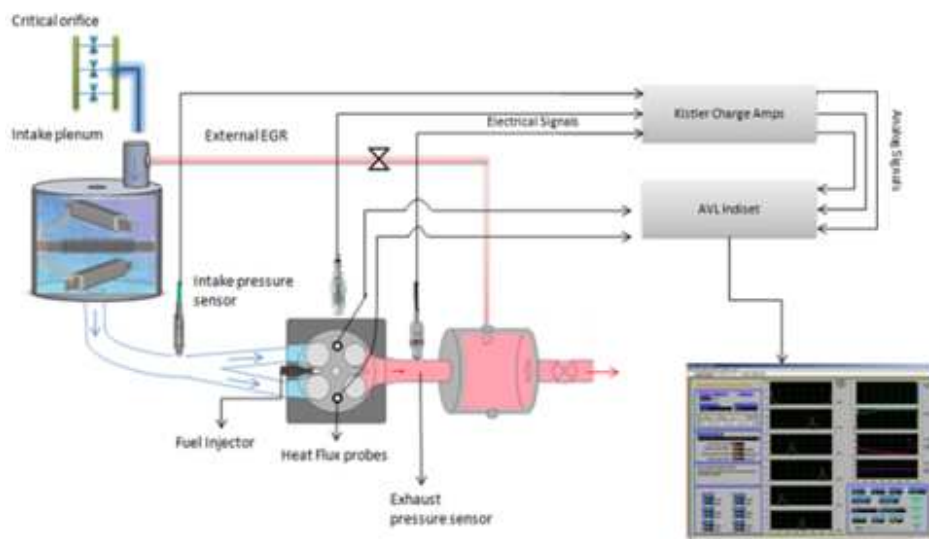


Figure 2.12 - High level schematic outlining the connection of high-speed pressure signals to the high-speed data acquisition system

The Kistler 4007B intake pressure transducer, which is a piezoresistive type, is capable of measuring absolute pressure in the intake runner leading to the combustion chamber. A Kistler 4045A piezoresistive pressure transducer in the exhaust runner is threaded into a Kistler exhaust switching adapter. The runner is cooled by two water lines run from the test cell trench, and actuated using the shop air. This configuration is advantageous, as the sensitive portion of the transducer is only exposed to high

temperature and corrosive exhaust gases for the amount of time necessary to record a data point (an extremely small fraction of the total run-time for an experiment). Finally, a Kistler 6125A transducer, outfitted with a flame arrester to mitigate thermal shock to the sensor, is used to measure cylinder pressure. This sensor has the capability to measure instantaneous, in-cylinder pressure from 0 to 250 bar, and is calibrated for both 0 to 50 and 0 to 250 bar ranges, though our operation rarely takes us above 50 bar peak pressure. As it only measures a differential pressure, an absolute reference given by the intake pressure transducer is required to get an absolute pressure. Because the signals from these devices are extremely miniscule, charge amplification is required to magnify the signals before they can be displayed. The lines from the transducers are run to the Kistler charge amplifiers for this purpose (a Kistler Type 4665 for the piezoresistive transducers and a Kistler Type 5064A2 for the piezoelectric sensor), and following the proper gain, the lines are then run into the AVL IndiSet Advanced Gigabit 642, a 16 channel data acquisition system capable of sampling rates as high as 800 kHz, which is more than adequate for this project.

Another instrument of substantial importance to collecting crank-angle resolved measurements is the Kistler 2614A crank-angle encoder. While the linkage arm of the encoder is rigidly affixed to the engine block, a circumferentially marked disk is fastened to the rotating crankshaft via a custom-made friction-grip adapter. As the crankshaft spins, the encoder is able to detect marks on the disk as they pass, allowing it to determine the absolute position in the cycle at which the engine is located. Of course, for an absolute measurement, the device needs a TDC reference, which is ascertained

while motoring the engine and measuring the position of TDC in the AVL Indicom software.

The raw pulses are sent from a Kistler 2614A crank angle encoder, to a pulse multiplier box that allows flexibility in establishing the crank-angle resolution of the encoder. It is possible to set the resolution as high as 0.1 CAD, however for the purposes of our experiments we have found 0.5 CAD is sufficient to draw worthwhile conclusions from an analysis of the data, and in this manner, a great deal of hard drive space can be saved from the larger files higher resolutions require. Moreover, the AVL Indicom software only responds to crank angle triggers of 0.5 CAD, interpolating in between for finer resolution. Using 0.1 CAD on the encoder would fail to provide any additional information with physical meaning, so the 0.5 CAD setting is appropriate for the studies presented in this document. While the ability to determine crank angle positions of the engine for pressure measurement is critical in combustion analysis, the angle encoder serves an additional purpose for running the engine; it provides two of the signals necessary to use the GM set point controller software, the operation of which is pictured in Figure 2.13 and Figure 2.14.

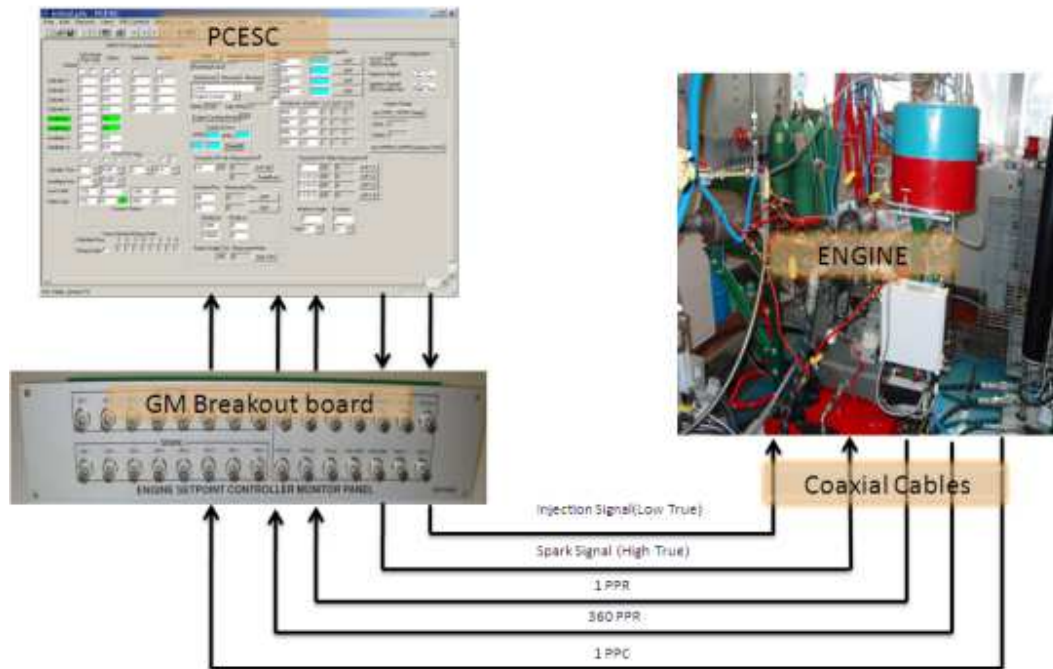


Figure 2.13 - Schematic showing the control signals and flow necessary for ignition and spark control on the HCCI fuels engine

The angle encoder has 360 marks on its wheel, and is able to send one pulse per mark, resulting in 360 pulses per crankshaft revolution (360PPR), and one pulse for each complete revolution of the crankshaft (1PPR). One further engine positioning signal is necessary to denote which revolution is that of combustion (TDCF) and which is that of exhaust (TDCE), hence, the angle encoder groups together pairs of 1PPR signals into cycles; this signal is dubbed the 1PPC signal.

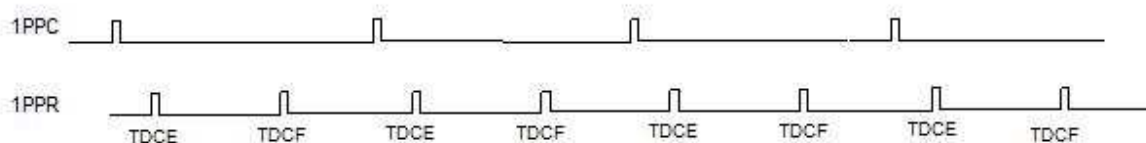


Figure 2.14 - The 1PPC and 1PPR signals are used to determine the separation between cycles, as well as what portion of the cycle the engine is currently undergoing

Capturing this signal is rendered relatively straightforward with the use of a Hall Effect sensor mounted to the valve cover and a ferrous piece of metal bolted to the camshaft wheel, which passes the magnetic field of the sensor once per engine cycle. Using simple electronics and circuitry (shown in more detail in Figure 2.15), it was possible to create a reliable sawtooth signal for the 1PPC. Once these signals are reliably collected, they are sent to a breakout board from GM which is connected to the engine set point controller via a 50-pin ribbon cable. Once the crankshaft position is determined, the software is able to decide when to send signals for the spark plug and fuel injector, that then run through the breakout board and back to the test cell, and the appropriate engine components.

The final pieces of high-speed hardware, explained in more detail in the coming chapter, are the specialized coaxial heat flux probes used for HCCI combustion and the deposit analysis in our experiments. A schematic of the probe sleeves, which the probes fit inside, are shown in Figure 2.15. As illustrated, the probe sleeves mount flush with the cylinder head, and are designed to have the same form factor as a Kistler 6125A pressure transducer. These sensors are then fitted into the mounting sleeve, which are screwed into the cylinder head to mount flush with the surface of the combustion chamber.

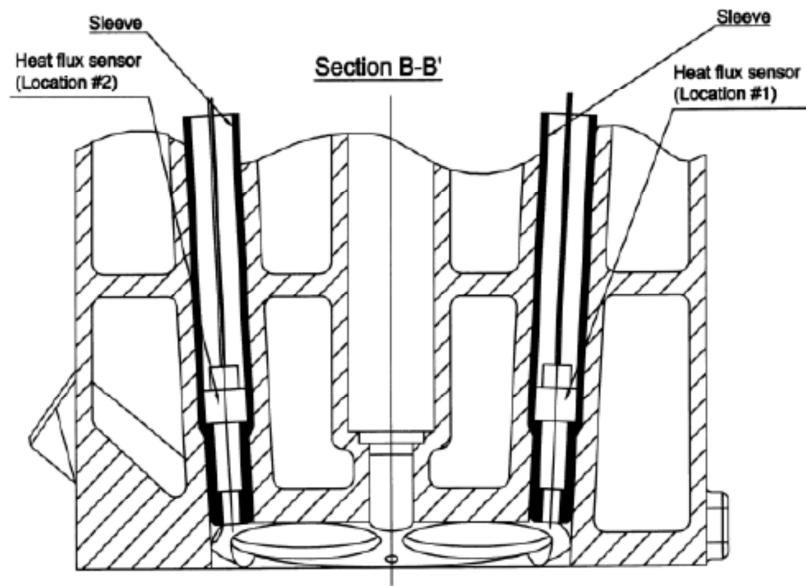


Figure 2.15 - Schematic showing the location of high-speed heat flux probes in the HCCI fuels engine cylinder head

This mounting scheme allows for instantaneous surface temperature readings on the cylinder head, and also doubles as an insertion coupon for the collection of deposits. The heat flux probes themselves are comprised of two, thin thermocouple junctions for response on the order of one microsecond, and are spaced 4 millimeters apart, as shown conceptually in Figure 2.16 and Figure 2.17.

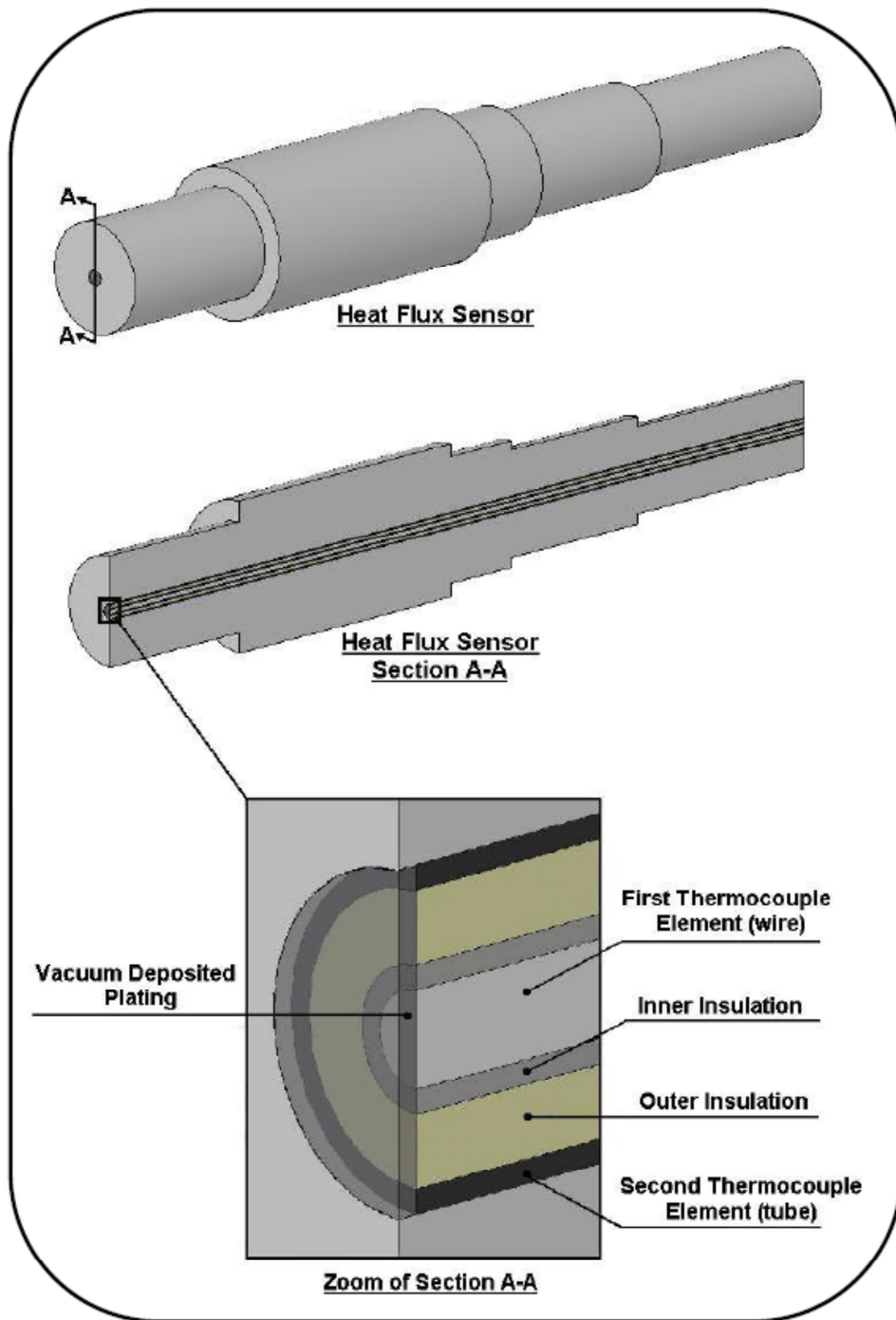


Figure 2.16 - Detailed schematic of the heat flux probe

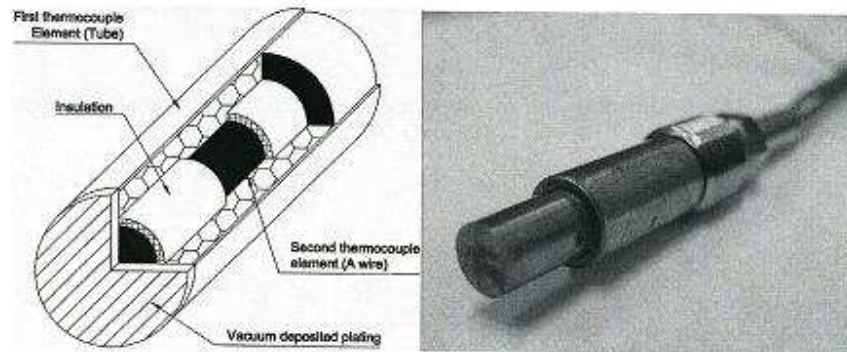


Figure 2.17 - High level schematic outlining the connection of high-speed pressure signals to the high-speed data acquisition system

Given the known thermal properties of the wall and distance between the junctions, as well as the measured temperatures at those junctions, we can obtain not only surface temperature, but also heat flux through the combustion chamber walls. Of further interest, there are additional methods for characterizing the thickness of deposition accumulated on the probes in-situ [73], which will be studied in the future. A simple model of the deposit-coated probe and theoretical approach to this method are summarized in Figure 2.18. These thermocouple signals, two per probe (one for each thermocouple junction), are run to an AVL 4FM2 I-FEM (front end module) signal amplification unit before the signals are connected to the IndiSet box. There is also a specialized mechanical linkage assembly that allows for heat flux measurements on the piston surface via a network of similar probes; the particulars of this assembly can be found in a number of publications from our lab [7, 72, 112].

In order to view and record the crank-angle resolved signals, we have implemented a software interface in AVL Indicom version 2.1, shown in Figure 2.19. This software provides the capability to display and monitor various measured and

calculated values to aid in conducting experiments, as well as saving high-speed data in files for later post-processing and analysis. Not only does the custom interface show pressure traces against crank-angle, it displays useful quantities that are cycle averaged as well, such as indicated mean effective pressure, burn durations (CA10, CA50, and CA90), ringing index and location of peak pressure.

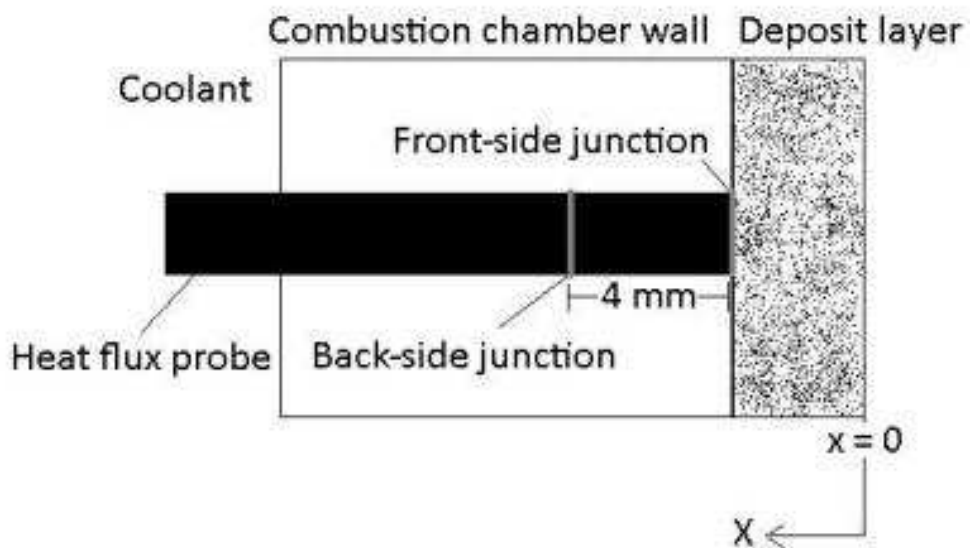


Figure 2.18 - Conceptual schematic of the heat flux probes with a CCD layer accumulated on the surface

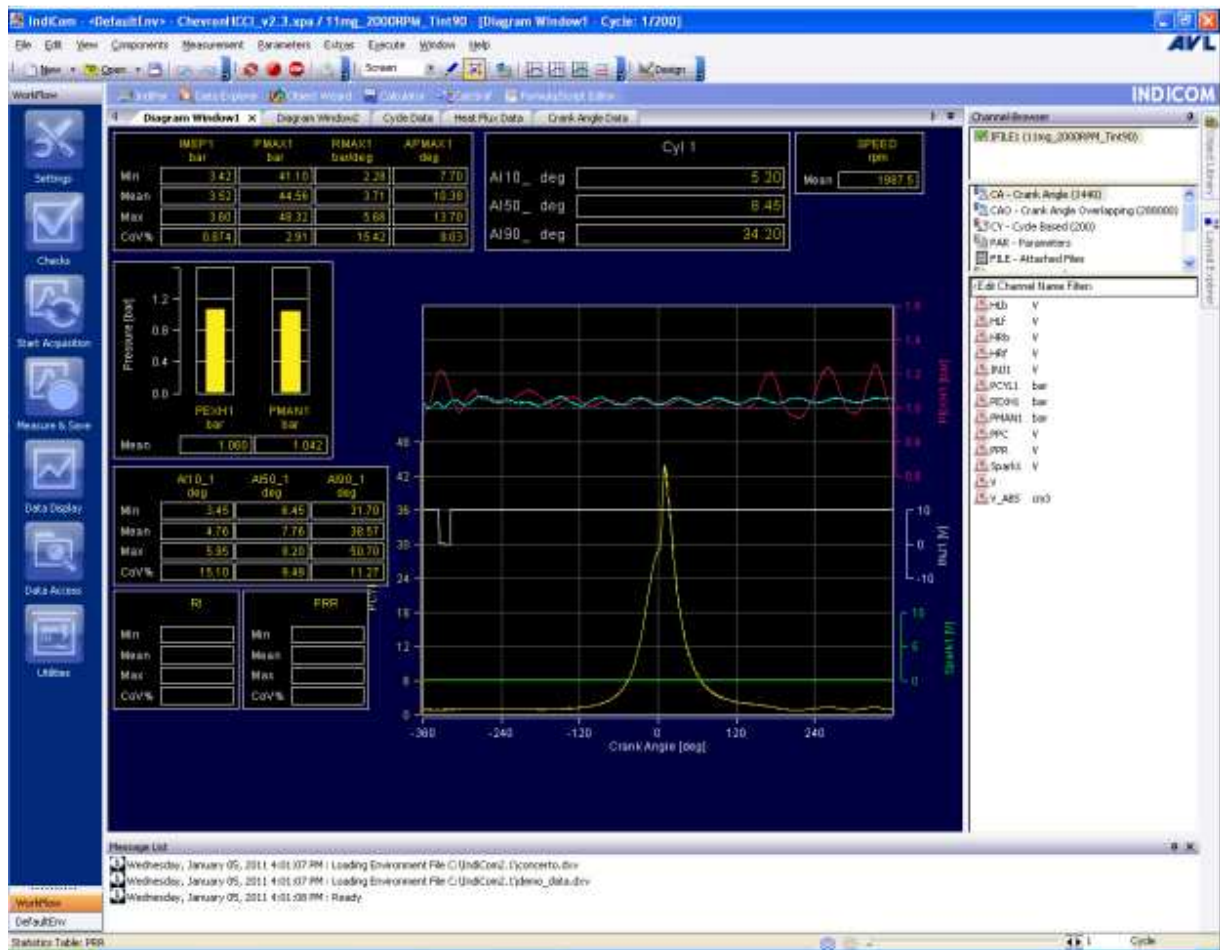


Figure 2.19 - Indicom version 2.1 software used to capture crank-angle resolved measurements

2.5.2 Time Resolved Measurements

For the purpose of capturing time-resolved measurements, National Instruments SCXI technology, shown in Figure 2.20, was selected because of the ease with which it can be interfaced with LabVIEW software.



Figure 2.20 - Low-speed, NI SCXI hardware with the chassis shown on the left, SCXI-1102 card on the top right, and SCXI-1300 isothermal block on the bottom right

Many temperature measurements and voltage signals are run through the NI hardware to later be processed, displayed and stored via a LabVIEW virtual instrument (VI). The SCXI-1102, 32-channel card, mounted in the SCXI-1000 chassis, is capable of housing four such cards for ready expansion when the need to arise. Furthermore, an SCXI-1300 isothermal block is coupled to the 1102 card, and all thermocouple and voltage signals are run into this module (including the grounds for the heat flux probes). The advantage of this arrangement is the cold junction compensation (CJC) provided by this terminal block, which can be activated through the LabVIEW software, and offers a reliable reference for thermocouple measurements using a built-in thermistor. These time-resolved measurements are enumerated in Table 2.3, where all the recorded signals given, except those of the emissions bench, are sent as voltages to the SCXI card in the chassis, located in the test cell boom. The emissions measurements for the

bench are read directly from the control computer using TCP control messages and UDP packets for data transmission to the LabVIEW interface.

Table 2.3 - Summary of Low-Speed Signals

Temperature Measurements (°C)		Voltage and Calculated Measurements	
1	Fuel flow meter temperature	19	Oil pressure (kPa)
2	Intake damper (before heater)	20	Barometric pressure (bar)
3	Intake manifold (after heater)	21	Air mass flow rate (kg/sec)
4	Exhaust manifold	22	Fuel flow rate (mg/cycle)
5	Dynamometer motor	23	Fuel frequency (Hz)
6	Coolant heater out	24	Speed (RPM)
7	Coolant heat exchanger in	25	Torque (N-m)
8	Coolant Engine in	26	CJC temperature (°C)
9	Coolant Engine in	27	CJC voltage (V)
10	Oil heater out temp	28	Power (kW)
11	Oil heat exchanger in	29	Air/Fuel ratio
12	Oil engine in	30	Equivalence ratio
13	Oil engine out		
Emission Measurements			
14	CO (% volume)		
15	CO2 (% volume)		
16	O2 (% volume)		
17	NOx (ppm)		
18	THC (ppm)		

These time-resolved measurements serve various purposes during experimentation, as some signals are used for monitoring the conditioning subsystems, others aid in setting the correct operating points for engine operation, and the remaining measurements can be utilized in post-processing to explain phenomena and observations shown in testing. For instance, temperature readings for the heaters and

heat exchangers are affiliated with the status of oil and coolant subsystems. Mass flow rate of fuel, mass air flow rate, equivalence ratio, engine speed and intake air temperature are all process values that are varied when conducting experiments to control the engine's operation. After completing a study, measurements such as emissions and torque are useful for analyzing data to explain the trends shown during experimental investigations.

As touched upon previously, National Instruments LabVIEW version 8.5 was the software selected for use with the user interface and subsequent collection of time-resolved low-speed data from the engine. LabVIEW provides several levels of convenience because it is designed to facilitate a straightforward connection with NI hardware, as well as hasten the programming process by using a graphical interface. The data acquisition (DAQ) for the HCCI fuels engine takes ten samples per second for all the signals, and then updates and displays the average reading every second in the virtual instrument (VI). The VI developed for the HCCI fuels project involved several parallel producer loops running simultaneously in order to capture several fundamentally different measurements, such as reading the CJC thermistor, sampling all the temperature and voltage signals, sending the TCP/IP command to the Horiba MCU to read emissions measurements and processing the frequency measurement from the fuel flow meter. The interface developed to sample and record time-resolved engine measurements is shown in Figure 2.21.

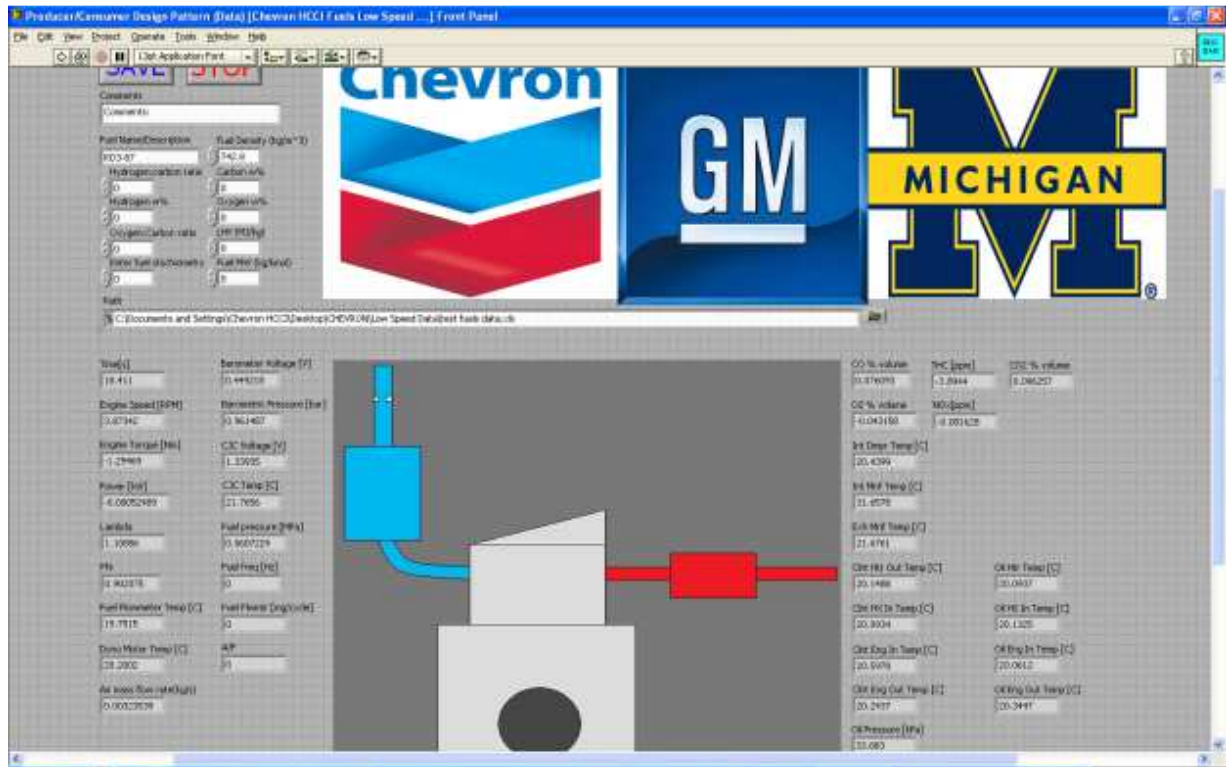


Figure 2.21 - Screen capture of the interface for the low-speed system; the boxes in the upper left are fuel properties which are entered before each experiment and saved with the low-speed data so that the Matlab post-processing code has access to these properties during analysis

CHAPTER 3

Techniques and Instrumentation to Study the Interplay of Fuels, HCCI Combustion and Deposits

3.1 Crank-Angle and Time-Resolved Measurements for Combustion Analysis

Once engine data is collected using the array of sensors and instruments detailed in the previous chapter, it is ready for post-processing and a conversion of the raw data to a form more suited for fuels and deposits studies. High speed engine data is first converted from an AVL iFile, which is a proprietary file that we cannot directly make use of, into an ASCII text file that can be conveniently read into a Matlab subroutine. The code for the HCCI fuels project has been developed thus far so that, using a prescribed directory structure, raw data files are dropped into a specific folder, and then Matlab script is run to process this raw data. After the post-processing routine is complete, the processed data is moved into a folder from which plots can later be generated, and the finished raw data is preserved in yet a different folder in case it needs to be referenced in the future. A simple Matlab GUI was developed to facilitate analysis of the post-processed data, so that common plots could be produced quickly without having to manually manipulate text data in Microsoft Excel spreadsheets.

3.2 Heat Flux Probes

The basic construction of the heat flux probes was discussed in the previous chapter, and here we will detail the manner in which data is collected using these devices. To begin, as mentioned previously, the raw voltages from the thermocouples in the probes are run into an AVL I-FEM where the voltage is amplified 500 times before the conditioned signal is run to the Indiset hardware. Once collected and recorded, the raw voltage signals from the thermocouples must undergo additional post-processing in software, which is conducted in one of the routines in the Matlab code. Because all the temperature measurements in our system are referenced to the cold-junction compensation module of the low-speed NI-DAQ, including the high-speed probes, it was appropriate to use Labview's scheme to convert the voltages into Celsius temperatures. The first step is to convert the measured CJC temperature into a voltage using a reverse polynomial correlation that is based upon the J-type thermocouple, as found in the probes, coupled with the CJC thermistor. This voltage is subsequently added to the measured voltage of the probes' thermocouples in order to include compensation for the reference. This final voltage can be converted into a linearized temperature with a further polynomial correlation, and we finally arrive at the quantity used for heat flux calculations.

Theoretical operation of the heat flux probes derives from the assumption that heat transfer to the probe can be approximated as unsteady, one-dimensional heat conduction normal to the probe surface, from the surface thermocouple to the back-side thermocouple. This is a reasonable assumption, as the distance between the two thermocouples is quite small (4 mm). The equation is solved by using two boundary

conditions, prescribed by the measured temperatures of the thermocouples and an initial condition in the form of an averaged surface temperature at zero time. The other fundamental supposition made is that the temperature measured by the surface thermocouple is cyclical and can be described by a Fourier series. Because the engine is assumed to be in dynamic equilibrium (as heat flux variations are cyclic), when run at a steady-state operating point, the location of the back-side temperature measurement is convenient for simplifying the analysis. As the back thermocouple in the probe is sufficiently far away from the surface reading, it is insulated from the heat flux variations seen at the surface, and its temperature can be taken as constant throughout the cycle. The mathematical derivation to follow can be conceptualized with Figure 3.1 below.

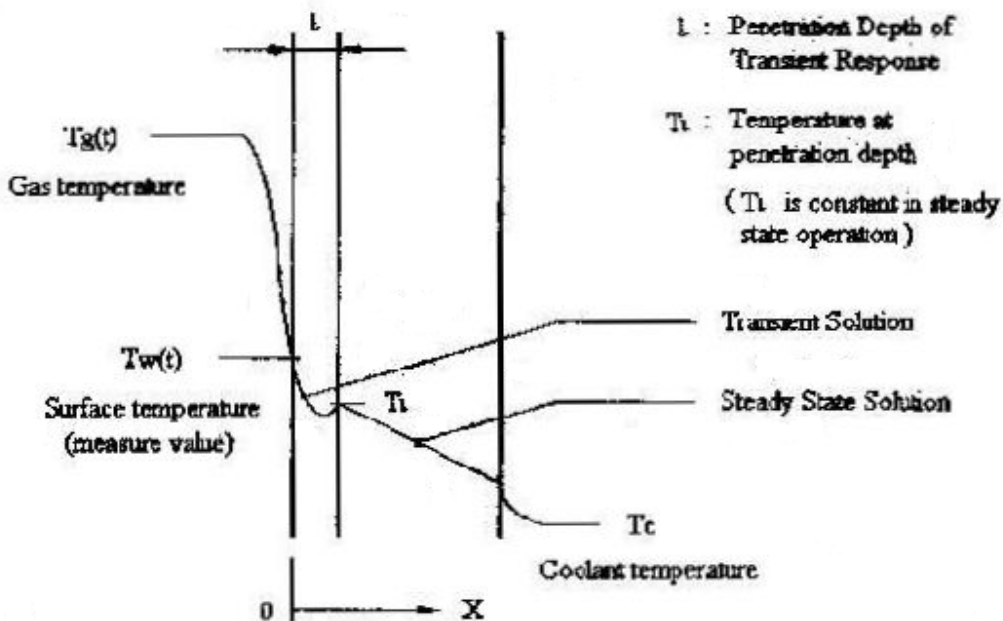


Figure 3.1 - A conceptual picture of the method used to calculate heat flux in the engine with the custom-made heat flux probes; reprinted from Overbye et al. [1]

To begin, we present the formula for unsteady, 1D heat conduction.

$$\frac{\partial T(x, t)}{\partial t} = \frac{1}{\rho c} \frac{\partial}{\partial x} \left(k \frac{\partial T(x, t)}{\partial x} \right) \quad (3.1)$$

Assuming constant properties for density, heat capacity and thermal conductivity we arrive at the following.

$$\frac{\partial T(x, t)}{\partial t} = \alpha \frac{\partial^2 T(x, t)}{\partial x^2}, \alpha = \frac{k}{\rho c} \quad (3.2)$$

The boundary conditions for the problem are summarized by Equation 3.3.

$$T(0, t) = T_w(t) \quad (3.3)$$

$$T(l, t) = T_l$$

As previously mentioned, the equation for the surface temperature can be expressed as a Fourier series, as shown below.

$$T_w(t) = \bar{T}_w(0) + \sum_{n=1}^N (A_n \cos n\omega t + B_n \sin n\omega t) \quad (3.4)$$

$\bar{T}_w(0)$ is a time-averaged, surface temperature initial condition, and the Fourier coefficients A_n and B_n are determined using a fast-Fourier transform of the measured

surface temperature data. When Fourier's Law is applied to Equation 3.4, the result is a calculated heat flux through the probe that consists of a time-independent, steady-state term, and a time-dependent transient portion of the solution.

$$\begin{aligned}
 -k \frac{\partial T(x, t)}{\partial t} \Big|_{x=0} &= \dot{q}_w(t) = & (3.5) \\
 \frac{k}{l} (\bar{T}_w(0) - T_l) & k \sum_{n=1}^N (n\omega/2\alpha)^{\frac{1}{2}} [(A_n + B_n) \cos n\omega t - (A_n - B_n) \sin n\omega t]
 \end{aligned}$$

In Equation 3.4, the harmonic number N is important, as too low a harmonic leads to the calculated surface temperature of Equation 3.4 not closely matching the measured periodic profile, and too large a harmonic leads to an excessive sensitivity to noise in the signal and non-physical fluctuations in the calculated profile. For our crank angle resolution of 0.5 crank angle degrees, Overbye et al. concluded that $N=40$ was appropriate [113]. The ability to calculate the instantaneous heat flux will be substantially useful during the conditioning of the combustion chamber by the CCD layer, because we expect that peak heat flux locations will vary with conditioning, and that the time required to detect changes in heat flux will vary with different fuels.

3.3 Heat Release Analysis

The in-cylinder pressure trace is one of the most fundamentally important measurements recorded in the engine, as this data is the basis for heat release calculations. Heat release analysis allows for the determination of mass fraction of fuel

burned, burn durations and net heat release rates, all of which will be addressed in later chapters. At the time of this document's creation, our code used a single-zone, ideal gas model, which is a reasonable estimation for HCCI combustion. The fundamental assumption of the single-zone model is that properties are averaged throughout the cylinder to ascertain the state of the combustion chamber contents, and that there is no spatial variation of cylinder pressure [72]. Conservation of energy in the cylinder is shown in Equation 3.6 in differential form.

$$\delta Q_{ch} = dU_s + \delta Q_{ht} + \delta W \quad (3.6)$$

The control volume for this energy equation encompasses all the space between the crown of the piston and the cylinder head, and says that the chemical energy released by the fuel, δQ_{ch} , is equal to the sum of the terms on the right-hand side of the equation. These terms are the sensible internal energy change during the combustion process, dU_s , the heat transfer from the gas to the walls, δQ_{ht} , and the work done by motion of the piston δW . The time derivative of Equation 3.6, which is the form ultimately used in the Matlab code to determine heat release, can be expressed via substitution of known thermal properties for these terms.

$$\frac{dQ_{ch}}{dt} = \frac{\gamma}{\gamma - 1} p \frac{dV}{dt} + \frac{1}{\gamma - 1} V \frac{dp}{dt} + \frac{dQ_{ht}}{dt} \quad (3.7)$$

As expressed by Equation 3.7, the ratio of specific heats gamma has a significant influence on heat release; therefore an accurate model for gamma at each time step is

necessary to reliably calculate heat release. Gamma is predominantly a function of mixture strength and temperature, though it has a stronger correlation with temperature than with composition--hence, most experimentalists employ a curve-fit based on temperature, for modeling gamma. Other studies have proposed their own correlations for gamma, but Chang [72] recognized the need for a specific expression of gamma for the purposes of our style of HCCI engine, which runs lean and utilizes a high percentage of internal residual gas. In the end, we decided that a third-order polynomial was appropriate for our in-cylinder conditions, and for the relevant portions of the temperature scale experienced during the cycle.

$$\gamma = -9.967 \times 10^{-12} \cdot T^3 + 6.207 \times 10^{-8} \cdot T^2 - 1.436 \times 10^{-4} \cdot T + 1.396 \quad (3.8)$$

The temperature in this equation is a bulk gas, cylinder averaged quantity that is determined from an in-cylinder mass estimate. The total mass of the cylinder contents includes the mass of fuel and air inducted, as well as any residual gas from internal or external EGR, although at the time of writing this document, we had not run any experiments with external EGR, nor were there plans to do so. So, for the purposes of the HCCI fuels engine, the total in-cylinder mass formula is as follows:

$$m_{total} = m_{air} + m_{fuel} + m_{iEGR} \quad (3.9)$$

The mass of inducted air and fuel are measured directly by instrumentation, as detailed previously, so we need only estimate the mass of residual that is re-inducted during the exhaust rebreathing event. For this we use an estimation based on Dalton's law, and the partial pressures of the incoming charge and the reinducted hot residual gas.

$$p_{IVC} = p_{intake} + p_{iEGR} \quad (3.10)$$

Using the ideal gas law, it is possible to obtain the partial pressure of the intake charge.

$$p_{intake} = \frac{m_{intake}RT_{intake}}{V_{IVC}} \quad (3.11)$$

The incoming fresh charge, which is the mass of the fresh air inducted into the cylinder, provides for the estimation of internal residual mass using the ideal gas law and Equation 3.10 and Equation 3.5.

$$m_{iEGR} = \frac{p_{iEGR}V_{IVC}}{RT_{iEGR}} = \frac{V_{IVC}}{RT_{iEGR}}(p_{IVC} - p_{intake}) \quad (3.12)$$

The temperature of the reinducted internal residual is assumed to be equal to the exhaust temperature measured at the exhaust port leading to the runner. As for the other terms in heat release Equation 3.7, the time derivative for heat transfer from the gas to the walls is calculated using the following correlation.

$$\frac{dQ_{ht}}{dt} = \alpha_{scaling} \cdot h_{global} \cdot \sum_i (T - T_{w,i}) \cdot A_i \quad (3.13)$$

The scaling term is necessary to correct the inaccuracies of the heat transfer model presented here. Its value is computed by the closure of the energy equation, balancing the expected amount of chemical energy release from the fuel with the integrated apparent heat release shown, in Equation 3.14.

$$\alpha_{scaling} = \frac{\eta_{comb} E_{fuel} - \int Q_a}{\int Q_L} \quad (3.14)$$

The first term in the numerator is the expected chemical energy released from the fuel (combustion efficiency multiplied by the energy content of the fuel), Q_a is the apparent heat release rate with no losses from heat transfer and Q_L is the heat transfer loss rate of the gas to the walls. The global heat transfer coefficient h_{global} was shown by Chang [72] to be a reasonable assumption, as there is a significant homogeneity of energy release in-cylinder during the HCCI combustion process, and consequently, relatively little spatial variation in instantaneous local heat fluxes. Based on this assumption and on the fact that the instantaneous local heat fluxes for each combustion chamber surface have a uniform heat flux profile, it is permissible to characterizing heat flux in the cylinder using a spatially averaged heat flux. Furthermore, the global heat transfer coefficient for the combustion chamber is directly correlated with this spatially averaged heat flux.

$$h_{global} = \frac{q_{spatial\ avg.}}{T - T_w} \quad (3.15)$$

The final equations used in the heat release code to calculate the global heat transfer coefficient, Equations 3.16, 3.17 and 3.18 are given as a modified form of the Woschni [114] model, with an alteration to gas velocity.

$$h_{global}(t) = \alpha_{scaling} \cdot L(t)^{-0.2} \cdot p(t)^{0.8} \cdot T(t)^{-0.73} \cdot v_{tuned}(t)^{0.8} \quad (3.16)$$

$$v_{tuned}(t) = C_1 \bar{S}_p + \frac{C_2 V_d T_r}{6 p_r V_r} (p - p_{mot}) \quad (3.17)$$

$$C_1 = 2.28 + 0.308 \frac{\pi B W_p}{\bar{S}_p}, C_2 = 0.00324 \quad (3.18)$$

The characteristic length L in Equation 3.16 is the instantaneous deck height of the engine, p is pressure, T is bulk gas temperature and v_{tuned} is the modified gas velocity term summarized in Equation 3.17 and Equation 3.18.

3.4 Fischer Dualscope

In order to measure the ex-situ thickness of deposit that accumulate on the piston surface and heat flux probes, the Fischer Dualscope shown in Figure 3.2 is used. The device is relatively simple and straightforward to operate, and yields a reasonable measurement of deposit coating thickness.



Figure 3.2 - Fischer Dualscope instrument used to measure the thickness of a layer over a substrate material

The Dualscope operates by sending an excitation current through a metallic probe, shown in the picture as the silver cylinder connected to the end of the black cable. When the probe lightly touches to a surface, the current is sent to the probe, generating a primary magnetic field. In turn, this primary magnetic field generates Eddy currents in the metallic substrate below the deposit layer, which weaken the primary field by some degree. The instrument is able to convert layer thickness by measuring the secondary effects of the Eddy current on the primary field of the probe. The conceptual details of the Eddy current method are summarized in Figure 3.3.

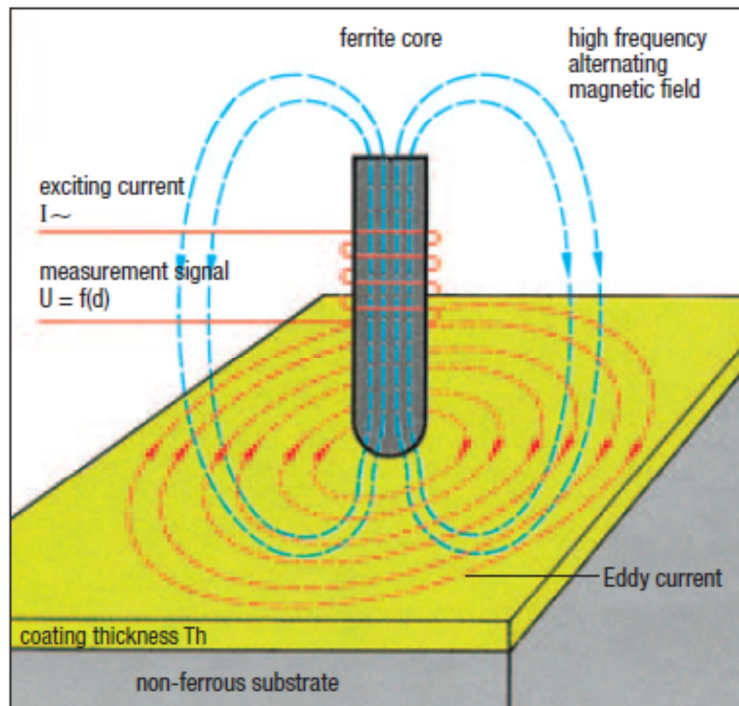


Figure 3.3 - Conceptual view of the Eddy current method [115]

3.5 Thermal Diffusivity Measurements

As mentioned in chapter 1, the calculation of thermal diffusivity is fundamentally an important method for characterizing the deposit layer. Specifically, the thermal diffusivity of the layer provides insight into how the deposition volume will respond to cyclic heating from HCCI combustion. The governing equations from Hopwood et al [73] to calculate thermal diffusivity are reiterated in Equation 3.19 and Equation 3.20.

$$t_{peak} - t_{clean} = \Delta t = x \frac{(1 + \sqrt{2})}{6} \sqrt{\frac{t_o}{\pi\alpha}} \quad (3.19)$$

$$\alpha = \left(\frac{x}{\Delta t} \frac{(1 + \sqrt{2})^2}{6} t_o \right) \frac{t_o}{\pi} \quad (3.20)$$

The Δt in these equations is the time, or phase, lag as shown in Figure 3.4, between the peak temperature of a clean heat flux probe and the peak temperature of a “dirty” probe, coated with deposits and subjected to a heat flux source. This phase lag arises as a natural consequence of the deposition, which acts as a sort of insulation layer over the probe surface. As a result, the heat flux produced by the graphite element is delayed from reaching the front-side thermocouple as it is conducted through the deposit layer, as shown by the temperature profiles in Figure 3.4. It is also possible to use this technique to calculate the thermal diffusivity in-situ, and the information generated will be invaluable in gaining a better understanding of the CCD layer in an HCCI engine.

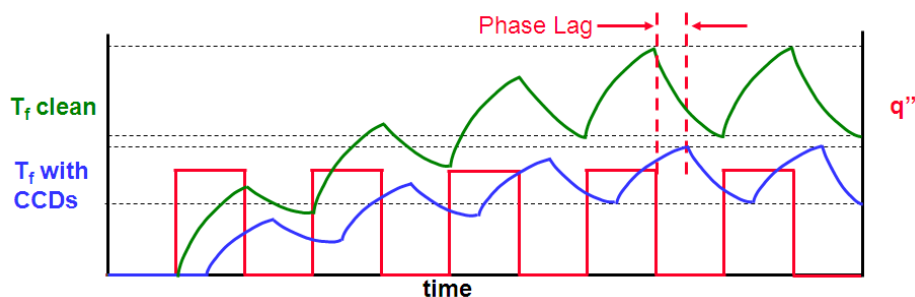


Figure 3.4 - A graphical example demonstrating how thermal diffusivity is calculated using the time difference in peak temperatures on a heat flux probe subjected to cyclic heating (in this case from a specialized laboratory oven, and not the HCCI engine); the red trace in the figure is the heat flux provided by the graphite element cut into square waves by the chopping wheel; reprinted from Hoffman [1].

3.6 Microscopic Instruments

There is considerable need for careful analysis of the samples, and consequently for precise and prudent procedures for obtaining and preparing samples for study. Mishandling the deposits during any stage of the collection or preparation could engender poor results from the subsequent microscopy and spectroscopy. In order to retrieve CCD samples, the engine must first be disassembled to allow access to the piston and the interior of the cylinder head, so that deposits can be harvested from the internal engine surfaces. The primary tool for this extraction is an X-Acto knife; a flat edged blade of 0.350" width and a triangular blade are used in combination to remove deposits from various areas on the piston crown. Great care must be exercised, so as not to gouge components with the knife, particularly those constructed of aluminum, which are readily susceptible to such damage. Once collected, the samples are stored in a small glass vial, where they can be safely contained for future preparatory action. Once the analysis instrumentation is available, the samples must undergo further preparation before testing procedures, such as scanning electron microscopy, transmission electron microscopy, energy-dispersive X-ray spectroscopy, X-ray photoelectron spectroscopy and small-angle X-ray scattering diffractometry, can begin. Scanning electron microscopy (SEM) and transmission electron microscopy (TEM) are used to study the physical structure of the deposits and their morphology. Energy dispersive X-ray spectroscopy (XEDS) and X-ray photoelectron spectroscopy (XPS) are used for atomic and molecular analysis of the samples. Small angle X-ray scattering (SAXS) can be used to measure porosity. By combining the results of these testing procedures, it becomes possible to adequately determine the fundamental

characteristics of HCCI CCD, and, ideally, to produce results that add to our current comprehension of HCCI combustion strategies.

The necessity of such deposit characterization in HCCI engines is best explained as follows; because HCCI combustion is highly sensitive to the temperature history of the engine, and because deposits greatly influence both in-cylinder temperatures and heat release, a detailed analysis of deposit composition is essential for the HCCI fuels project. Critical information regarding the structure of combustion chamber deposits and how it impacts HCCI combustion can be gleaned from such a study. One area of interest is in gaining an understanding of deposits' porous microstructure, which may yield insight into the thermal conductivity, thermal diffusivity and heat capacity of the deposits [37], all characteristics which relate to the ability of engine deposits to form a thermal insulating layer which will play a significant role in HCCI combustion. Furthermore, while the overall quantity of deposit formation affects temperatures in the engine, it is important to note that altering the deposit chemistry or morphology impacts temperatures as well [30]. A number of testing procedures were utilized to thoroughly characterize these deposits. In addition, several instruments were needed to photograph and study morphology, as well as to analyze the underlying atomic structure of CCD during HCCI engine operation via some manner of spectrum investigation. These instruments are available through the University of Michigan, and are located at the Electron Beam Microanalysis Lab (EMAL), in the Space Research Building.

3.6.1 SEM/ESEM

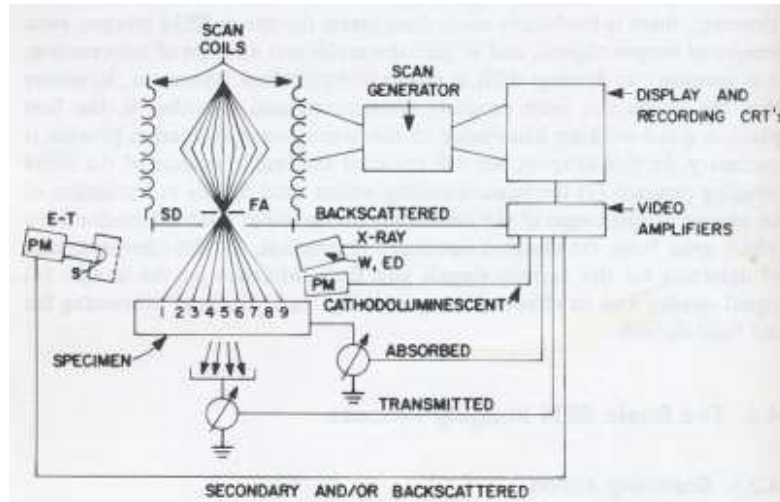


Figure 3.5 - A diagram showing the schematic of a scanning electron microscope [116]

Using a scanning electron microscope, or SEM, pictured in Figure 3.5, provides one critical avenue for analyzing the morphology of the depositions that result from various fuels [37, 117]. The SEM operates principally by utilizing a beam of concentrated electrons, which are focused on the specimen. The incidental electron collisions between the surface of the sample and the beam are measured to produce an image. Specifically, a set of lenses within the microscope direct and focus the beam over the object, causing secondary electrons to be removed from the sample surface. The backscattered electrons are collected by a detector element to create an image of the sample on a connected monitor. Where the electron beam is incident upon the sample is often referred to as the interaction volume, and is commonly visualized as a sort of teardrop penetration of the beam into the sample, which produces the electron scattering [116]. The particular model of SEM, in the EMAL facility, used was the

Philips XL-30 ESEM, which can operate in one of several detection modes, and requires specimens be placed into a vacuum sealed chamber before being analyzed. For the standard SE (secondary electron) mode, when examining a material with low electrical conductivity, a sputter-coating process must be utilized to ensure that excess charge does not build on the outer surface of a sample, and distort the picture signal. Sputter-coating is carried out by adding a thin layer of conductive material to the sample (in this case carbon). Even for conductive samples, sputter-coating can be beneficial in augmenting the contrast quality of the scan. The carbonaceous deposit samples taken from the HCCI test engine exhibit varying amounts of electrical conductivity depending on the composition of the fuel that created the deposition [118]. CCD electrical conductivity tends to increase as the result of an increase in the aromatic content of a fuel; increasing aliphatic concentration dilutes the aromaticity of the deposit, and hence its conductivity. Due to the utilization of cold-mounted deposit samples (detailed further in the section about XEDS) and the undesirable possibility that carbon sputter coating could impact the measurements of a predominantly carbon sample, sputter coating was not employed for the studies discussed in this document.



Figure 3.6 – Standard Electron Microscope (SEM) mounting stub; samples are attached to this specimen pin, and loaded into the vacuum chamber

A sample is prepped for viewing by first obtaining an SEM specimen pin mount, depicted in Figure 3.6. A layer of conductive copper tape is affixed to the flat portion of this mounting plate. Deposits are then placed on top of the layer of tape. At this point, the sputter coating procedure, mentioned previously, can be carried out. When completed, the specimen is ready to be placed in the SEM chamber. Once the chamber is sealed and a proper vacuum within the SEM cylinder is in place, study of the sample can begin. Conventional SEM study, with deposit samples attached to a pin mount, will likely play a small role in the study of HCCI fuels, because the information obtained from a sample in this form has limitations. Generally, this method is only useful for capturing pictures with which to study the high-level morphology of deposits.

Another mode of ESEM operation is called GSE (gaseous secondary electron) detection, designated as such because in this mode the vacuum chamber is partially filled with water vapor. This mode of ESEM shares more traits with a natural environment than other modes of conventional electron beam microscopes that place the specimen into a complete vacuum. It is necessary to employ this form of microscopy when viewing epoxy cold-mounted samples (which will be detailed in the discussion concerning XEDS), because, in normal SE operation, cold-mounts are generally carbon-coated to provide conductivity to the mount. This is problematic when studying engine deposit samples, because they are largely comprised of carbon, and thus, the carbon-coating process can mask certain structures or color the accuracy of the measurements. Using the GSE detector does not require non-conductive specimens to be coated since they are not being studied under a vacuum, where excess charge could build. Therefore, the ESEM in GSE mode is ideal not only for

viewing the mounted deposit samples, but also for XEDS analysis. The manner in which an image is produced in the GSE mode is similar to that of the standard SEM, in that the detector still collects secondary electrons emitted from the sample. However, in the case of GSE, a small voltage bias is applied to prevent electrical arcing, due to the presence of gas inside the chamber, which is a medium that can facilitate the phenomenon. An SEM mode is also available that utilizes an intermediate low vacuum, which straddles high vacuum SEM and ESEM operations. This mode, which was the method employed in this study, uses another form of a GSE detector called a Large Field Detector (LFD). Using the LFD, XEDS collection and calculation is provided via EDAX software that interfaces directly with the microscope viewing application.

3.6.2 TEM

The transmission electron microscope, or TEM, schematically pictured in Figure 3.8, operates on a principle not totally dissimilar from that of the SEM. However, the TEM allows for significantly higher resolutions, which may be necessary to evaluate the size of micro-pores and the graphitic nature of some combustion deposits. While an SEM device operates by measuring the back-scattered electrons off of a surface, a TEM relies on the ability to pass an electron beam through an extremely thin sample, in order to produce an image. There is a trade-off for this increased microscopic power, chiefly in the form of the intensive process required for viewing a sample once it is in the vacuum chamber. For the purposes of this HCCI research, the resolution limit of the SEM is not sufficient for study of the micro-pores which characterize the structure of CCD, therefore the high resolution capability of the TEM must be utilized to determine

the details of deposit porosity. The JEOL3011 Transmission Electron microscope, in the EMAL, is the specific instrument used in this study. There are a number of different methods for preparing TEM samples, but the one best suited for the examination of engine deposit specimens is accomplished by suspending the deposit particles scraped from the piston in a glass vial of ethyl alcohol. This mixture is then either prepared via a centrifuge, or shaken vigorously by hand for at least two minutes, at which point the specimen is ready to be dropped onto a copper TEM grid. The grid and storage device can be viewed in Figure 3.7.



Figure 3.7 – Transmission Electron Microscope (TEM) grid storage device shown on the left with an individual grid for TEM study on the right

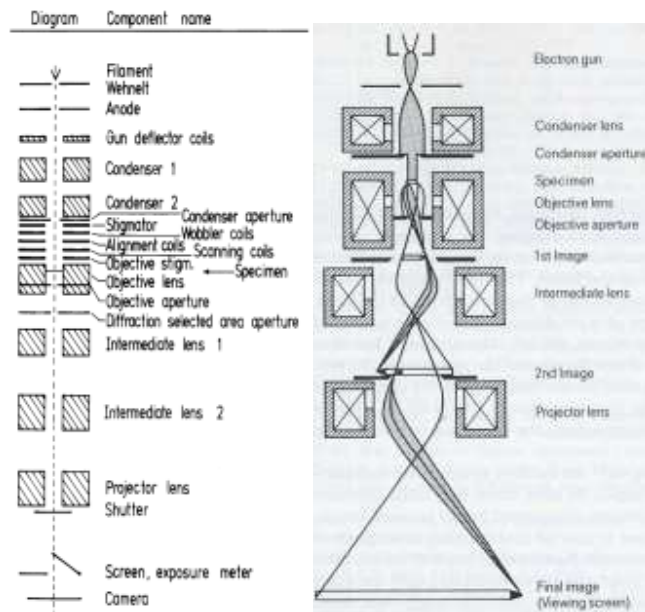


Figure 3.8 - A schematic of the lens system in a TEM (left) [119] and an example of bright-field imaging (right), the preferred technique that will be used to study engine deposits (right) [120]. In bright-field imaging, the optical and objective aperture axes are collinear so that only a direct beam is transmitted through the microscope; electrons scattered or diffracted at large angles are filtered out by the objective aperture and do not contribute to the image [119].

To finish, the copper TEM grid is held using a pair of tweezers, and dipped into the ethanol and deposit mixture to secure a few deposit particles to the grid. This grid is then placed onto a glass microscope slide and dried for a period of 10 minutes, to ensure none of the ethanol remains. This is as a precaution against any kind of future reaction occurring between the ethanol and the engine deposit specimen. The sample is adequately prepared, and can be placed into a grid holder until it is ready for analysis.

An important issue to note in the use of the TEM is the inevitability of damage to the sample as a result of irradiation from the electron beam. Damage done to

specimens is largely a function of the charge density focused on the sample (i.e. the incident electrons per unit area) and the amount of time the specimen is exposed to the electron beam. The irradiative damage results primarily from inelastically back-scattered electrons during the TEM process [121], whose energy is converted into either vibration energy of incident molecules or bond scission, which is of primary concern in engine deposit analysis. The CCD layer, by nature, is composed of a number of carbon-hydrogen bonds, which are prone cleaving because these chains exhibit a more aliphatic construction. Therefore, even for more aromatic deposit accumulations, where some aliphatic chains still exist, it is important to carry out observations of the sample in a timely manner, and vital to realize that repeated study of the same sample is likely impossible. For this reason, it is imperative that beam energy be kept at the minimum level that still provides an adequate view of the morphological structure of the CCD [119], in hopes of subjecting the sample to as little radiative damage as possible.

3.7 Spectroscopic Devices

The techniques outlined in the previous section are useful for the imaging of deposit samples, and can potentially reveal structural information about the layer. However, in order to obtain detailed data about the chemical composition of the deposits, a set of spectroscopic instruments must be used.

Due to the nature of internal combustion with hydrocarbon based fuels, the bulk of CCD specimens is composed of carbon and oxygen. However, there are other non-negligible elements present that need to be measured in order to deduce the nature of the CCD sample in question [122]. Nitrogen, a product from the intake air, and trace

amounts of sulfur, a component of the fuel, should be present in deposit samples, as well as some hydrogen [122]. In addition, diminutive amounts of metals and other substances present from the engine and the lubricating oil may be present in the elemental spectra, including, but not necessarily limited to iron, aluminum, silicon, magnesium, nickel, calcium, zinc and phosphorus [123]. Having an estimate of the materials comprising the deposits is of utmost importance, particularly during spectroscopic analysis, as it will allow for more accurate elemental peak identification, and, ideally, will help to expedite the post-processing. When characterizing the elemental spectra produced during spectroscopic measurement it is immensely useful to understand what elements are expected to occur within the sample. To this end reading several published accounts has been of great aid.

3.7.1 XEDS

In X-ray energy-dispersive spectroscopy, or XEDS, which is an available component of the Philips XL30 ESEM in the EMAL facility, a high energy X-ray beam is used in conjunction with a detector to measure the energy of emitted photoelectrons, for the purpose of determining elemental composition. The XEDS technique bombards the specimen with a powerful electron beam that penetrates the sample's surface in order to obtain a bulk composition of the specimen. Chemical analysis using an SEM involves measuring the energy and intensity distribution of X-rays resultant from the focused electron beam on the sample [116]. A brief summary of this process is shown in the illustration of Figure 3.9, and an overall view of the measuring apparatus is pictured in Figure 3.10.

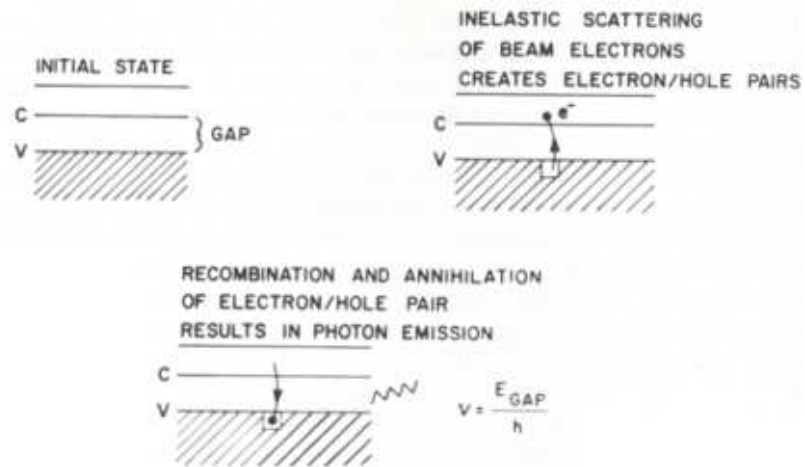


Figure 3.9 - The electron-hole interaction that occurs during X-ray Energy Dispersive Spectroscopy (XEDS) analysis [116]

XEDS operates on the principle of creating electron-hole pairs in atoms via atomic ionization from the incident electron beam; the beam is of sufficient energy to energize an electron to unbind from its shell, and thus an atom is ionized. The atom then has an empty space, which can be filled by an electron at a higher energy level. During this period of decay, the excess energy is emitted in the form of an X-ray which can be collected by an XEDS device. Based on the energy level of that X-ray (photons from ionization decay are emitted only at discrete energy levels based upon the atomic shell they are released from), the elemental origin can be determined. While the technique is useful in qualifying the elemental components of a sample, it is important to note that the accuracy of a *quantitative analysis* is quite difficult to discern, as a result of a number of factors which can impact the results of XEDS. One of these is the Z correction factor (ZAF), where Z refers to the atomic number of an element. Because

lighter atoms have a higher ratio of atomic number to atomic weight and the cross-section for electron capture increases as Z decreases, lighter elements will interact with disproportionately more electrons than will heavier elements. ZAF correction can be used to mitigate these discrepancies. However, calculating the correcting factors would require the use of pure elemental samples, which were not available. Therefore, the Z correction factor was not utilized.

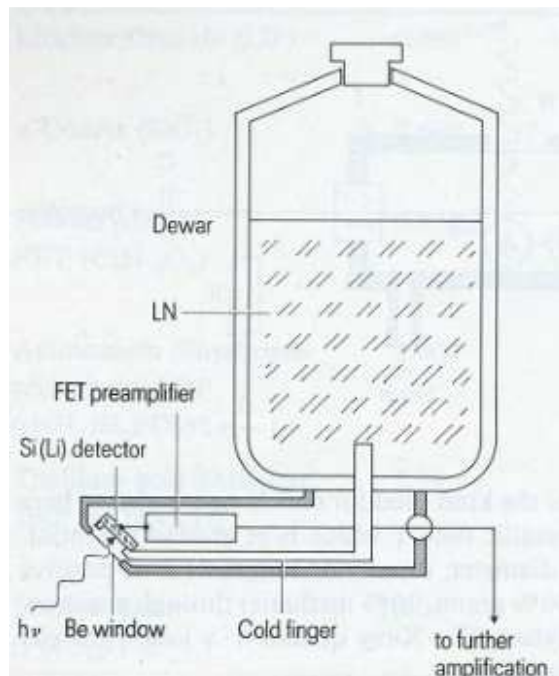


Figure 3.10 - This schematic diagram of an Energy Dispersive Spectroscopy (EDS) mechanism shows how an incoming X-ray is received by the detector, and the corresponding voltage pulses which are seen as X-rays hit the detector are amplified for further processing by a field effect transistor (FET). Note that both the collector and the FET are kept at approximately 100K by the supply of liquid nitrogen, in order to minimize background noise and hinder Li atoms from drifting within the detector apparatus [120].

Another challenge to accurate quantification based on XEDS is the fact that the amount of X-ray absorption is largely a function of the tilt of the sample in respect to the X-ray detector [124], and it becomes exceedingly problematic to obtain reliable XEDS results from a specimen that is not completely flat, necessitating the use of flat-mounted samples. Also, corrective techniques in the XEDS software (such as the ZAF correction) are only applicable to specially prepared samples [124]; to this end, it is necessary to flat-polish and grind SEM engine deposit samples before they can undergo XEDS examination [116]. The process to produce a flat-polished specimen consists of several steps, beginning with the mounting of the engine deposits sample. First, a two part epoxy substance is mixed together, combining a resin and slow-hardening agent, which must cure for 24 hours. The engine deposits sample is placed into the bottom of a Teflon molding cup, shown in Figure 3.11, and the epoxy mixture is then carefully poured over the CCD. The entire apparatus is then placed into a light vacuum environment, of approximately half an atmosphere (50 kPa), in order to evacuate air bubbles that could potentially cause complications during SEM and XEDS analysis.



Figure 3.11 - Engine deposits cold-mounted in epoxy and molding cup used for the mounting process

This evacuation process is performed for approximately two minutes, and once completed, the molding is left to cure overnight underneath a vent hood. After a sufficient curing period, the resulting mount is ready to be ground and polished, to ensure the best possible results from spectroscopic examination. To begin the procedure, the grinding wheel is placed on the polishing/grinding machine, and an appropriate grit of grinding paper is selected and affixed to the wheel, which after some experimentation on the epoxy mounted samples was determined to be 600 grit. Water is turned on from a small faucet above the wheel (the coarser the grit, the more flow is needed), and with the water is running, a knob is turned to set the amount of time the wheel will spin. As the wheel is spinning, the surface of the specimen is gently run in a clockwise motion around the wheel (the wheel turns counterclockwise). This is performed for 3 to 4 minutes, taking exceptional care to keep the specimen surface as flat as possible. After checking the surface underneath a light microscope, located in

the lab, to ensure the grind was done properly, a finer 1200 grit is applied to the wheel. Again, another 3 to 4 minutes of grinding are necessary, and if at this point the surface is satisfactory, the polishing procedure can begin. At this juncture the water is turned off; the wheel is changed to a 9 micron diamond polishing wheel, and then sprayed with a special polishing liquid intended specifically for the 9 micron wheel. A fair amount of force is applied to hold the epoxy mount against the polishing wheel while simultaneously moving the mount in a small circular motion, to ensure the surface of interest is polished evenly and remains flat. Once another 4 minutes has elapsed, a similar procedure is employed for a 6 micron wheel, and finally the mounting is ready for microanalysis. Before placing the prepared specimen onto an SEM pin mount, the whole sample is briefly cleansed with ethanol, to ensure any remaining film on the epoxy is removed.

To reiterate, quantitative analysis using XEDS is at best an approximation, due to a number of factors which can influence the detection of X-rays (due to X-ray fluorescence, reabsorption, et cetera). Despite cold-mounting efforts to enhance the flatness of the sample, uncertainties that exist in the surface topography and the homogeneity of the specimen's composition renders precise specification of a quantitative analysis from SEM-XEDS work implausible [124]. In light of these challenges, the XEDS analysis will primarily be used to derive an approximate idea of the bulk composition of deposit samples, and can provide a reliable relative comparison between the elemental compositions of different areas of one sample, i.e. intra-specimen variation of composition. An example of an XEDS scan used for such analysis is given in Figure 3.12, showing relevant features of the intensity trace.

Given the challenges to accurately establishing elemental characterization with XEDS, another spectroscopic option to consider is X-ray photo electron spectroscopy (XPS). The XPS measurement of elemental constituents may provide more exact insight, and because of the inherent differences in the techniques, XPS is not subject to as many corrective factors.

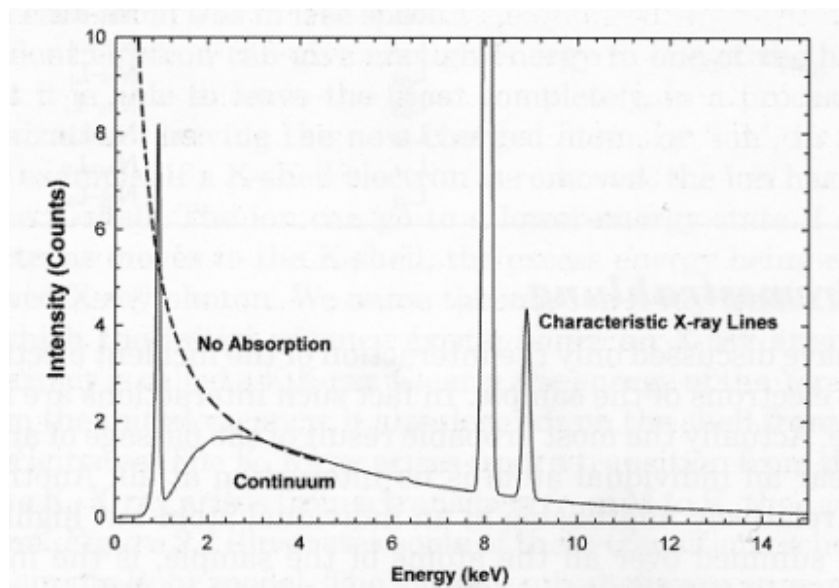


Figure 3.12 - An example of the spectrum collection from an XEDS device; the solid line represents the observed SEM spectrum, while the dashed line indicates background continuum X-rays generated when electrons come close to an atomic nucleus and slow down; due to the loss in kinetic energy, the electron emits an X-ray, which can be at any wavelength and energy, unlike the characteristic X-rays [124].

3.7.2 XPS

X-ray photoelectron spectroscopy is another method of mass spectrometry that will be used to investigate HCCI CCD with EMAL's Kratos Ultra Axis XPS. Essentially, photoelectron spectroscopy operates by irradiating a sample with "soft" x-rays, and then measuring the kinetic energy of photoelectrons that are emitted as they reach a state of excitation from the received radiation [125, 126]. This measurement is governed by Equation 3.21.

$$KE = h\nu - BE - \phi_s \quad (3.21)$$

Here, KE is the kinetic energy of the photoelectron, BE is the binding energy of the atomic orbital the electron inhabited before emission, $h\nu$ is the energy of the photon (given as Planck's constant times the speed of the photon, which is generally taken as the speed of light), and ϕ_s is the work function to remove an electron from the spectrometer [126]. The possibilities of electron behavior from XPS excitation are depicted below in Figure 3.13.

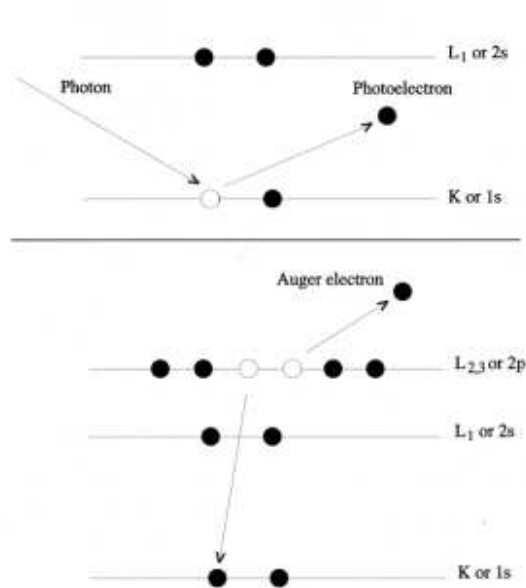


Figure 3.13 - Here, the scenarios of electron emission when utilizing an X-ray Photoelectron Spectroscopy (XPS) analysis method are displayed

The upper portion of the figure shows an incident electron being acted upon, excited by X-ray absorption and consequently releasing a photoelectron that then collected and measured by an XPS device. This is in contrast to XEDS which provides enough energy to ionize the atom, and the resulting X-ray is a consequence of the atomic decay back to a lower energy state. It is also possible that when a photoelectron is emitted, an electron from a higher energy level will move down to fill the vacancy, thus releasing another electron, in what is referred to as the Auger effect [126]. These Auger electrons are not part of the XPS spectrum, but must be accounted for during analysis.

Using this method, XPS provides a detailed quantitative report on the elemental constituents of the sample substance, as well as detail about the uniformity of the distribution of these elements. However, this technique can only detect the elemental

composition for a thin layer, on the order of 1 to 10 nm (10 to 100 angstroms). Therefore, XPS analysis can only be used to determine the CCD layer's atomic properties on the surface of the material in question. However, this understanding of the CCD's surface chemical structure may prove to be quite important in the future in helping to determine if there is a catalytic effect between the layer and unburned hydrocarbons produced in the HCCI combustion process. So, in moving forward the surface scan of the XPS device should be sufficient to provide relevant insight regarding the deposition layer. This superficial scan examination coupled with the XEDS semi-quantitative analysis will be used to achieve an overall perspective of the composition of HCCI engine deposits.

The XPS sample preparation method is not a particularly complicated one; the specimen is attached to a sampling bar, and affixed with double-sided copper tape. One limitation that results from this sample preparation is the size, which has to fit within the constraints of the bar's dimensions (10mm by 120mm in the case of the Kratos XPS). Given the physical characteristics of the deposits, this constraint should not prove problematic, as flakes and particles scraped off of engine components should fit easily within those dimensions. In addition, samples must be able to withstand the high vacuum found in the XPS device, which, again, should not prove to be an issue for CCD samples. The XPS device produces a spectrum of peak intensities of the elements present in the sample, though it is not satisfactory to use these intensity measurements as a relative measure of comparison between different deposit samples. Furthermore, some software post-processing is required for a given spectrum to calculate a quantitative atomic percentage for the specimen. This is accomplished by exploiting a

ratio calculation of the intensity of a particular element to the total number of electrons collected. Thus, even if the absolute number of electrons changes due to alterations in the experimental setup between scans, the relative calculated atomic percentages should remain approximately constant. However, there are additional measures that must be taken to ensure the quantitative elemental analysis is an accurate characterization of the CCD. While there is an accepted peak energy for the elements of the periodic table, a chemical shift for elemental peaks can occur due to the oxidation state of the atom the electron is ejected from, as well as the local physical and chemical environment, for instance, if the electron came from an atom in a molecule [125]. These nuances must be considered during peak matching analysis, as identifying the magnitude of the shift can provide information as to what sort of molecule the electron originated from, lending further insight into the elemental constituents of the sample being studied. So, despite the limitations of surface sensitivity, XPS quantitative analysis provides an intrinsically more accurate elemental breakdown than using XEDS with cold-mounted samples in an ESEM device, because it is not subject to many of the phenomena that plague the accuracy of XEDS on an SEM device. However, the juxtaposition of both analyses should prove meaningful for discerning deposit properties.

XPS can provide a core scan of a sample that finds all elemental peaks, however its real power lies in the ability to scan the peak of an individual element. Every electron (based on valence shell and orbital type) in all elements has a characteristic energy peak. However, this peak can be shifted slightly depending on the presence of other atoms or molecules surrounding the scanned elemental peak. By fitting the

experimentally measured spectrum with a model, it is possible to determine the relative percentages of molecules and elements surrounding the scanned peak. Of course, in order to perform this fitting and move forward with XPS analysis, we must know or assume the underlying structure of the sample. For the case of engine deposits, the model utilized is taken from work by Price et al. [19] that proposes a mechanism for deposit formation. In Equation 3.22, the R is representative of a hydrocarbon group that can bond to carbon atoms (note the equals sign is a double bond, and the dash is a single bond).



Because there are four groups in this model, a 4-peak fit was used for the experimental XPS data to determine the surface, molecular composition. A graphical illustration of this process is shown in Figure 3.14. Once the energy levels of the 4 peaks in the fit are established, the surface composition can be found by looking up which elements and molecules correspond to a given energy level using an XPS handbook.

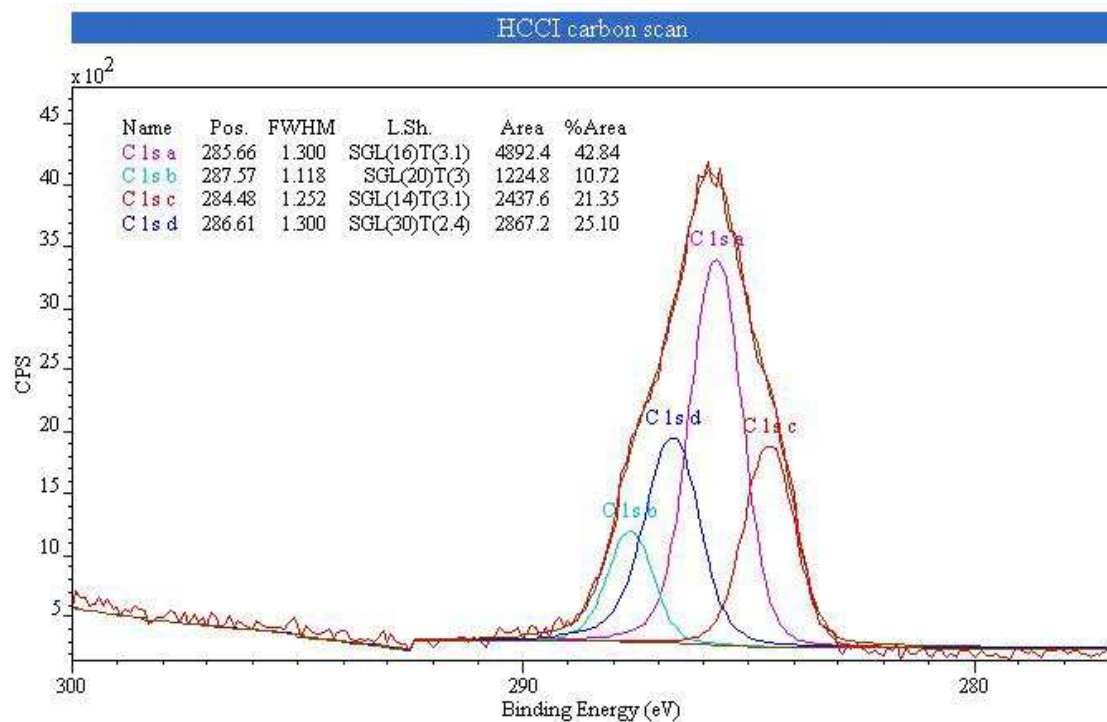


Figure 3.14 - A sample carbon scan of engine deposits (taken from another engine at UM) showing the 4-peak fit method; the experimental data is the more jagged curve

3.8 Small-Angle X-Ray Scattering (SAXS)

Another potential manner by which to determine the effects of deposit morphology upon HCCI combustion involves studying the porosity of the CCD layer. There are a number of methods available for determining porosity as a percentage of empty volume to sample volume, a surface area to volume ratio or a pore diameter distribution. The more orthodox methods employ adsorption techniques, whereby a known volume of inert gas, generally nitrogen, is forcibly injected into an evacuated chamber, and the subsequent flow of gas out of the sample is correlated with a porosity of the substance under study. While such techniques provide useful insight, there are a

number of drawbacks which make alternative testing procedures more attractive. The relative unavailability of the gas sorption equipment, and the substantial amount of sample size needed to perform such testing present significant obstacles to achieving porosity measurements of the CCD layer. Fortunately, an alternative method exists, in the form of X-ray diffractometry, which utilizes the angles of scattered X-rays to infer the structure of a substance. This method is well-established and has been used extensively in previous work that involves porous media [127-131]. Specifically, the small-angle X-ray scattering, or SAXS, technique can be used to determine the porosity of samples [132-134]. SAXS is particularly attractive because its results agree well with established methods like gas sorption. The fundamental theory behind this test is derived from Bragg's Law ($n\lambda = 2d\sin\theta$), which governs the angles at which X-rays are scattered by a crystal lattice. Moreover, this law allows us to determine an important property of the structure of the sample in question. As given by the formula, at small angles, the angle of scattering is almost inversely proportional to the distance of separation between diffracting planes [128]. For the specific case of a porous deposit specimen, this distance is indicative of a characteristic pore width. This idea is incredibly powerful, and provides a method that requires relatively small amounts of sample and is virtually non-destructive to the material being tested. The instrument used for these measurements was a Bruker AXS Nanostar featuring a 3-pinhole collimation system, a rough schematic of which is shown below in Figure 3.15.

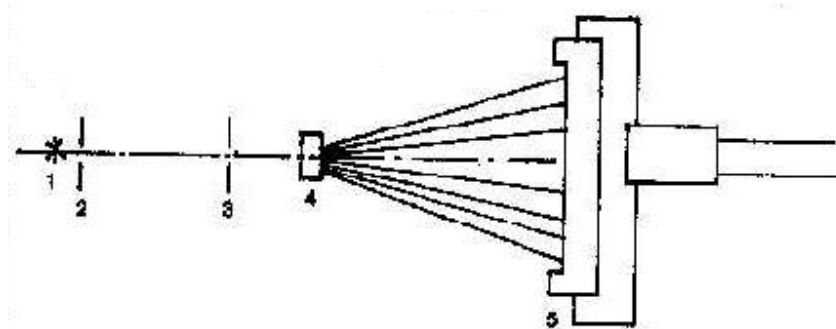


Figure 3.15 - Diagram of a position-sensitive SAXS instrument pictured with 1) the radiation source, 2) and 3) the collimation diaphragms for focusing the beam, 4) the sample, and 5) the 2-D detector surface [127]

Angular resolution is a key component of any small-angle scattering device, as we are seeking to measure scattering intensities for small values of the scattering vector [127] that satisfy the conditions in Equation 3.23. In this equation, q is the scattering vector, which will be detailed further in the following section, and a is the characteristic dimension for the particles under examination.

$$0.1 \leq qa \leq 10 \quad (3.23)$$

For the Bruker Nanostar AXS, the nominal range of particle sizes that can be measured is 1 nm to 100 nm [135]. However, based on the range of scattering angles measured from 0.1° to 2.8° in this study and considering the resolution condition of the instrument in Equation 3.23, the SAXS analysis is most accurate in a range from about 10 nm to 50 nm. The study of particles on these small length scales requires instrument beam wavelengths approximately that of interatomic distances. In particular, the

Nanostar uses Cu $K\alpha$ -radiation, with a wavelength of 1.5418 Å. Other characteristic X-rays and wavelengths of other background radiation are filtered out by a monochromator system. A collimation subsystem focuses the beam into a system of two circular diaphragms (pinhole geometry) that project the X-rays onto the sample. The scattering results are subsequently captured on a 2-D recording plane, as illustrated in Figure 3.15. The radius of the diaphragms, as well as the distance between those diaphragms and the distance from the sample holder to the recording plane, determine the value of the scattering angle.

The basic operation of the measurement technique is relatively straightforward; X-rays are scattered by electrons; so the measurement of these scattered X-rays will be substantial when there is a change of electron density in a region (i.e. an “empty” pore space versus solid, carbonaceous deposits) [136]. The direct measurement that is obtained from the SAXS scan is intensity (count of scattered x-rays) against scattering angle curve, which can then be used to derive the structural properties of the sample under observation. As alluded to, one of the chief quantities that must be calculated is the scattering vector, q .

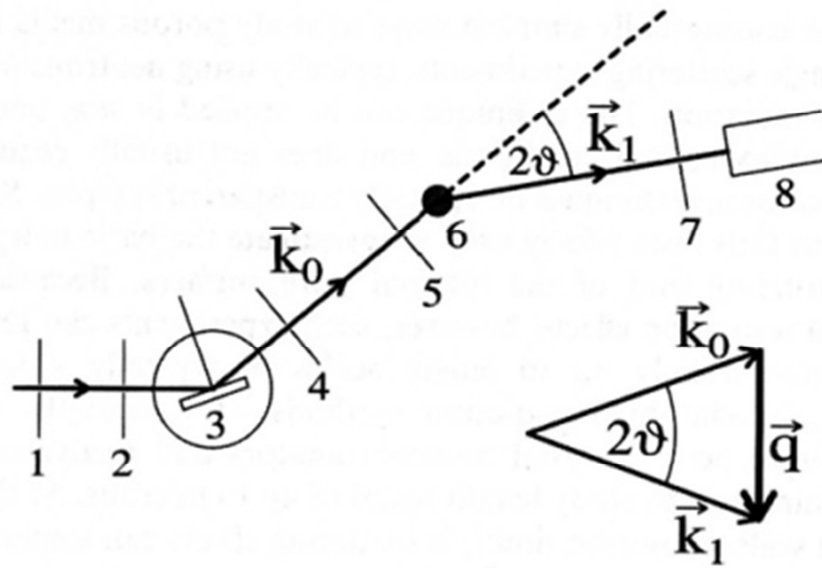


Figure 3.16 - Classical manner to visualize the diffraction of X-rays by a single particle where 3 is the monochromating crystal, 6 is the sample, 8 is the detector and other numbered lines are collimating and guard slits in the apparatus; reprinted from Sinha [129]

The importance of the scattering angle is highlighted in Figure 3.16; it measures the angle of scattering when the incident beam hits a particle, and is integral to the definition of the scattering vector, which is needed for the quantification of pore structure.

$$\vec{q} = \vec{k}_1 - \vec{k}_0 \tag{3.24}$$

The magnitude of the scattering vector is given by a simple relationship derived from Figure 3.16.

$$q = 2k_0 \sin \theta \quad (3.25)$$

In Equation 3.25, θ is half of the 2θ scattering angle, and k_0 is proportional to the wavelength of the X-ray beam incident upon the sample (1.5418 Å for CuK α X-ray from the Nanostar). Given that $k_0=2\pi/\lambda$, where λ is the X-ray wavelength mentioned above, we arrive at the classical definition for the magnitude of the scattering vector q in Equation 3.26.

$$q = \frac{4\pi}{\lambda} \sin \theta \quad (3.26)$$

When the angle 2θ is less than 7 degrees, the sin of θ is nearly equal to θ . Therefore, the scattering vector is considered to be directly proportional to the scattering angle for small values of θ . With Equation 3.26, it is possible to relate the calculated scattering vector back to the experimental measured intensity, because the SAXS instrument measures intensity against scattering angle. Once intensity is established as a function of q , it is possible to develop integral relationships to characterize the structure of the sample. Figure 3.17 is the intensity trace versus q from a previous study on carbon aerogels. The specific region of q that is utilized to study HCCI engine deposits encompasses the portion of the black trace from the dashed gray line to the beginning of the dotted red line. Scattering curves from the collected samples of engine deposits are contained in Chapter 13.

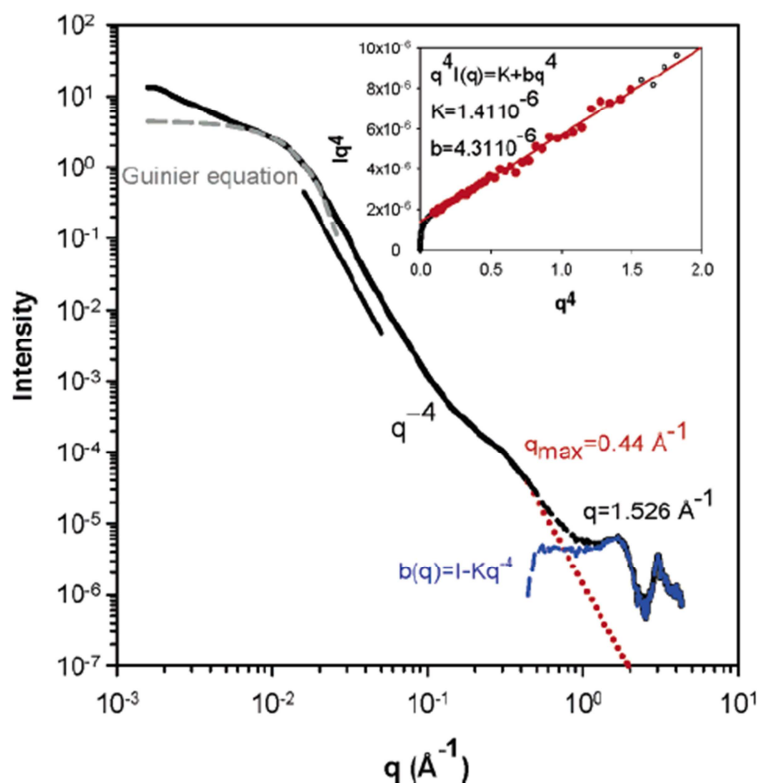


Figure 3.17 - The black trace is an example of a scattering curve of measured intensity against the scattering vector q for carbon aerogel. The blue region highlighted in the bottom right corner of the plot is approaching the region of wide-angle SAXS which is not studied in this work; reprinted from Fairén-Jiménez et al. [132]

Once the scattering intensity curve is captured for a specimen and the scattering vector calculated, a post-processing code (written in Matlab) is applied to provide structural information about the porosity of the engine deposits. First, it is important to develop a characteristic function for each sample. The idea of this function was developed by Porod, and has the advantage of having no intrinsic connection with the form factor of the particle being studied [128]. It can be visualized using Figure 3.18 as a function that describes the overlapping fraction of the volume of a particle (a pore in

this case) and the same volume translated by a vector, \vec{r} . Assuming isotropy, for the purposes of this investigation, the vector notation will be dropped as $|\vec{r}| = r$.

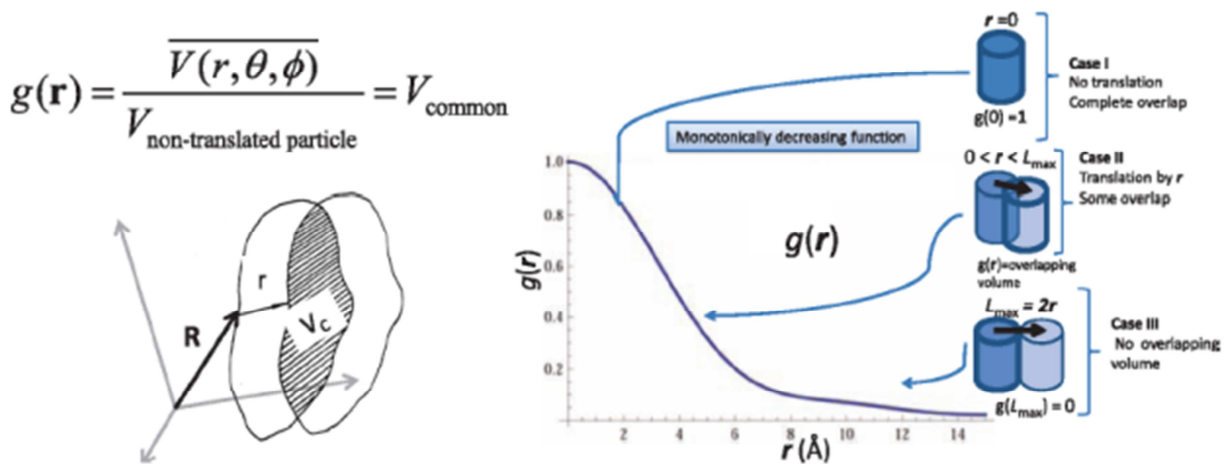


Figure 3.18 - Simplified visualization of the characteristic function for small-angle scattering. Note that the $\gamma(r)$ has been replaced with $g(r)$ using the notation of in this publication; reprinted from Kraus [133]

It follows that the characteristic function, commonly referred to as $\gamma(r)$, must be equal to unity at $r=0$ when the particle volume is not translated, and must overlap itself and equal 0 at some maximum R where the particle volume and translated volume no longer overlap. The determination of $\gamma(r)$ is formulated from an integral relation using a Fourier transform of the experimentally measured scattering data. To evaluate the resulting improper integral, it is necessary to fit a Guinier function [128] that is a simple exponential equation to either end of the experimental curve. This fitting approximation extends the finite range of the experimentally recorded data from zero to infinity. The

integral form of the characteristic function is given in Equation 3.27, and an exhaustive derivation can be found in Sinha's work [129].

$$\gamma(r) = \frac{\int_0^{\infty} q^2 I(q) \frac{\sin(qr)}{qr} dq}{\int_0^{\infty} q^2 I(q) dq} \quad (3.27)$$

The Porod Invariant, Q , is defined as the denominator of the above equation, and it too does not require any assumptions regarding pore structure.

Once $\gamma(r)$ has been established, a great deal of information can be extracted in order to describe the porosity of the deposit sample. Using several previous works that deal with porous media, including glass and other carbonaceous material [133, 137-139], and assuming the pore structures can be described by a long cylinder or elongated rod, it is possible to determine a characteristic pore width [133]. The functional form of the cylinder is shown in Equation 3.28, in which the subscript 0 is used to denote the correlation function of single pore.

$$\gamma_0(r, W_1) = 1 - {}_2F_1\left(-\frac{1}{2}, \frac{1}{2}; 2; \frac{W_1^2}{r^2}\right) \Bigg|_{r=W_1} = 1 - 8/3\pi \quad (3.28)$$

The second term on the left-hand side of the equation is a Gauss hypergeometric function and is evaluated for $r=W_1$, where W_1 is the characteristic width of the cylinder, i.e. the pore. Thus, by graphically locating the intersection of Equation 3.28 with the

previously calculated characteristic function for the deposit sample, a representative width of the pores in the sample can be established.

Porosity information is obtained by finding the intersection of $r \cdot \gamma_0(W_1, W_1)$ and $r \cdot \gamma(r)$. The point where the two plots meet also corresponds to W_1 . Finding the distance from this location to the first inflection point of $r \cdot \gamma(r)$ allows for the detection of changes in length scale. The change corresponds to a spatial sequence of pore plus solid (deposit) matrix $W_1 + C_1$ [138, 139]. Here, C_1 is the average width of the carbon matrix surrounding a pore. With the quantities W_1 and C_1 , a simple relationship yields the porosity of the deposit sample.

$$\frac{V_{\text{pores}}}{V_{\text{sample}}} = \phi = \frac{W_1}{W_1 + C_1} \quad (3.29)$$

One other useful physical property that can be calculated from the scattering curves is the surface area to volume ratio of the deposit sample, referred to as S_v . This particular quantity can reveal some information about the “roughness” of the pores, as for a given porosity and characteristic pore width, an increasing S_v intimates that the surface between the pore and solid deposit has more surface features and protuberances, which raise the ratio of surface area to unit volume. Once the porosity is calculated, the quantity S_v , measured in units of m^2/cm^3 , is found using Equation 3.30 [134].

$$S_v = 10^4 \pi \phi (1 - \phi) \frac{K}{Q} \quad (3.30)$$

Here, Q is the Porod Invariant, mentioned previously, and K is a factor describing the scattering from the final surface, given as $\lim_{q \rightarrow \infty} [q^4 I(q)]$.

The results from the SAXS analysis, and a comparison of these results against a nitrogen sorption validation test performed to assess the applicability of this method to engine deposits, are addressed in Chapter 13.

CHAPTER 4

Experimental Uncertainty in Instrumentation and Methods

4.1 Introduction to Sources of Uncertainty

This chapter discusses the sources of experimental uncertainty that arise as a consequence of the measurement equipment and techniques used in data collection, processing and analysis. Several types of error are possible in the experiments considered by this document, including accuracy errors inherent in the various measuring devices, precision errors from some of the measurement techniques, which average multiple readings, and resolution error arising from the analog to digital conversion in the data acquisition equipment. Resolution errors are considered to be half of the finest gradation an instrument is capable of measuring. For example, if the resolution of a device is 1 V, then the resolution error is ± 0.5 V.

4.2 Pressure Transducers and Crank-Angle Resolved Measurements

As mentioned in a Chapter 3, there are several types of pressure transducers used in the experimental HCCI setup for this project. There are transducers in the intake and exhaust that measure pressure on an absolute basis, and an in-cylinder

transducer that records pressure on a relative basis and depends on an absolute reference. Pressure is a crank angle resolved measurement, and the encoder mounted rigidly to the engine provides the basis for the crank angle resolution. The Kistler 2614A crank angle encoder is set at a 0.5 CAD resolution, therefore there is resolution error of ± 0.25 CAD for all pressure measurements. The maximum accuracy error for this device is relatively ± 0.02 CAD [140]. After approximately 10 hours of engine operation, the Kistler 6125A in-cylinder pressure transducer is calibrated using a Kistler hydraulic calibration device, to ensure that the sensitivity of the sensor remains reasonably close to the factory setting. Over the course of experimentation, this sensitivity deviated by less than 1% from the sensitivity stated by the factory (15.79 pC/bar), which instills confidence in the fidelity of the cylinder pressure traces from one test to another. The overall accuracy error of this sensitivity is also less than 1% of the value [141]. For the Kistler 4007B pressure transducer in the intake runner, the accuracy error of the sensitivity of 2 V/bar over a 0 to 5 bar total range is less than 0.1% [142]. There is an accuracy error of less than 0.2% for the stated sensitivity of 100mV/bar [143] associated with the Kistler 4045A exhaust pressure transducer.

Besides the pressure transducers, there is only one other type of high-speed measurement in the experimental setup, the heat flux probes mounted flush in the two cylinder head locations. These probes each utilize two J-type thermocouples, and there is an accuracy error of $\pm 2.2^{\circ}\text{C}$ associated with each thermocouple [144]. Naturally, the crank angle location of the temperatures measured by the probe is also subject to the same encoder resolution error as the pressure transducers.

4.3 Temperatures, Mass Flows and other Time-Resolved Signals

The vast majority of the signals measured from the engine are captured on a low-speed, time-resolved basis. Theoretically, when running at reasonably stable, steady state points, temperatures, mass flows and emissions readings do not vary significantly from cycle to cycle, and therefore, there is no need to record them at a crank angle level of resolution. All of the time-resolved signals are sampled for a full minute with the high-speed data recording simultaneously. The reported values are an average of these samples (taken at 10 samples per second). This obviously introduces some precision error in the time-based measurements, which are calculated from twice the standard deviation in the sampled data to cover a 95% confidence interval. However, in many cases, such as with temperature and certain emissions signals, this type of error is negligible because there is little variation while running at steady state. Therefore, the dominant source of errors is the intrinsic accuracy errors associated with the instruments.

All of the subsystem processing temperatures and relevant engine temperatures are measured using K-type thermocouples that have the same $\pm 2.2^{\circ}\text{C}$ accuracy error as the J-type thermocouples in the coaxial heat flux probes [144]. The accuracy error of the Max Machinery fuel flow meter is $\pm 0.2\%$ of the reading [145], while the uncertainty of the Fox Instruments hot-wire anemometer is $\pm 1\%$ of the reading [146]. Due to the low accuracy error of the flow meter, the dominant source of uncertainty, as referenced in the previous paragraph, results from the precision, and the overall error on a root-mean square basis is at most ± 0.1 mg/cycle.

The Micro-Dyn 35 engine dynamometer from Electromechanical Associates also contributes important signals in the low-speed data acquisition system. Engine speed and torque, which are available as voltage outputs from the dynamometer itself, are routed into the NI low-speed DAQ. While the dynamometer does a reasonable job of keeping the engine at steady speed, there is still some variation of speed at each data point, on the order of ± 5 RPM. The load cell used to measure engine torque was the Interface SM-250, which has a maximum error of $\pm 0.05\%$ of the full scale range (~ 0 -1100 N), taking into account all the sources of accuracy error [147]. The vast majority of error in the torque measurement comes from the cyclic variability of the HCCI process, which results in precision error as these readings are averaged. At stable points of operation, torque typically varies by ± 0.05 - 0.1 Nm, although at points of higher ringing intensity, such as the upper load limits of HCCI operability, the precision uncertainty of the torque can be as high as ± 0.2 Nm.

For the measurements of λ (the ratio of actual air/fuel ratio to stoichiometric air/fuel ratio) a Bosch LSU 4.9 broadband lambda sensor was used in conjunction with an ETAS LA4 lambda meter. All the experiments in this document were conducted at constant λ (thus constant equivalence ratio) of approximately $\lambda = 1.37$ ($\Phi = 0.73$). In this range, the sensor has an uncertainty of, at most, ± 0.05 for the measured λ [148].

Finally, the Horiba MEXA 7100D-EGR emissions bench has uncertainty for all the individual analyzers and exhaust species that it measures [149-152]. The CO/CO₂ analyzer has an accuracy error of $\pm 2\%$ of the reading of noise in the signal, and has some error from the interference of other gases in the sample. These errors are on the order of $\pm 0.005\%$, and are negligible compared with the accuracy error inherent to the

Nondispersive Infrared Sensor (NDIR). A $\pm 2\%$ accuracy uncertainty is also present in the NO_x , O_2 and THC analyzers, as well as the THC measurement device which has some additional error due to the interference of O_2 , which adds a cumulative $\pm 2\%$ uncertainty.

4.4 Resolution Error Associated with Analog-to-Digital Data Acquisition Hardware

Both the low and high speed data acquisition systems must convert the analog voltages they receive into digital values. This process requires dividing the measured voltage range into discrete intervals, based on how many bits are available in the system's analog-to-digital conversion. Both the NI low-speed and AVL high-speed data acquisitions, or DAQs, accept voltage inputs in the range of -10 V to +10 V. Their respective resolutions differ slightly because the NI SCXI conversion occurs using 16 bits, while the Indiset utilizes 14 bits [153, 154]. Dividing the voltage range by the number of discrete gradations, the computer software creates results with a resolution error of $\pm 1.53\text{E-}4$ V for the low-speed signals and $\pm 6.10\text{E-}4$ V for the high-speed signals. As mentioned previously, these resolution errors are quite small compared to the accuracy uncertainty of the sensor devices, and accuracy error is the main source of uncertainty for most of the recorded measurements.

4.5 Propagation of Errors in Derived and Calculated Quantities

Because of the uncertainty in directly measured quantities, such as the mass fuel flow rate or the torque from the dynamometer load cell, errors are propagated into the derived quantities that are the focus of this thesis. It is relatively straightforward to evaluate how the uncertainty in measured quantities influences a derived quantity by using a simple perturbation method, as illustrated in Equation 4.1 and Equation 4.2.

$$\text{BMEP} = 4\pi\tau / V_d \quad (4.1)$$

$$\text{BMEP}_{\text{error}} = 4\pi(\tau \pm \delta e_{\tau}) / V_d - \text{BMEP} \quad (4.2)$$

In these equations for brake mean effective pressure (BMEP), τ is the measured torque and δe_{τ} is the error in the torque used to perturb the equation to calculate the uncertainty in BMEP. By using this method, the uncertainty in the calculated quantities examined in this thesis can be evaluated in a relatively simple manner. The uncertainty for several derived values of interest is presented alongside a typical magnitude for these measurements in the table below, to provide some perspective as to the significance of these errors.

Table 4.1 – Uncertainties for Important Derived Quantities

Quantity	Error	Typical Value
BMEP	± 0.04 bar	3.0 bar
ISFC	± 2.4 g/kW*hr	210 g/kW*hr
Combustion Efficiency	± 0.04 %	96.5 %

4.6 Precision Error and Uncertainty for Other Measurement Methods Employed

There are several other types of ex-situ (out of the engine) measurements made in repetition that induce precision error for some of the results that will be presented in future chapters of this document. These errors will be discussed in more detail in their specific sections, but they include the collection of deposit thickness measurements taken with the Fischer Dualscope and the method used to quantify deposit porosity that requires an average to be taken over several sample points.

Heat release analysis is a major focus of this work, and the manner in which it is calculated engenders some precision error. At each operating point recorded, 200 cycles of high speed pressure data is saved. These pressure traces are employed to create one ensemble-averaged pressure, which is then used for heat release calculations. By performing heat release processing on the individual cycles and determining the standard deviation of that data set, it is possible to quantify the uncertainties in heat release on a cycle-to-cycle basis. As the crank angle of 50% mass fraction burned location (CA50) is a common metric to describe the HCCI combustion event, we can scrutinize this uncertainty to get some idea of precision error in the post-processing code methodology. During experiments where the combustion phasing

changes little, such as during the compensated load sweeps, the precision uncertainty in CA50 is approximately ± 0.5 CAD. However, during points where there is more cyclic variability, such as during the determination of the HCCI operating limits, this error can rise as high as ± 2 CAD. Ringing intensity (RI) is used primarily to establish the upper constraint for HCCI high load limits, as well as to assess if the engine is operating in a safe regime. RI is a common metric used in the automotive industry to assess excessive ringing, but the quantity innately has a high precision error due to the cyclic variability of the “controlled knocking” in the HCCI combustion process. Typically, RI has as much error as ± 1.6 MW/m² for an average value that only ranges, roughly, from 0.5-5.0 for most of these experiments.

Finally, there is one other important method used to quantify experimental findings that contains uncertainty. This is the American Society for Testing and Materials (ASTM) D6730 test for determining the lower heating value of a fuel, which is only accurate to roughly $\pm 2\%$ of the value. Uncertainty in this value has some implications on specific fuel consumption analysis that will be addressed in Chapter 6.

CHAPTER 5

Experimental Methods to Characterize the Effects of Fuels on HCCI Combustion

5.1 Experimental Details

In order to adequately determine the effects of refinery stream fuel properties on HCCI combustion, a set of test matrices was developed that emulates pump gasoline, representing the significant amount of variability that is inherent in commercially available gasoline in the U.S. market. A suite of different experiments was run for each fuel in the test matrices in order to characterize how the refinery stream fuels would operate in an HCCI engine. The test fuels matrix used for the experiments in this document are listed below in Table 5.1, and a simplified visualization of some of the test fuels is shown in Figure 5.1. The parameters that were varied in the fuels array include RON, sensitivity (S) and the volumetric concentration of aromatics (A) and olefins (O). Each of the test fuels was blended from refinery streams, instead of using pure chemical components. Due to the use of this blending strategy, it was not possible to hit exact targets for RON, S and chemical composition. Therefore, fuels are grouped by high/low RON, high/low S and high aromatics/high olefins. All the fuels in the cube, other than a non-oxygenated fuel used to establish a baseline for the engine (RD3-87), contain ethanol to mimic the typical composition of today's U.S. pump gasoline. While

the inclusion of ethanol in the blends could potentially mask some of the other chemical and property differences between the fuels, it was important to use ethanol in order to gain a more practical understanding of how fuels similar to pump gasoline would behave in an HCCI engine. The fuel designations for all of the 10% ethanol fuels are suffixed with a 10, as in B10, and the 20% ethanol fuels are suffixed with a 20, such as B20.

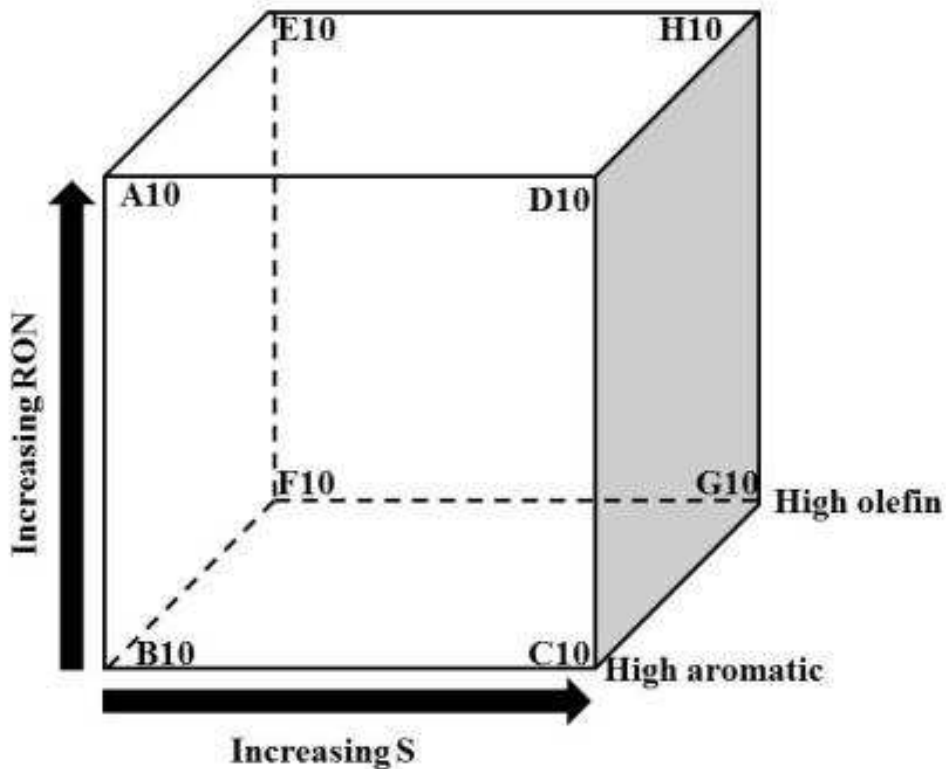


Figure 5.1 - Matrix of test fuels' properties showing the relative locations of the 10% ethanol blends

Table 5.1 – Fuels Specifications

Fuel	RON	S	A (%vol/vol)	O (%vol/vol)	Sat (%vol/vol)	Eth (%vol/vol)
A10	98.4	9.1	23.2	0.3	66.8	9.7
B10	88.5	6.4	23.8	0.9	65.6	9.7
B20	90.2	7.8	15.9	1.7	62.3	20.1
C10	89.5	8.6	37.2	4.2	48.9	9.7
C20	90.5	8.8	28.5	4.3	46.8	20.4
D10	98.1	10.8	37.0	3.5	49.8	9.7
D20	98.3	11.0	44.9	4.1	31.4	19.7
E10	98.8	9.3	4.0	8.6	77.8	9.7
E100	107	18	0.0	0.0	0.0	100
F10	90.3	8.2	3.6	11.7	75.0	9.7
F20	90.5	8.5	4.1	11.1	64.2	20.6
G10	90.4	10.4	11.2	22.3	56.8	9.7
G20	90.8	10.7	7.0	18.7	53.3	21.0
H10	99.0	11.2	5.5	15.4	69.4	9.7
H20	98.6	11.9	4.6	17.3	57.0	21.2
MM10	93.5	8.9	17.8	7.8	64.7	9.7
RD3-87	90.5	7.9	26.1	4.4	69.6	0.0

In order to establish an equitable comparison between fuels, it was necessary to normalize the baseline operating points for each fuel. This normalization was performed by adjusting two variables: the injected fuel energy and intake air temperature. The reference fuel for these experiments is RD3-87, an 87 Octane Number (ON) research grade, non-oxygenated gasoline. RD3-87 has been used in previous HCCI experimentation at the University of Michigan [5, 7, 72, 155], providing clear characterization of the fuel’s behavior in similar engine hardware. Therefore, it was a reasonable choice as a baseline fuel. In general, the results presented from this point on will include only the oxygenated fuels; the main purpose of the RD3-87 was to

establish the baseline engine operating conditions of a fuel with well-established behavior, for our particular valve strategy and engine geometry. Baseline conditions are summarized in Table 5.2 for all the fuels considered in the experiments of the following four chapters.

Table 5.2 - Baseline Operating Conditions*

Fuel	LHV (kJ/kg)	Fuel injected (mg/cycle)	Tint (°C)	Density (kg/m³)
A10	41479	11.4	103	740.8
B10	41389	11.4	87	736.3
B20	39754	11.9	60	745.1
C10	40963	11.5	65	781.0
C20	39383	12.0	51	779.6
D10	40945	11.6	81	770.9
D20	39076	12.1	55	801.9
E10	42295	11.2	100	708.0
E100	26929	17.6	76	789.0
F10	42382	11.2	65	696.2
F20	40181	11.8	56	720.1
G10	41920	11.3	53	722.9
G20	39917	11.9	52	736.7
H10	42253	11.2	85	707.9
H20	40050	11.8	64	715.3
MM10	41657	11.4	77	729.7
RD3-87	42992	11.0	90	743.6

* All baseline points were taken at 2000 RPM

The first variable matched across all fuels was the amount of injected energy per cycle in the engine, given as the product of a fuel's lower heating value and mass fuel flow rate. The mass flow rate of fuel was measured using a Max Machinery piston-style

flow meter that has an error of $\pm 0.2\%$ of the reading, and the LHV test used has an experimental error of about $\pm 2\%$. Using the previously established RD3-87 baseline point of 11 mg/cycle of fuel at 2000 RPM, a relatively simple formula was employed to determine the baseline for each fuel at the same engine speed (2000 RPM). This is shown by Equation 5.1. The mass flow rate terms and LHVs in this equation are for RD3-87 and the matrix test fuel for which reference fuel flow rate is being determined.

$$\dot{m}_{\text{matrix fuel ref pt}} = \frac{LHV_{\text{RD3-87}} * \dot{m}_{\text{RD3-87 ref pt}}}{LHV_{\text{matrix fuel}}} \quad (5.1)$$

In addition to keeping injected fuel energy per cycle consistent with that of the reference fuel, intake air temperature was adjusted to hold combustion phasing constant at the baseline condition. This accounts for the differences in temperature shown in Table 5.2, as fuels required varying amounts of reduction or increase in the intake air temperature to match the phasing of RD3-87. In this manner, ignition delay differences which could arise from varied fuel constituents were compensated for beforehand, thus the study of every fuel began at a similar operating condition.

Combustion efficiency for the fuels at each operating condition is determined utilizing the measured emissions. Equation 5.5 is an extension of a formula proposed by Stivender [156]. Here, N is the moles of sampled exhaust per mole of fuel, and y is the ratio of hydrogen to carbon in the fuel. The exhaust species in the following equations are mole fraction quantities for carbon monoxide (CO), carbon dioxide (CO₂), C₃ hydrocarbons (C₃H_{3y}) and hydrogen (H₂). Because the emissions are sampled on a dry basis, the amount of water in the exhaust must be calculated and then used to

determine the quantity of dry hydrogen in the sampled gas. The basis for the calculation of combustion efficiency is found in Equations 5.2 through 5.4, which leads to the final calculation in Equation 5.5.

$$N = \frac{100}{(\text{CO}) + (\text{CO}_2) + 3(\text{C}_3\text{H}_{3y})} \quad (5.2)$$

$$\text{H}_2\text{O} = \frac{\frac{y}{2} \frac{100}{N} - \frac{3y}{2} (\text{C}_3\text{H}_{3y})}{\frac{(\text{CO})}{K \frac{(\text{CO})}{(\text{CO}_2)} + 1}} \quad (5.3)$$

$$\text{H}_2 = \frac{y}{2} \frac{100}{N} - \text{H}_2\text{O} - \frac{3y}{2} (\text{C}_3\text{H}_{3y}) \quad (5.4)$$

$$\eta_{\text{comb}} = 100 - N \left((\text{CO}) \frac{\text{LHV}_{\text{CO}}}{\text{LHV}_{\text{fuel}}} + (\text{H}_2) \frac{\text{LHV}_{\text{H}_2}}{\text{LHV}_{\text{fuel}}} + 3(\text{C}_3\text{H}_{3y}) \right) \quad (5.5)$$

The underlying idea behind combustion efficiency is to calculate the percentage of the injected fuel's enthalpy of combustion released in the engine. Any injected fuel that is not completely consumed leads to the presence of species characteristic of incomplete combustion, primarily comprised of CO, hydrogen and unburned hydrocarbons. These species are captured by the formula in Equation 5.5.

5.1.1 Compensated Load Sweep

There are three sets of experiments, each grouped by the operating parameter that was varied during testing, that were used to characterize HCCI combustion for the fuels in the test matrix. In the first type of study, the fuelling rate is varied and the intake air temperature is adjusted so that the combustion phasing, given by CA50, remains constant at 6.5 ± 0.5 CAD after top dead center (aTDC). This is referred to as a compensated load sweep.

5.1.2 HCCI Limits of Operability

The second category of tests is used to establish the operating limits of HCCI for each fuel. During these experiments, intake air temperature is kept constant at the baseline reference temperature, mentioned previously, and the engine is taken to different speed points in 200 RPM increments from, 1200 RPM to 2400 RPM. At each speed, the load is decreased to the point of engine instability, defined as a COV% of IMEP equal to 5%, and then the load is raised until excessive ringing occurs, at a RI of 5 MW/m^2 . The RI is calculated in real-time using measured quantities in the high-speed data acquisition software, and is given by Equation 5.4 [97].

$$RI = 2.88 * 10^{-8} * \frac{(MPRR * RPM)^2}{PP} \quad (5.4)$$

The maximum pressure rise rate (MPRR) and peak pressure (PP) terms are in units of kPa/CAD and kPa , respectively. This upper limit of ringing intensity is not an arbitrary boundary; it is both the limit at which the engine is deemed too acoustically loud for a customer to tolerate, and the point at which the engine begins to experience excessive mechanical stresses that could accelerate harmful engine wear.

5.1.3 Intake Air Temperature Sensitivity

The third series of experiments conducted is a sweep of intake air temperature to test the sensitivity of each fuel to changing charge temperature. While fuelling rate is kept constant, as well as engine speed (at 2000 RPM), the intake air temperature is adjusted high enough to cause the engine to hit the knocking limit, again defined as an RI of 5 MW/m^2 , and cooled as much as ambient test cell conditions will permit. As with the compensated load sweep experiments, the injected fuel energy matches that of RD3-87, but instead of using 11 mg/cycle , 10 mg/cycle is utilized (see Table 5.3). The reason for using a reduced fuelling rate is that a more useful range of temperature could be run with the experimental setup described previously; running lower amounts of injected fuel energy allows for higher intake temperatures before excessive knocking occurs, and permits a larger overall range of intake air temperatures to be run for a given fuel (as the intake runner cannot be cooled beyond what ambient test cell conditions permit).

Table 5.3 - Fuelling Rates for Temperature Sensitivity Studies

Fuel	LHV (kJ/kg)	Fuel injected (mg/cycle)
A10	41479	10.4
B10	41389	10.4
B20	39754	10.8
C10	40963	10.5
C20	39383	10.9
D10	40945	10.5
D20	39076	11.0
E10	42295	10.2
E100	26929	16.0
F10	42382	10.1
F20	40181	10.7
G10	41920	10.3
G20	39917	10.8
H10	42253	10.2
H20	40050	10.7
MM10	41657	10.3
RD3-87	42992	10.0

Note that in all studies described in this paper, equivalence ratio was maintained at a constant 0.73. As the mass of fuel flow varied, small changes to the intake air pressure were required to achieve the constant equivalence ratio, however intake pressure was always close to naturally aspirated conditions (~1 bar). Coolant and oil temperatures were also kept at a constant 95°C, and the exhaust back pressure was regulated to be in the vicinity of 0.1 bar (i.e. the difference between the exhaust and intake pressures). This back pressure was controlled via an electronic gate valve in the

exhaust stream, which could be adjusted in order to create a consistent back pressure for the re-breath event.

5.2 Isolating the effects of Fuels from Deposit Growth

As the experiments described previously in this chapter focus specifically on the effects of fuel properties on HCCI combustion, it is important to minimize any influence the growth of deposits might have on the combustion event. As explained in chapter 1, previous HCCI studies at the University of Michigan concluded that deposits will inevitably grow in the combustion chamber, and that this growth will significantly impact combustion [5, 7]. While it is not possible to operate in a truly “clean” chamber where no CCD growth is present, it is necessary to mitigate the impacts that a CCD layer might have on the combustion event, and isolate these effects from those of the fuels being tested. In order to accomplish this goal, it was first necessary to designate an appropriate “window” of operation for the engine to run in while the fuels tests were conducted. Initial testing calibration with the baseline fuel, RD3-87, revealed that the engine ran stably at a COV% of IMEP of roughly 1, with a relatively low RI of less than 3 at 6.5 ± 0.5 CAD aTDC, at the baseline operating condition of 11mg/cycle of fuel and 2000 RPM engine speed. More importantly, while there was initially a large amount of deposit growth on the clean metal piston when the engine was first started (this issue is explored in the following chapters on deposits), the window in which experiments were run is situated at the point where the rate of growth had slowed. This growth rate was gauged indirectly, by monitoring the LPP and CA50 on our high-speed system and observing the rate at which combustion phasing advanced. Obviously, it is desirable to

operate in an area where the rate of this advance of combustion phasing can be minimized to avoid including the effects of the CCD layer on the fuels study. Because the first few hours of growth were too significant, and our goal was to not completely “dirty” the chamber, the operating point where the rate of deposit growth had slowed was decided upon as the baseline point at which to begin testing for all fuels. Before any new fuel tests began, a baseline point with RD3-87 was taken to ensure the combustion chamber was at the proper level of conditioning, in order to establish a reference condition for each new fuel. At any point during testing, if it was determined that the combustion event was too advanced (indicating the chamber was overly conditioned with CCD) it was necessary to “clean” the combustion chamber to re-establish optimal phasing. In order to facilitate an effective and simple cleaning procedure, it was decided that an in-situ method was preferable to dismantling the cylinder head multiple times. For the in-situ cleaning method, we wished to utilize a two-tiered approach for deposit removal, using both high wall temperatures and high RI to both burn off the top portion of the layer, and possibly cause flakes to crack off the CCD layer as well. This was accomplished by running the engine for several hours at an equivalence ratio of approximately 0.9 (much closer to stoichiometric than all the experiments), an engine speed of 2500 RPM and a RI of 9-10. Due to the relatively low peak pressures run during this cleaning sweep (on the order of 43-45 bar) this level of RI run for a sustained period of time posed relatively little risk to the mechanical safety of the engine. The choice of a “cleaning” fuel was also important, in that it needed to ensure that no further deposition would accumulate and that the amount of time cleaning had to be run was kept to a minimum. Initially RD3-87 was run with the

cleaning dose of Techron (1 ounce per gallon of fuel) which seemed to minimally affect the deposit layer, as the CA50 changed only slightly. Next, a refinery stream component, rerun alkylate (RRA), was used with the cleaning dose of Techron. As it is mostly composed of paraffins, and not prone to deposit formation, it was theorized that this fuel would be “cleaner” than RD3-87 and perhaps remove deposits more effectively. The results, as summarized below in Figure 5.2, show that using the RRA with the cleaning dose of additive engendered a noticeable retardation in the peak heat release for the fuels.

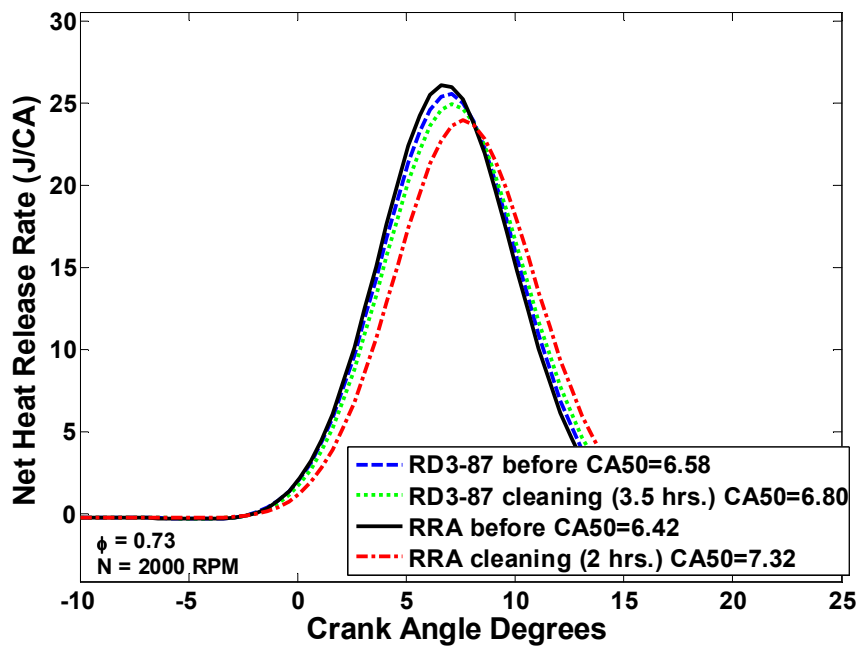


Figure 5.2 - Effect of the cleaning methodology on the location of net release rates, and ultimately on the location of the combustion event before and after cleaning for RD3-87 and RRA using the cleaning dose of Techron (1 ounce/gallon fuel); bear in mind that the combustion chamber is never truly ‘clean’ using this method, but in fact, always contains some level of CCD growth

The heat release peak decreasing and moving later in the cycle is a clear indication of less deposition in the cylinder. During the course of the testing cycle to determine the effects of fuel properties on HCCI combustion, all fuels were run without any additive package, necessitating frequent cleaning in the case of some of the more aromatic fuels. Using RRA with the cleaning dose of Techron, at the aforementioned operating conditions, performed sufficiently to remove some CCD from the combustion chamber when required.

CHAPTER 6

Impact of Refinery Stream Fuels Property Variation on Load Sensitivity of HCCI Combustion

6.1 Introduction

This chapter explores the impact of the differing properties of various refinery stream fuels on HCCI combustion, on two distinct fronts. The first is to check the sensitivity of fuels in the test matrix to changes in fuelling, in other words, how much intake air temperature compensation is necessary for each load sweep in order to maintain desired combustion phasing. Second, the topic of specific fuel consumption for these refinery stream fuels is broached, as it is important to determine if the LHV of each fuel is the only factor to establish the fuel economy of running a particular refinery stream fuel. For these analyses, indicated values such as ISFC and IMEP are considered to present a best-case scenario for the engine.

6.2 Sensitivity to Load

As previously mentioned, the HCCI combustion process is extremely sensitive to in-cylinder thermal conditions and chemical kinetics, thus changes in the fuelling rate lead to significant changes of engine performance beyond just higher energy release [85, 86]. To demonstrate the complex effects, a compensated load sweep was performed with each fuel, starting initially from the baseline point, and then working from the lowest fuelling load to the highest. The intake air temperature was decreased simultaneously with fuelling increase to ensure the combustion phasing matched the reference throughout the experiment. The slopes of the lines in Figure 6.1 and Figure 6.2 indicate how sensitive or robust the HCCI operation is depending on the fuel properties. To make the discussion easier, the results obtained with high-aromatic and high-olefinic fuels are plotted separately.

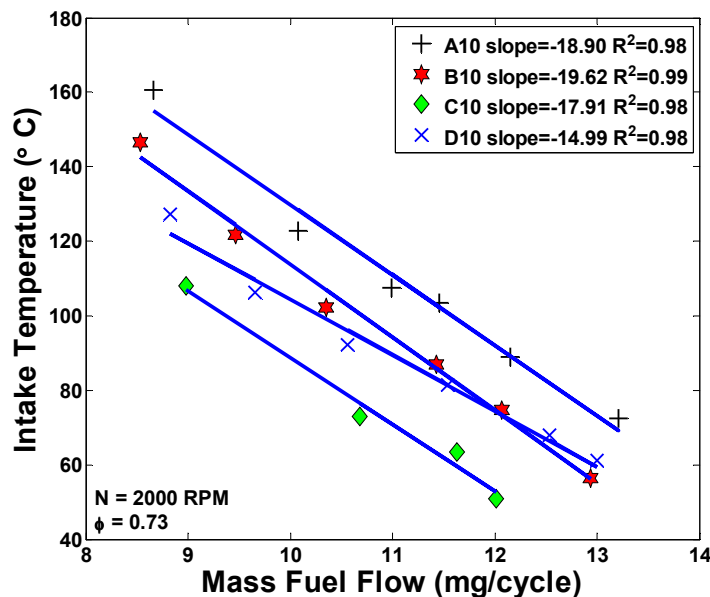


Figure 6.1 - Intake air temperature compensation required to maintain constant combustion phasing over a range of engine loads – high aromatic fuels

Figure 6.1 shows the variations of the intake temperature over a compensated load sweep for all four high aromatic fuels. The relative location of each curve is tied directly back to the baseline operating point for each fuel – see Table 5.2. Fuels with a lower reference temperature had their curve shifted down, as in the case of C10 which has the lowest baseline intake temperature of 65°C. Operating at an elevated baseline temperature causes the curve for A10 to move up. This reference temperature does not appear to be tied to the fuel's octane number. Rather, there is a more complex relationship between the ignition characteristics of the fuel and its specific composition. For instance, B10 and D10 were on opposite ends of the test spectrum for RON, but required similar baseline intake air temperatures (87°C and 81°C, respectively). The observation that the auto-ignition behavior of fuel is not solely tied to octane rating is in agreement with work performed by Kalghatgi et al [90, 157, 158].

In addition to the change of the relative position of the curves, the slopes of the temperature lines for the compensated load sweep also change from fuel to fuel. For the fuels of similar RON in Figure 6.1, increasing sensitivity (S) causes the reduction of slope, suggesting that a more sensitive aromatic fuel requires less temperature compensation for a given RON. This is an advantage in the context of developing robust HCCI control. Between A10 and D10, which both have an approximate RON of 98, the D10 curve is less steep because it has the higher S of the two (10.8 to 9.1). A similar observation can be made regarding to B10 and C10. Looking from a different angle, fuels with high aromatic content (C10 and D10) demonstrate lower slopes.

Figure 6.2 contains a comparable compensated load sweep for the high olefin fuels. The vertical shift of lines is even more pronounced, with a temperature spread

between E10 and G10 of 47°C, at reference conditions. The slopes, i.e. the variation of temperature over a range of load, fluctuate in a similar range as in the case of high aromatic fuels. Also, the slopes are less steep for fuels with a lower olefinic fraction.

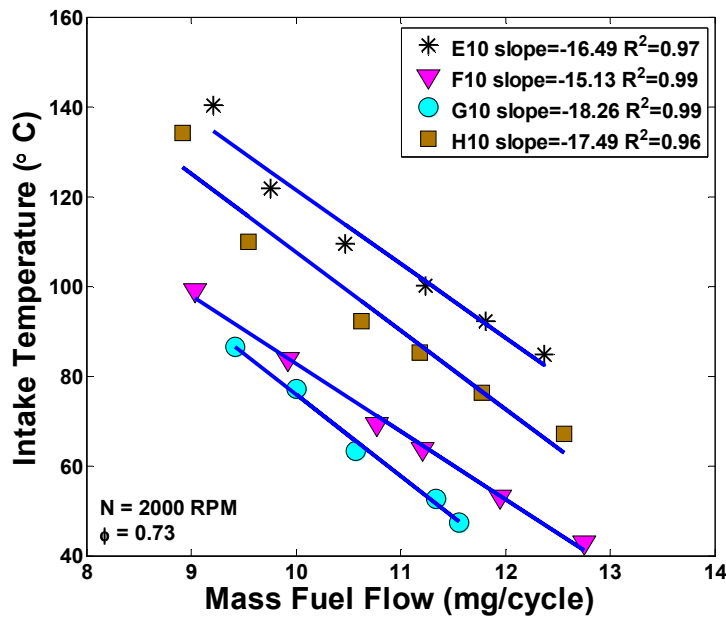


Figure 6.2 - Intake air temperature compensation required to maintain constant combustion phasing over a range of engine loads – high olefin fuels

The key distinction between the aromatic and olefinic fuels is their behavior as a function of MON for a given RON. As mentioned previously, for the fuels with more aromatics, increasing S at a given RON results in a reduced amount of temperature compensation. With the olefin fuels presented in Figure 6.2, this trend is reversed; raising S at constant RON necessitates *more* intake temperature compensation as fuelling rate is increased. In other words, the slope of the curve becomes steeper at elevated S. The findings for all fuels are summarized in Figure 6.3. Here, the aromatic

content of highly aromatic fuels is given in the plot on the left, and for the highly olefinic fuels the olefin content is displayed on the right. The lines connecting the points indicate fuels of almost constant RON. The difference in behavior between aromatic and olefinic fuels likely stems from dissimilar auto-ignition chemical pathways. Whereas many olefin molecules are in a form that can be readily auto-ignited, aromatic chain structures generally must be broken apart into simpler molecules (often olefins) before auto-ignition can begin to propagate. Olefinic kinetics are, in general, much better understood and more straightforward than the complex reactions involved in aromatic auto-ignition.

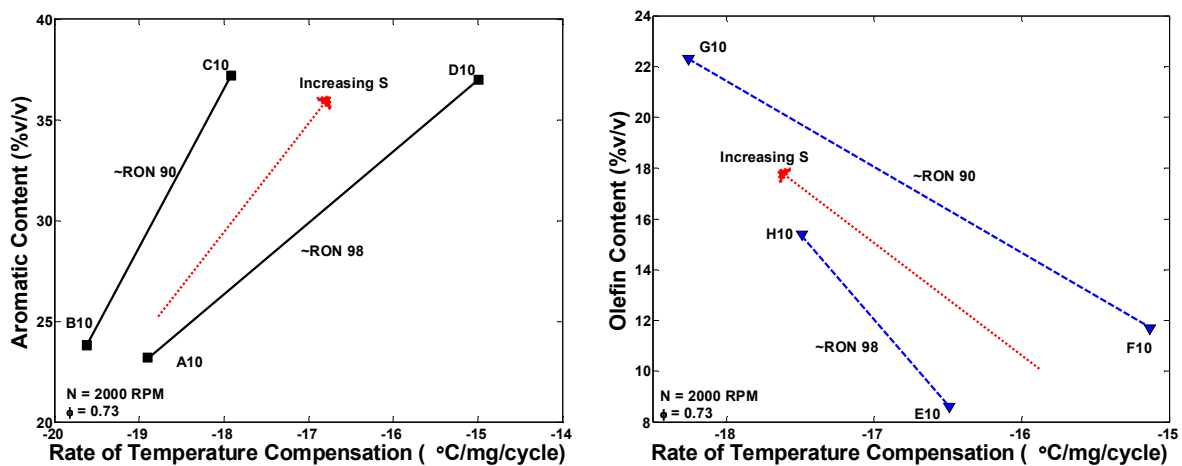


Figure 6.3 - Comparison of the changing sensitivity of engine operation to fuelling rate for highly aromatic (left) and olefinic fuels (right)

In reference to Table 5.1, an increase of sensitivity for a given RON requires a higher volumetric content of aromatics or olefins, in order to create a suitable matrix of refinery stream fuels of varying properties for this study. Examples of this are found

when considering A10 and D10 or E10 and H10. Primary reference fuels, or PRFs, which are saturates, do not exhibit fuel sensitivity between the RON and MON tests. Therefore, some hydrocarbon species that have $S > 0$ have to be used in the test matrix for those experiments. Because it was necessary to increase the volumetric content of aromatics and olefins with increasing S , the importance of those components during auto-ignition is simultaneously exacerbated. Essentially, when S is increased, the fuels in the matrix become more aromatic or more olefinic.

Testing with PRFs and surrogate fuels in previous HCCI experiments has found that olefins, as compared to aromatics, show a tendency to advance high-temperature heat release [86]. Therefore, it is reasonable to imagine that increasing the content of olefins in a refinery stream fuel might result in a faster rate of combustion phasing advance over a load sweep, if there were no intake air compensation. The results in Figure 6.3 imply that this is the case with increased olefin fuels; increasing the volumetric content of olefins at a given RON requires a higher rate of intake temperature compensation to maintain constant phasing over the range of load than the case of highly aromatic fuels.

To reiterate, this is shown in Figure 6.3 as higher rates of intake temperature change (more negative rates) necessary to maintain constant combustion phasing with changing fuelling rates for the fuels of increasing olefinic content on the blue lines (moving in a right to left direction on the right portion of the figure). Conversely, the addition of aromatic content displays the opposite behavior, as shown with black lines in Figure 6.3 looking from a left to right direction on the left part of the figure. The rate

values become less negative with respect to increasing aromatic content, indicating lower rates of temperature compensation are needed with higher levels of aromatics.

6.3 Fuel Efficiency Analysis

The compensated load sweeps contain additional, useful information regarding engine performance and efficiency. The ISFC and IMEP are considered in the analysis to identify the best-case fuel consumption efficiency scenario. The choice of ISFC in these plots is intended to provide some practical amount of fuel economy comparison between the blends. The impact of indicated thermal efficiency will be explored later as a complement to the ISFC study. First, the directly measured points for the aromatic and olefinic fuels are plotted in Figure 6.4 and Figure 6.5, respectively. Secondly, the lines indicating expected values, predicted purely based on the energy content of a particular fuel, are added. The predicted trend lines, in Figure 6.4 for high aromatic fuels and Figure 6.5 for high olefinic fuels, are generated by taking the percentage difference between the lower heating value of the 10% ethanol fuels and that of RD3-87 and applying a multiplication factor to the RD3-87 IMEP versus ISFC curve (which was acquired in previous testing, and is not pictured here). This calculation is summarized in Equation 6.1, where $ISFC_{fuel,predicted}$ is the calculated value for the expected ISFC of the test fuel, $ISFC_{RD3-87}$ is the ISFC of the RD3-87 baseline fuel determined from previous experimentation, LHV_{fuel} is the LHV of the test matrix fuel and LHV_{RD3-87} is the LHV of RD3-87.

$$ISFC_{fuel,predicted} = ISFC_{RD3-87} * \left[1 - \left(\frac{LHV_{fuel} - LHV_{RD3-87}}{LHV_{RD3-87}} \right) \right] \quad (6.1)$$

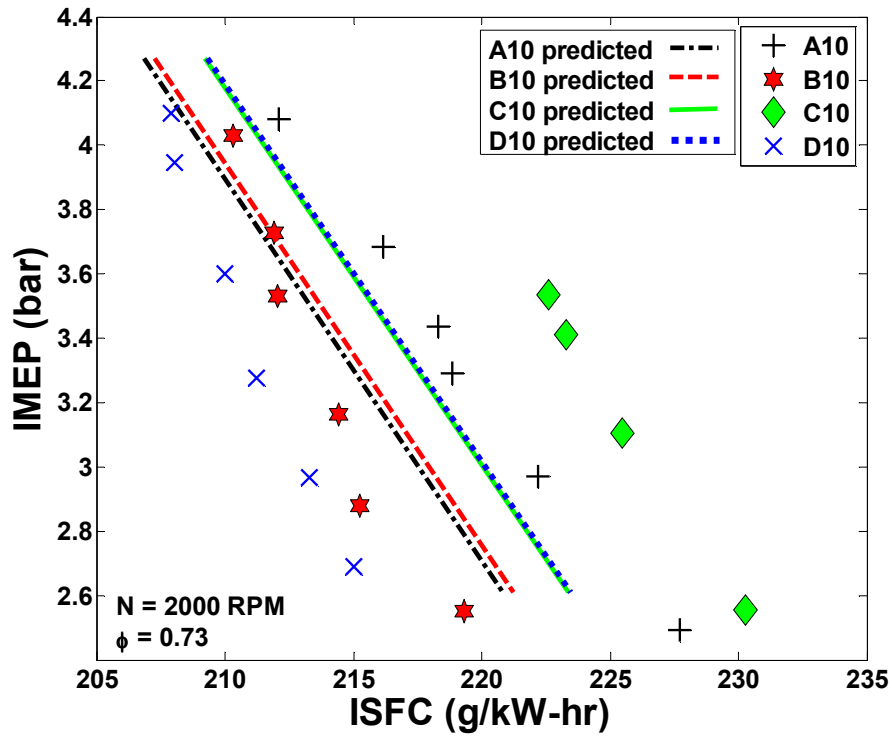


Figure 6.4 - Indicated Mean Effective Pressure vs. Indicated Specific Fuel Consumption on a mass basis for high aromatic fuels; measured points and predicted trend lines

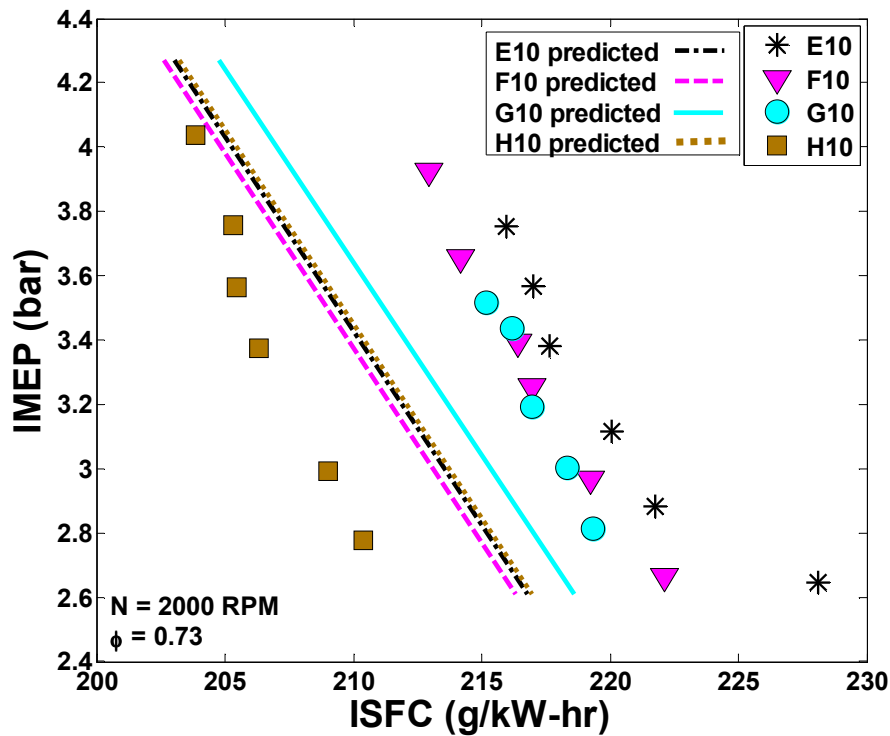


Figure 6.5 - Indicated Mean Effective Pressure vs. Indicated Specific Fuel Consumption for the high olefin fuels on a mass basis; measured points and predicted trend lines

The predicted lines represent the expected ISFC based solely on lower heating value reductions of the test as fuels compared to RD3-87. In addition, plots in Figure 6.6 and Figure 6.7 show a visual portrayal of fuel efficiency in volumetric terms, which is important as pump gasoline is sold by volume and not by mass.

With ISFC by mass or volume, each set of fuels shows a wide spread of specific fuel consumption, despite similar energy injected into the cylinder and matched phasing for all operating points. Figure 6.6 and Figure 6.7 also show that in general, the HCCI engine runs more efficiently with highly aromatic fuels than with the group of high olefinic fuels. This is due to the efficiency benefit gained from higher densities when

considering specific fuel consumption on a volumetric basis. Note that both Figure 6.6 and Figure 6.7 are plotted on the same scale for the abscissa, and from this it is possible to obtain a qualitative picture about the efficiency implications of using any fuel.

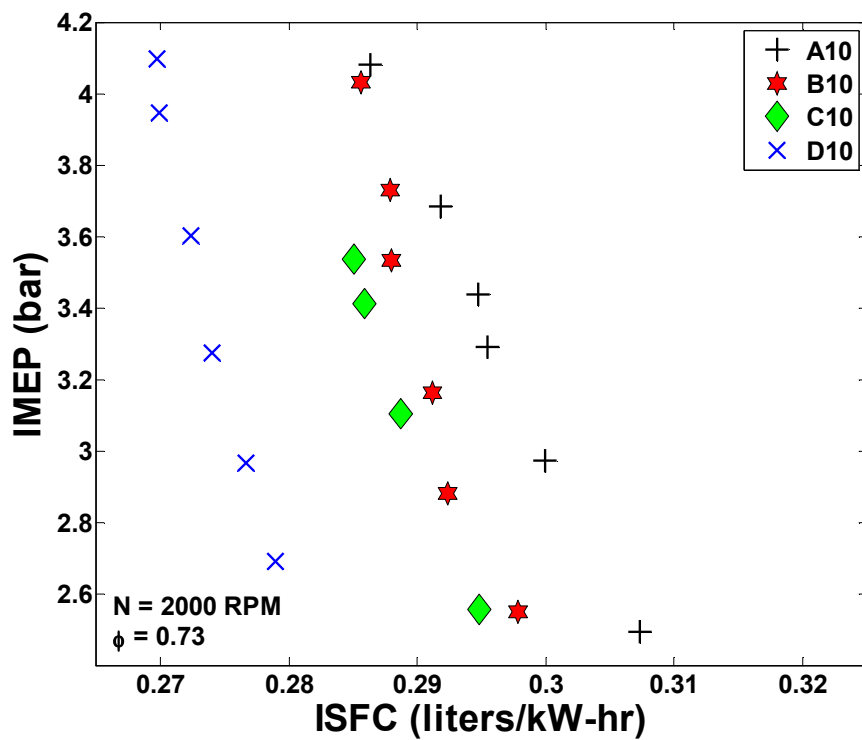


Figure 6.6 - Indicated Mean Effective Pressure vs. Indicated Specific Fuel Consumption on a volumetric basis for high aromatic fuels; this more accurately reflects “pump” efficiency as gasoline is sold on a volumetric and not a mass basis

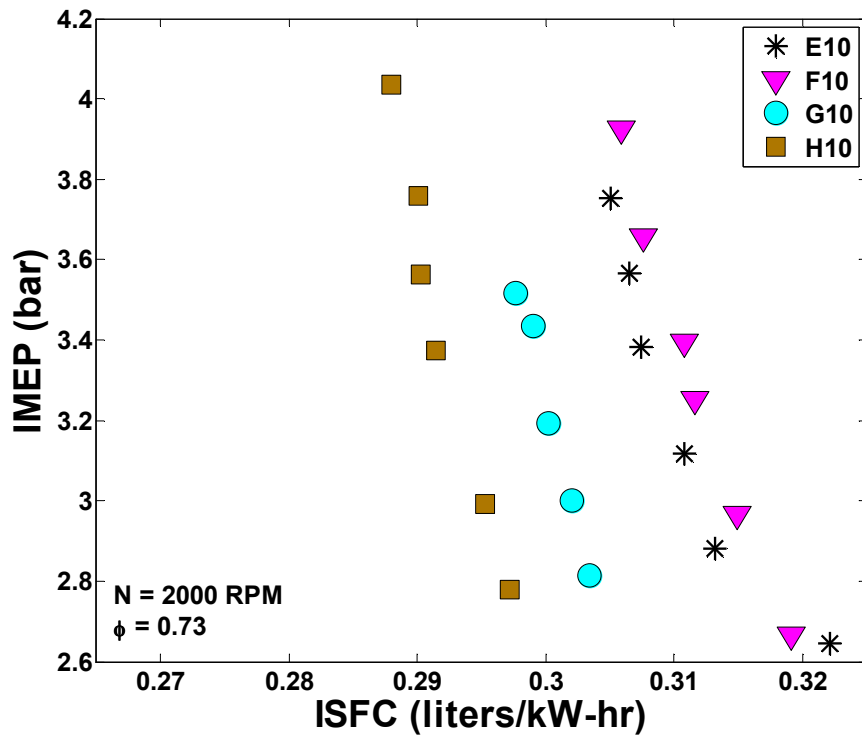


Figure 6.7 - Indicated Mean Effective Pressure vs. Volumetric Indicated Specific Fuel Consumption for the high olefin fuels

Considering the ISFC on a mass basis, the difference between the points and predicted lines for any given fuel indicates that there are factors overriding the disparity in heating values. To aid in understanding the fuel efficiency trends, Figure 6.8 and Figure 6.9 show the IMEP values for all the compensated load sweeps versus the amount of available fuel energy in-cylinder. There are clearly effects beyond the energy content in the cylinder that affect measured IMEP. Some fuels, such as B10 and C10, display higher IMEP for a given level of injected energy.

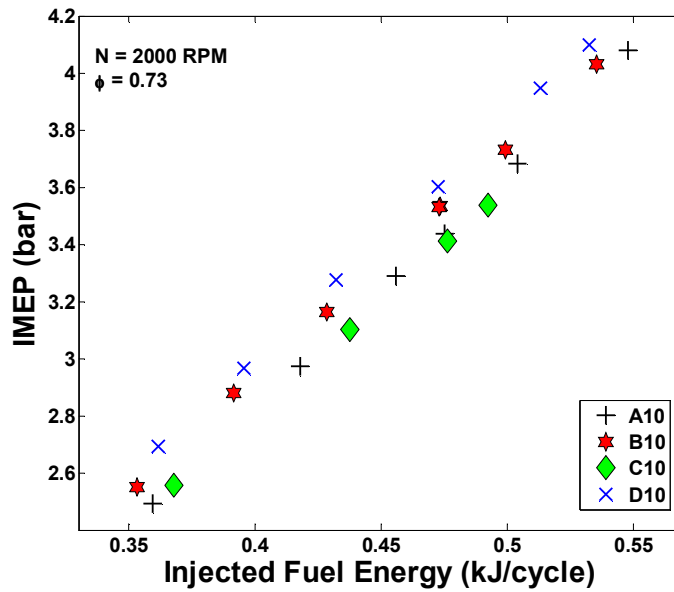


Figure 6.8 - Indicated Mean Effective Pressure plotted vs. the total energy content of the injected fuel into the cylinder per cycle for the high aromatic fuels

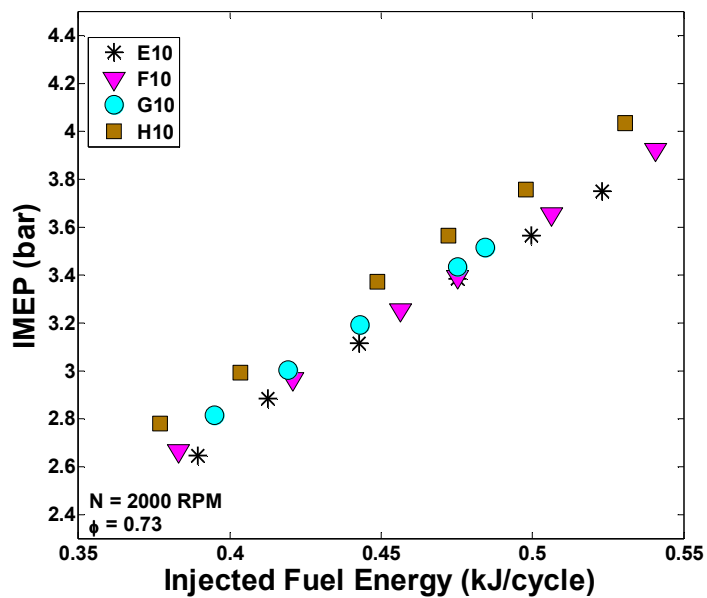


Figure 6.9 - Indicated Mean Effective Pressure vs. the total energy content of the injected fuel for the high olefin fuels

There are three distinct possibilities when it comes to the mechanism responsible for affecting efficiency. Firstly, there is a difference of thermodynamic conditions in the cylinder due to the characteristics of each fuel which requires variations of intake charge temperature. Resulting heat transfer effects have an impact on thermal efficiency. Because the coolant temperatures are fixed throughout all the experiments, keeping the combustion chamber walls at similar temperatures, fuels that require more intake air heating and have a hotter intake charge will have more heat transfer to the walls, because there is a larger temperature difference between the gas and walls. Additionally, if there are any charge cooling effects that arise from the difference in physical properties and distillation curves of the fuels, this could also impact heat transfer.

The indicated thermal efficiencies ($\eta_{i,\text{thermal}}$) for all the fuels at their baseline conditions are plotted in Figure 6.10. Recall that the fuels whose measured ISFC curves lay to the left of their predicted ISFC curves in Figure 6.4 and Figure 6.5 (more efficient than expected based solely on LHV differences) are B10, D10 and H10. Concordantly, these three fuels exhibited a noticeably higher indicated thermal efficiency than the other five test fuels. For all the fuels with below 40% indicated thermal efficiency, the more measured ISFC curves are shifted to the right (i.e. more inefficient than predicted only by LHV differences) the lower their $\eta_{i,\text{thermal}}$ is. Thus, thermodynamic effects that impact indicated thermal efficiency play a role in the ISFC trends shown in previous plots. It is important to note that the thermal efficiency differences are not solely a function of charge temperature for these fuels, as the most thermally efficient fuels B10, D10 and H10 do not have the lowest intake air

temperatures of all the fuels (although they do not have the highest, either). To reiterate, physical differences in the fuel blends such as density and their distillation curves might also be impacting the thermodynamic state of the incoming charge to the cylinder.

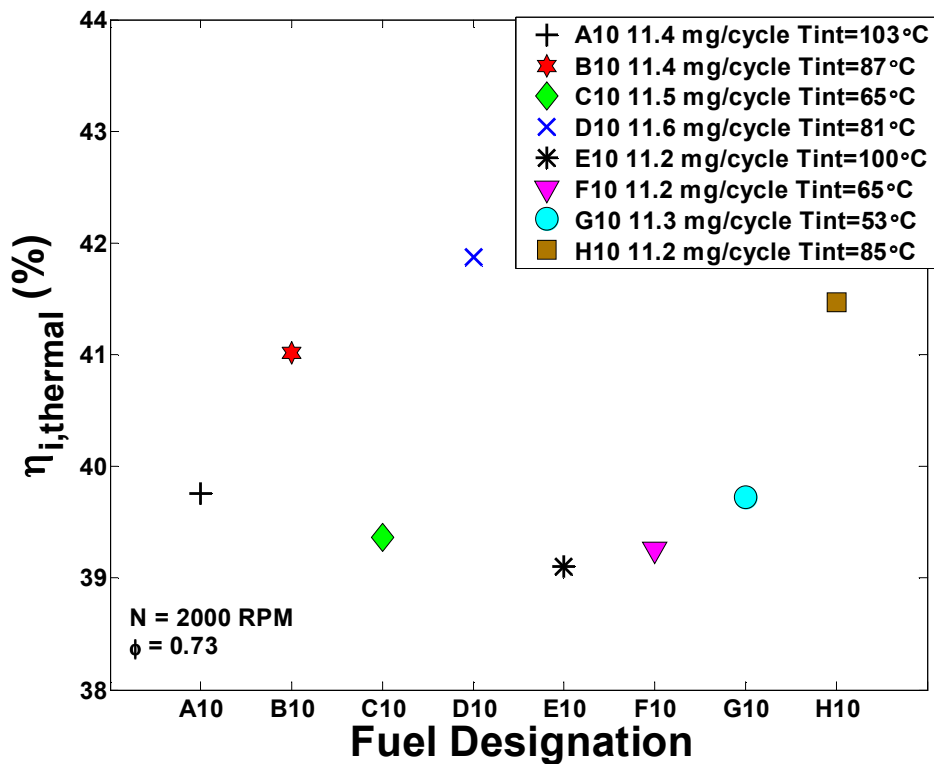


Figure 6.10 - Indicated Thermal Efficiency for all the test fuels at the baseline condition

Secondly, there is some variation in the combustion event and from which it can be hypothesized that combustion efficiency is a factor. Figure 6.11 and Figure 6.12 are plotted to check this hypothesis. The net heat release rates (NHRR) for all the test matrix fuels are plotted at the reference condition in Figure 6.11. The curves nearly lie on top of one another. Thus, the heat release process, and consequently the

combustion event, seems to be similar at the baseline condition, where combustion phasing and injected fuel energy are matched. Figure 6.12 contains two additional distinct data sets. The points on top represent the combustion efficiency at reference condition obtained with all fuels. The load at the baseline point for all fuels is roughly IMEP of 3.4 bar. The triangular markers on the bottom illustrate the burn duration, represented with the crank-angle interval between 10% and 90% mass burned (CA10-CA90). Combustion efficiencies are similar across the complete set of refinery stream fuels, indicating that IMEP differences are likely not a product of differing amounts of fuel actually combusting in-cylinder. Furthermore, the CA10-CA90 burn durations for all the fuels are remarkably similar given the range of compositional changes, as all the burn durations are within ± 0.5 CAD of a 9 degree average value. The findings disprove the hypothesis that combustion efficiency plays a role in fuel consumption trends, and instead bring into focus the thermodynamic differences during compression and expansion.

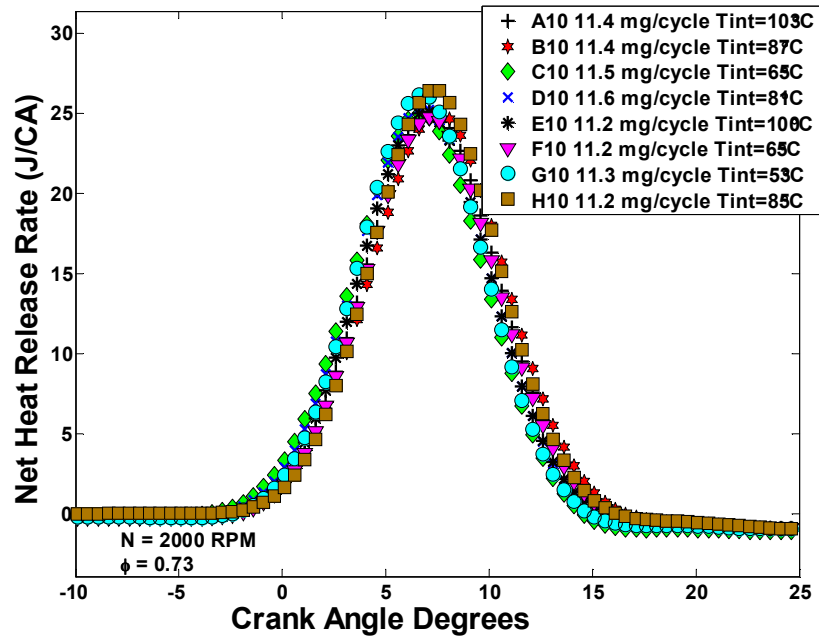


Figure 6.11 - Net Heat Release Rates for all the test fuels at their baseline operating point

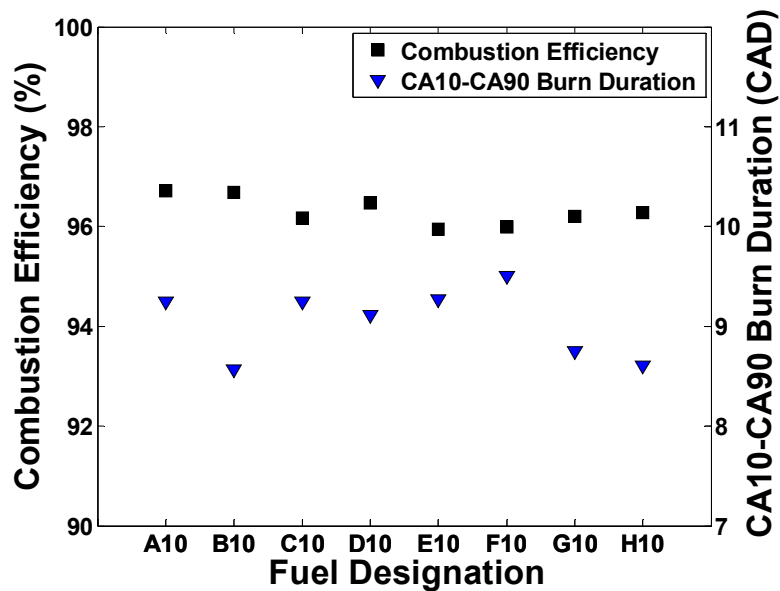


Figure 6.12 - Combustion efficiency and CA10-CA90 burn duration determined at the baseline operating points for the complete range of fuels tested

Thirdly, there is the possibility of an error in LHV measurements that could directly affect predicted ISFC values. The ASTM D6730 method used to test the LHV of all the fuels specifies an error tolerance of up to $\pm 2\%$ of the values shown in Table 5.2. While this uncertainty could account for some of the discrepancies, it is not significant enough to account for all the differences between the predicted and the experimental ISFC data. In summary, the discrepancies between the predicted and experimental ISFC trends that occur with variations of fuel can be attributed largely to thermodynamic conditions in the HCCI engine with re-induction of residual, and to a lesser extent to uncertainty in determining the LHV of each fuel. However, it is important to keep in mind that the absolute measurements hold, and indicate a wide range in which consumption in liters varies across the fuels matrix.

Figure 6.12 also brings to light another discovery about these refinery stream test fuels. For the compensated load sweep tests, every fuel is matched to have the same combustion phasing, so that every fuel will have a similar CA50. Even though these fuels exhibit a wide range of ignition characteristics, confirmed by the need for various intake air temperatures in Table 5.2, this disparity does not seem to affect the progression of the combustion event, as long as the phasing is constant. The underlying implication is that as long as in-cylinder thermal conditions can be coordinated between fuels and ignition differences can be compensated for beforehand, the chemical kinetics of dissimilar fuel chemical composition is not important for determining the length of the combustion event. It is widely known that the auto-ignition chemistry between aromatics and olefins is quite different [8, 159-161], however it seems that for refinery stream fuels the burning in an HCCI engine is so rapid that the

impact of fuel composition is significantly diminished. This must be considered with a caveat: the conglomeration of dissimilar chemistries in fuel blends containing high aromatics, as well as also olefins and saturates in smaller quantities, may result in competing effects playing out against one another. The same can be said of the high olefin fuels, which are constituted of aromatics and saturates as well.

CHAPTER 7

HCCI Limits of Operability for Refinery Stream Gasoline

7.1 Introduction

Chapter 7 examines how variability in refinery stream fuels can influence HCCI operability at the limits of combustion. The instability and ringing limits for the 10% ethanol fuels are considered, and also heat release analysis is used to compare the combustion phasing and burn durations at the limits, for different fuels.

7.2 HCCI Operating Range

In the context of a dual-mode SI/HCCI engine, the more the HCCI operating range can be extended, the higher the potential benefit for vehicle fuel economy and reduction of engine-out emissions. Some variation in the limits of operability based on the properties of refinery stream fuels, notably RON and sensitivity, is expected and the goal is to quantify the variations. An additional question that can produce useful guidance for future research, is how well can the observed changes be correlated to fuel properties, primarily the RON and S.

First consider Figure 7.1 and Figure 7.2, which depict the limits of operability for the fuels with high aromatics and high olefins in separate plots. As mentioned previously, the high load limit (HLL) is determined when the engine rings excessively and the low load limit (LLL) established when the instability of the combustion process becomes unacceptable.

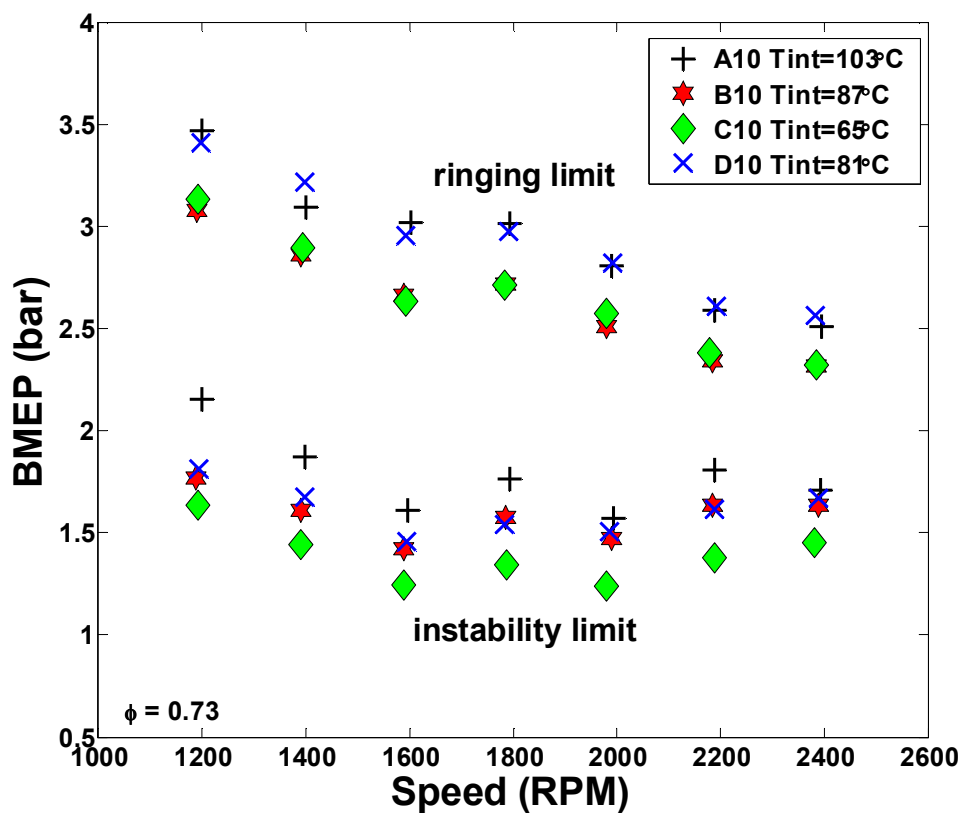


Figure 7.1 - Limits of operability for high aromatic fuels in the test matrix

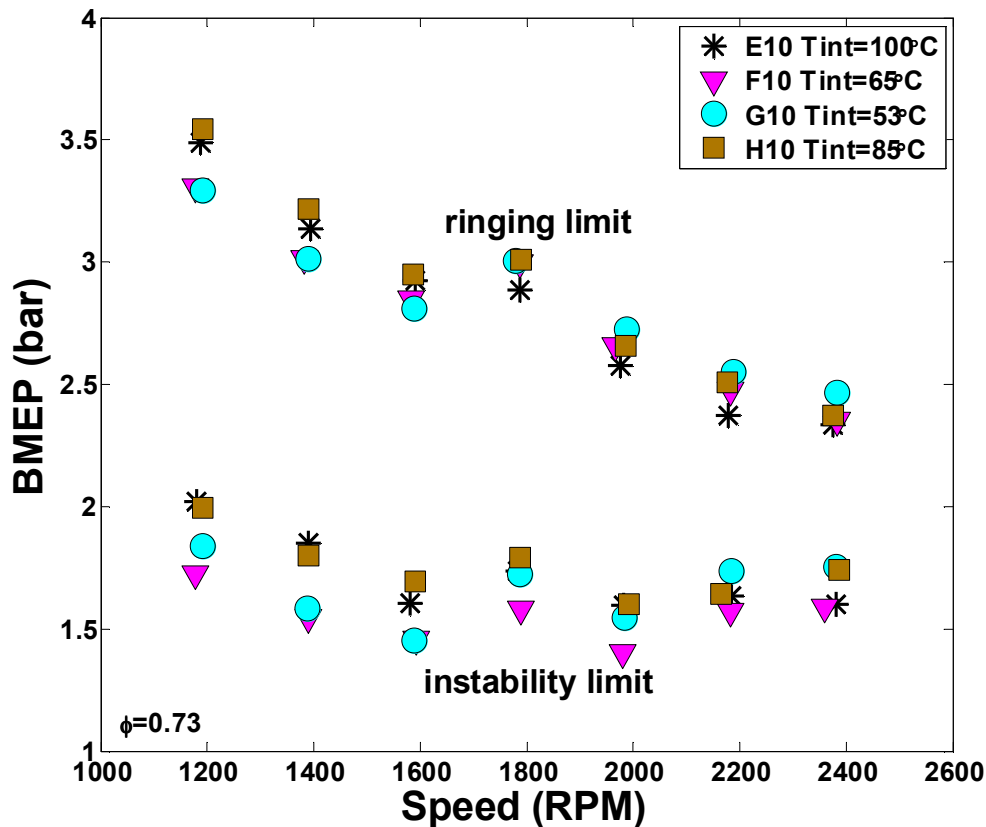


Figure 7.2 - Limits of operability for the test matrix high olefin fuels

The operability limits seem to change in a tangible manner between fuels of different composition, RON and S. Furthermore, the differences between the limits of the fuels are more than what is expected from any uncertainty in the BMEP values, as calculated from the measurement of torque, only accounts for less than a tenth of a bar BMEP. Considering the high load limits in Figure 7.1, the two high aromatics fuels with the highest RON, A10 and D10, have the most elevated HLLs across the speed range. This is as expected, since the RON of the fuel should give some indication of its resistance to auto-ignition, and a fuel of higher RON should be able to run at higher loads before excessive ringing occurs. However, for the high olefin fuels, this trend is

not readily apparent. At speeds below 1800 RPM, the higher RON fuels (E10 and H10) do have higher HLLs, but with increased speed the HLL becomes similar for all four high olefin fuels. An anomaly is shown with G10 fuel operating points beyond 2000 RPM, with slightly higher loads for a *lower* RON fuel. This alludes to the fact that RON alone is not sufficient to adequately predict the HLL for refinery stream fuels in a HCCI engine. More comprehensive considerations of the fuel properties are necessary. There is also less variation in the HLLs with the high olefin fuels compared to the high aromatic fuels, particularly at higher speeds. Again, sufficient disparity in some of the HLL trends suggests that the composition of the fuels, in addition to the RON, must be considered in characterizing the high load HCCI limits.

As with the HLL, intuition leads one to believe that a fuel of lower RON, and thus more prone to auto-ignite, should have a reduced LLL as compared to higher RON fuels. For the most part, this is true in the case of both the high aromatic and high olefin fuels. Take for example C10 (a high aromatic fuel) and F10 (a high olefin fuel) in Figure 7.1 and Figure 7.2 respectively; both these lower RON fuels ran at the lowest loads across the speed range. However, as before with the HLLs, the RON is not the only factor involved in determining the limit of instability in the engine. The high aromatic fuel, D10, which has a RON of approximately 98, had the LLL comparable to that of B10, a fuel with a RON of about 88.5. Also, in considering the other three high olefin fuels (E10, G10, H10), the instability limits become similar at engine speeds greater than 1800 RPM, where LLLs for many fuels fall on top of each other, regardless of RON. One other item to note from Figure 7.1 and Figure 7.2 is the slight increase in both the LLL and HLL at 1800 RPM that is shown with all the fuels. Because this

behavior is shown with all the test fuel blends it is not caused by a characteristic of the fuels, but rather an artifact of the engine hardware. Because the engine for these experiments uses a high amount of exhaust residual to promote combustion, it can be highly sensitive to plenum dynamics in the exhaust, which is likely the cause for the slight rise in operating limits at 1800 RPM.

In summary, for the refinery stream fuels tested, it appears that operability limits cannot be determined as a simple function of RON. This is possibly due to dissimilar S between the fuels, which likely plays a role in overall operability range, as well as due to the impact of different chemical components of the fuels on reaction mechanisms.

The operating “area” of each fuel is computed in Figure 7.3 using a simple trapezoidal method, and then normalized to the calculated area of the baseline fuel, RD3-87. Essentially, the values of these bars can be pictured as a percentage gain in operating range the fuel enables versus RD3-87. The first interesting observation to take from this plot is the wide gap between some operating ranges of the fuels in the test matrix.

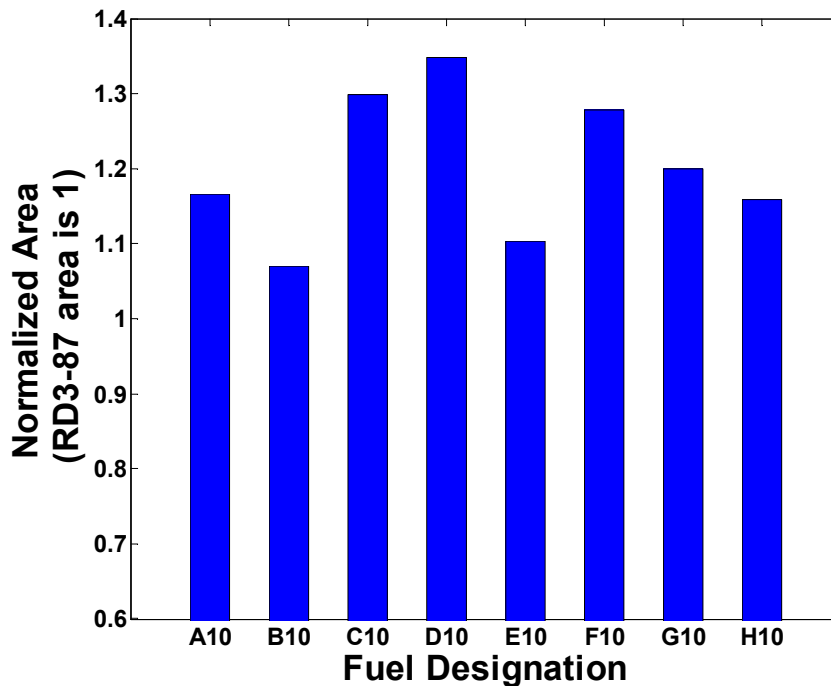


Figure 7.3 - Comparing the overall operating map area for the test matrix fuels, normalized to the area for RD3-87 (not shown in previous figures)

The fuels with higher aromatic content, C10 and D10, both of which have roughly 37% aromatics by volume, display an impressive increase in range as compared to the other fuels. The comparison of these operating range areas seems to be the most significant area where the sensitivity of a fuel has an impact. Increasing sensitivity for a given RON generally allows for an increased span of operation, as shown with the pairs of similar RON fuels A10 and D10, B10 and C10 and E10 and H10.

This is not always the case, as with F10 and G10, where F10 actually has a lower S but a larger operating range than G10. This could be related, in part, to the appreciable differences between the composition F10 and G10, as G10 has a substantially lower volumetric percentage of saturates than the other high olefin fuels. It

also highlights the fact that while RON and S are sufficient to give initial guidance pertaining to the expected relative HCCI range, fuel composition also plays a role in this complex interplay.

7.3 Variation in Limits with Engine Speed

Another method of characterizing the operating ranges for the refinery stream fuels is in Figure 7.4 (high aromatics) and Figure 7.5 (high olefins). At each engine speed, the data point for each fuel represents a difference in combustion phasing (given by CA50) between the HLL and LLL. Simply put, the CA50 at the LLL is subtracted from the CA50 of the HLL to provide insight into how much the combustion event changes in location from instability to excessive ringing.

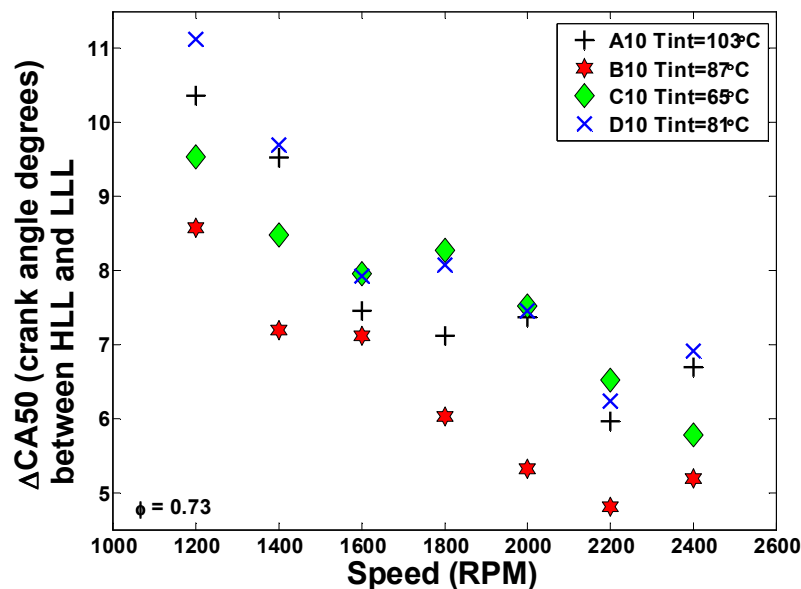


Figure 7.4 - Differences between CA50 at the HLL and LLL for fuels with high aromatics

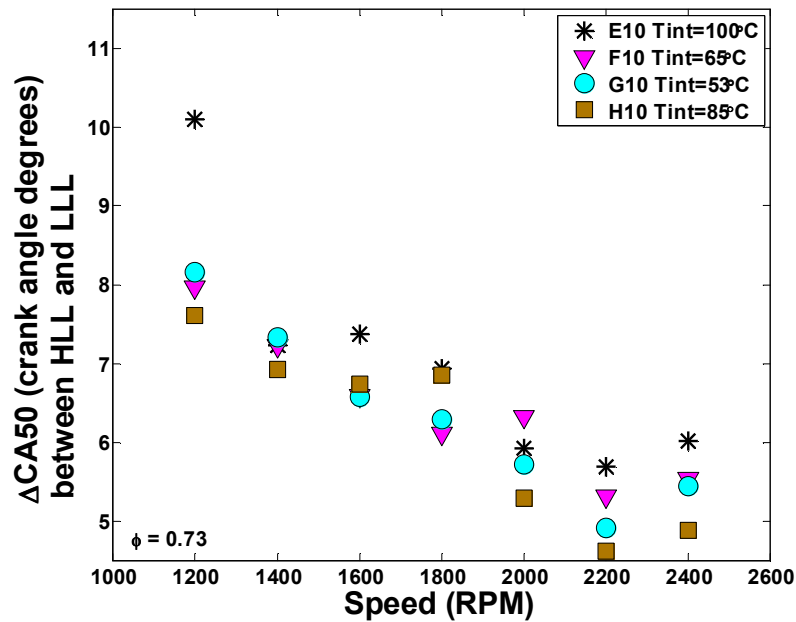


Figure 7.5 - Differences between the CA50 at the HLL and LLL for high olefin fuels

Perhaps the most obvious feature differentiating these two graphs is the relative “spread” in the data points between the fuels. Note that both of these figures are plotted on the same range of CAD on the y-axis. Across the speed range, the high aromatic fuels exhibit a larger variation in the combustion behaviors from LLL to HLL, as than the high olefin fuels. The relative locations of the high aromatics fuels’ curves are more spread apart from each other. In contrast, the high olefin fuels have a fairly tight distribution across the speed range, and this implies that similar combustion phasing change from LLL to HLL exists in the case of high olefin fuels. The high aromatic fuels, on the other hand, exhibit different behavior through the speed range, as there are often several CADs separating the HLL and LLL combustion phasing changes between fuels. This is likely due to the differences in auto-ignition chemistry that exists with aromatics, which are substantially more complex than those of olefins.

Another point to take from these results is the rate at which the CA50 differences drop with increasing speed, given by the slopes of the curves in Figure 7.4 and Figure 7.5. As the HCCI range of operability generally decreases with speed because of HCCI load limitations, we expect that the difference between the LLL and HLL will decrease, resulting in the negative slope of the curves. However, the slopes of the curves for the high aromatic fuels, in general, have a steeper slope across the speed range, as the change in CA50 is relatively higher at the lower speeds than those of the high olefin fuels. This suggests that as speed is decreased, the fuels with higher aromatic content will undergo more change in the location of the combustion event as load is varied. Another manner to consider the effect of compositional differences in Figure 7.4 and Figure 7.5 is to look at the highest and lowest Δ CA50 for each fuel. For the high aromatic fuels this ranges from roughly 4-5 degrees, whereas for the high olefin fuels it is approximately 3-4 degrees, with F10, G10 and H10 at nearly 3 degrees. Larger swings in the location of combustion phasing have implications for engine control. The more olefinic fuels, that naturally display less overall CA50 sensitivity with load changes over a sweep of speed, would reduce the controller effort. However, as shown previously, highly aromatic fuels have the largest range of operation in the HCCI engine, so there is an opportunity to work on an optimum tradeoff between the two prevailing chemistries.

To reiterate a previous point, the CA50 differences for the curves in Figure 7.4 and Figure 7.5 decrease with speed, although there are some notable exceptions to this trend, particularly at the highest speed for these sweeps, 2400 RPM. This is primarily attributable to a phenomenon that is further explored in the following section, and in

Figure 7.6. At the highest engine speed, while the CA50 of the LLL stays relatively constant from previous speeds, the HLL CA50 begins to become more advanced as the combustion event becomes faster. This results in an increased difference in the LLL and HLL CA50 values, shown as a slight increase from 2200 to 2400 RPM in the curves of Figure 7.4 and Figure 7.5. Some other fuels have small increases in Δ CA50 at lower speeds such as 1800 RPM, and as before, when considering the limits, this is likely due in part to the exhaust plenum dynamics observed at this engine speed.

7.4 Heat Release Analysis of HCCI Operating Limits

To further supplement the characterization of the HCCI combustion event at the limits for the refinery stream fuels, additional heat release analysis is performed in the following graphs. Figure 7.6 and Figure 7.7 show different sets of burn duration data for the LLLs and HLLs of the limits sweep for the fuels shown previously in Figure 7.1 and Figure 7.2. Figure 7.6 shows the CA50, while Figure 7.7 contains the main combustion event burn duration (CA10-CA90). In these plots, the lower load limit points are near the top of the plot, due to the longer crank angle durations (the combustion event is much slower at the LLL, so burn durations are longer), and the high load limits are at the bottom of the figure. The major highlight of these two plots is the contrast of combustion behavior at the LLL and HLL for all the test matrix fuels. At the HLL, the combustion phasing given by CA50 displays a certain level of scatter across the matrix of fuels, as shown in Figure 7.6. In contrast, the CA10-CA90 burn duration for all the fuels at HLL is remarkably similar across the speed range, as shown by Figure 7.7.

The story for the LLL is quite different, as there are noticeable variations in the CA10-CA90 burn duration among the fuels. In fact, most of the spread in the LLL burn lengths is attributable to the high aromatic fuels (A10 through D10), as the high olefin fuels (E10 through H10) are quite similar through the speed sweep.

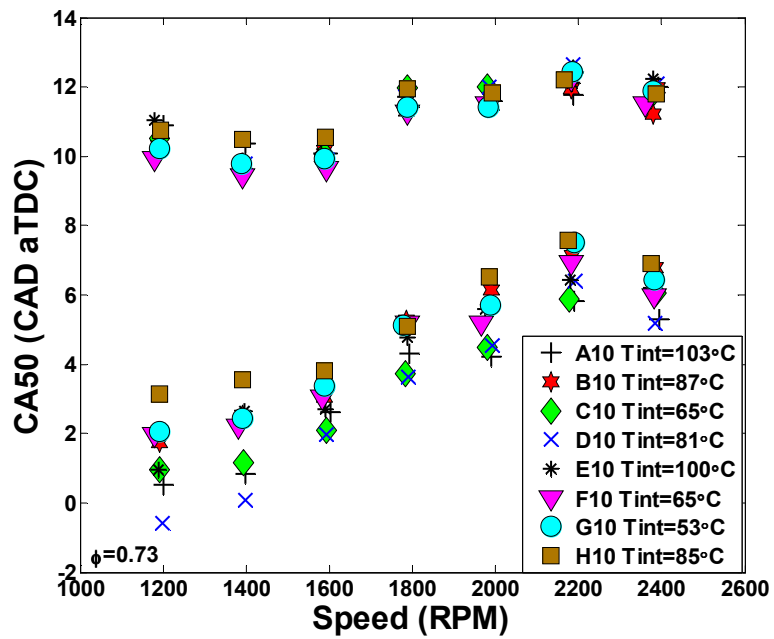


Figure 7.6 - CA50 for the lower and upper limits of the operating range sweep

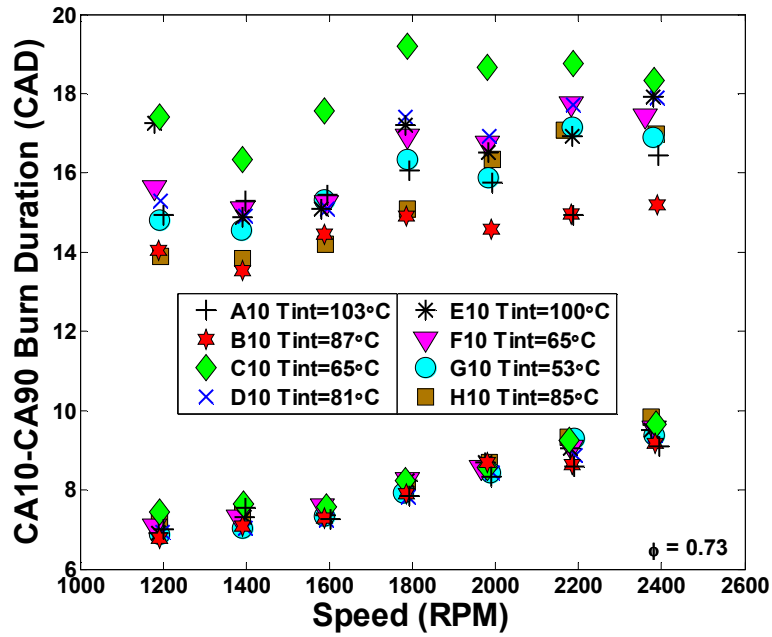


Figure 7.7 - CA10-CA90 burn durations for the limits of operability sweep for all the test matrix fuels

To provide additional insight, the discrepancy between the behaviors of the refinery stream fuels with respect to the LLL and HLLs is visualized in an alternative manner in Figure 7.8 and Figure 7.9. Here, the burn durations for all the LLL and HLLs are plotted against engine load on the abscissa, forming two clusters of points with LLLs in the upper left corner, and HLLs grouped in the lower right of each plot.

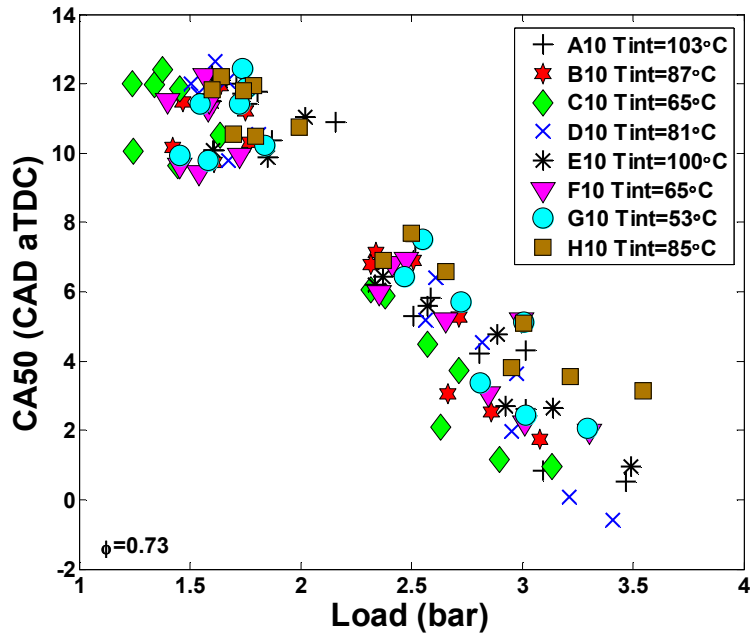


Figure 7.8 - CA50 versus engine load for all the LLL and HLL points with each refinery stream fuel

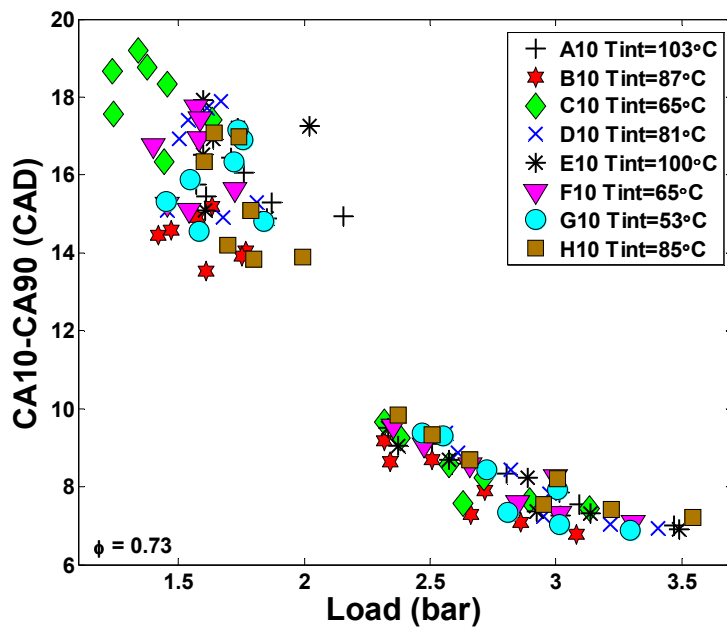


Figure 7.9 - CA10-CA90 burn durations against engine load for the operating range sweep of all the test matrix fuels

In Figure 7.8, there is a much closer spread of CA50 points over the range of loads at the LLLs than at the HLLs. In contrast, the group of HLL points is closely clustered in Figure 7.9, and there is less change in the burn duration over the load range at the HLL as compared to the LLL. This contrasting combustion behavior matches with what is shown in Figure 7.6 and Figure 7.7 with engine speed. Thus, the fuel composition impacts the HCCI combustion event at the limits; the behavior of highly aromatic fuels compared to highly olefinic is different, and the extent of that impact varies depending on whether the engine is close to misfire or at the ringing limit.

To gain more insight into some of the observations from the previous figures, consider the following heat release profiles. Figure 7.10 shows the Net Heat Release Rate (NHRR) for all the fuels' LLL at a single speed, 1600 RPM. The HLLs are shown at the same engine speed in Figure 7.11. At the instability limit, the curves for the fuels that ran at lower engine loads flatten, although the peaks of the NHRR curves occur at similar crank angle locations. As mentioned, the combustion phasing of the LLLs are quite similar, but the burn durations vary considerably and obviously impact the shape of the NHRR profiles.

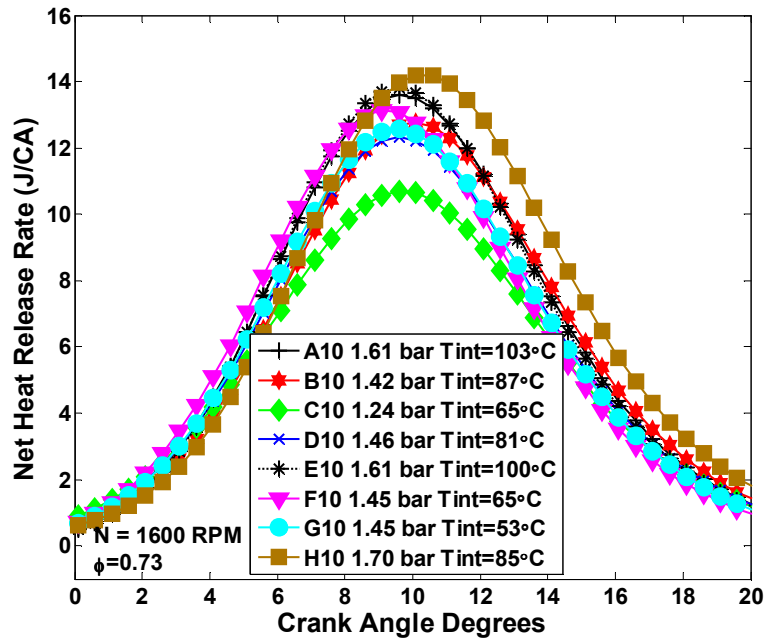


Figure 7.10 - Net heat release rates in the instability limit for all test matrix fuels at 1600 RPM; the engine loads (BMEP) for each of these points is listed in the legend

For the HLLs at 1600 RPM in Figure 7.11, the opposite type of effect is apparent; the peaks of the NHRR curves are different for each test fuel, while the shapes of the curves are now remarkably similar. In other words, the combustion phasing at the ringing limit is different among the fuels tested, but the overall CA10-CA90 burn durations are nearly the same. Another point to note from these figures is that the overall NHRRs at the HLL are much higher than those at the LLL, which is to be expected, as in-cylinder temperatures are much lower at the instability limit.

While differences in the fuels' properties and chemical components limit the engine loads that can be achieved before excessive ringing occurs, they do not play as large a role in the length of the main burn event, which is nearly the same for all the

fuels, at each engine speed tested. Clearly the ringing intensity is closely tied to the burn rate profiles. However, at the low end of the operating map, different fuel composition seems to impact the burn time of the combustion event more significantly, whereas combustion phasing changes little for each fuel at each speed.

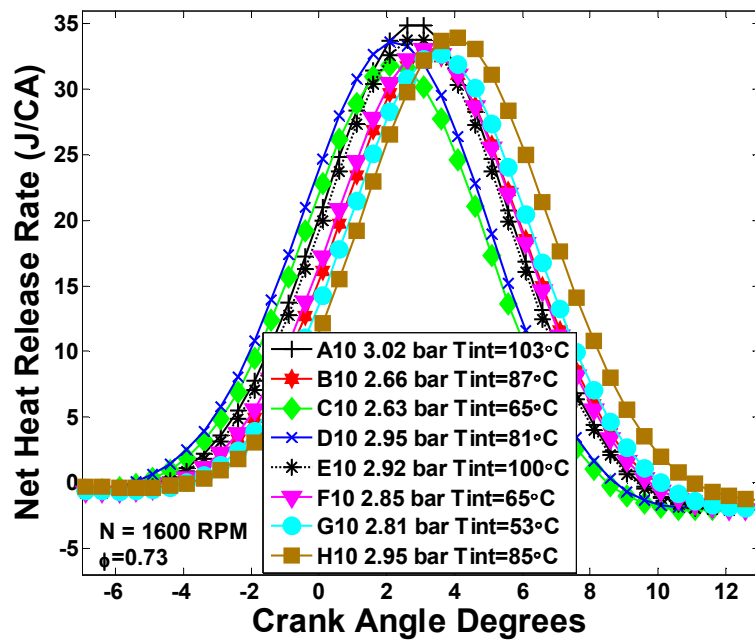


Figure 7.11 - Net heat release rates in the ringing limit for all test matrix fuels at 1600 RPM; as with the previous figure, the BMEP for each point is given in the legend for each point

CHAPTER 8

Effects of Ethanol Addition on HCCI Combustion

8.1 Introduction

In many areas of the United States, pump gasoline contains up to 10% ethanol by volume, and discussions in recent years have proposed increasing this concentration even further [162]. This chapter discusses the possible ramifications of ethanol addition into refinery stream fuels, as it relates to HCCI combustion.

8.2 Load Sweeps with Matched Combustion Phasing

The load sweeps with intake air temperature compensation for the 20% ethanol fuels and 10% ethanol fuels are displayed in Figure 8.1 and Figure 8.2, respectively. There are a few key observations revealed by comparing the two sets of fuels.

The obvious difference in the two sets of fuels is the position of the curves in the plots. Notice that the intake temperature scale is much smaller for the 20% ethanol fuels than for the 10% ethanol fuels. The position of these curves relative to one another is based upon the reference temperature of each fuel, from Table 5.2. For the 20% ethanol fuels, the baseline temperature ranges only 8°C, from 52°C to 60°C. In the

case of the lower content ethanol fuels, this range is substantially larger, encompassing a separation of 24°C, from 53°C to 87°C. This is an interesting discovery, as even though the overall chemical makeup of the 20% ethanol fuels varies considerably, as illustrated by the volumetric fractions of aromatics and olefins in Table 5.1, the fuels have similar ignition characteristics (as evident from the small range in reference temperatures) and the fuels all require similar intake air temperatures to maintain constant combustion phasing over the same range of load. The 10% ethanol fuels exhibit a more significant departure in behavior, suggesting that the addition of ethanol to the refinery stream fuels is masking the effects of the other competing chemical components (aromatics and olefins).

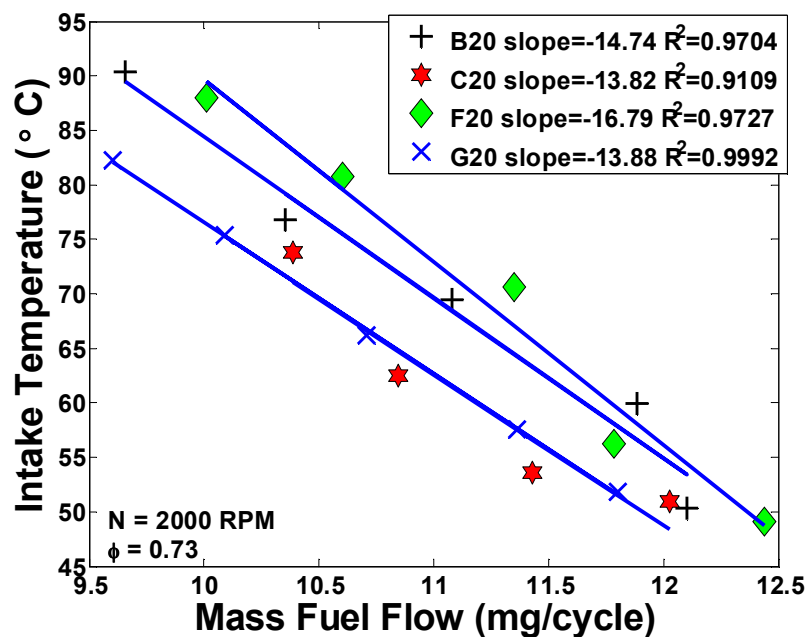


Figure 8.1 - Intake air temperature compensation required to maintain constant combustion phasing over a range of engine loads – 20% ethanol fuels

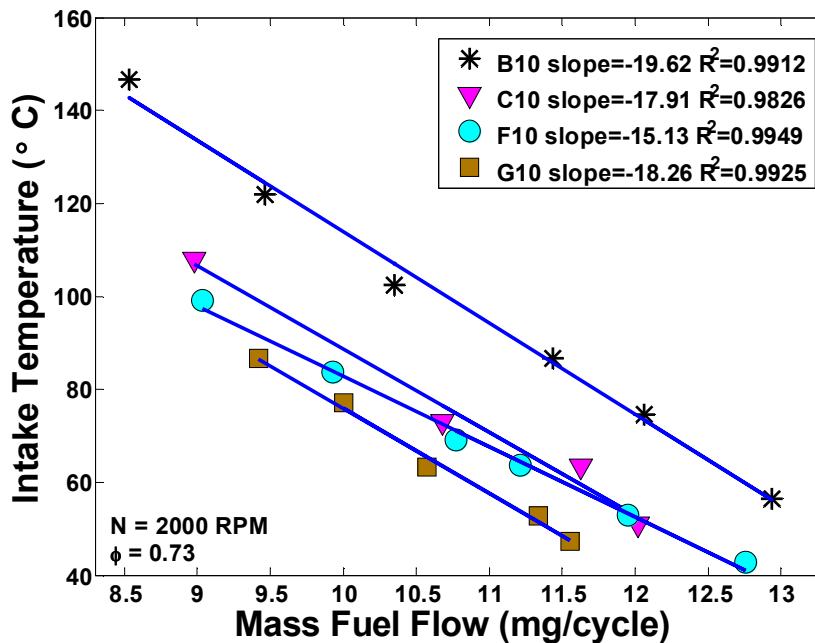


Figure 8.2 - Intake air temperature compensation required to maintain constant combustion phasing over a range of engine loads – 10% ethanol fuels

Further corroboration of this theory is found by considering the slopes of the curves in Figure 8.1 and Figure 8.2, which represent the rates of temperature compensation needed to maintain constant CA50. The relevant information from Figure 8.1 and Figure 8.2 is summarized in a more convenient format in Table 8.1, to highlight how the rate of temperature compensation differs as S (RON-MON) and fuel composition change.

For the fuels in this study, an increase in S between two fuels requires an increase in fuel components that have a sensitivity ($S > 0$) between the RON and MON tests, e.g. aromatics and olefins. The more prevalent chemical components, visible in the bolded volumetric fractions in Table 8.1, rise as the S is increases for a pair of fuels. The trend of intake air temperature compensation rate (slope) is different when

considering the 10% and the 20% ethanol fuels. For the lower ethanol fuels, when the amount of aromatics is increased to elevate S (going from B10 to C10) the rate of intake temperature compensation decreases (shown as a less negative slope). The opposite is true when going from F10 to G10, where additional olefin content is added to increase S. Between these two fuels, the rate of intake air temperature compensation increases, as shown by the more negative slope of G10 as compared to the slope of F10.

Table 8.1 - A summary of the rates of intake temperature compensation from Figures 8.1 and 8.2; here, the “dominant” chemical component is bolded, whether the fuel was a high aromatic fuel, or a high olefin fuel

Fuel	S	A (%vol/vol)	O (%vol/vol)	Slope (°C/mg/cycle)
B10	6.4	23.8	0.9	-19.62
C10	8.6	37.2	4.2	-17.91
F10	8.2	3.6	11.7	-15.13
G10	10.4	11.2	22.3	-18.26
B20	7.8	15.9	1.7	-14.74
C20	8.8	28.5	4.3	-13.82
F20	8.5	4.1	11.1	-16.79
G20	10.7	7.0	18.7	-13.88

This contrasting behavior is not present with the higher ethanol fuels, as both the high aromatic (B20 and C20) and high olefin fuels (F20 and G20) with 20% ethanol require lower rates of intake air temperature compensation as S increases. Again, as the positioning of the compensated load curves and baseline temperatures is similar for the 20% ethanol fuels, it appears that the additional ethanol content is screening some of the differences that were present in the lower ethanol content refinery stream fuels.

Further analysis of the compensated load sweeps provides detail regarding the specific fuel consumption of the refinery stream fuels. Using previously collected data for the baseline fuel, RD3-87, an indicated load curve was generated against ISFC. Using the LHV information from Table 5.2, a relatively straightforward approach was used to calculate a predicted ISFC for the test matrix fuels, based solely on the difference in LHV from that of RD3-87. This relationship is displayed below in Equation 8.1; this is the same analysis that was used in Chapter 6 for predicted ISFC trends.

$$ISFC_{\text{fuel, predicted}} = ISFC_{\text{RD3-87}} * \left(1 - \left(\frac{LHV_{\text{fuel}} - LHV_{\text{RD3-87}}}{LHV_{\text{RD3-87}}} \right) \right) \quad (8.1)$$

In Figure 8.3 and Figure 8.4, the predicted trend lines, based solely on LHV differences, are displayed alongside the experimentally measured operating points. The 20% and 10% ethanol fuels are each grouped separately in these plots, and graphed against the same scale (although, not over the same range) on the abscissa to facilitate easy comparison.

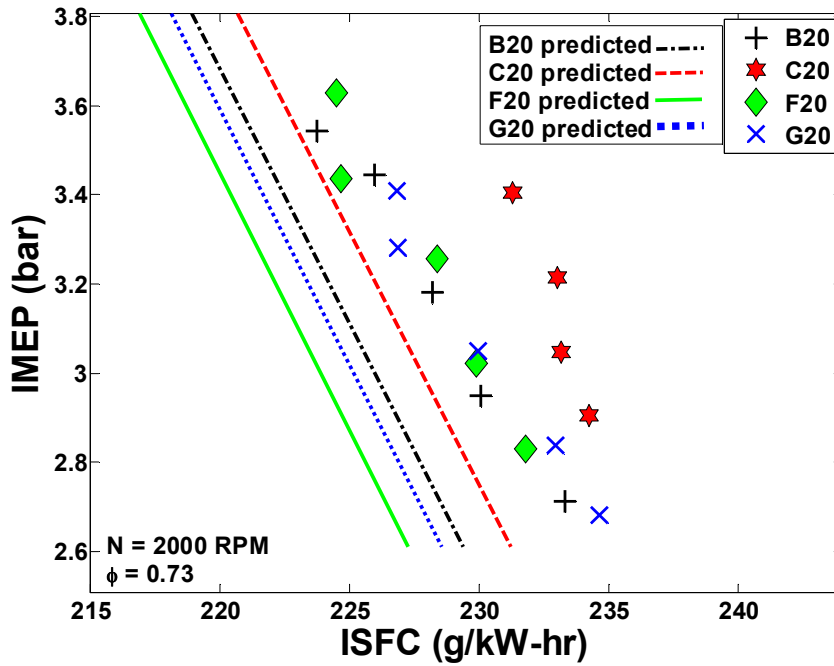


Figure 8.3 - Indicated Mean Effective Pressure vs. Indicated Specific Fuel Consumption on a mass basis for the 20% ethanol fuels; measured points and predicted trend lines

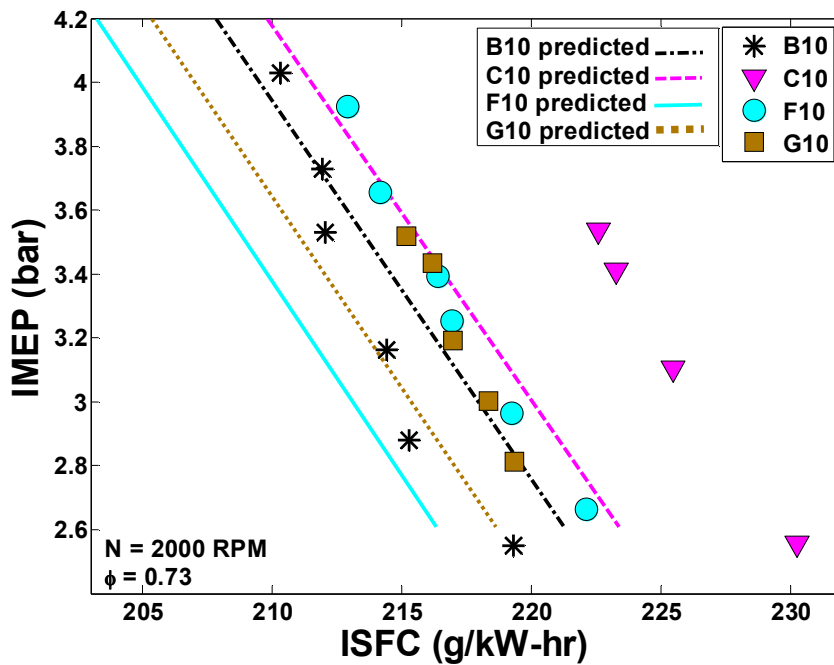


Figure 8.4 - Indicated Mean Effective Pressure vs. Indicated Specific Fuel Consumption on a mass basis for the 10% ethanol fuels; measured points and predicted trend lines

Of chief importance is the relative location of the curves to one another. For the higher ethanol fuels, the ISFC behavior is fairly similar between the four fuels over the sweep of engine load. In fact B20, F20 and G20 nearly lie on top of one another. The 10% ethanol fuels have more overall spread in fuel efficiency between test fuels. And while both sets of fuels have a similar change in ISFC over the range of engine loads shown (given as the slope of the curves in Figure 8.3 and Figure 8.4), the overall specific fuel consumption is more favorable in the case of the 10% ethanol fuels. This is as expected, since the fuels with 20% ethanol by volume contain lower energy content and require more fuel mass to achieve similar loads as the 10% ethanol fuels. However, both sets of experimentally measured data for the different ethanol blends show a departure from the trend lines established only on LHV dissimilarities.

One additional plot characterizing fuel efficiency is found in Figure 8.5. Here, rather than use ISFC on a mass basis, the indicated engine load is displayed against ISFC on a volume basis, as gasoline is sold at the pump by volume, and not by mass.

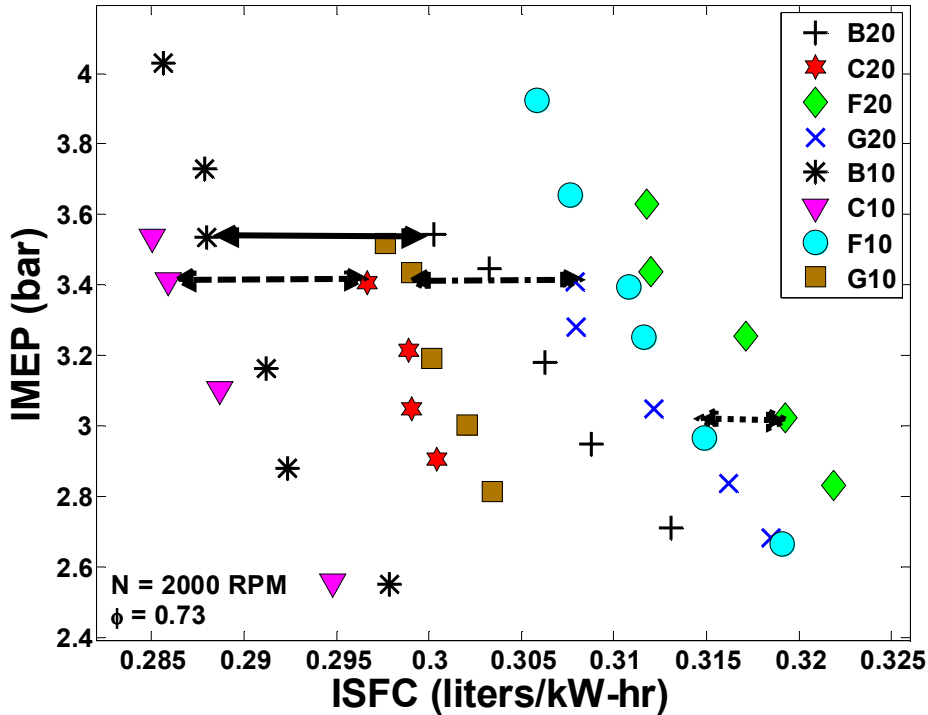


Figure 8.5 - Indicated Mean Effective Pressure vs. Indicated Specific Fuel Consumption on a volumetric basis; this is a better representation of a fuel efficiency that consumers would realize, because gasoline is sold by volume and not by mass. The arrows in the plot connect pairs of similar fuels that differ chiefly by ethanol content, e.g. B10 and B20

As with the previous ISFC figures, the 10% ethanol fuels are shifted towards more favorable ISFC ranges for the sweep of engine load. Also, fuels of higher density, namely those of higher aromatic content, have better ISFC values among both the 10% and 20% ethanol fuels. The arrows in Figure 8.5 are drawn between pairs of data sets representing two fuels of similar chemical composition but different concentrations of ethanol, such as B10 and B20. These arrows highlight the fuel consumption penalty inherent in the addition of ethanol, when many other properties of the fuel remain the same. And while the relative loss of specific fuel consumption is nearly the same

between B10/B20, C10/C20 and G10/G20, it is much smaller between F10 and F20. This may be attributable to the manner in which the fuel blends were created, transitioning from a 10% to a 20% ethanol blend. In the case of B10/B20, C10/C20 and G10/G20, the volume percentages of olefins and aromatics is reduced to accommodate the increased amount of ethanol. However, in the case of the F10/F20 pair the volumetric content of olefins and aromatics remains almost the same, and instead, in going from a 10% to 20% ethanol blend the percentage of saturates is reduced. This compositional trade-off, results in a larger percentage difference in density going from F10 to F20 as opposed to the other fuels pairs – see Table 8.2. Though the addition of ethanol in F20 results in higher ISFCs for the same load, the relative amount the ISFC curve shifts to the right from F10 in, Figure 8.5, is somewhat offset by a large increase in density, which shifts the ISFC curves to lower values (to the left). In short, the smaller gap between F10 and F20 as compared to the other fuel pairs is due to a larger disparity in density.

Table 8.2: Change in density between 10% and 20% ethanol fuel pairs

Fuel Pair	% Difference in Density
B10/B20	1.20
C10/C20	-0.18
F10/F20	3.50
G10/G20	1.91

A previous study with some of the same refinery stream fuels [163] demonstrated that the spread in fuel efficiencies and departure from the predicted trend lines of Figure 8.3 and Figure 8.4 is due mainly to thermodynamic differences between the fuel, though

experimental error in the measurement methods used to quantify LHV is also a contributing factor. It was also concluded that differences in the combustion event between the fuels were minimal, and that this was not a contributing factor to the discrepancies in specific fuel consumption values. This observation is reiterated by now including data from the 20% ethanol fuels, as shown in Figure 8.6.

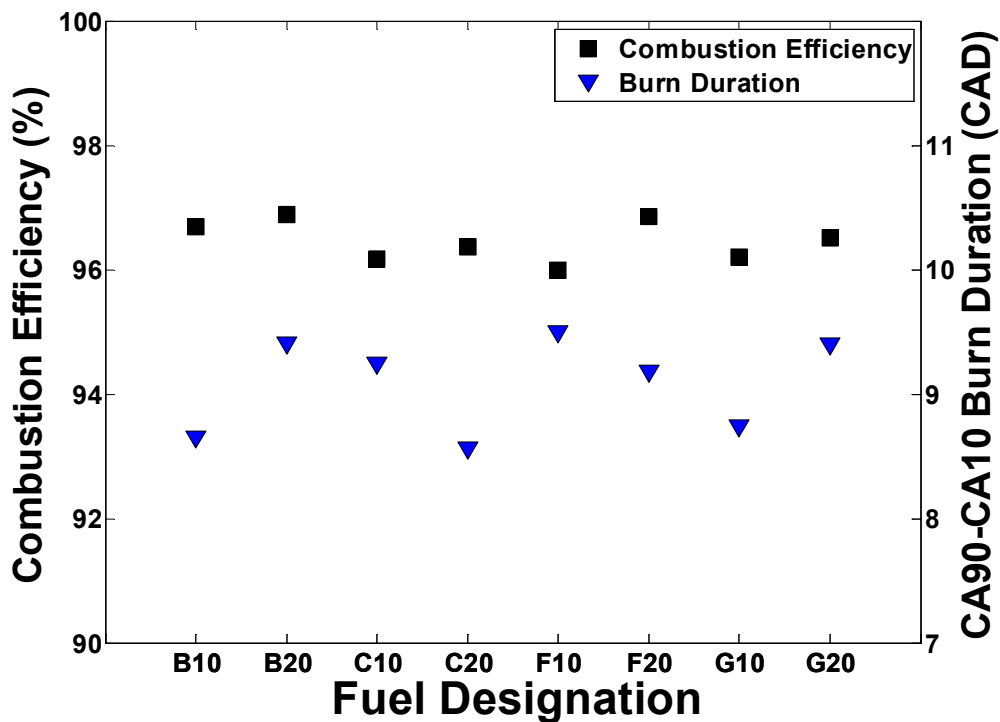


Figure 8.6 - Combustion efficiency and CA10-CA90 burn duration determined at the baseline operating points for the 20% ethanol fuels

This figure shows the baseline points for each fuel from the refinery stream test matrix, which correspond to an engine load of approximately 3.4 bar IMEP. All of these points have the same combustion phasing (CA50 ~6.5 CAD aTDC) and what is shown is that despite significant differences in chemical composition, with matched injected

fuel energy and phasing, the combustion event is remarkably similar. All the fuels have a roughly 96-97% combustion efficiency and a main combustion event burn length of roughly 9 CAD, indicating that the dissimilarities in chemical makeup, even between 10% and 20% ethanol blends, do not play a significant role in the combustion event itself nor do they contribute to the efficiency differences shown previously.

8.3 HCCI Limits of Operability

Despite the disadvantages in regards to specific fuel consumption, ethanol addition to gasoline often helps to run at higher loads, due to its high RON and auto-ignition resistance [164, 165]. Figure 8.7 shows the 20% ethanol fuels, which have almost equivalent RONs, but have different operating ranges from the LLL to HLL.

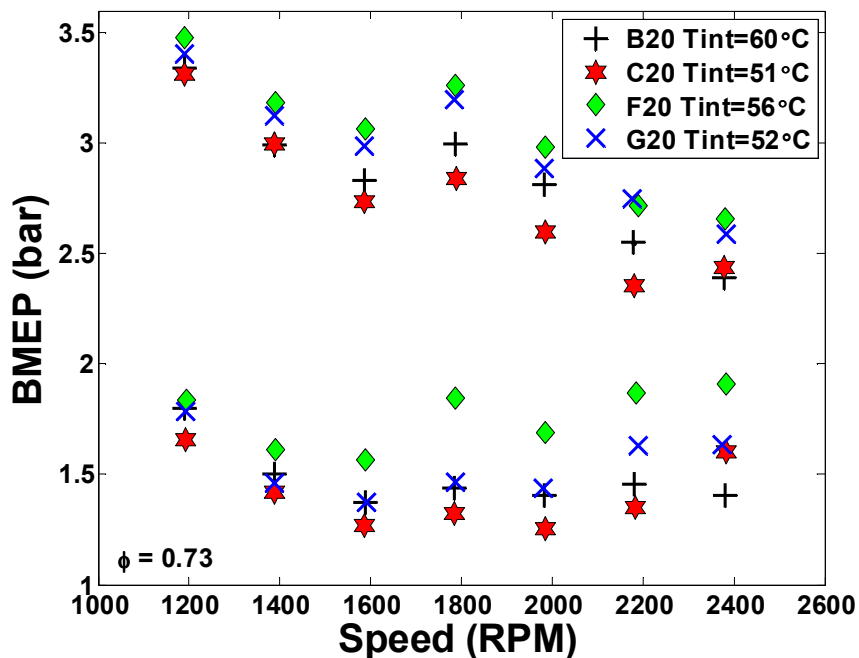


Figure 8.7 - HCCI operating limits for the 20% ethanol fuels over the speed sweep

It is clear that RON is not the only determining factor in where the loads at the instability limit and the point of excessive ringing occur. In fact, it might be practical to theorize that the fuels with higher LLLs and HLLs have a higher percentage of components that can resist auto-ignition; the converse to this is that fuels with lower LLLs and HLLs have a lower relative percentage of components that hinder auto-ignition. To isolate the effects of the higher ethanol content of these four refinery stream blends, the following four figures show the 20% ethanol fuel's operating range against its 10% ethanol counterpart.

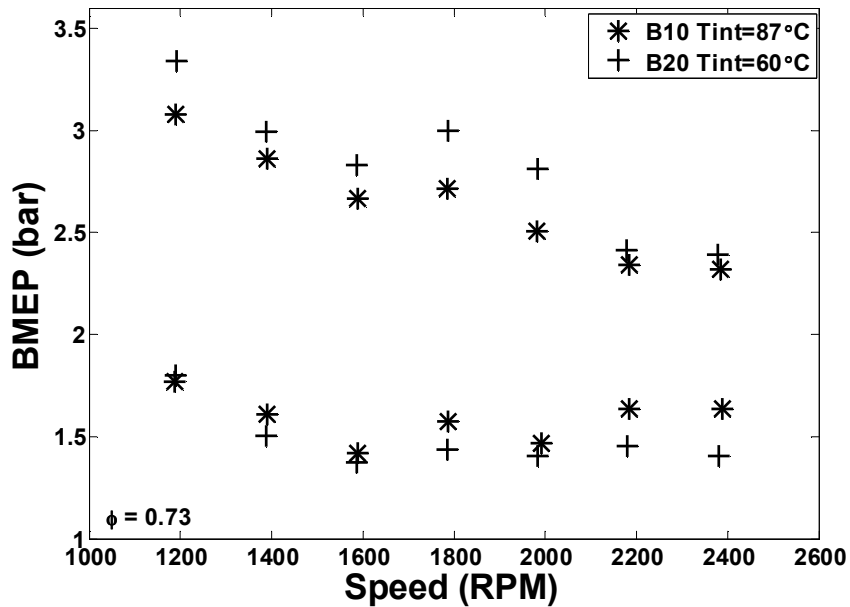


Figure 8.8 - Comparison of the HCCI operating limits of B10 and B20 over a sweep of speed

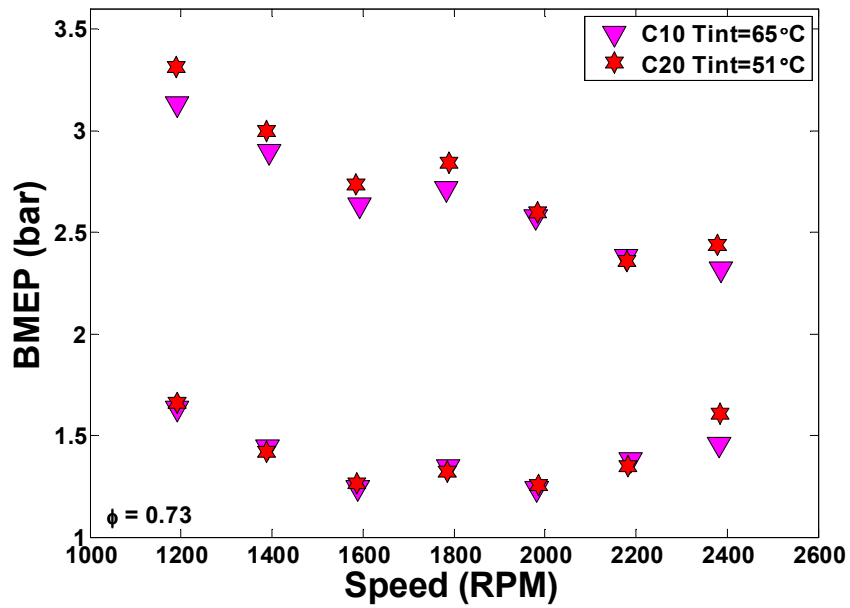


Figure 8.9 – Comparison of the HCCI operating limits of C10 and C20 over a sweep of speed

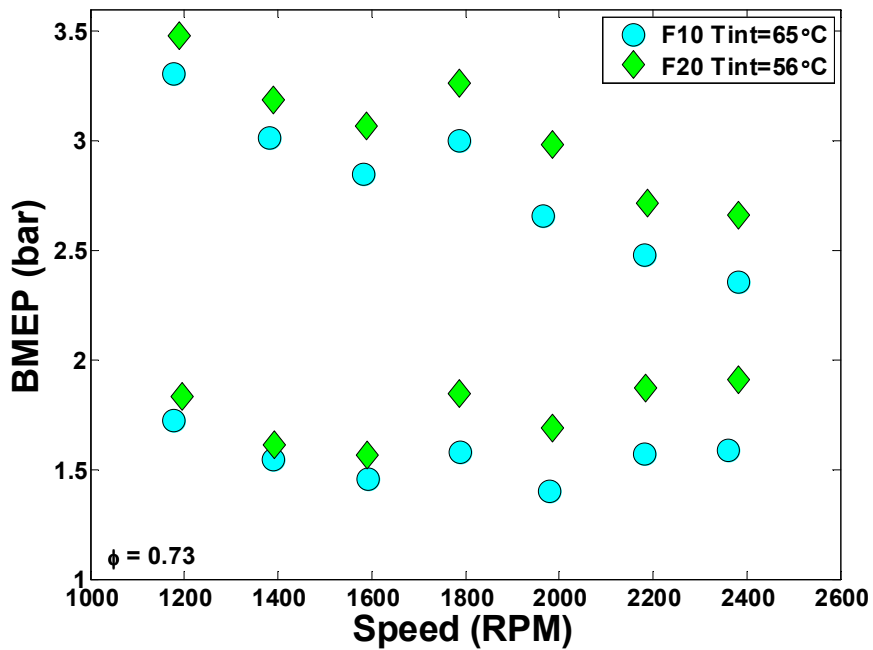


Figure 8.10 – Comparison of the HCCI operating limits for F10 and F20 over a sweep of speed

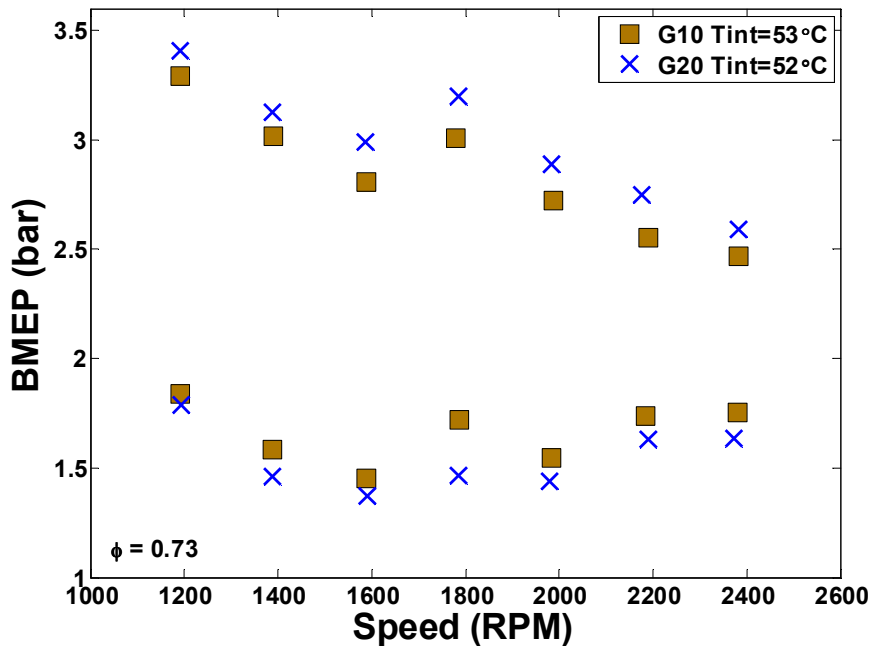


Figure 8.11 - Comparison of the HCCI operating limits of G10 and G20 over a sweep of engine speeds

The common trend shown with the 20% ethanol fuels is the benefit gained at the upper load limit across the speed range. At every speed point, the 20% ethanol fuel is able to operate at, at least the same load as its 10% ethanol counterpart, and in the vast majority of cases, at a higher load. This observation is consistent with the knowledge that ethanol is an auto-ignition inhibitor, and thus, the inclusion of additional ethanol content in a refinery stream fuel should allow higher loads to be reached before the ringing limit is hit.

At the LLL, the behavior of the higher concentration ethanol fuels is not so well-defined. In some cases, the LLL of the higher ethanol blend closely mirrors that of the lower ethanol blend, as shown in Figure 8.9 by C10 and C20. In other cases, it is possible to achieve reduced LLLs with the higher ethanol content, as in Figure 8.8 and Figure 8.11. With F10 and F20 in Figure 8.10 a third scenario is encountered, where

the lower ethanol blend (F10) is able to run at lower loads throughout the speed range before the instability limit occurs. Recall that between the 10% and 20% ethanol blends, concentrations of aromatics and olefins remain the same with the addition of ethanol, except in the case of F10 and F20 – see Table 5.1. F10 and F20 may represent a more “pure” effect of the addition of ethanol, as the other fuel components with $S>0$ (aromatics and olefins) remain largely unchanged. The entire operating map shifts up towards higher loads when going from F10 to F20. With the other three pairs of fuels, there are more complex interactions between the fuel components and the increased ethanol, which impacts the LLL. B20, C20 and G20 all have lower aromatic content than B10, C10 and G10. Considering that aromatic components are generally of high RON and resistant to auto-ignition, it is not unreasonable to postulate that the reduction of aromatics (causing a fuel to be more prone to auto-ignition) in the higher ethanol fuels is sufficient to offset some of the knock resistance provided by the increased ethanol content in the 20% blends. However, this behavior does not manifest itself at the high load limit, as the effects from the additional ethanol seem to dominate over the reduced aromatics, leading to auto-ignition inhibition which allows for higher loads over the 10% ethanol blends. This difference in interplay between the kinetics of the different refinery stream components could be related to fundamental differences in the HCCI process at the limits, because while at the LLL combustion approaches the lower bound of requisite thermal energy to continue, at the HLL there is an issue of the kinetics happening too quickly.

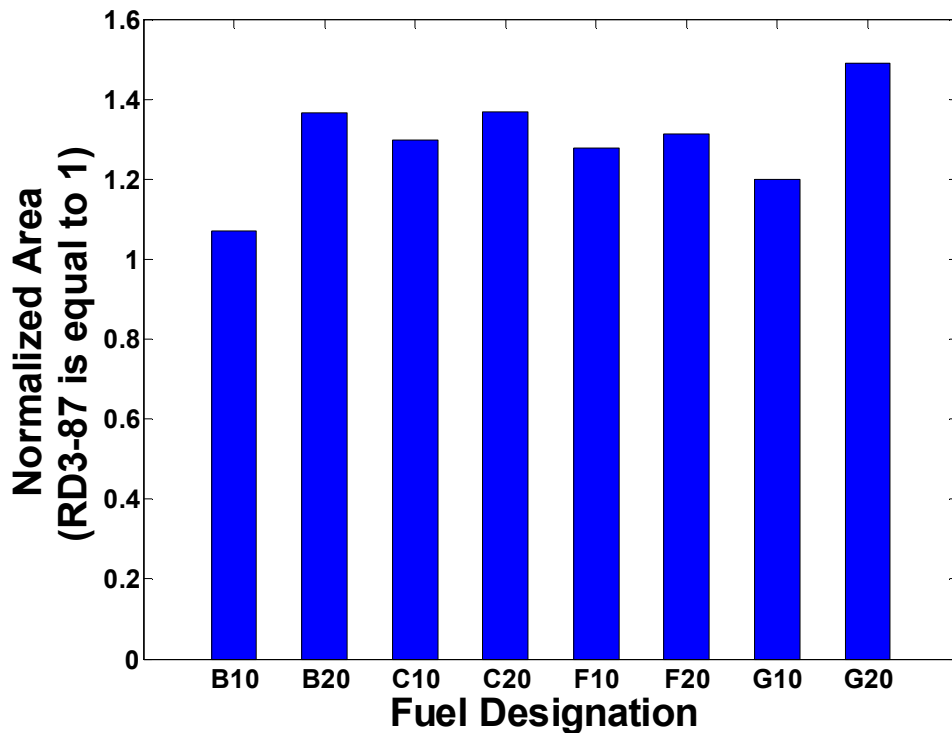


Figure 8.12 - Normalized HCCI operating range area of all the 10% and 20% ethanol fuels, where the previously calculated area of the baseline fuel RD3-87 is equivalent to 1 (not shown); essentially, this represents a percent improvement of each fuel's operating range over the range of RD3-87

The effects of ethanol addition extend not only to the load locations of the LLL and HLL, but also to the overall area of the HCCI operating range, as shown in Figure 8.12. In every case, the operating range of the 20% ethanol blend was greater than that of the 10% blend, though the extent of the increase varied depending on the fuel pair, i.e. between B10 and B20. In the case of F10 and F20, where previously it was shown in Figure 8.10 that the operating map simply shifts up, we now see the least amount of change in the operating range area going from F10 to F20. For some of the 10%/20% ethanol pairs the change was much more significant, with nearly 25% improvement in the operating area between B10 and B20, as well as G10 and G20. In short, the

addition of ethanol helps to increase the overall range of the HCCI map, though the extent to which the size of the map increases relies on how the relative amount of other refinery stream components changes with ethanol addition.

In addition to ethanol's effects on the HCCI operating limits and range, are its effects on combustion phasing when running a limits sweep. Figure 8.13 and Figure 8.14 show the 20% and 10% ethanol fuels separated out from one another, and display the change in combustion phasing given by the difference of CA50 at each speed progressing from the LLL to the HLL.

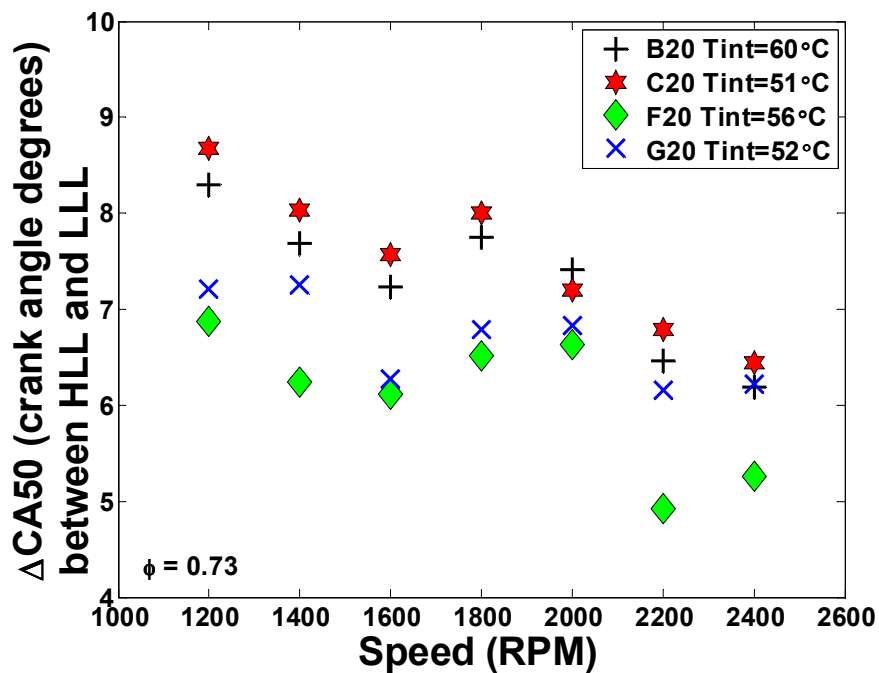


Figure 8.13 - Differences in combustion phasing, given by CA50, between the HLL and LLL across the speed range for all 20% ethanol fuels

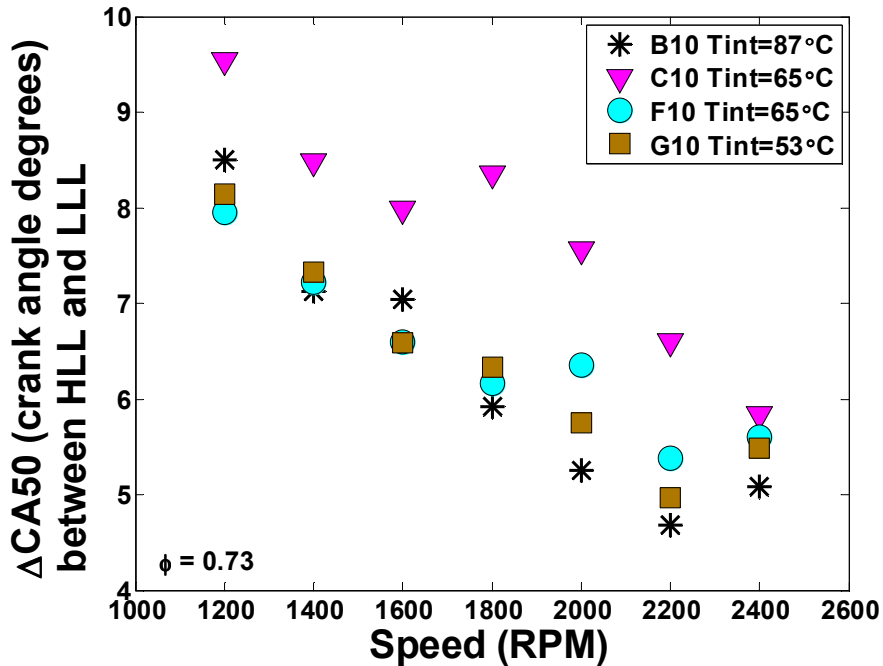


Figure 8.14 - Changes in combustion phasing over the speed sweep, given as the difference in CA50 at the HLL and LLL, for the 10% ethanol fuels

On examination of these two plots, it becomes apparent that the higher content ethanol fuels exhibit less change in phasing differences across the speed range, visible as a shallower slope for the 20% ethanol fuels' curves as opposed to those of the 10% ethanol fuels. Another way to visualize this concept is using Table 8.3, which takes the difference between the maximum and minimum values for each fuel data set in Figure 8.12 and Figure 8.13 as a way to compare the maximum amount of deviation in $\Delta CA50$ from the LLL to HLL across the entire sweep of speed. All the 10% ethanol blends are arranged on the top rows of Table 8.3 and the 20% blends are on the bottom. Despite the fact that the higher ethanol blends have greater areas of load range, as demonstrated in Figure 8.12, they display less variation of $\Delta CA50$ than the 10% ethanol fuels. This reinforces the previous discussion of the compensated load sweeps, where

in several respects the ethanol addition attenuates some of the differences in operation between the 10% refinery stream blends. In this particular case, while the overall range between the LLL and HLL change as speed varies, the increased ethanol content reduces the amount of change in combustion phasing with speed.

Table 8.3 - Differences between the maximum and minimum $\Delta CA50$ for a given fuel in Figures 8.13 and 8.14

Fuel	Max $\Delta CA50$-Min $\Delta CA50$
B10	3.4
C10	3.7
F10	2.4
G10	3.2
B20	2.1
C20	2.2
F20	1.0
G20	1.0

8.4 Sensitivity to Intake Air Temperature

In order to determine the HCCI combustion sensitivity for different fuel compositions to a wide range of charge temperatures, intake air temperature sweeps were conducted. In Figure 8.15 and Figure 8.16 the combustion phasing for each fuel is plotted versus the intake air temperature; several operating points of similar intake temperature are highlighted in rectangular boxes to provide a simple qualitative comparison between the 20% ethanol blends in Figure 8.15 and the 10% ethanol blends in Figure 8.16.

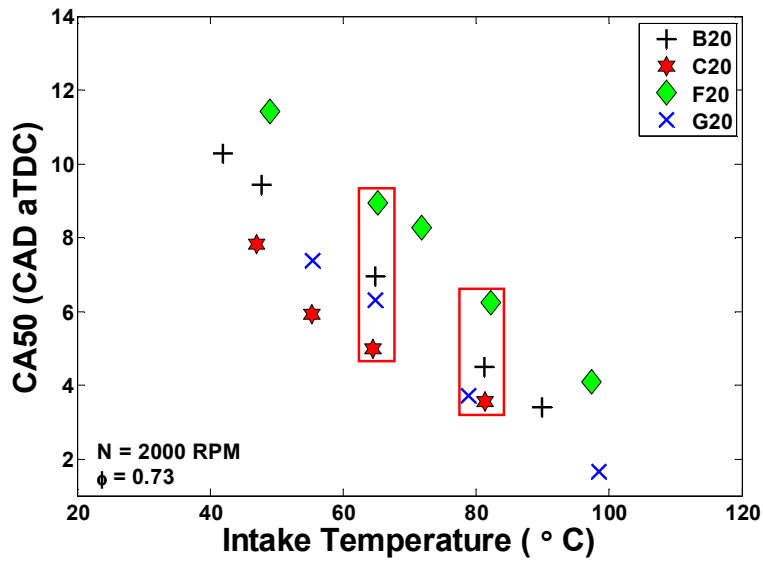


Figure 8.15 - CA50 against intake air temperature sweep at constant fuelling rate for the 20% ethanol fuels

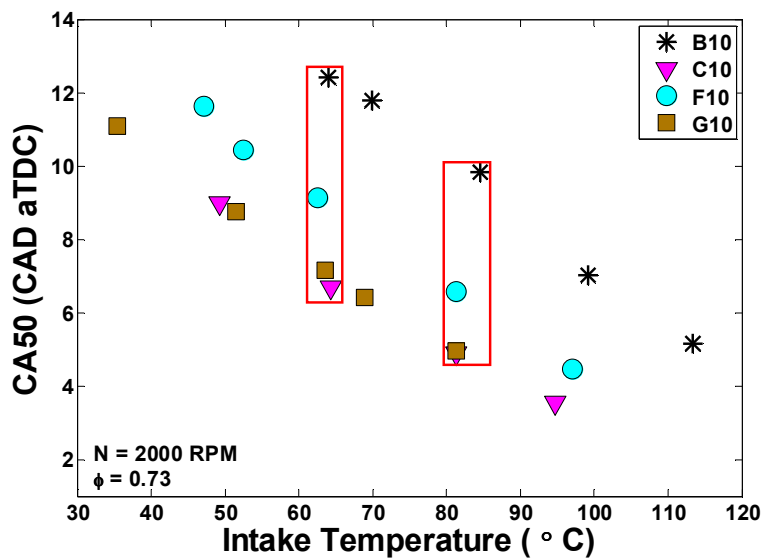


Figure 8.16. CA50 against intake air temperature sweep at constant fuelling rate for the 10% ethanol fuels

The key difference between the fuels of dissimilar ethanol content is the amount of dissimilarity in combustion phasing at similar intake air temperatures. Qualitatively,

the rectangular boxes in Figure 8.15 are smaller in height than those of Figure 8.16, both of which are plotted on the same scale, indicating that at the same intake air temperature, the group of fuels with higher ethanol content display less dissimilarity in CA50 as opposed to those with lower amounts of ethanol. As witnessed with the previous experiments, the ethanol addition masks some of the chemical differences in the fuel blends causing them to behave more like one another. Another way to view these plots is from left to right, looking at a constant CA50 and seeing the spread in intake temperature needed for each fuel to achieve the same phasing. Again, the 20% ethanol fuels are grouped more tightly, and display a smaller span of intake temperature when the plots are considered in this fashion.

One final set of plots to consider are the early portion of the combustion process, given as CA10-CA50 burn durations, shown in Figure 8.17 and Figure 8.18. As with the CA50 combustion phasing, the 20% and 10% ethanol fuels are each separated into one of the two plots; the spread in the experimental data is smaller for the increased ethanol fuels. At a given intake temperature, such as 65°C, there is more variation in the CA10-CA50 burn duration with the 10% ethanol fuels in Figure 8.18 than there is in Figure 8.17 for the 20% ethanol fuels. Another view that examines how ethanol addition partially muddles some of the chemical differences between refinery stream fuels is in looking at all of the highest intake air temperatures run for each fuel. Recall that, in this test the hottest intake air temperature run for each fuel was the point at which the RI was equal to 5 MW/m². So the farthest right point for each fuel data set in each plot is the point where charge temperature causes the ringing limit to be reached. These points also have matched injected fuel energy, as shown in Table 5.3. At the ringing

limit, the 10% ethanol blends span an intake air temperature range of about 35°C, as opposed to the 20% ethanol fuels whose charge temperature extent is roughly 20°C. It is also interesting to note that regardless of ethanol concentration or other chemical components, the early burn durations converge at roughly the same length, about 4 CAD. At the ringing limit imposed as a constraint for these experiments, although the location of combustion, given by the CA50 in Figure 8.15 and Figure 8.16, differs based on the fuels' chemical makeup, the burn durations are similar.

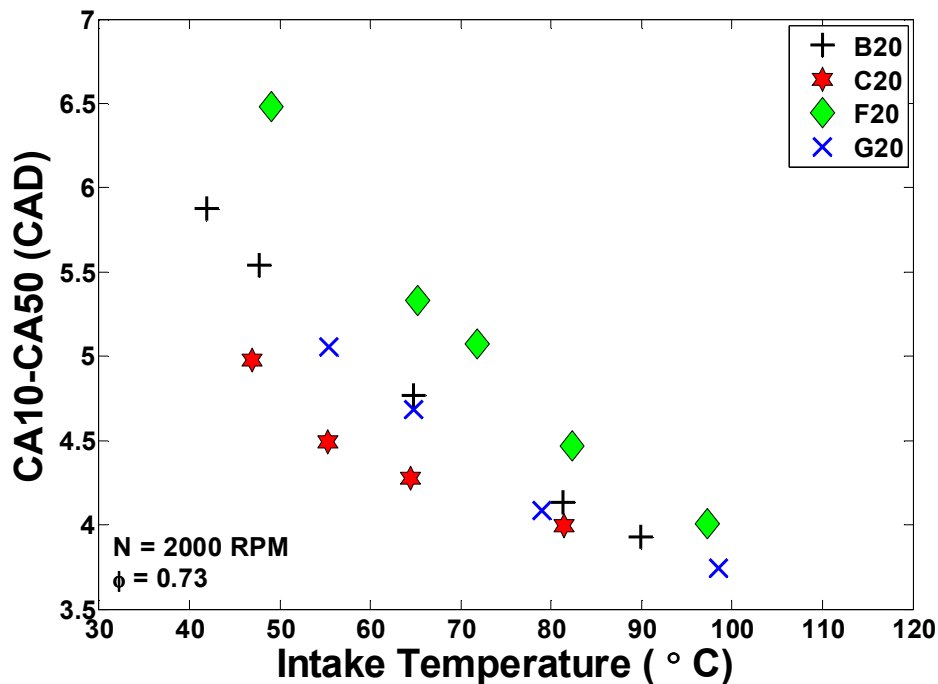


Figure 8.17 - CA10-CA50 burn duration for 20% ethanol fuels over the sweep of intake air temperature

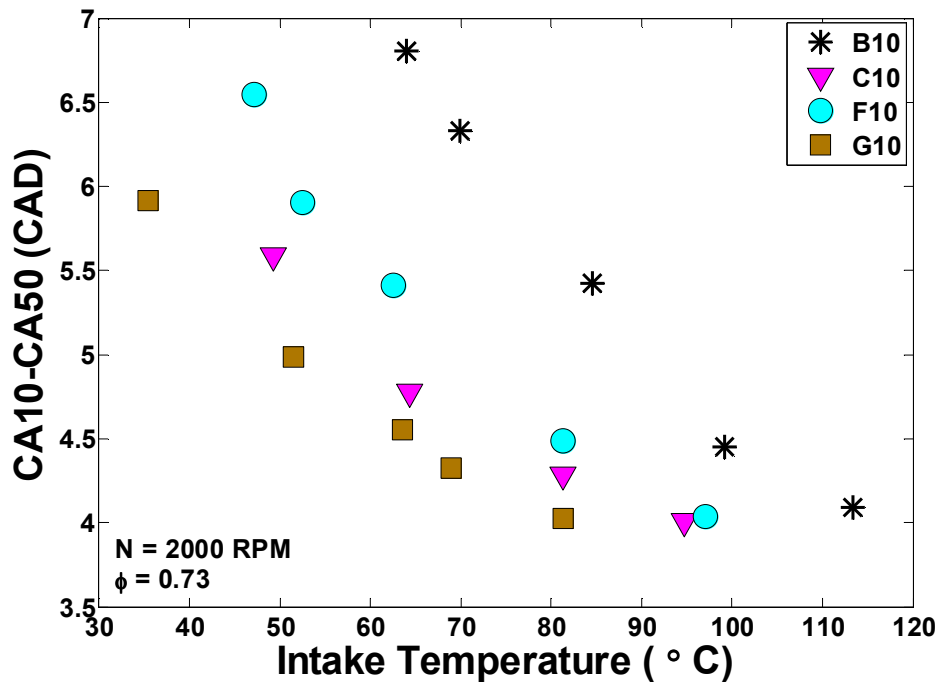


Figure 8.18 - CA10-CA50 burn duration for 10% ethanol fuels over the sweep of intake air temperature

The property of ethanol addition that engenders this masking behavior when mixed with refinery stream fuels is its single-stage auto-ignition characteristics. These traits result in ethanol not exhibiting low temperature heat release (LTHR) and burning in one rapid combustion event [164]. Because of this single-stage nature of ethanol, it requires less intake air temperature compensation with changes in engine speed and load. This finding resonates in the previous results of this chapter which showed that the range of intake air temperature at the baseline for the 20% ethanol fuels was much smaller than the 10% ethanol fuels. Furthermore, this effect from ethanol is displayed between Figure 8.13 and Figure 8.14, as the higher ethanol fuels have relatively less change in combustion phasing between operability limits across the sweep of speed than that of the lower ethanol fuels. Ultimately, this is a highly non-linear behavior, as

going from 10% to 20% ethanol concentration resulted in substantial alterations of a fuel's behavior in the engine. Even at what seems like a relatively low concentration of 20% ethanol in a refinery stream fuel, the single-stage auto-ignition characteristics begin to assert dominance over the other distillate components, as these 20% ethanol fuels behave similar to one another despite the appreciable differences in hydrocarbon constituents.

CHAPTER 9

Intake Air Temperature Sensitivity and the Octane Index Model

9.1 Introduction

Intake air temperature sweeps for a wide variety of refinery stream fuels were examined to determine an appropriate auto-ignition quality model for these multi-component fuels. The fuel studies of this chapter are an extension of the Kalghatgi Octane Index (OI) model.

9.2 Octane Index Background

Previously published works have claimed that RON and MON alone cannot sufficiently characterize the auto-ignition behavior of a given fuel. In an initial study by Kalghatgi [166], knocking behavior in SI engines was characterized and the conclusions prompted research into the auto-ignition behavior of HCCI engines. Other studies by Kalghatgi [90, 167-169] have shown that the auto-ignition behavior of different fuels cannot be explained by conventional knocking parameters like RON and MON. In the case of HCCI operation, Kalghatgi compared the RON and MON values to the CA50 of the engine and found there was little correlation between the phasing of the combustion

event and the RON or MON. This promoted development of the Octane Index (OI), which was intended as the rating or “quality” of a fuel in an HCCI engine. Kalghatgi defines the OI as:

$$OI=(1-K)RON+K \cdot MON \quad (9.1)$$

K is a constant dependent on the physical conditions experienced by the charge in the engine, and S is the sensitivity of the fuel (RON – MON). K varies with the change in engine conditions and can be negative, zero or positive. For PRFs, the RON is equal to the MON and sensitivity is zero, hence the OI for a PRF is exactly equal to the RON. Additionally, K is zero for RON test conditions and unity for the MON test. One method for visualizing the significance of OI is explained by the following example: at a negative K, a fuel of $S>0$ ($RON-MON>0$) will have an OI higher than its RON, and show more resistance to auto-ignition than the RON indicates.

Mathematically, the relationship between CA50, RON and MON can be found by a linear regression analysis of the following terms and can be written as:

$$CA50=c+aRON+bMON \quad (9.2)$$

$$CA50=c+(a+b)OI \quad (9.3)$$

Using these equations the octane index can be written as $OI = \frac{a}{(a+b)} RON + \frac{b}{(a+b)} MON$.

This demonstrates how OI can be used to assess the HCCI quality of a fuel, as it is

related to the CA50 metric that is so often used to characterize HCCI combustion. The two equations also lead to the definition of the parameter K as $\frac{b}{(a+b)}$.

In regards to K, Kalghatgi also discovered that T_{comp15} [167], a generic engine parameter that describes the temperature of the inducted charge before any heat release occurs, provides a way to estimate K. There is a strong correlation between T_{comp15} and the K found from the coefficients in the regression. This intuitively makes sense, as T_{comp15} is a function of the physical state of the combustion chamber (based on engine speed, intake temperature, etc.), and K is a parameter which is dependent only upon the engine operating condition, and not fuel.

Kalghatgi's OI has been shown to work reasonably well for most PRF blends and surrogates composed of a few pure chemical components. In many cases, the OI correlates strongly with CA50 for a given fuel and engine condition. While studies since Kalghatgi's work have usually favored PRFs and fuel surrogates, to date pump gasoline has received little attention. The complex chemical nature of pump gas, which contains hundreds of different species, could potentially cause issues with the relevance of the OI correlation.

The importance of a fuel's chemical components was the crux of a study by Shibata and Urushihara [87], in which a fuel quality metric called the HCCI index was derived based on the effects of low and high temperature heat release. Their fuels matrix consisted of 11 pure components blended in different proportions to cover a large variety of fuel types with diverse dominant chemistries, e.g. aromatics, olefins, paraffins and ethanol. They showed that OI is not enough to characterize the auto-ignition behavior of fuels that have similar RON and MON but different fuel composition. The

derivation HCCI index correlation is based on the analysis of heat release characteristics of different chemical components of the fuel. The final form of the equation is derived by statistical regression of MON and the volumetric percentage of aromatics, olefins, paraffins and ethanol in a given fuel. MON is used in the correlation because the in-cylinder conditions for their tests were close to that of a MON test. Equation 22 [87] gives the HCCI Index, which is also the HTHR CA20. The applicability of both the Kalghatgi and Shibata-Urushiara metrics to refinery stream fuels will be examined in this chapter.

9.3 Octane Index analysis - Kalghatgi model

The results from five charge temperature conditions are used to formulate a correlation between the intake air temperatures and CA50 that is then used to derive the OI through multiple linear regressions. The concept of OI can be used to better explain auto-ignition characteristics of a fuel and to help predict the CA50 for a fuel at a specific engine condition, for a particular engine.

9.3.1 Calculation of 'K'

As mentioned previously, K is an engine condition specific parameter used in the correlation for OI. Kalghatgi showed that K is strongly dependent on the temperature of the mixture under compression. $T_{\text{comp}15}$, the temperature in the cylinder when pressure is equal to 15 bar during the compression stroke, is defined [167] as a generic engine parameter that can be used to determine K. Also, by regressing CA50, RON, MON and

the sensitivity of different fuels at a given intake temperature, K can be calculated by using the constants of the regression in the equation $K=b/(a+b)$. Table 9.1 below lists the K values for the experimental single-cylinder engine setup at different intake temperature conditions.

Table 9.1 - Values of K for different intake air temperature conditions

Intake Temp (°C)	K
115	2.54
98	1.99
81	1.88
65	1.84
50	1.55

K has a monotonically decreasing trend with respect to the intake air temperature. This trend is expected since the in-cylinder gas temperatures are reduced with a decrease in intake air temperature and because K is directly proportional to T_{comp15} , K drops with a reduction in T_{comp15} .

9.3.2 Calculation of Octane Index

Octane indices for each fuel at each engine operating point are calculated using the relation $OI = RON - KS$. For each of the intake temperature conditions, K was found using the mathematical regression of measured CA50, RON, MON and sensitivity. CA50 was plotted against OI for all the fuels at each intake temperature

condition to study the relationship between OI and combustion phasing, as given by CA50. Figure 9.1 shows a plot of CA50 against OI at an intake air temperature of 81°C.

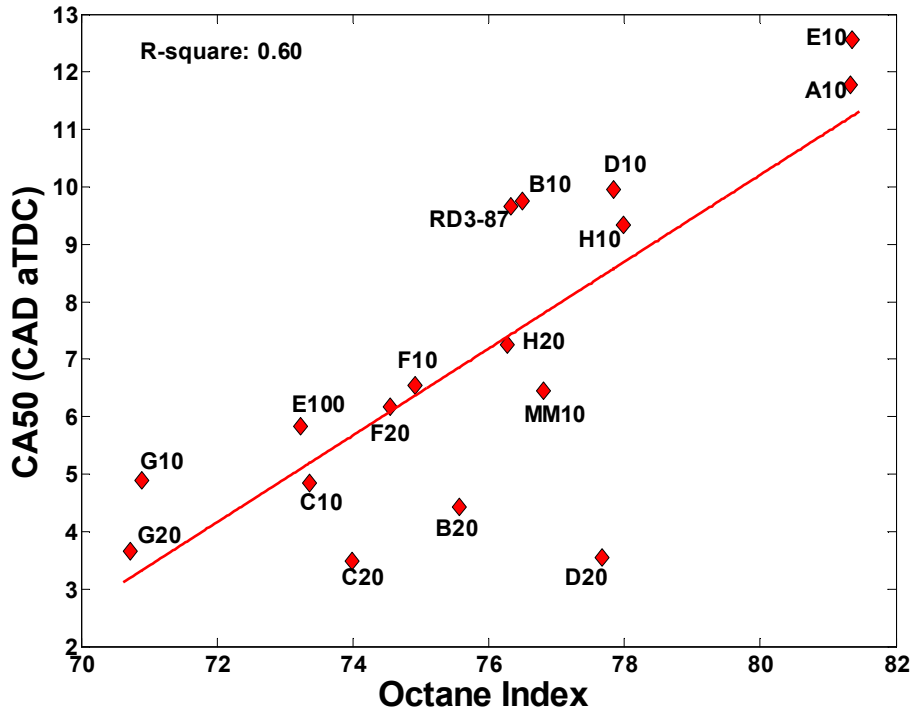


Figure 9.1 - CA50 versus Octane Index (OI) at an intake air temperature of 81°C

Table 9.2 - Strength of correlation between CA50 and OI for all the intake temperature conditions given by R^2 value of the best fit line

Intake Temp (°C)	R^2
115	0.75
98	0.87
81	0.60
65	0.41
50	0.21

The strength of the Kalghatgi correlation decreases as the intake air temperature is reduced (as charge temperatures are lowered). At an intake air temperature of 115°C, very few fuels operate without excessive ringing, and no 20% ethanol fuel could be tested due to their low reference temperatures, established in Table 5.3. The decreasing strength of the correlation can be attributed to the fact that most of experimentation done to derive the Kalghatgi model used high compression ratio engines, high intake temperatures and boosting with PRFs and fuel surrogates. The present conditions are vastly different, as the engine setup has a relatively low compression ratio, no NVO (re-breathing is used instead), relatively low intake temperatures and fuels made from refinery stream components. The OI correlation in its current form is not able to capture the auto-ignition behavior of the refinery stream fuels in this engine environment.

In order to discover “outlier” fuels that do not agree with the OI formulation, 10% and 20% ethanol blends were plotted separately, in Figure 9.2, to study any underlying trends. These plots do not include RD3-87 and E100. The K value used to calculate the octane indices is obtained by performing a regression on RON, MON, S and CA50 as before.

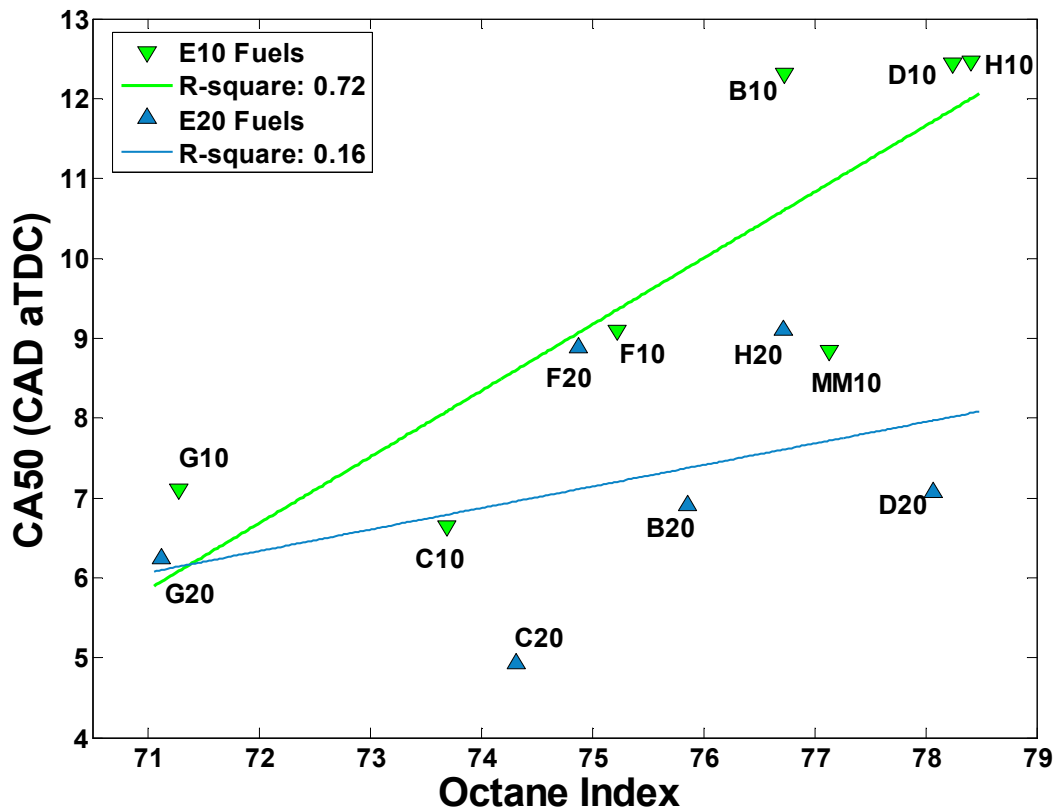


Figure 9.2 - CA50 vs. OI at intake temperature 65°C for 10% and 20% ethanol fuels

Table 9.3 - Strength of correlation with fuel blends of 10% and 20% ethanol as determined from a best fit line

Intake Temp (°C)	R ²	
	10% ETOH	20% ETOH
115	0.83	N/A
98	0.87	0.95
81	0.86	0.07
65	0.71	0.16
50	0.71	0.23

Once again, the correlation between the OI and the CA50 of a fuel decreases with decreasing intake temperature for both 10% and 20% ethanol fuels. The most important observation is that the relationship between CA50 and OI for the 20% ethanol fuels is very weak (except at 98°C where relatively little data was available). At an intake temperature of 81°C, where all the fuels could run, there is an excellent fit for 10% ethanol fuels and virtually no correlation with the 20% ethanol fuels. It is clear that the additional ethanol has a significant effect on the CA50 and the OI, even for fuels with similar RONs and sensitivities. The higher ethanol content refinery stream fuels constitute some of the 'outlier' behavior observed previously. This can be attributed to the similar reference temperatures for all 20% ethanol fuels, which had baseline intake temperatures in the range of 51°C to 61°C. Due to the similar baseline intake air temperatures, the charge temperature sweeps for 20% ethanol fuels all displayed more similar combustion phasing than the lower content ethanol fuels. Figure 9.3 and Figure 9.4 show the comparison of CA50 of 10% and 20% ethanol fuels, respectively, at various intake temperatures. The boxes are indicative of the qualitative size of the variation of CA50 for a sample of fuels at the same intake temperature. The additional ethanol content in the gasoline blends causes there to be less spread in combustion phasing; because there is less ability to differentiate between the 20% ethanol fuels as opposed to 10% ethanol blends, the OI correlation breaks down, which suggests the need for an ethanol term in the regression.

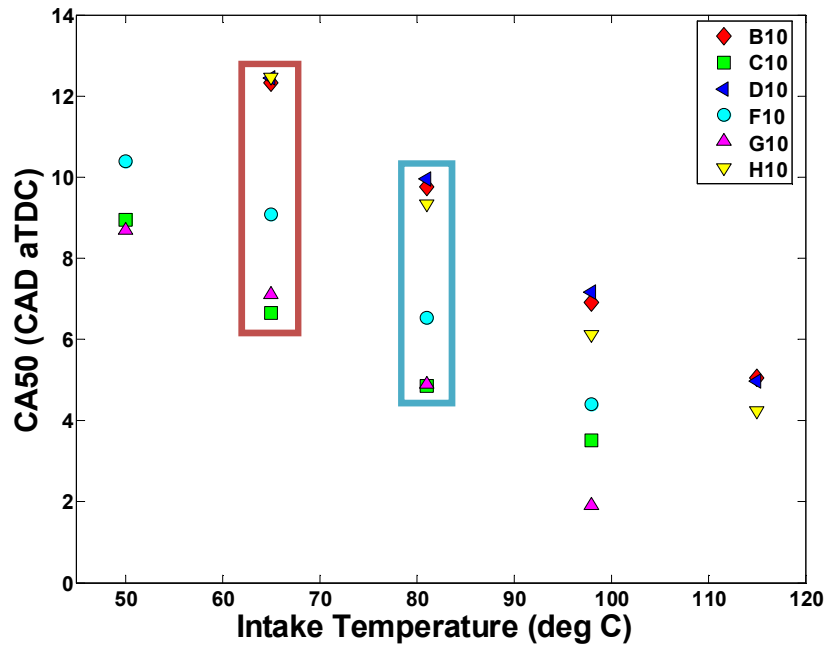


Figure 9.3 - CA50 for 10% ethanol fuels at all intake temperatures

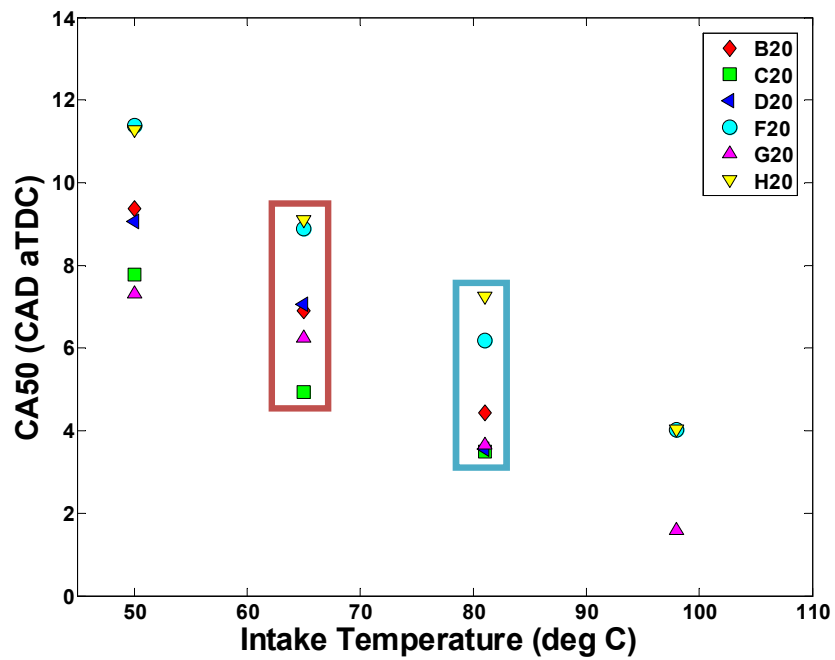


Figure 9.4 - CA50 for 20% ethanol fuels at all intake temperatures

To continue studying the effect of chemical composition on OI, the same analysis performed for the sets of ethanol concentrations is repeated, with high aromatic and high olefin fuels. Figure 9.5 shows a plot of CA50 against OI at intake temperature of 50°C.

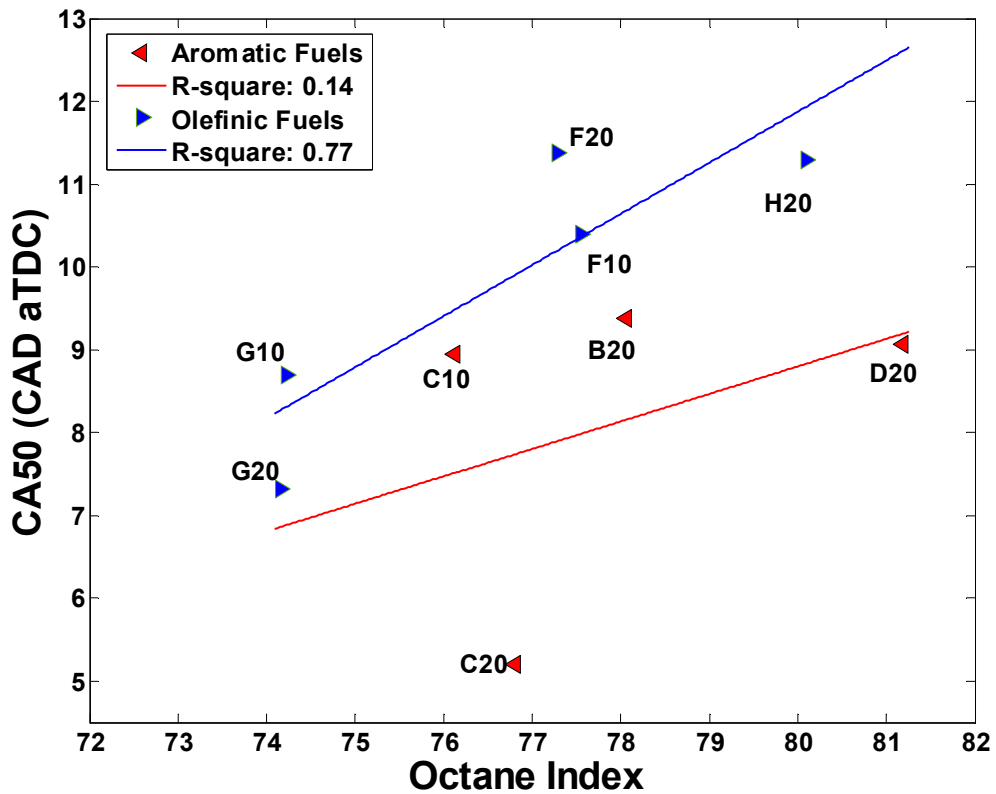


Figure 9.5 - CA50 vs. OI at intake temperature 50°C; high aromatic and olefin fuels plotted separately

Table 9.4 - Strength of the OI correlation with high aromatics and high olefins separated as given by the best fit line

Intake Temp (°C)	R ²	
	High Aromatics	High Olefins
98	0.94	0.94
81	0.52	0.95
65	0.41	0.88
50	0.14	0.77

Again, the strength of the correlation between CA50 and OI decreases as intake air temperature is reduced and cooler mixtures are run in the engine. In this instance, highly aromatic fuels show a particularly poor correlation between CA50 and OI at the lowest intake air temperature condition. Kalghatgi [90] encountered a similar problem with high toluene PRF blends (which are highly aromatic); and these fuels represented extreme outliers that ultimately were excluded from his OI analysis. From Figure 9.2 and Figure 9.5, it is clear the refinery stream fuels that present the most substantial problem to the validity of the OI model were those of 20% ethanol and high aromatic content, e.g. B20, C20 and D20.

Figure 9.6 and Figure 9.7 show the variation of CA50 of different fuels at all intake temperatures. High aromatic fuels are in Figure 9.6 and high olefin fuels are in Figure 9.7. The key observation to take away from the figures is that in some cases the CA50 for completely different fuels in terms of RON, MON and chemical composition are phased almost exactly the same. For example, while B10 has a low RON and low S and D10 has a high RON and high S, their CA50 values nearly overlap at all intake temperatures depicted in Figure 9.6. The same applies to C10, B20 and D20. This is

problematic, because any auto-ignition fuel quality model with only RON and MON cannot possibly capture the combustion phasing of these highly aromatic refinery stream fuels. This indicates the need for a term based on aromatic composition in the OI formulation.

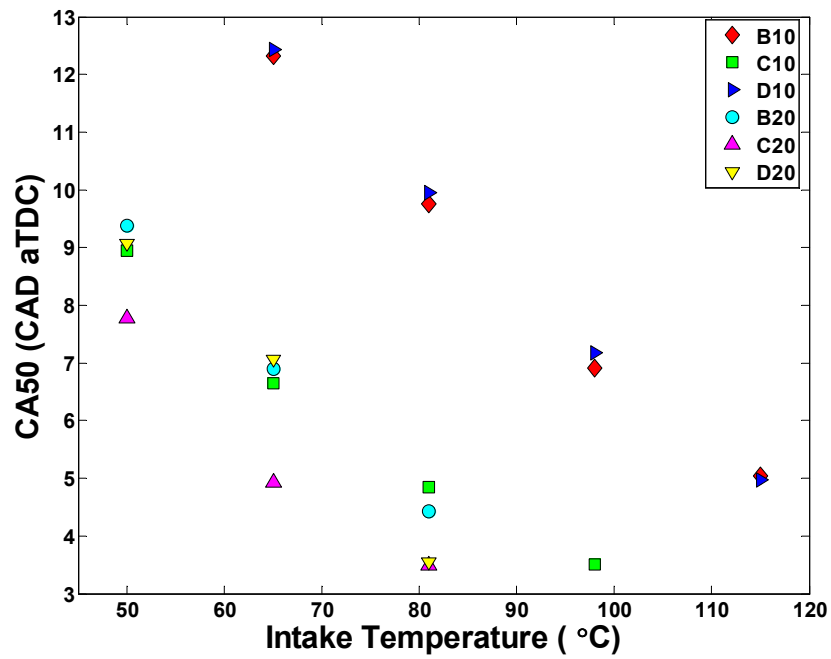


Figure 9.6 - CA50 for high aromatic fuels at all intake temperatures

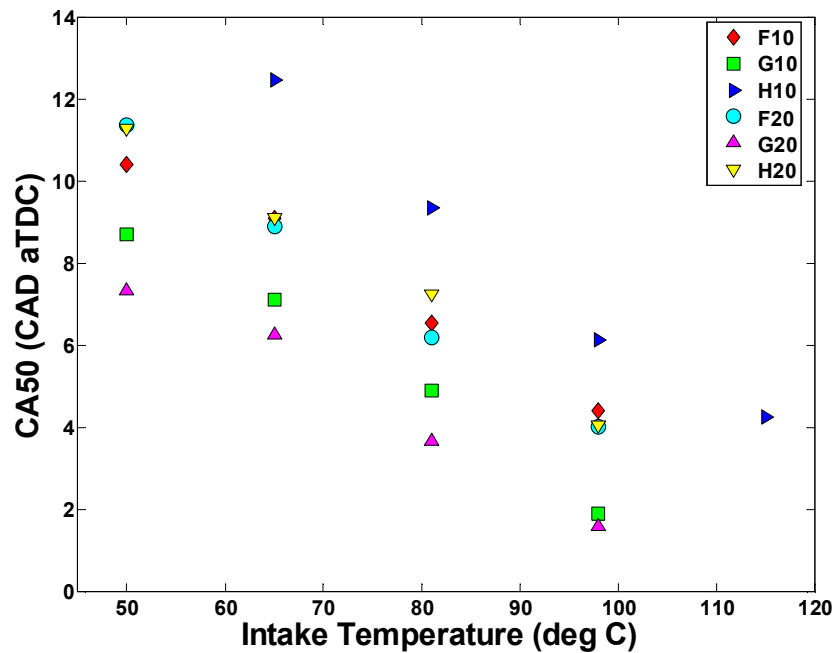


Figure 9.7 - CA50 for high olefin fuels at all intake temperatures

9.4 Modifications to the Correlation

Given the information presented in the previous section, it is possible to augment Kalghatgi's OI model to better suit the refinery stream fuels in this study. Specifically, composition terms will be added to the original OI correlation to extend the formula to the "outlier" fuels described previously; those fuels containing high aromatics and high ethanol content, by accounting for the varied chemical components of these fuels. After some iteration, the correlation best defining CA50 with respect to RON, MON, S and chemical composition of the refinery stream fuels is shown in Equation 9.4.

$$CA50=c+aRON+bMON+d(Aromatics)^2(Olefins+Saturates)+e(Aromatics \cdot Ethanol) \quad (9.4)$$

In this equation, Aromatics, Olefins, Saturates and Ethanol represent the percentage by volume of each respective component in the fuel. The two composition interaction terms play an important role because aromatics and ethanol have a significant effect on the strength of the correlation between OI and CA50. The first composition term was included to accentuate the complex interactions between aromatics and other major fuel components (olefins and saturates), but place relatively more importance on fuels with high aromatics (hence the higher exponential degree on Aromatics) due to the results shown in Figure 9.6. Recall that in the figure, fuels that have aromatics as the dominant chemical component do not agree well with the OI formulation, whereas the OI of fuels with relatively more olefins had a much stronger connection with CA50. The second interaction term was conceived as a method for capturing the behavior of the largest outlying fuels, e.g. those of high aromatic and 20% ethanol content by volume.

Here two new parameters, κ and ϵ , are introduced to be used in conjunction with the K defined previously, in order to keep the same conventions as the Kalghatgi OI model. The coefficients a, b, d and e are the same as in Equation 9.4.

$$K=b/(a+b) \quad (9.5)$$

$$\kappa=d/(a+b) \quad (9.6)$$

$$\varepsilon=e/(a+b) \tag{9.7}$$

OI is now calculated using the modified formula:

$$OI_{\text{modified}}=RON-K \cdot S+\kappa \cdot (\text{Aromatics})^2(\text{Olefins}+\text{Saturates})+\varepsilon(\text{Aromatics} \cdot \text{Ethanol}) \tag{9.8}$$

Using this modified equation, the calculated K, shown in Table 9.5, is still close to the previously reported K values, in Table 9.1, from the original OI correlation. This is an encouraging result signifying that the addition of extra composition terms does not affect K, which is an engine condition specific parameter not tied to the chemical composition of fuel and therefore should remain the same.

Table 9.5 - K, κ and ε values at different intake temperature conditions

Intake Temp (°C)	K	κ	E
115	2.4	36.12	-71.99
98	1.97	46.21	-90.46
81	1.9	50.77	-124.44
65	1.86	48.37	-116.5
50	1.85	12.38	-84.57

OI is now recalculated from Equation 9.8 using the K, κ and ε values listed in Table 9.5 above. Figure 9.8 has the measured CA50 values of the fuels against the modified OIs at the 81°C intake air temperature condition. The strength of the new OI fit for all intake temperature conditions is summarized in Table 9.6.

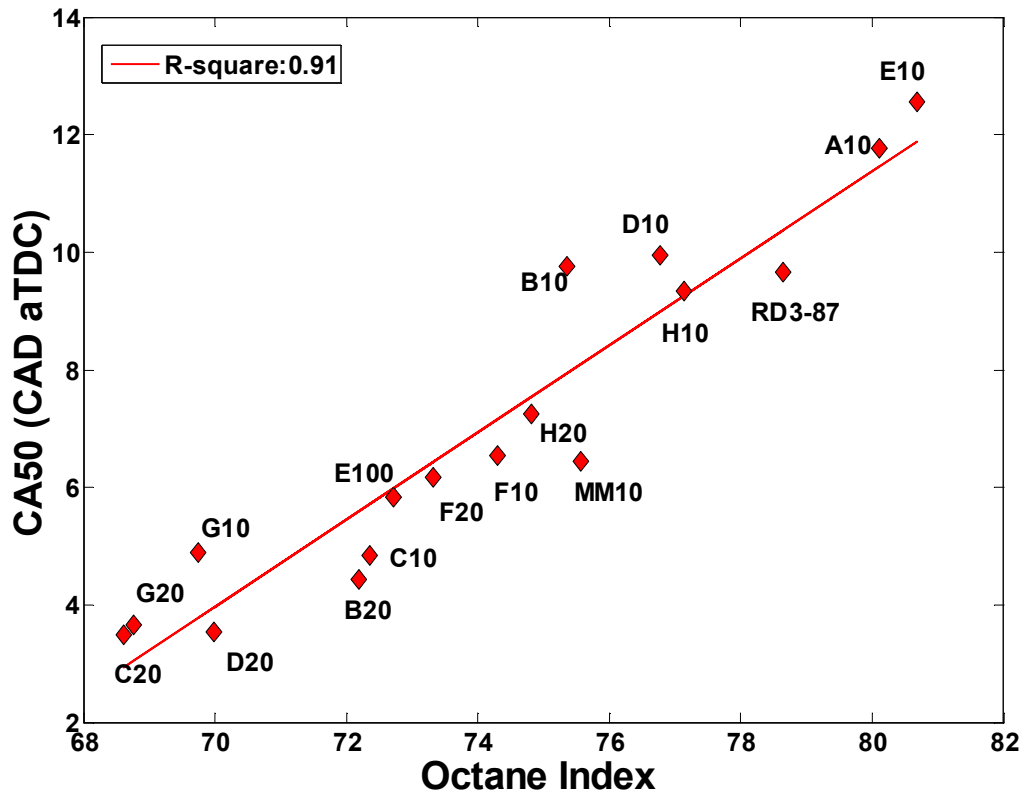


Figure 9.8 - CA50 vs. OI at intake temperature 81°C; OI calculated with new correlation

Table 9.6 - Strength of correlation with new OI model for tested intake air temperatures

from the best fit line

Intake Temp (°C)	R ²
115	0.87
98	0.91
81	0.91
65	0.83
50	0.80

This correlation proves to be more capable of capturing the auto-ignition behavior of the refinery stream fuels, as well as RD3-87 and E100, for all intake temperature conditions, and especially low intake temperatures. To reiterate, the chief difference between the old OI formula and the new is the inclusion of compositional interaction terms that are better equipped to provide the auto-ignition quality of refinery stream fuels that are high in aromatics and ethanol content.

The breakdown of the original correlation for the high aromatic fuels at low temperatures can be attributed to the complex auto-ignition chemistry of aromatics. The aromatic ring structure is far more stable than alkyl and olefinic bonds. The ring is stabilized by a strong molecular resonance. Under high temperature oxidation of aromatics, a phenyl radical ($C_6H_5\cdot$) [159] is produced by either O_2 attack or thermal pyrolysis. This phenyl radical undergoes further degradation with the ejection of CO, to produce a cyclopentadienyl radical ($C_5H_5\cdot$). The cyclopentadienyl radical has a relatively slow reaction rate due to its resonance stability. The alkylated part of the molecule is oxidized at high temperature by pyrolytic cleavage of the C-C bond. The alkyl portion undergoes conventional high temperature oxidation without affecting the aromatic ring structure. The overall reaction rate is relatively slow and is further exacerbated by the lower intake temperatures [170]. In summary, aromatic molecules must undergo more complicated chain-breaking reactions to be converted into olefinic and paraffinic structures that can be oxidized more easily. In the context of refinery stream fuels, the juxtaposition of these aromatic reactions with other gasoline components, particularly at lower charge temperatures, results in more unpredictable combustion phasing behavior.

Even with the new OI correlation in place, there is still some discrepancy between high and low ethanol fuels, summarized by Figure 9.9 and Table 9.7, and high and low aromatic fuels, shown in Figure 9.10 and Table 9.8. This discrepancy emphasizes that the behavior of these incredibly complex refinery stream fuels, which contain hundreds of chemical species, is challenging to capture at a wide range of operating conditions.

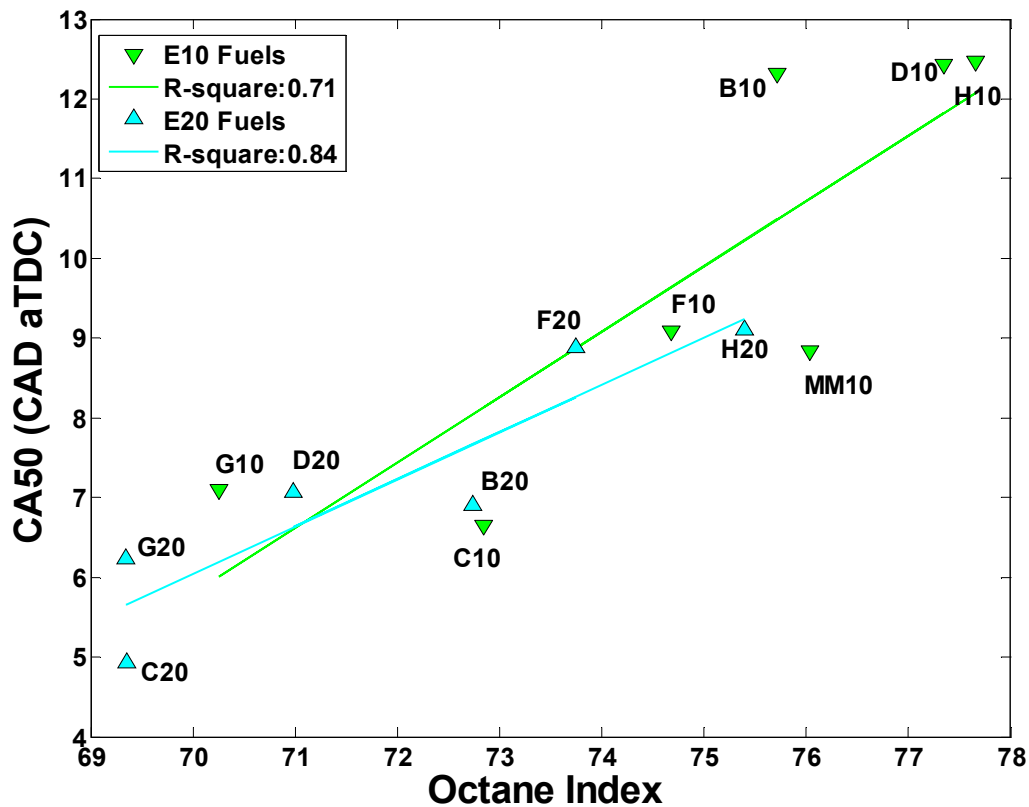


Figure 9.9 - CA50 vs. OI at intake temperature 65°C with the new OI correlation; 10% and 20% ethanol fuels plotted separately

Table 9.7 - New OI correlation strength at several intake air temperature conditions using a best fit line; 10% and 20% ethanol fuels are separated from one another

Intake Temp (°C)	R ²	
	E10	E20
98	0.90	0.96
81	0.86	0.89
65	0.71	0.84
50	0.92	0.89

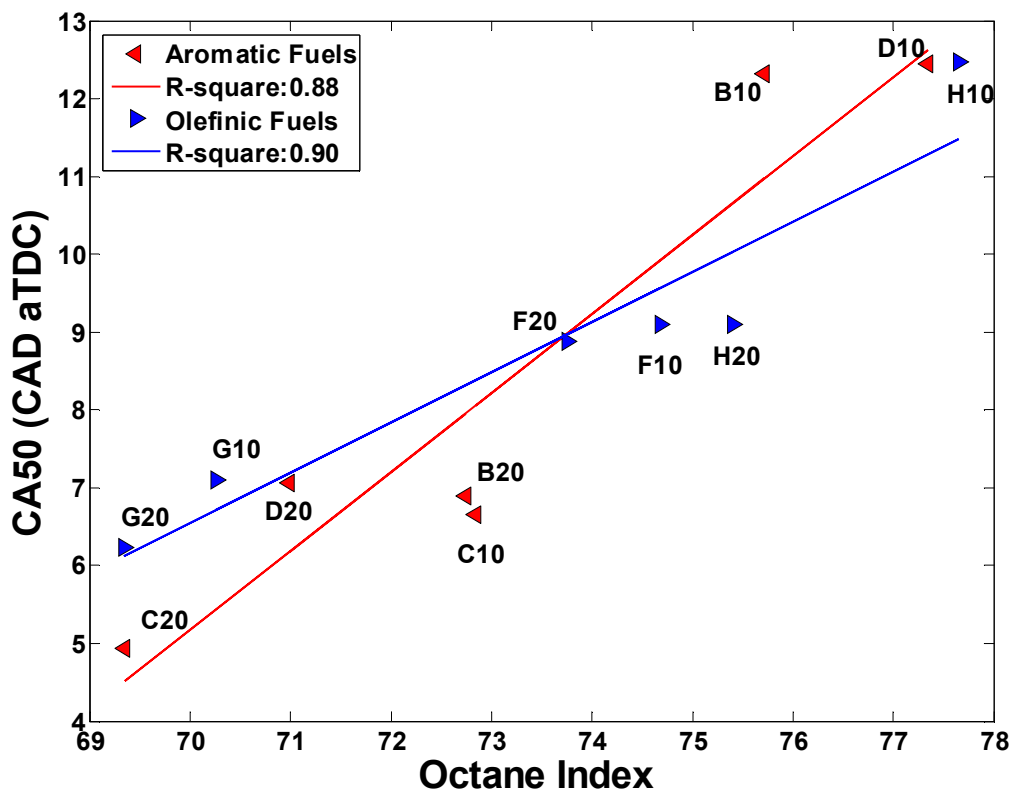


Figure 9.10 - CA50 vs. OI at intake temperature 65°C with new OI correlation; high aromatic and high olefin fuels plotted separately

Table 9.8 - Strength of correlation with new OI model using a best fit line; high aromatic and high olefin fuels are separated out

Intake Temp (°C)	R ²	
	High Aromatics	High Olefins
98	0.92	0.94
81	0.92	0.96
65	0.88	0.90
50	0.83	0.86

With the use of the new OI formula, there is a significant improvement in the correlation for the aromatic fuels and high ethanol fuels, especially at low intake temperature. There is now more confidence that the OI is representative of the auto-ignition quality of the fuels tested in this study.

9.5 Comparison to Shibata-Urushihara model

The proposed OI model is not the first effort to utilize fuel composition to quantify the auto-ignition quality of a fuel. In the Shibata-Urushihara (SU) model, mentioned previously, low and high temperature heat release were analyzed for different fuels blended using combinations of 11 pure hydrocarbons. Significant low temperature heat release (energy release before the main combustion event) was observed at low intake temperature conditions which influenced the high temperature heat release. Different fuel composition terms are used in a linear regression for the parameter high temperature heat release (HTHR) CA20, which is the crank angle during the high temperature heat release in an HCCI engine test, equivalent to the “compression ratio

at knocking intensity level of 50” of the ON measurement by a CFR engine [87]. In terms of the mass fraction burned curve, this point is the same crank angle position where 20% of the mass in the HTHR portion of the combustion event has been consumed. This parameter is used to describe the HCCI combustion event for the SU model because it directly relates back to the conventional RON and MON tests in a CFR engine.

The pure hydrocarbon components used to make the test fuels were broadly classified into aromatics, olefins, paraffins and ethanol. Each component had a different effect on the auto-ignition characteristics of the fuel. For example, olefins have low temperature heat release (LTHR) inhibiting characteristics and paraffins exhibit LTHR boosting characteristics. The HCCI index for the SU model is given in Equation 9.9.

$$\text{HCCI index} = m\text{MON} + a(nP) + b(iP) + c(O) + d(A) + e(OX) + Y \quad (9.9)$$

Here MON is the motor octane number, nP is the volume percentage of n-paraffins, iP is the volume percentage of iso-paraffins, O is the volume percentage of olefins, A is the volume percentage of aromatics, OX is the volume percentage of oxygenates and Y is a constant for the y-intercept.

The UM engine is a low compression ratio engine running with large quantities of residual at a relatively higher engine speed. This suppresses LTHR during compression making the only heat release was the high temperature heat release. For the purposes of comparison, the CA20 values from the UM engine data is plotted against the calculated HCCI Index using the SU model from Equation 9.9, and is shown in Figure 9.11 for the lowest intake air temperature condition. Table 9.9 assesses the

strength of the correlation between the HCCI index and CA20 for the test fuels at all intake temperatures. As before, the high olefin and high aromatic fuels are separated at one intake air temperature in Figure 9.12 using the SU HCCI index, and 10% and 20% ethanol fuels are divided in Figure 9.13.

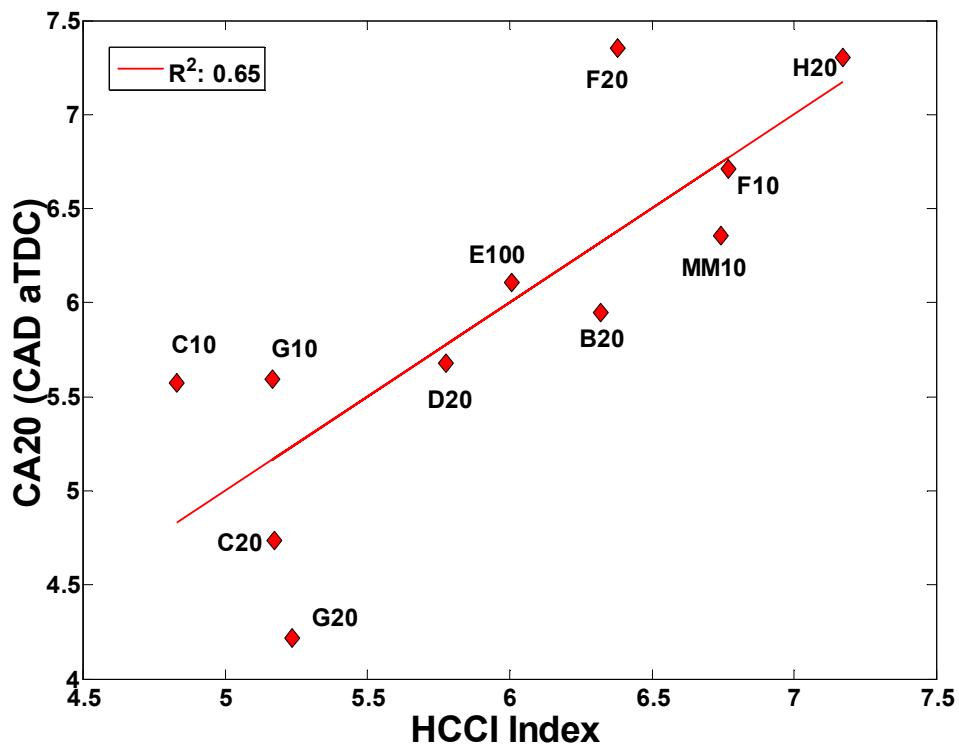


Figure 9.11 - CA20 vs. HCCI Index at intake temperature 50°C; SU model using UM engine data

Table 9.9 - Strength of SU HCCI Index correlation with all fuels using a best fit line

Intake Temp (°C)	R ²
115	0.84
98	0.91
81	0.82
65	0.69
50	0.65

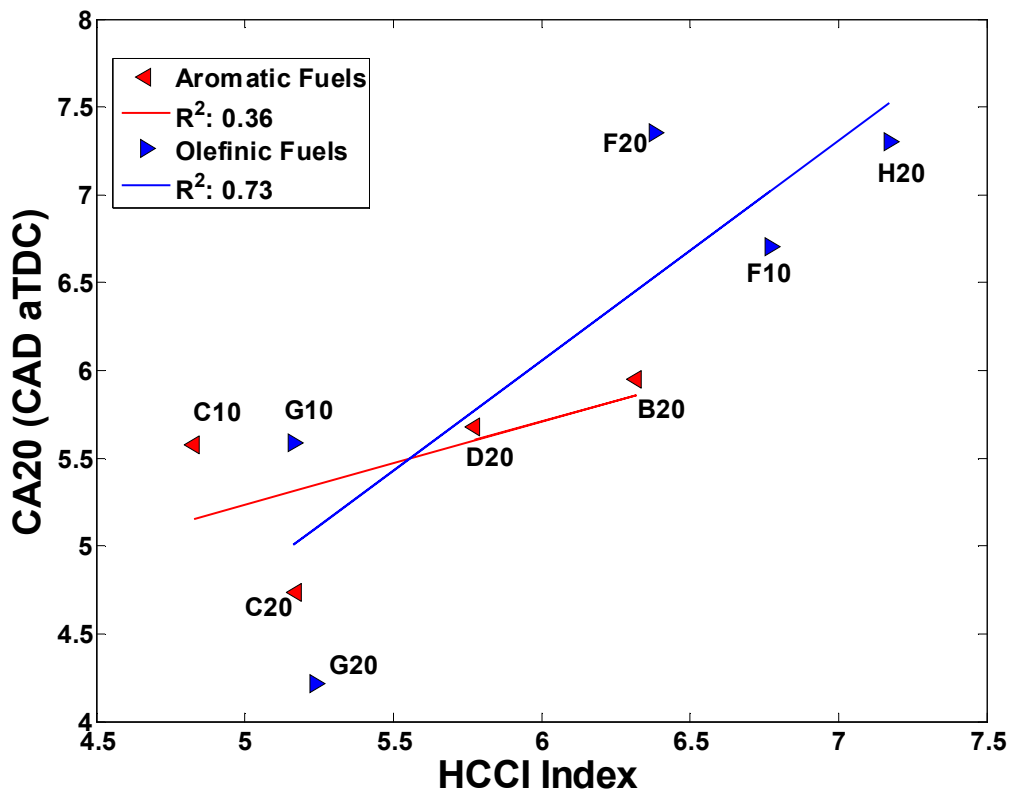


Figure 9.12 - CA20 vs. HCCI Index at intake temperature 50°C using the SU model; high aromatic and high olefin fuels plotted separately

Table 9.10 - Strength of the HCCI Index correlation from the SU model against CA20

using a best fit line; high aromatic and high olefin fuels are separated

Intake Temp (°C)	R ²	
	High Aromatics	High Olefins
98	0.94	0.96
81	0.82	0.95
65	0.69	0.94
50	0.36	0.73

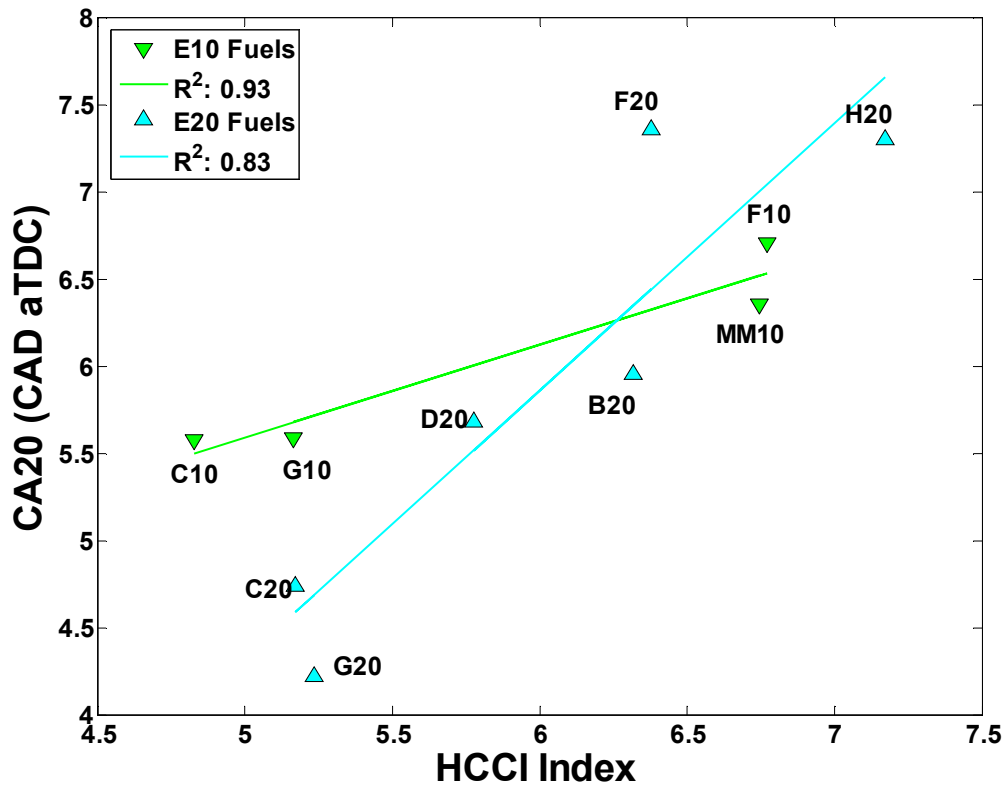


Figure 9.13 - CA20 vs. HCCI Index at intake temperature 50°C; 10% and 20% ethanol fuels plotted separately

Table 9.11 - Fit for the HCCI Index of the SU model to CA20 using a best fit line; 10% and 20% ethanol fuels are separated

Intake Temp (°C)	R ²	
	E10	E20
98	0.88	1
81	0.77	0.56
65	0.62	0.42
50	0.93	0.83

Table 9.10 and Table 9.11 list the intake temperature conditions and the strength of correlation for each case. The SU model works well with the higher intake air temperature points, but there are still some issues with this correlation when characterizing high aromatic fuels at lower charge temperatures, as shown by the last two rows in Table 9.10. There are also some intake temperature conditions in Table 9.11 where the HCCI index does not seem to capture the behavior of the 20% ethanol fuels. It is apparent that fuel composition is certainly critical in developing a metric to qualify the auto-ignition behavior of a fuel, but using the existing SU model for each type of fuel component in refinery stream fuels is not the best way to capture the auto-ignition quality for the fuels run in the UM HCCI engine.

9.6 Heat Release and the Modified Octane Index

Another method to validate the merit of the modified OI is to consider net heat release curves looking specifically at how the peak rate of heat release corresponds to OI. The maximum net rate of heat release gives a relative indication of the combustion phasing for a fuel. As the modified OI is designed to provide information about the

CA50 of fuels, there should be a commensurate trend with peak NHRR. A higher OI physically means that a fuel has more inhibition towards auto-ignition and thus, should have a more retarded peak NHRR. The opposite is true for lower OI, where heat release curves should be more advanced for a fuel that better promotes auto-ignition. Figure 9.14 shows the heat release profiles of high aromatic fuels at 65°C intake temperature. The legend shows the new OI values for each fuel. After observing the close-up view of the peaks in Figure 9.15, the trend of the peak NHRR with OI is evident, as increasing OI generally results in more retarded peaks in the heat release curves. This is a desirable trait of a numerical scale to assess the “HCCI quality” of a fuel, as a higher OI should correspond to a fuel that is harder to auto-ignite and a lower OI should indicate a fuel that can be combusted more readily.

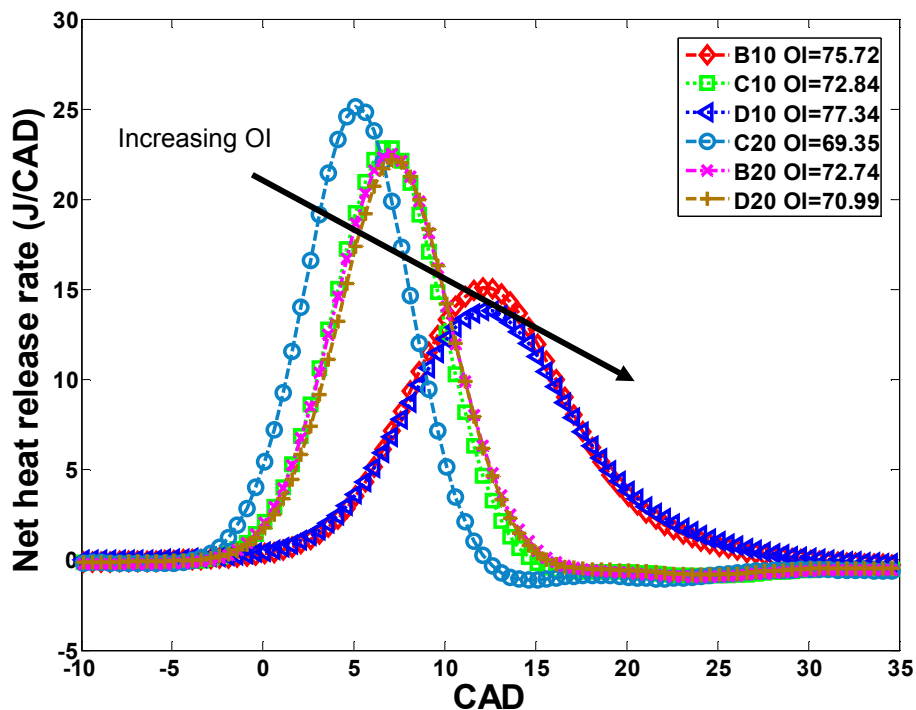


Figure 9.14 - Net heat release rate at 65°C intake temperature for a selection of fuels

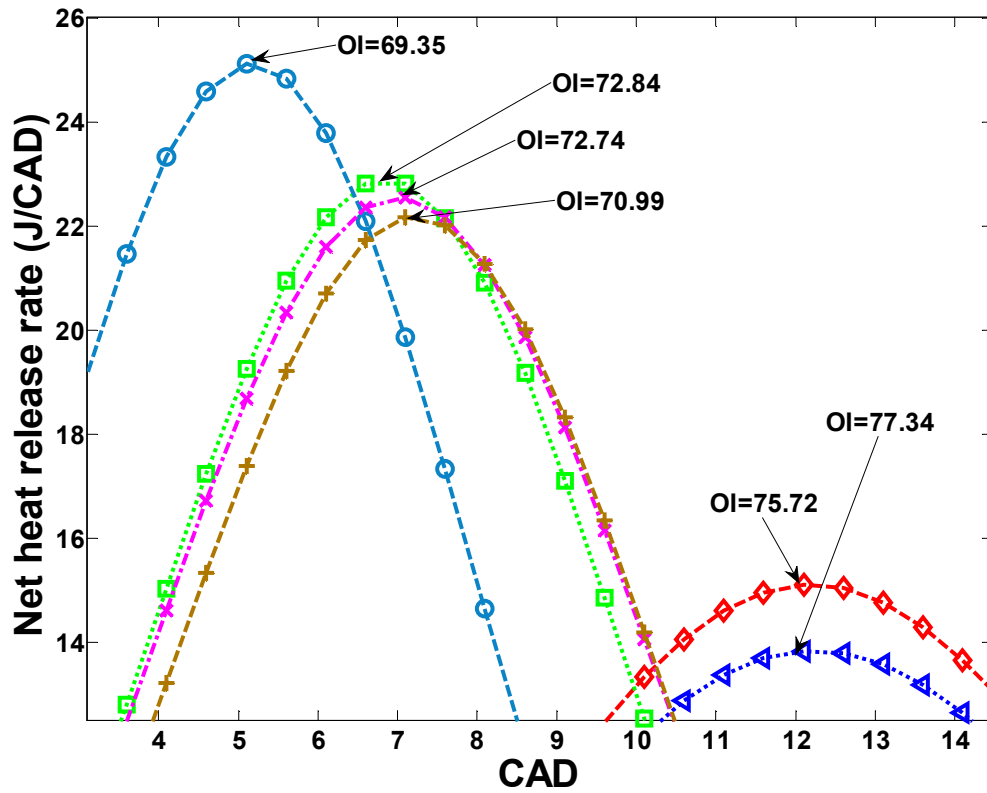


Figure 9.15 - Zoomed in version of Figure 9.14 highlighting the relationship between the location of net heat release rate and OI

CHAPTER 10

Experimental Methods for Combustion Chamber Deposits Studies

10.1 Conditioning Sweeps

To characterize the growth of deposits that result from different types of refinery stream fuel and additive packages, tests are run for a number of hours of engine operation to form a layer of deposits. The matrix of test fuels for the conditioning sweeps consisted of two base fuels, as well as samples of those fuels with two distinctly different additive packages referred to as polybutene amine (PBA) and polyether amine (PEA) (summarized below in Table 10.1). The specifics of these two additive packages are detailed in Chapter 1, but will be briefly reviewed at this point. Both of these types of additives are commonly found in pump gasoline, and are commercially available. Each additive package can be used in a maintenance capacity (a lower dosage that is generally included in pump gas) or a “clean up” role, where an entire tank of fuel pumped up is dosed with a bottle of the additive. For the test fuels in this study, the maintenance dose of 0.1 ounces of additive per gallon of fuel was utilized. The chief differences between the two additive packages are the chemical structure and the type of the deposits they are rated to remove. PBA additives have a backbone structure composed completely of hydrocarbons, so they tend to have higher boiling points and

are more difficult to break down in an engine. This type of additive is rated to clean intake valves and fuel injectors, but it can actually increase the level of CCD in some cases. The PEA additive, on the other hand, has more oxygen atoms in its backbone structure and has a lower boiling point than PBA. PEA additive, which is the active ingredient in Techron, can be used to clean all forms of deposits in an IC engine, including those that form on the valves, fuel injector and in the combustion chamber itself. The testing regimen of fuels in Table 10.1 was developed with these two additive packages in mind, as well as the test matrix of fuels from Chapter 4. Note that the physical properties of the fuels with the additive blends were identical to those without. Chapter 4 also contains the details for how the reference condition points were determined.

Table 10.1 - Fuel Properties for the Deposit Studies Test Matrix

Fuel	RON	S	A (%vol/vol)	O (%vol/vol)	Sat (%vol/vol)	Eth (%vol/vol)
D10	98.1	10.8	37.0	3.5	49.8	9.7
D10+PBA	Same as the base D10 fuel					
D10+PEA						
CARBOB*	92.5	9.3	28.2	3.7	68.1	10.0
CARBOB+PBA*	Same as the base CARBOB+10%EtOH fuel					
CARBOB+PEA*						

* All CARBOB blends contain 10% EtOH by volume

Table 10.2 - Reference Conditions for Test Matrix Fuels

Fuel	LHV (kJ/kg)	Fuel injected (mg/cycle)	Tint (°C)	Density (kg/m³)
D10	40945	11.6	81	770.9
D10+PBA	Same as the base D10 fuel			
D10+PEA				
CARBOB*	41621	11.4	99	748.4
CARBOB+PBA*	Same as the base CARBOB+10%EtOH fuel			
CARBOB+PEA*				

* All CARBOB blends contain 10% EtOH by volume

The runs are done at steady state, with constant fuelling, based on the baseline points established in Chapter 4, and at an engine speed of 2000 RPM. Before the testing begins, the engine's cylinder head is removed, and the valves and pistons are cleaned to remove any previously existing deposits using a commercially available oven cleaner. Starting from a clean head and metal piston, the engine is then run for a period of time until the CCD growth stabilizes and ceases to accumulate. At this equilibrium point, it is said that the engine is "fully-conditioned", i.e. the deposits are burned off as fast as they are condensing onto the walls. As mentioned in the introductory material in Chapter 1 [31], this state of equilibrium occurs when the surface temperature of the CCD is sufficiently high to prohibit further CCD growth. Thus, the deposits do not grow indefinitely in the combustion chamber, and furthermore, it is possible to determine the location of this equilibrium state in terms of engine operations hours when the combustion event is no longer changing.

10.1.1 Tracking the Advance of Combustion Phasing and Equilibrium

As the conditioning sweep is run, several key engine parameters are tracked in real-time, using the high speed data acquisition software, in order to monitor and assess the growth of the deposit layer and when it reaches an equilibrium thickness. Figure 10.1 is shown in Chapter 1, and again here to give insight into how the combustion event is tracked during the course of a conditioning sweep.

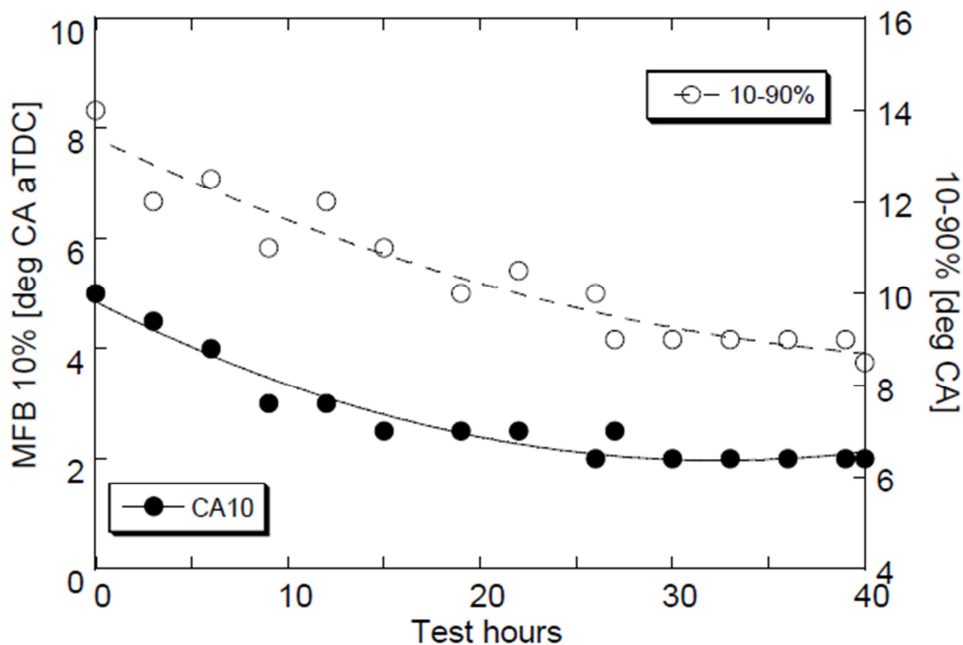


Figure 10.1 – Plot showing the changes the combustion event undergoes as the layer builds in an HCCI engine; these particular curves were generated from data taken in an engine of similar geometry using our baseline RD3-87 fuel, in a previous University of Michigan study [5]

Consider the black data points in the graph, which represent the crank angle location of the 10% fraction of fuel mass burned, MFB10. As this conditioning sweep was run, notice how the MFB10 point kept steadily advancing closer to TDC (to a CAD of 0), indicative of the accumulation of CCD. However, the rate at which the MFB10 advances begins to decrease with time, and eventually at 40 hours the curve asymptotes at a final crank location, signifying that the CCD layer has reached equilibrium and is no longer growing. Using the high-speed data acquisition software, the advance of LPP and CA50 are constantly checked to determine when the combustion chamber has reached the fully-conditioned state, noted by the time when LPP and CA50 no longer changes.

10.1.2 Compensated Intake Temperature Points for Thermal Diffusivity

As the CCD layer accumulates, a “compensated operating point” is occasionally taken to assess the thermal properties of the layer. As is shown in Figure 10.2, the surface temperature measured by the coaxial heat flux probes described, in Chapter 3 changes over the course of a conditioning sweep.

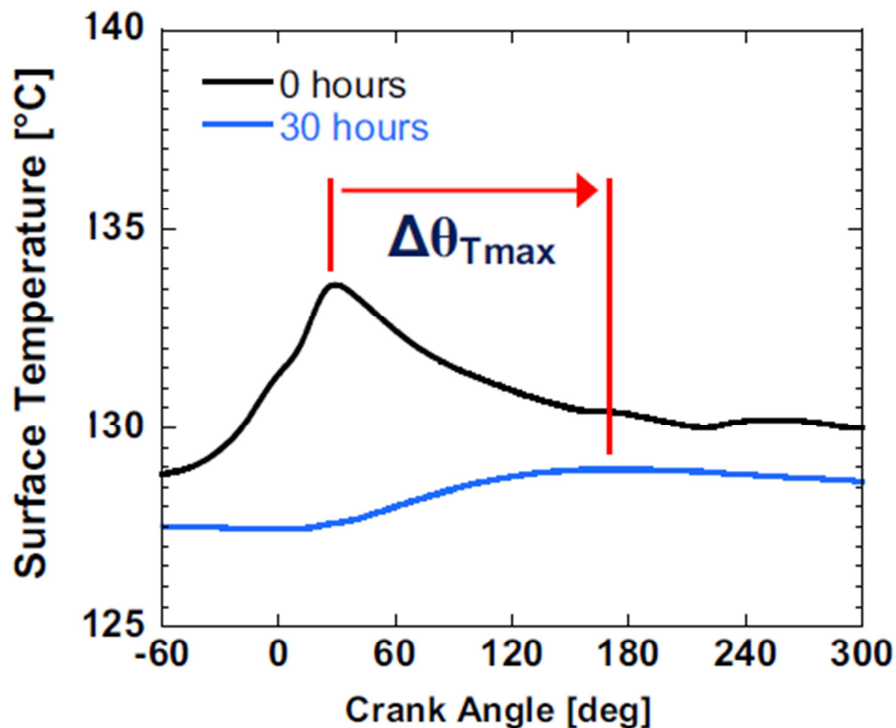


Figure 10.2 - Evolution of cylinder head surface temperature profile with engine run-time as the CCD layer grows on the walls [7]

As deposits accumulate on top of the surface thermocouple junction, the peak of the temperature profile retards to later crank angle degree locations in the cycle, and the magnitude of that peak also decreases. Because at this point, the surface thermocouple in the heat flux probe is physically measuring the temperature at the interface of the CCD and the probe, this effect is expected, as the CCD layer acts as an insulating thermal barrier that inhibits heat transfer to the probe. In order to assess the thermal properties of the layer, it is important to attempt to isolate the effects of the CCD layer on the phase delay realized at the CCD to probe interface, indicated as $\Delta\theta_{Tmax}$ in Figure 10.2, from the advancing CA50 combustion phasing in the engine due to the

CCD layer growth. This is where taking a compensated point is utilized; the intake air temperature is reduced to match the CA50 combustion phasing when the piston was “clean”, at the beginning of the conditioning sweep. At this point, the surface temperature profiles between “clean” and “conditioned” can more readily be compared to determine $\Delta\theta_{T_{max}}$, as the differences seen in temperature phase delay are purely the result of the CCD layer. Using these compensated points, it was possible to characterize in-situ thermal diffusivity (using the method described in Chapter 3) of the CCD layer as it evolves throughout the growth process.

10.2 Testing in a Fully-Conditioned Combustion Chamber

Once the combustion chamber is fully-conditioned and has reached an equilibrium point for combustion phasing advance, a series of other tests are conducted to assess the impact of a fully-conditioned chamber. These tests, in a sense, are intended to link back to the experimental investigations described in Chapters 4-8, which were conducted in “clean” combustion chambers.

10.2.1 “Dirty” Operating Limits

As outlined in Chapter 4, the limits of operability sweep is run once the engine is dirty to see how the deposit layer affects the HCCI operating map. For layers of significant thickness, it is expected that the deposits will shift the map down appreciably, lowering both the low and high load limits. An example of this was shown in Chapter 1, and is repeated here for clarity in Figure 10.3.

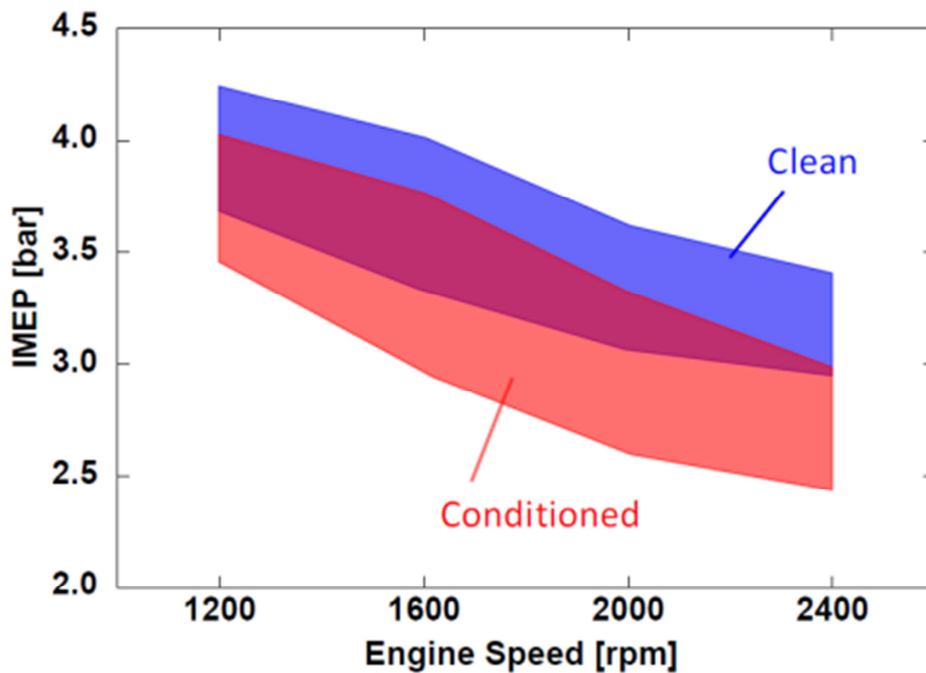


Figure 10.3 - Effect of deposits on HCCI limits of operability; notice that the “clean” operating map is shifted down when the combustion chamber is fully-conditioned

The specifics of this limits sweep are virtually the same as the process described in Chapter 4. The engine is taken to a given speed, and then the fuelling rate is decreased until the COV% of IMEP reaches 5. To determine the excessive ringing limit at each engine speed, fuel is increased until the RI reaches 5 MW/m². Once complete, it is possible to compare the overall load ranges with those from the “clean” limits tests performed in Chapter 6 to discover the impact of different fuel and additive package on the limits of HCCI combustion.

10.2.2 Intake Temperature Sweeps for a Fully-Conditioned Combustion Chamber

During the “clean” tests outlined in Chapter 4, part of the suite of experiments conducted was an intake air temperature sensitivity study. With these tests, the intake temperature was adjusted at a constant engine speed of 2000 RPM until it was high enough to reach the ringing limit, and cooled until instability in the engine, or the lowest temperature that ambient test cell conditions would reasonably permit, was reached. A similar series of tests was conducted with the fully-conditioned combustion chambers to observe the degree to which the deposit layer would impact these sensitivity studies. Instead of matching the energy content of the RD3-87 baseline point, an operating point of 10 mg of fuel per cycle was utilized, to facilitate running a wider range of intake temperatures. For the method used to determine the equivalent fuelling rate for test matrix fuels see Chapter 4.

Table 10.3 - Equivalent Fuelling Rates for Intake Air Temperature Sweeps

Fuel	LHV (kJ/kg)	Fuel injected (mg/cycle)
D10	40945	10.5
D10+PBA	Same as D10 base fuel	
D10+PEA		
CARBOB	41621	10.3
CARBOB+PBA	Same as CARBOB base fuel	
CARBOB+PEA		

For the purposes of comparison with the “clean” tests conducted in Chapter 4, the following procedure was used for the CCD studies, test matrix fuels. First, for each intake air temperature point collected during the clean test, the CA50 and LPP were

determined using the heat release post-processing code. Then, with the fully-conditioned chamber from the base fuels, in Table 10.3, the intake temperature was adjusted to match the same phasing as the “clean” point. For the fuels with additives, the same intake temperature was used as the points from the conditioned base fuels’ tests to make a comparison across the matrix, and connect the base fuels back to early “clean tests” where only unadditized base fuels were run.

10.2.3 Coolant Temperature Studies for the CCD Coated Combustion Chamber

One further test was conducted once the CCD reached equilibrium, where the coolant temperature was successively dropped and the change in phasing recorded, with all other operational parameters held constant. In particular, the temperature was noted where the CA50 of the clean baseline was recovered, with the fuels all run over the same sweep of coolant temperatures, from approximately 95°C down to 70°C. These tests were run at the baseline fuelling, shown in Table 10.2, in order to compare similar phasing for less conditioned operating points with those of fully-conditioned combustion chambers. In this manner, it is possible to determine some of the effects of coolant temperature compensation on burn rates and the HCCI combustion event.

10.2.4 Thickness Mappings

Once all the experiments were completed for a particular fuel, the engine cylinder head was disassembled and removed so photographs could be taken of the resulting CCD layer on both the piston and valve area. Thickness readings were taken using the

Fischer Dualscope, mentioned in Chapter 2, by averaging ten different measurements for each location. This results in a precision error in the readings, on the order of about 5% of the average value (i.e. 50 μm would have an uncertainty of $\pm 2.5 \mu\text{m}$). The images shown in Chapters 11 and 12 have these average thicknesses superimposed over the pictures of the CCD layer on the piston and cylinder head.

CHAPTER 11

Effect of Fuel Composition on HCCI Combustion Chamber Deposits

11.1 Introduction

This chapter investigates deposit conditioning sweeps run for the two unadditized refinery stream fuels detailed in Chapter 10. To characterize the impact of a fuel's chemical components on the CCD layer, deposit thickness maps were created to provide a qualitative comparison of the amount of in-cylinder growth that results from each fuel. Additionally, engine operation and emissions measurements were tracked over the duration of the conditioning process to see how combustion phasing changes. Finally, the data from the coaxial heat flux probes was analyzed and the process of deposit accumulation on the cylinder head was compared to the combustion event happening in the chamber.

11.2 Deposit Conditioning Sweeps

As mentioned previously, once the experimentation for a given fuel was complete, the engine was disassembled to further explore and qualitatively analyze the resulting CCD layer that had accumulated in the combustion chamber, using digital imaging. The following figures provide a pictorial indication of the accumulation of deposits in-cylinder for each test fuel, as well as the thickness measurements acquired using the Fischer Dualscope. The orientation of the piston and cylinder head in each picture is consistent; the side of the engine with the intake runner and fuel injector is always on the right side of the photograph, while the exhaust is on the left side. Also, all the locational thickness measurements are given in micrometers.

The piston coatings evaluated in Figure 11.1 and Figure 11.2 from the D10 and CARBOB+10%EtOH blends, respectively, cover the entirety of the piston bowl and periphery. As shown by these photographs, using the base fuels with no additive resulted in a piston top that appears completely black due to the presence of a ubiquitous CCD layer. However, there is an appreciable difference in the relative thicknesses of the layers, as well as the locations where more deposits accumulate. The CCD layer created by D10 fuel, for instance, is substantially thicker around the entire top of the piston, which is likely due to the fuel's chemical components and the high concentration of aromatics, a recognized deposit precursor. Several previous studies of deposits in SI engines concluded that fuels containing more complex molecules with higher boiling points, such as aromatics, lead to increased buildup of deposits [15, 19]. D10 is composed of a much higher concentration of aromatics by volume than CARBOB+10%EtOH (37.0% to 23.2%, respectively), so it is reasonable to

deduce that in the case of HCCI combustion, fuel composition does indeed play a role in the overall deposition of partially unburned fuel species that condense on the chamber walls, much as it does in SI combustion.

Furthermore, the physical properties of the fuel itself may induce varied growth in different portions of the combustion chamber, and this effect is most likely exacerbated by the directly injected fuelling strategy used in this experimental setup. The thickest regions of the CCD layer created by each fuel are not located in the same region of the piston. For the D10 fuel blend, in Figure 11.1, the most appreciable growth is on the interior of the bowl closest to the fuel injector. There is also a substantial amount of deposition just outside of the bowl on the flatter region located just below the fuel injector spray. With the CARBOB+10%EtOH blend, while there is a similarly thick region located on the periphery of the piston, on the outside of the bowl near the fuel injector, there is substantially less growth inside the bowl. The thickest regions are shifted slightly, to the bottom, inside part of the bowl and there is a region of heavy growth on the “squish” downward sloping region of the piston. Whereas the D10 blend also has its thickest layer of deposition in the middle of the bowl, the CARBOB+10%EtOH has relatively little deposit growth in the bowl, with the exception of the bottom location.

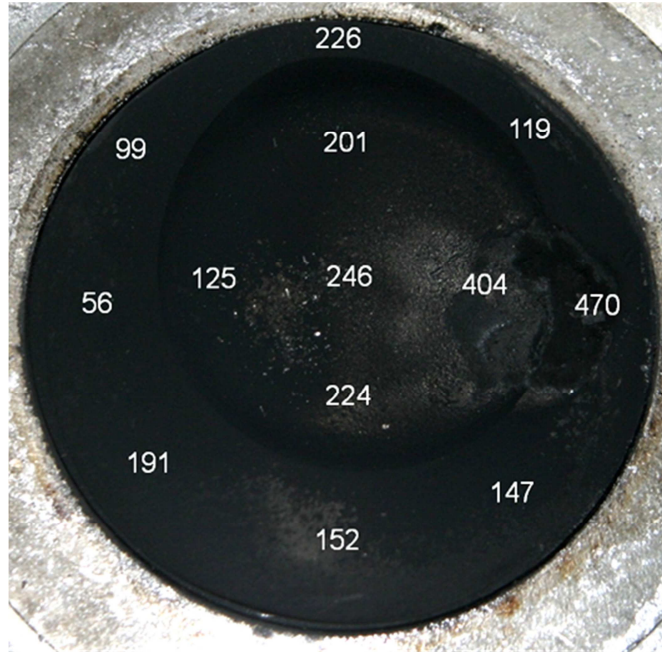


Figure 11.1 - Deposit layer formed by D10 fuel on the piston; measurements given in μm



Figure 11.2 - CCD layer formed by CARBOB+10%EtOH on the piston; measurements given in μm

The slight differences in deposit distribution could be attributable to the varying location of available partially unburned, hydrocarbon species in-cylinder that condense on the piston's surface. This may result from small variations in spray dynamics that are the product of properties (i.e. distillation curves and densities) of the fuel blends. Fuel injection occurs at a constant pressure, of about 110 bar for both blends, so there is no adjustment or normalization attempted to compensate for dissimilarities between fuels' properties. Based on the thickness of deposits closest to the spray of the fuel injector and on the variation in thickness created by each of the two blends, it is reasonable to conclude that dissimilar, directly-injected fuels accumulate relatively more deposits in different regions. Most likely, this phenomenon is largely a function of piston geometry.

The pictures in Figure 11.3 and Figure 11.4 show the CCD layer that accumulated on the cylinder head. Again, the orientation is the same as in the piston photos, with the intake on the right side of the pictures and exhaust on the left. The "squish" side heat flux probe is located at the top of the photos and the "anti-squish" probe is at the bottom. As illustrated in the figures, the overall thickness of the CCD layer from the D10 blend is appreciably more than that created by the CARBOB+10%EtOH blend over the entire cylinder head surface. In fact, for the CARBOB+10%EtOH fuel, the only significant buildup on the cylinder head occurs on the intake valves (the two larger valves on the right side of Figure 11.3 and Figure 11.4) where the surfaces is somewhat cooled by the flow of incoming fresh air.

In summary, there is clear evidence that the chemical composition of fuel plays a role in the thickness of accumulated deposits at all locations in-cylinder, on both the

piston and the cylinder head and valves. The difference likely results from the presence of elevated levels of more complex molecules, chiefly aromatics, in the D10 blend. These aromatics appear to have a similar deposit promoting effect in HCCI engines as has been previously shown in SI engines.



Figure 11.3. Deposit layer on the cylinder head resulting from the D10 fuel; measurements given in μm



Figure 11.4 - CCD layer on the cylinder head resulting from CARBOB+10%EtOH; measurements given in μm

11.3 Advancement of Combustion Phasing and Characteristics of the Engine Performance as Deposits Accumulate

To this point, only the condition of the deposit layer at the equilibrium point, with the engine disassembled, has been considered. But in moving forward it is also necessary to characterize how these layers impact engine performance and operation during the accumulation period, prior to this equilibrium point. The first metric to consider is the advance of combustion phasing as the layer accumulates in-cylinder, which is tracked during experimentation by the CA50.

As Figure 11.5 shows for the evolution of CA50 for the two test fuels, there are a number of marked dissimilarities between the two accumulation processes. Chiefly, the D10 fuel blend takes roughly twice the length of engine run-time to reach an equilibrium

point. Additionally, the equilibrium CA50 of the D10 blend is slightly more advanced and closer to TDC than that of the CARBOB+10%EtOH. The overall change in recorded CA50 from clean to fully-conditioned is noticeably different between the fuels, nearly 11.5 degrees of overall CA50 advance for the D10 blend and only 3.5 CAD for the CARBOB+10%EtOH fuel. One further observation of note is the first recorded starting point of each fuel, as the CARBOB+10%EtOH begins at a much lower CA50 than the D10 blend. This is likely a consequence of the speed with which the initial layer coats the piston and cylinder head. Recall that the first data points are taken after the engine has had some time to warm up and stabilize following start-up. However, deposits accumulate on the metal surfaces as soon as fuelling begins, so there is an initial part of the deposit building process that is not captured. In this phase of growth, it is difficult to decouple combustion advance due to the engine warming up from the advance due to deposit growth.

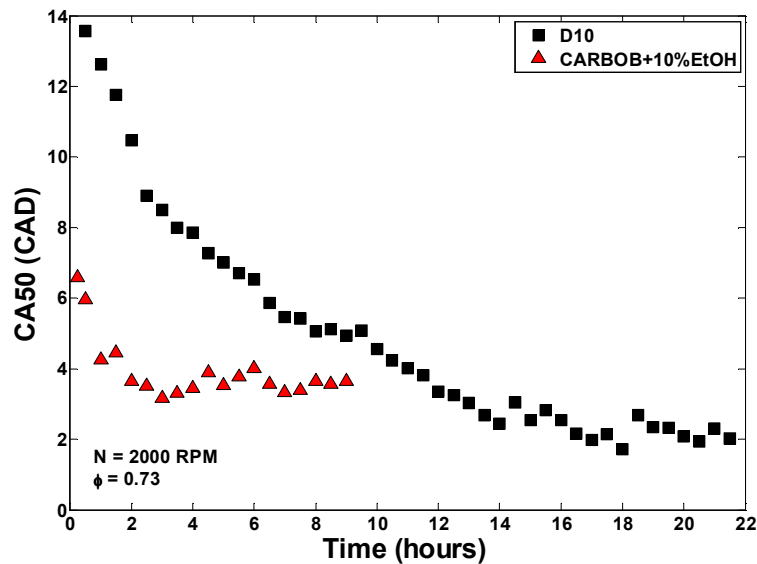


Figure 11.5 - Change in combustion phasing given by CA50 as the deposit layer accumulates

When starting from a completely clean engine, combustion was extremely unstable for both fuels after the first 3-5 minutes of run-time. However, an initial data point during the conditioning sweeps was not collected until after the engine had sufficient time to warm-up and had truly reached a steady-state condition, a period of at least 15 minutes. In this early start-up period, the CARBOB blend seemed to build a base CCD layer more quickly than the D10, which took nearly 5 hours of running to reach the same combustion phasing as the starting mark for the CARBOB blend. So, while the CARBOB+10%EtOH was a “cleaner” fuel in terms of the thickness of deposits that accumulated in-cylinder (shown previously in Figure 11.2 and Figure 11.4) and in terms of final crank angle location of the equilibrium CA50, it actually has a much faster rate of initial buildup than D10. The CARBOB blend can also be thought of as a cleaner fuel due to its significantly lower concentration of aromatic compounds as compared to the D10 blend, since aromatics are considered to be a precursor to in-cylinder deposit formation in gasoline engines. In this directly-injected HCCI engine application, what would be regarded as a chemically “clean” fuel in fact forms deposits more quickly on a metal piston free of deposition. However, in the end, the CCD growth caused by “dirtier” fuel containing higher aromatics, eventually overcomes and far surpasses the growth caused by “cleaner” fuel.

Further examination of the CCD accumulation period is presented in Figure 11.6 and Figure 11.7, which show the evolution of RI and COV% of IMEP, respectively. As expected, because the initial coating occurs so quickly (within the first 15 minutes) with the CARBOB blend, it begins at a much lower COV% of IMEP than the D10, and as a result the engine runs more stably at an earlier time. Because substantial deposit

growth occurs earlier, the RI of the CARBOB is also high at the outset of the conditioning sweep. Consistent with the advancement of CA50, as time progresses with the D10 blend, the CCD layer thickness eventually exceeds that of the CARBOB, and the COV% of IMEP reaches a lower point, as the RI climbs to high levels that greatly surpass the acceptable upper noise constraint of 5 MW/m².

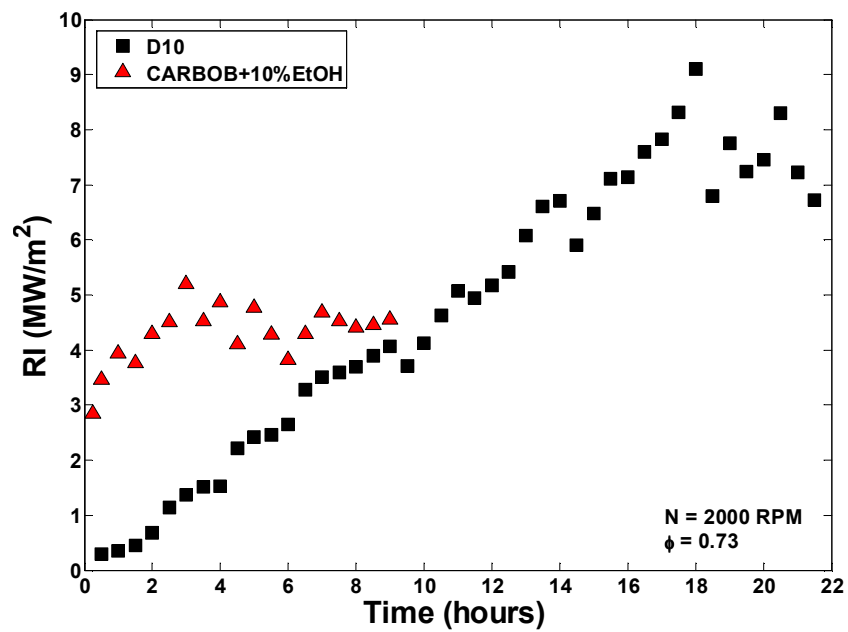


Figure 11.6 - Ringing intensity increase as deposits build in-cylinder over the conditioning sweep

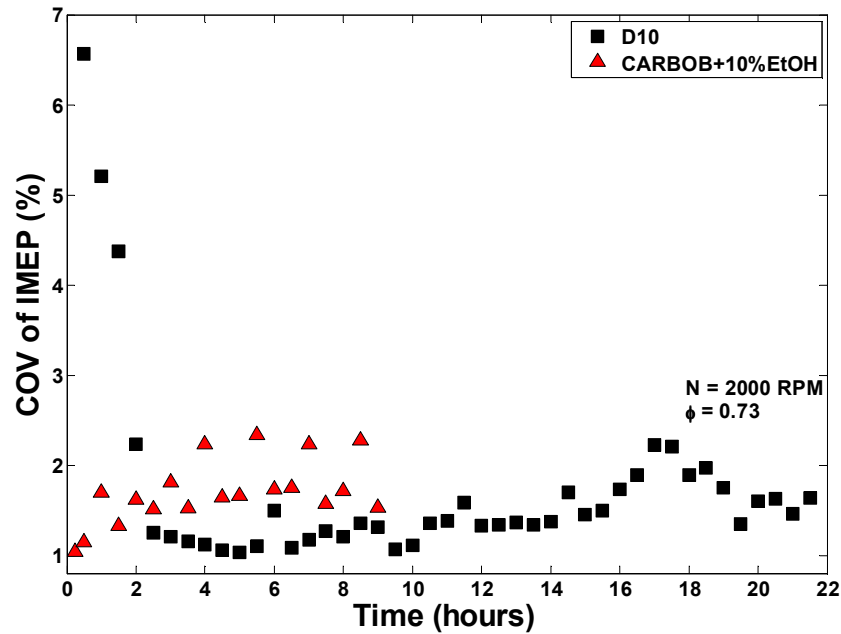


Figure 11.7 - Coefficient of variance (COV) percentage of indicated mean effective pressure (IMEP) during the conditioning sweeps of the two fuels

One interesting behavior to note in Figure 11.7 is that the COV% does not monotonically decreasing as time progresses and the CCD layer builds, and in the case of the CARBOB+10%EtOH it actually vacillates about 0.5% throughout the conditioning sweep. Even the D10 blend has an appreciable swing in COV% from 16-19 hours of operation. This could be an indication of deposit burn-off or flaking, and subsequent regrowth, which is a phenomenon that has been observed in SI gasoline engines [73, 171]. As was mentioned, there is a rapid initial development of deposits using the CARBOB+10%EtOH fuel, therefore it is not surprising to see that this burn-off and regrowth behavior occurs at a more frenetic pace than the gradual process observed in Figure 11.7 for the D10 blend. It is possible to imagine a scenario in which, if burn-off or flaking of the CARBOB+10%EtOH CCD layer reveals a clean patch, a rapid rebuilding

period, as is shown with the completely clean metal piston, would occur. This could account for the more pronounced wavering of the COV% of IMEP shown with the CARBOB blend, as opposed to the D10, which does not display such oscillations, and has one large hump late in the conditioning sweep.

In order to gain further insight into the phenomena surrounding changes in the combustion event as the CCD layer accumulates, it is necessary to consider a few emissions plots. The emissions indices for NO_x and hydrocarbons (HC) are shown in Figure 11.8 and Figure 11.9. NO_x species are strongly tied to higher in-cylinder temperatures, and they should thus correlate well with more advanced combustion phasing and higher ringing intensities. Indeed, as the CARBOB+10%EtOH sweep begins at a more advanced CA50 and higher RI, there is a commensurate level of higher NO_x emissions than is initially produced by D10. With longer engine run-time, the D10 emissions eventually reach and surpass those of the CARBOB blend. Both of these fuels, at the equilibrium level of CCD growth, are above the desired level of 1 g/kg fuel for EINO_x.

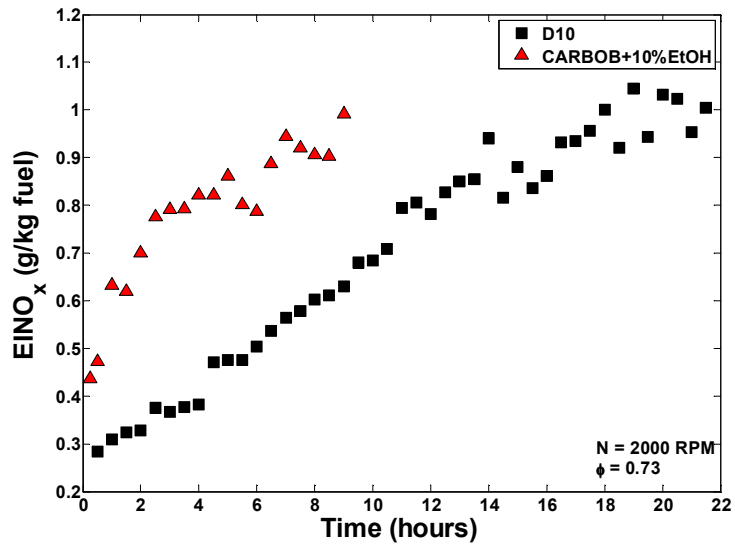


Figure 11.8 - Emissions index for NO_x (EINO_x) over the course of the conditioning sweep for each fuel

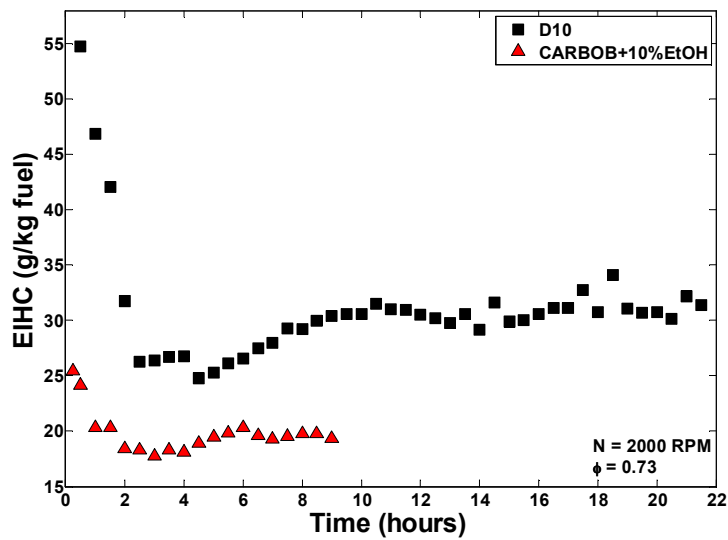


Figure 11.9 - Emissions index for hydrocarbons (EIHC) while deposits accumulate in-cylinder for each fuel

The HC emissions plotted in Figure 11.9 display some interesting phenomena, including some which are unexpected. With both fuels, there is a steep initial decline in HC, which is to be expected as the deposit layer begins to accumulate and in-cylinder temperatures rise, resulting in higher combustion efficiency and less HC emissions. This initial behavior is confirmed by Figure 11.10, which shows that there is initially a sharp increase in combustion efficiency for both fuels during the initial buildup stage of CCD formation. The D10 blend also maintains a higher overall EIHC over the course of the conditioning sweep, owing in large part to lower combustion efficiencies during the sweep.

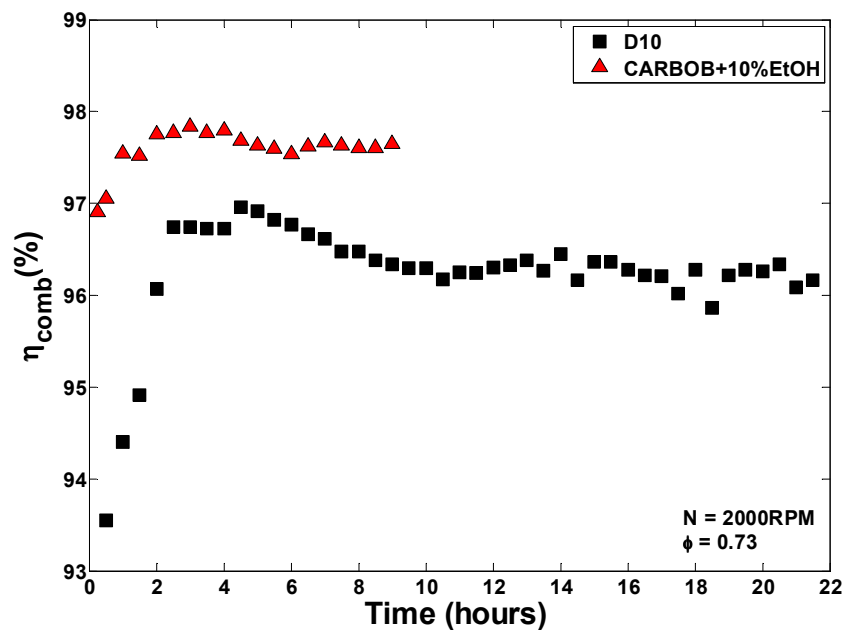


Figure 11.10 - Change in combustion efficiency calculated from emissions measurements as a function of engine run time

This phenomenon may be influenced by the compositional differences in the two fuels, as D10 has significantly more aromatics by volume, a molecule that is more difficult to auto-ignite. Most likely, this increased resistance to auto-ignition results in the slightly decreased combustion efficiencies shown when D10 is compared to the CARBOB+10%EtOH. It appears that the chemical components of refinery stream fuels play a role in the total percentage of fuel burned and the resultant HC emissions.

The one development shown in Figure 11.9 that is surprising is that the EIHC is not a monotonically decreasing quantity, as was expected with increased CCD growth, higher in-cylinder temperatures and more advanced combustion. At roughly the same time for both fuels (around 4 hours of engine operation) the EIHC actually begins to increase with subsequent run time. Eventually, in the case of both fuels the EIHC levels off and starts to asymptote, but the behavior raises an important question as to why this might occur. Looking again at Figure 11.10, there is a small dip in combustion efficiency for both fuels at roughly 4 hours, which correlates strongly to the point at which HC emissions begin to increase. It is reasonable to conclude that there is some in-cylinder event occurring which causes less fuel to be burned during the combustion process. This occurs despite what appears to be more robust, and likely higher temperature combustion, as is shown in Figure 11.5 by the advancing CA50 over the conditioning sweep. A likely explanation is one that involves the physical mechanism by which the fuel is delivered in-cylinder; the spray impinges on the piston in the middle of the offset bowl. Previous work in SI engines has revealed that as the CCD layer grows, it becomes a porous network across the combustion chamber [117]. It is possible that when the fuel spray impinges on this layer, some of the fuel may become trapped in the

pores of the CCD layer during combustion, and is later outgassed into the exhaust. This would account for the loss of combustion efficiency and the increase in EIHC that arises as the layer accumulates with increasing engine run time. The dip in combustion efficiency also highlights potential competition between the effects of a higher temperature incoming fuel/air mixture, as increased CCD thickness causes more charge heating, and the effect from fuel becomes entrained in the CCD's pores. Initially, the charge heating and combustion phasing effect is more dominant, but after a few hours the wetting of the CCD layer becomes more prevalent, with dips in the combustion efficiency and slight increases in EIHC. As time passes, and the CCD layer approaches its equilibrium thickness, it appears that for either fuel, the two effects begin to balance each other out, as the combustion efficiencies and EIHC measurements asymptote.

11.4 Cylinder Head Surface Temperature and Heat Flux

As the deposit layer accumulates on top of the specialized, coaxial heat flux probes located in the cylinder head, the surface temperature profile measured at the CCD layer-probe interface changes accordingly. The front-side, thermocouple junction in the probes is only measuring the temperature at the metal surface, where the CCD layer and the probe meet. Thus, as CCD accumulates on this face, and conducted heat encounters a resistive path to reach the probe, the surface temperature profile is altered. The nature of this change relates to the thickness and properties of the layer that atop the probe surface.

For the following plots, recall from Figure 2.4 and Figure 2.5 that there is one heat flux probe at location 1 over the “squish” region of the piston where the clearance

volume is at a minimum, and another probe at location 2, in the “anti-squish” region of the piston. Figure 11.11 and Figure 11.12 display the surface temperature profiles measured from the front-side thermocouples heat flux probe at location 1 over the course of the conditioning sweep, for the D10 and CARBOB+10%EtOH fuel blends. Figure 11.13 and Figure 11.14 show similar profiles for the probe at location 2. While there is some similar behavior between the fuels, there are significant differences in the evolution of the temperature profiles, implying that, at least on the surface of the cylinder head, the CCD accumulation process is dissimilar between these two fuels.

The first set of phenomena to consider is the location of the peak temperature and the shape of the temperature profile. As discussed previously, the more the deposit layer builds on top of the front-side thermocouple, the more it retards the location of the peak temperature during the engine cycle, and flattens the curve. Recall from Figure 11.3 and Figure 11.4 that at the equilibrium the thickness of deposits measured from the D10 fuel blend is roughly two and half times that of the CARBOB+10%EtOH. Therefore, the expectation is that the D10 fuel will exhibit more retardation of the location of peak temperature and a more severe change in the shape of the temperature profile. In fact, this is what was observed at both probe locations over the course of the conditioning sweep, as the much “dirtier” D10 fuel causes a significant change in the shape of the temperature curve, which becomes nearly flat after 20 hours at location 1 shown in Figure 11.11. In contrast, while the CARBOB+10%EtOH blend had some retardation of the peak temperature at each probe location, the shift is less significant than what is exhibited with the D10 fuel, and the shape of the curve flattens noticeably less than with D10. Again, this difference is related to the varied thickness of

deposits on the thermocouple junction of the heat flux probe, as the CARBOB blend deposits were thinner than the D10 deposits.

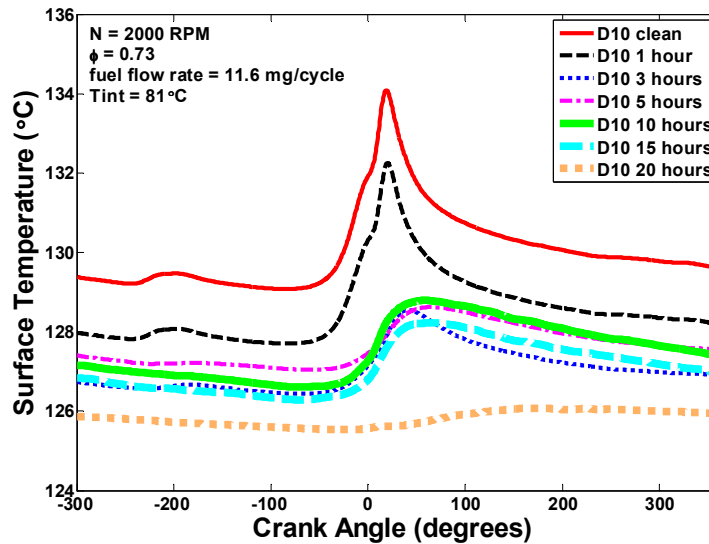


Figure 11.11 - Probe 1 surface temperature for the D10 blend while the deposit layer accumulates

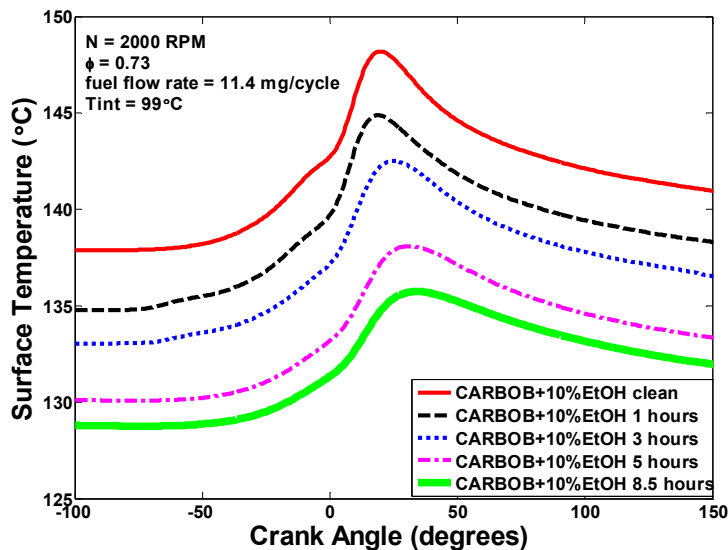


Figure 11.12 - CARBOB+10%EtOH temperature at the interface between the surface of probe 1 and CCD interface, changing with engine run-time

Another interesting observation to consider is the change in surface temperature profiles that occurs at both probe locations during the conditioning sweep. Recall from Figure 2.4 and Figure 2.5 that the piston's surface geometry creates a "squish" and "anti-squish" region where probe 1 and 2 are located, respectively. The "squish" region has the smallest clearance volume in-cylinder and generates the highest temperatures, while the "anti-squish" side has a higher clearance volume and lower overall temperatures during combustion. This configuration results in a higher temperature swing, which is the difference between the maximum and minimum temperatures at the probe's surface at location 1 as opposed to location 2. Initially, at the "clean" points for D10, the swing for location 1 is roughly 5°C, whereas in location 2 it is approximately 2.5°C. In examining Figure 11.11 and Figure 11.13 there are some noticeable differences in the accumulation of the CCD layer on the heat flux probes in location 1 and location 2, particularly in the measurements taken at the higher values of engine run-time. Looking specifically at the 20 hour point, at which the CCD growth has reached an equilibrium (in Figure 11.5 the CA50 reaches an asymptote at this time), there is more attenuation of the surface temperature signal for the probe on the "squish-side" location (location 1) as opposed to the probe on the "anti-squish" side (location 2). This initially seems counter-intuitive, as the overall thicknesses for the heat flux probes in each location were fairly similar, 83µm in location 1 and 82µm in location 2. But, as stated previously, the thickness is determined by taking a number of measurements around the probe junction and averaging them. Therefore, this measurement is not necessarily representative of the exact thickness of deposits over the surface of the thermocouple junction, and it is the exact thickness which directly affects the surface

temperature profile readings. In Figure 11.15, despite the fact that there is a thick accumulation of deposits over the entirety of the heat flux probes, in the small area of the thermocouple junction there is less CCD growth at location 2 (shown on the right) than at location 1 (shown on the left). Referencing Figure 11.13, the peak of the surface temperature is slightly retarded at 20 hours versus 15 hours of operation, indicating that some of the deposit layer may have burned off or flaked off during that time, causing the junction to be less covered.

Turning to the CARBOB blend, when surveying the temperatures of the two probes in Figure 11.12 and Figure 11.14, it becomes apparent that there is a steady progression of overall temperature, decrease as well as phase shift in the location of peak temperature, as the CCD layer accumulates. The chief implication inherent in this data is that the CCD growth rate is steady throughout the conditioning sweep (albeit small overall compared to the D10), and occurs in a more uniform manner across the two cylinder head locations than growth CCD growth from the D10 fuel. Hence, the difference in the fuels' chemical composition clearly has an impact on the distribution of deposits on the cylinder head. Furthermore, reconsidering Figure 11.5 for the CARBOB+10%EtOH blend, from the point at 3 hours to the point at 5 hours, it becomes apparent that there is actually a slight retardation of CA50, indicating the potential removal of deposits cylinder-wide. However, in both locations on the cylinder head, from 3 to 5 hours there is a slight advance in the location of peak temperature and small reductions in the maximum temperature, as shown in Figure 11.12 and Figure 11.14, both of which suggest that deposits on the cylinder head are actually *increasing* in thickness. The underlying theme is that deposits do not necessarily grow at a steady

rate in different parts of the cylinder in an HCCI engine, and where the deposits actually accumulate has an impact on the combustion event. More specifically, in the case of the CARBOB+10%EtOH fuel and the resulting CCD layer, the growth of CCD on the piston has a more dominant influence, affecting the overall combustion process; while head deposits grew and piston deposits decreased, combustion retarded, which is indicative of an overall layer loss.

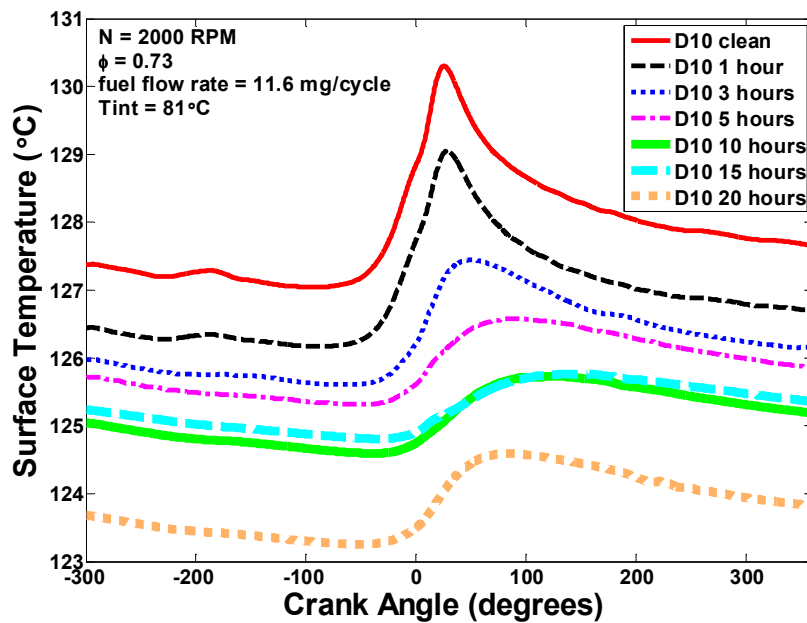


Figure 11.13 - Surface temperatures for probe 2 located in the “anti-squish” region as deposits build over the surface of the thermocouple for D10 fuel

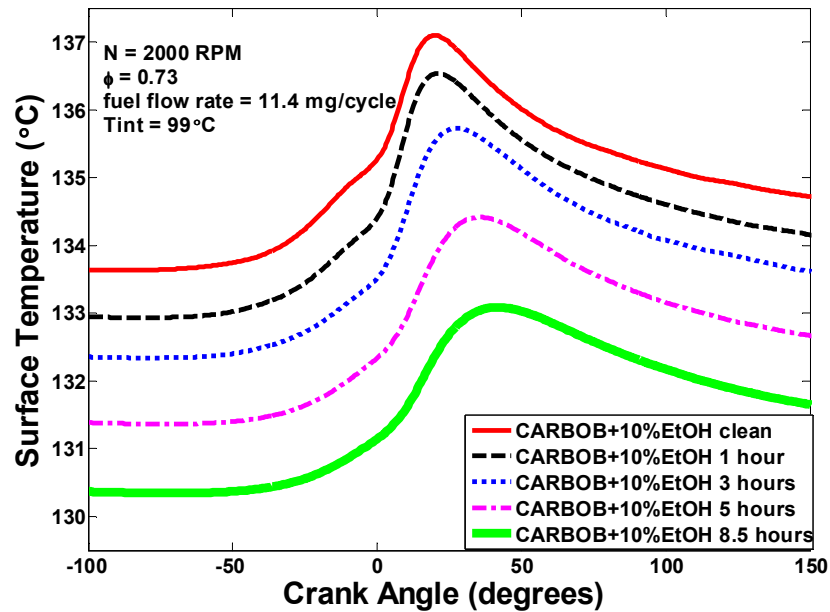


Figure 11.14 - The surface temperature for probe 2 (“anti-squish”) for CARBOB+10%EtOH at the CCD interface, changing with engine run-time



Figure 11.15 - D10 heat flux probes after engine disassembly from the fully-conditioned state; the probe from the “squish” region is on the left and the probe from the “anti-squish” region is on the right; the thermocouple junction partly visible is highlighted by the box in the picture

Another useful way to view and analyze the accumulation of deposits is to use the heat flux through each probe. Figure 11.16 and Figure 11.17 show the heat flux through the “squish” side probe for the D10 and CARBOB blends, respectively, and Figure 11.18 and Figure 11.19 show the heat flux for both fuels on the “anti-squish” portion of the cylinder head. As expected, as temperatures are higher in the “squish” side of the combustion chamber where there is a lower clearance volume, the heat flux at the probe in location 1 is at a higher level than in location 2 for both fuels, just as with the surface temperature profiles. Another finding confirmed by the heat flux traces is the relative difference in apparent deposit growth between the two fuel blends. For the D10 blend in Figure 11.16 and Figure 11.18 there is a significant drop off in heat flux between the 1 hour point and the 3 hour point, since there is significant growth during this initial period. However, this slows considerably after 5 hours of engine run time. The CARBOB+10%EtOH blend is considerably steadier in its rate of heat flux change; the peak of the heat flux retards and its magnitude decreases more regularly than the heat flux for the D10 blend. Another observation deduced from these figures is that the total heat flux for the cycle through the probes is unchanged despite the insulating properties of the deposit layer. As is shown from the highly attenuated heat flux signals for the thick buildup on the D10 probes, the overall amount of cycle time (crank angles) over which the heat flux transpires is lengthened as the peak retards and the peak magnitude decreases. In the case of D10 a thicker layer has a heat flux at the wall that occurs over a longer period of time than occurs with the much thinner layer created by the CARBOB+10%EtOH blend.

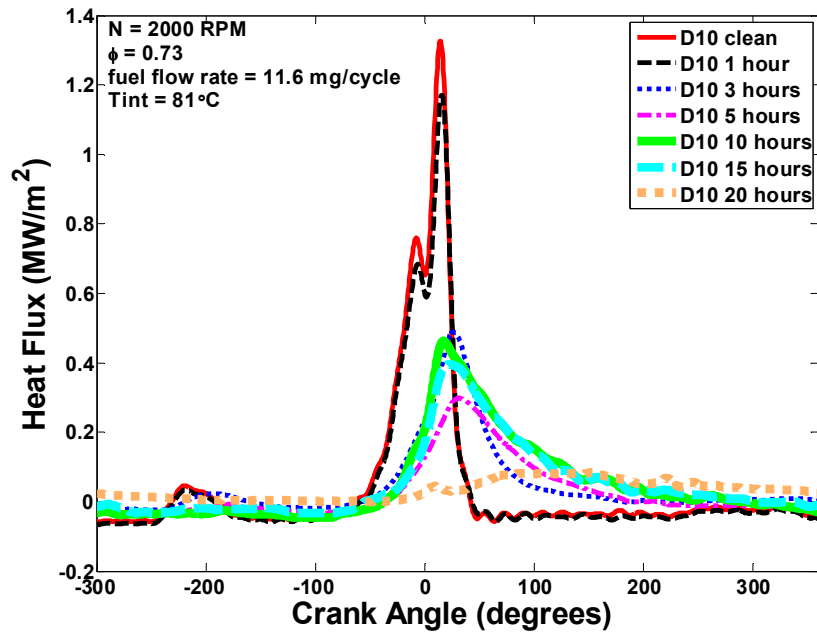


Figure 11.16 - Heat flux through the squish side probe in the cylinder head as the CCD layer evolves for D10 fuel

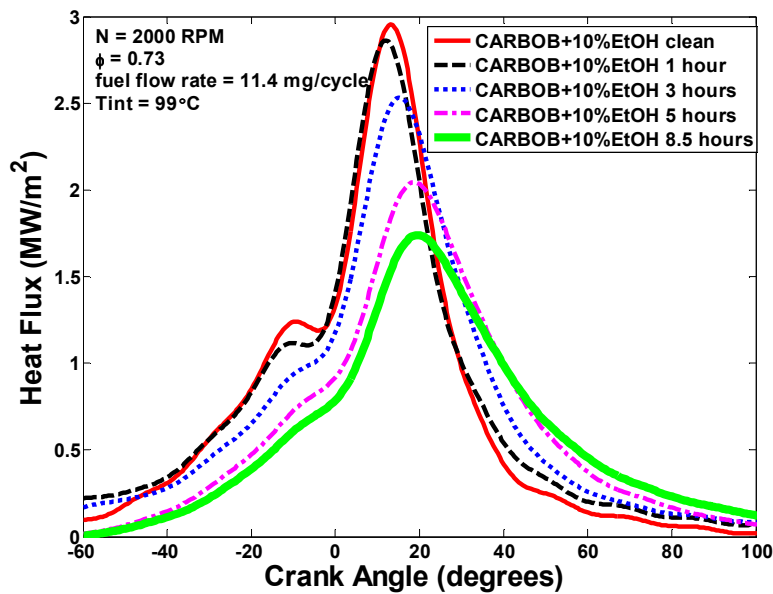


Figure 11.17 - CARBOB+10%EtOH heat flux at location 1 in the cylinder head as the CCD layer accumulates

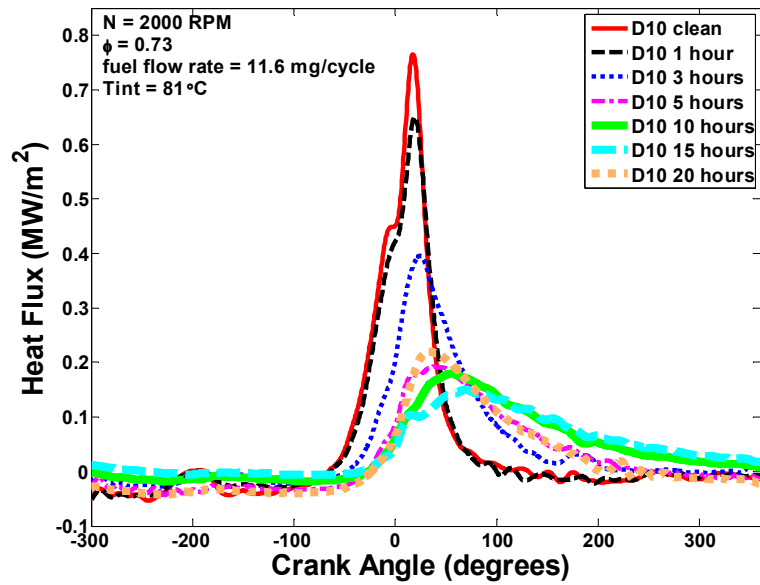


Figure 11.18 - Cylinder head probe 2 heat flux during the deposit conditioning sweep for D10

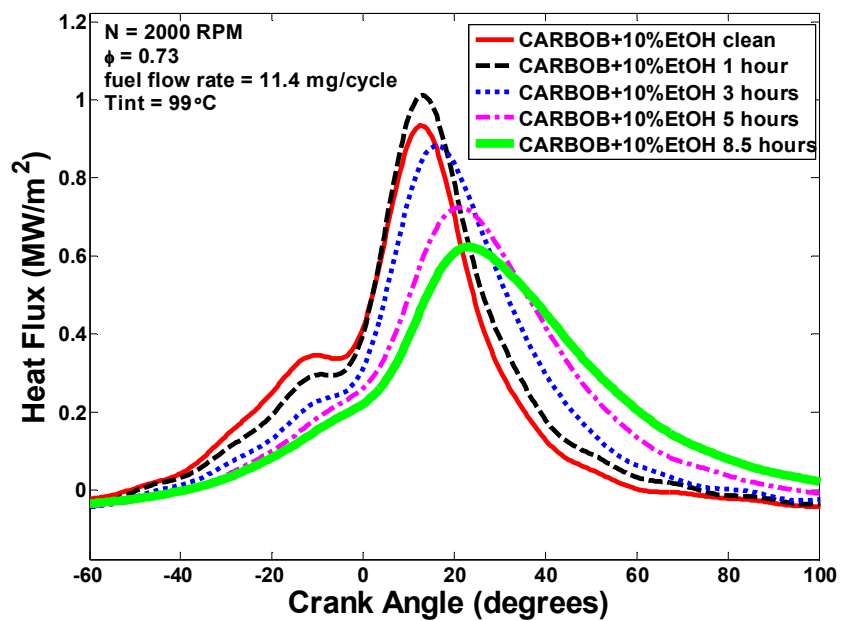


Figure 11.19 - CARBOB+10%EtOH heat flux at cylinder head location 2 as the deposit layer builds over the probe

The final set of plots to consider is the net heat release rates in-cylinder during the deposit accumulation process, for each fuel. Here, the presence of deposits is detected from the advance in phasing of the peak NHRR and the increased magnitude of that peak. Additionally, as the deposit layer accumulates and the heat release speeds up, the total amount of crank angles over which that heat release occurs is shortened. For the D10 change in NHRR (shown in Figure 11.20) there is a much more significant increase in the amount of peak magnitude and peak phasing advance than for CARBOB+10%EtOH (shown in Figure 11.21). Again, for both fuels, as the engine run-time increases, the rate at which the NHRR changes decreases, and for much of the CARBOB+10%EtOH conditioning sweep there is little growth occurring. Moreover, from the 3 hour mark to the 8.5 hour mark of the sweep, there is a slight decrease in the magnitude of the peak and a small retardation in the peak location, which alludes to the fact that there has been some burn-off or flaking of deposits in the cylinder as a whole. This fact is consistent with the CARBOB+10%EtOH results in Figure 11.5, which show a slightly more advanced CA50 combustion phasing at 3 and 5 hours, than at the end of the CARBOB blend sweep, at 8.5 hours.

Scrutinizing Figure 11.20 further substantiates a previous point that perhaps the evolution of deposits on the piston and the cylinder head does not necessarily follow the same development mechanism, depending on a fuel's chemical components. While the buildup from the CARBOB+10%EtOH blend is gradual over the course of the entire conditioning sweep, as shown previously and again in the NHRR plot, the D10 heat flux probes have an uneven change in surface temperature and heat flux. Hence, it appears that CCD growth on the cylinder head from the D10 fuel is, at times, sporadic.

However, the NHRR has a steadier advance than the surface temperature profiles of the cylinder head probes. This complements the notion that the overall cylinder-wide deposit growth does not necessarily follow the trend of growth on the cylinder head, and furthermore, that the piston deposits play a more integral role in the entire combustion event than CCD accumulation on the cylinder head.

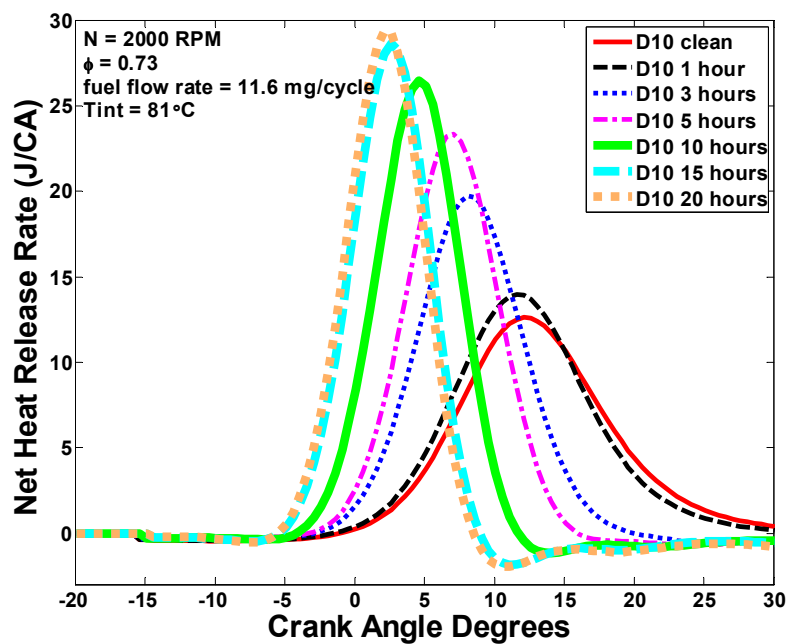


Figure 11.20 - In-cylinder net heat release rates for the D10 blend as deposits grow

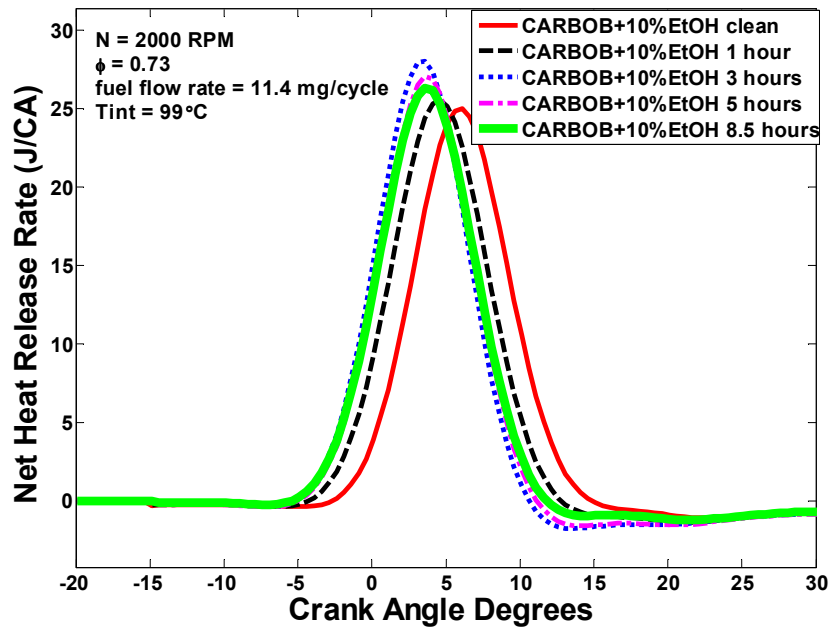


Figure 11.21 - CARBOB+10%EtOH net heat release rates in-cylinder with engine run-time

11.5 A Brief Note on Repeatability of Conditioning Results

Towards the end of the experimentation for the deposit studies presented in this chapter and the next, the base D10 fuel which remained following the first conditioning sweep was retrieved and rerun through the engine. The drum containing this leftover D10 sat in the fuel shed for roughly 5 months, and other critical experiments were run in the interim. This virtually guarantees that the results will not be exactly the same, however, some agreement between the two runs is still expected. Figure 11.22 has the CA50 results against time for the original D10 conditioning sweep, as well as the results of the sweep run 5 months later.

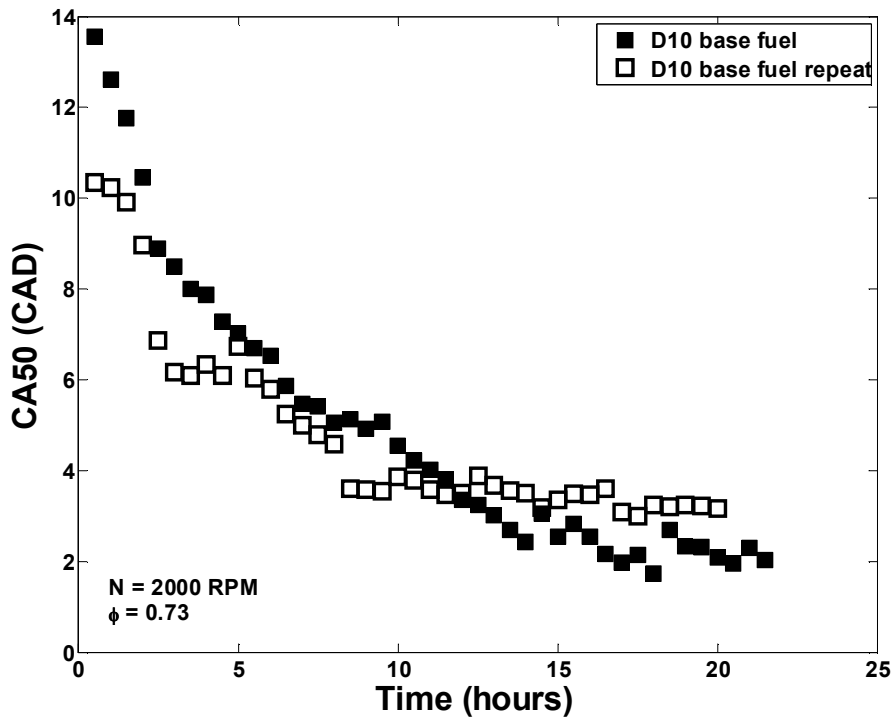


Figure 11.22 - Two conditioning sweeps for the base D10 fuel with no additive, showing CA50 against engine run time

There are a number of similarities between the two sets of measurements, indicating that the impact of deposits from the base D10 fuel on combustion phasing is repeatable and not specific to the way in which the experiment was conducted. Both of these processes have a rapid advance in CA50 during the first few hours of operation, followed by a more gradual rate of phasing change, and finally an asymptote at the equilibrium CA50 for the fully developed CCD layer. The original run ended at a CA50 of about 1 CAD lower than the later test, although it bears repeating that these two fuels are not exactly the same. As soon as the barrel of fuel is first opened and the seal is broken, the light fraction components of the gasoline vaporize, escaping from the drum. This has a slight effect on the chemical makeup of the fuel, which is exacerbated as

more time elapses and the fuel sits dormant. Hence, the results in Figure 11.22 are not expected to be exactly the same, as the fuel is marginally different. But it is encouraging that the general trends remain consistent from one run to the next.

CHAPTER 12

The Role of Additive Packages in HCCI Deposit Accumulation

12.1 Introduction

The previous chapter explored the impact of refinery stream fuels' chemical composition on the CCD layer that accumulates in the HCCI engine. In this chapter, the focus shifts to the role of fuel additive packages in the formation of HCCI deposits. Specifically, the equilibrium CCD layers are examined in detail with the engine disassembled, and in-situ engine changes are analyzed over several conditioning sweeps in a similar fashion to the experiments discussed in Chapter 11.

12.2 Thickness Mappings for PBA and PEA Derived Deposits

The coming figures show the thickness mappings of deposits grown on top of the piston from additized versions of the base fuels D10 and CARBOB+10%EtOH. All the thickness measurements are given in μm . Figure 12.1 and Figure 12.2 show the thicknesses of the deposit layers for D10+PBA and CARBOB+10%EtOH+PBA respectively. The pistons in the images both have a layer with substantial thickness near the bottom of the bowl region, as well as relatively high accumulation in the

“squish” region. To review, the “squish” region of the piston is depicted at the bottom of the images as the “ring” that surrounds the piston bowl. In the “squish” region, there is the least amount of clearance volume at TDC, and consequently this is where combustion temperatures are the highest.



Figure 12.1 - Deposits on the piston after a conditioning sweep with D10+PBA fuel

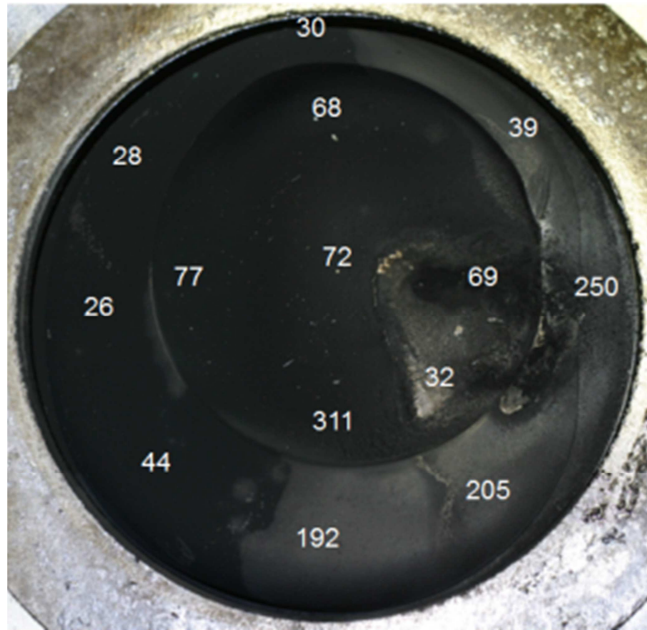


Figure 12.2 - CARBOB+10%EtOH+PBA piston deposits after a conditioning sweep

When compared to the results in the previous chapter, it is evident that the PBA additive does not aid in preventing against CCD growth on the piston, as the overall thickness of the layers is still quite high in certain areas. This is not completely unexpected, as the PBA additive has a backbone consisting of hydrocarbons that can be difficult to break down, thus, the addition of PBA contributes to additive-based deposit precursors that can promote deposit growth. Rather than reduce deposition, the main effect of the PBA additive is a redistribution of deposits over the surface of the piston. In Chapter 11, the thickest regions of CCD on the piston resulting from D10 were towards the center of the bowl; with the addition of PBA the thickest regions are in the lower portion of the bowl and in part of the "squish" region. Also in the previous chapter, CCD from the CARBOB+10%EtOH base fuel had the largest amount of growth in the locations just mentioned. Adding the PBA package increased the thickness of the

layer in the bottom of the bowl as well as in the bottom center region of Figure 12.2, which is the highest point of the “squish” region.

The pair of images in Figure 12.3 and Figure 12.4 displays the piston deposits from the base fuels dosed with a PEA additive package. There are some appreciable differences between these mappings and those in Figure 12.1 and Figure 12.2 (from the base fuel and PBA additive), most noticeably, an overall decrease in the deposit thickness. There are small regions in the piston bowl where there appears to have been some flaking of the D10+PEA deposit layer. In the case of the CARBOB+10%EtOH+PEA, for the first time with any of the conditioned pistons, it is possible to see some of the bare metal of the piston crown. Also, the layer is lighter in color and has a shinier appearance than any of the other CCD layers pictured in this chapter or the previous chapter.

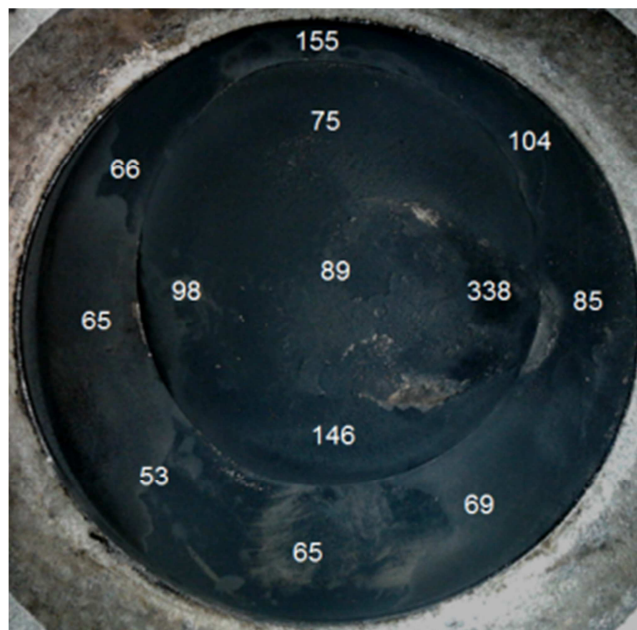


Figure 12.3 - D10+PEA deposits on the piston top after conditioning



Figure 12.4 - CARBOB+10%EtOH+PEA piston deposits at the equilibrium thickness

This provides a glimpse at the early development of the CCD layer in the HCCI engine, as the deposits in Figure 12.4 are thin and lack some of the more powdery characteristics of thicker layers, which accumulate on top of surfaces with higher temperatures.

Figures 12.5 through Figure 12.8 show mappings of the deposit thickness on the cylinder head for both of the base fuels with each of the two additive packages. The difference between the effects of the two additive packages is minimal for the D10 layers, as the resulting thicknesses across the cylinder head are fairly similar. For the CARBOB+10%EtOH blends, however, there is a drastic reduction of deposit growth when the PEA additive package is used instead of the PBA package. As with the piston mapping shown in Figure 12.4, the CARBOB+10%EtOH+PEA forms only a thin CCD

layer over the entire cylinder head, and in places such as the exhaust valves there are virtually no detectable deposits.



Figure 12.5 - D10+10%EtOH+PBA cylinder head CCD layer at the equilibrium thickness



Figure 12.6 - CARBOB+10%EtOH+PBA cylinder head deposits at the equilibrium thickness

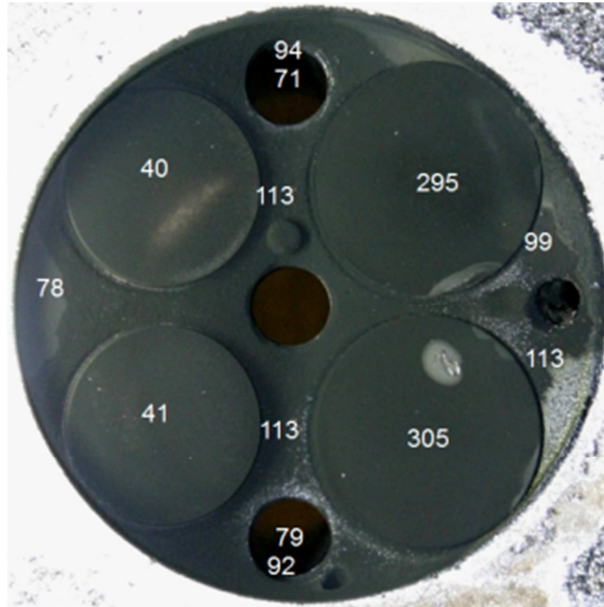


Figure 12.7 - Cylinder head deposit layer thicknesses for the D10+PEA fuel after conditioning

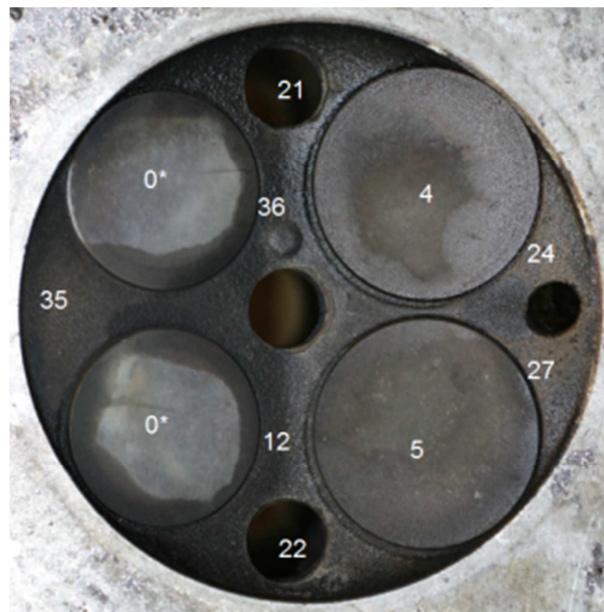


Figure 12.8 - CARBOB+10%EtOH+PEA deposits on the cylinder head after a conditioning sweep; the asterisks for the exhaust valve measurements refer to the fact that the layer was so thin a measurement could not be taken with the Dualscope

With the exception of the CARBOB+10%EtOH+PEA, there is relatively little variation in the thickness of deposits on the cylinder head (including the results of Chapter 11). Valve deposits are consistently around 35-40 μm for the hotter exhaust valves and roughly 250-300 μm on the intake valves, regardless of the type of fuel or additive package run (again, with the notable exception of CARBOB+10%EtOH+PEA). This phenomenon may be the result of the fuel delivery method for this particular experimental engine, which is direct injection into the cylinder. Fuel additives are all rated to clean combustion deposits from injectors and valves, although much of the testing to confirm these claims is performed on port-fuel injected engines, where the fuel/air/additive mixture flows through the intake ports over the intake valves. In the case of the HCCI setup used in these experiments, a fuel/additive mixture is sprayed into the combustion chamber directly onto the piston, where it eventually atomizes and interacts with the cylinder head. Because much of the additive may be impinging on the piston and not necessarily reaching the valves of the cylinder head, there may be little difference in deposit reduction between the CCD created by the unadditized base fuels mapped in Chapter 11, and the maps in Figure 12.5, Figure 12.6 and Figure 12.7.

12.3 In-Situ Engine Analysis during the Accumulation Process

To supplement the static mappings of equilibrium deposit layers from the previous section, in-situ engine data is presented in this section to track the changes in the HCCI combustion event as the CCD layer evolves. First, consider Figure 12.9 and Figure 12.10 which show the change in combustion phasing given by CA50 over the course of deposit conditioning sweeps. When both of the base fuels (“dirty” and “clean”)

are dosed with additives, the inclusion of the PBA additive resulted in more CA50 advance by the end of the conditioning sweep. Recall that the PBA additive promotes in-cylinder deposit growth in some cases, and that thicker CCD layers lead to more charge heating during the compression stroke, resulting in more advanced combustion phasing. Thus, this behavior is expected based on the maps of deposit thickness shown previously. However, there is variation in the CA50 advancement behavior of each individual fuel blend, over the course of the conditioning sweep.

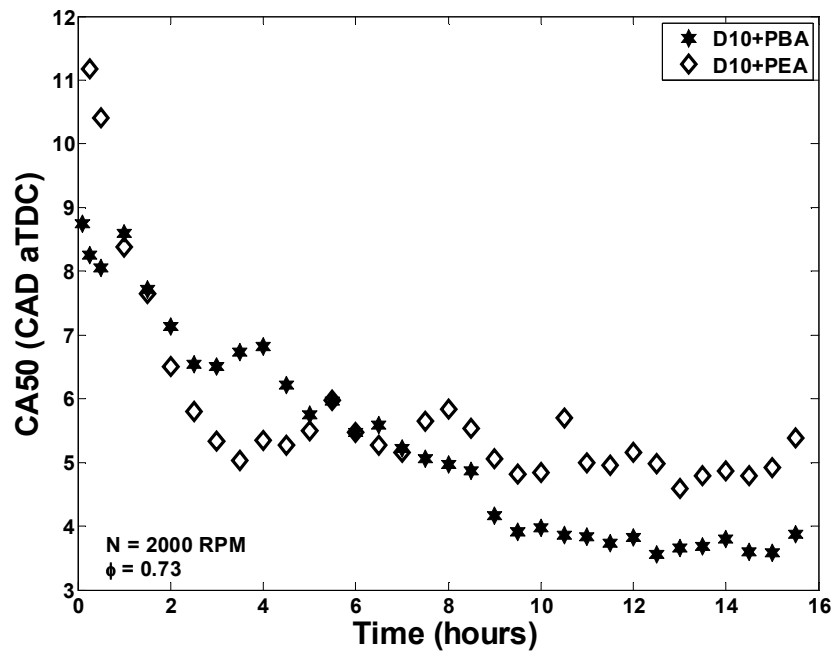


Figure 12.9 - Change in combustion phasing (CA50) over the course of a conditioning sweep for D10+PBA and D10+PEA

As shown in Figure 12.9, there is a cross-over point at approximately 7 hours of engine run-time, where the combustion phasing of the PBA additized D10 fuel reaches a lower level than that of the PEA additive package. Moreover, the initial growth rate,

i.e. the slope of the CA50 curves, is higher in the case of the D10+PEA. This type of behavior is exhibited indirectly by comparing the starting CA50 values between Figure 12.9 and Figure 12.10. Notice that the CARBOB+10%EtOH additized blends have a much lower initial CA50 than the D10 blends. When the engine is started, with a completely clean metal piston, all the fuels begin at the same combustion phasing (approximately 12.5-13 CAD aTDC). However, data is not collected until the engine is allowed to warm-up and reach a steady-state operating condition. The issue is that there is an initial base layer of deposits that coats the piston and cylinder head during this period, and this activity is not directly captured as in the case of the data pictured in Figure 12.10. Essentially, combustion phasing advances so rapidly during the first 10 to 15 minutes of operation, while the engine is first warming up, that by the time the first “steady-state” point can be taken a fair amount of deposition has already accumulated and pushed the combustion phasing closer to TDC. At this early stage of accumulation, it is difficult to decouple the impact of deposit growth from that of the engine warming up on the advance of CA50. This same issue was observed in Chapter 11 when considering the deposit layers that result from the base fuels. Based on the data from all the conditioning sweeps in this chapter and the previous chapter, it appears that a “cleaner” fuel, like CARBOB+10%EtOH, which contains less deposit forming precursors (lower aromatic content), as well as PEA additized blends will progress through the initial phase of growth more quickly than “dirtier” fuels. Also, the PEA additized fuels approach the equilibrium condition in less time than the fuels additized with a PBA package. In the case of D10, the D10+PEA layer reaches its steady-state CA50 value at about 4 hours of operation, whereas the D10+PBA took nearly 10 hours to approach

an asymptote in combustion phasing. For the CARBOB blends, the steady-state CA50 value is reached at roughly 3.5 hours for the PEA blend and 6 hours for the PBA blend. According to the results of the previous two figures, the PEA additive package becomes more effective once a base layer of deposits has accumulated. This could be the result of the dosage amount of additive that was used (0.1 ounces per gallon of fuel), which is intended as a “keep clean” dose rather than a “clean-up” dose, or the directly injected method of fuel delivery which effects how the fuel and additive mixture is dispersed throughout the combustion chamber or some combination of the two. Overall, the CCD layer derived from a fuel in conjunction with a PEA additive package results in a phasing advance that stabilizes in less time and at a more retarded CA50 at equilibrium than the same fuel additized with a PBA package.

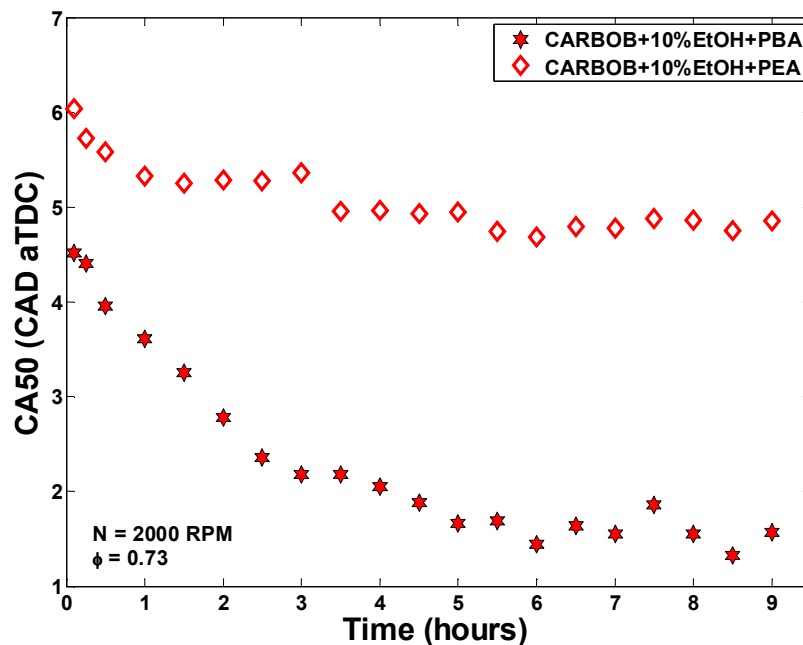


Figure 12.10 - CA50 advance during a deposit accumulation sweep for CARBOB+10%EtOH+PBA and CARBOB+10%EtOH+PEA

Another important ascertainment to take from Figure 12.9 and Figure 12.10 is that while the overall thickness of the CCD layer plays a substantial role in the equilibrium CA50 of the engine, the distribution of thickness between regions of the same layer also impacts this phasing advance. Notice that the CARBOB+10%EtOH+PBA deposits are, in general, thinner than the CCD layer of D10+PBA, as shown in Figure 12.1 and Figure 12.2. This appears to contradict the findings in Figure 12.9 and Figure 12.10, as the CARBOB+10%EtOH+PBA ends up at a more advanced CA50 than the D10+PBA does as it approaches asymptotic behavior.

To resolve this apparent inconsistency, Figure 12.2 shows that there is a substantial amount of growth in the “squish” region of the piston for CARBOB+10%EtOH+PBA, and in one area more than D10+PBA (the region just right of the bottom, center location). The combination of the CARBOB+10%EtOH+PBA’s distribution of deposit thickness coupled with the increased intake air temperature of the CARBOB+10%EtOH fuel (determined by the baseline condition from Table 10.2) creates a scenario in which CARBOB+10%EtOH+PBA runs at a more advanced CA50 when conditioned than does D10+PBA. While this effect is obviously specific to the piston geometry of this setup, it does have more far-reaching implications. Localized regions of a combustion chamber, with a reduced clearance volume, that are subjected to a thermal coating such as deposits will exhibit a similar (or even more severe) phasing advance than the same piston with a thicker coating of deposits in an area of larger clearance volume will.

The emissions index for NO_x (EINO_x) is plotted for all the additized test fuels in Figure 12.11 and Figure 12.12, which provides information not only for species in the

sampled exhaust, but also for in-cylinder temperatures. NO_x production in an engine is strongly tied to temperatures during combustion. As mentioned in Chapter 11, increased NO_x emissions will result from conditions where in-cylinder temperatures are higher. More favorable conditions for the production of NO_x occur as combustion advances closer to TDC, and RI and temperatures rise. Thus, of the four blends compared in this chapter the CARBOB+10%EtOH+PBA which has the most advanced CA50 at the equilibrium point (about 1.5 CAD aTDC), also had the highest EINO_x at the end of conditioning sweep. The D10 sweeps of both additized blends manage to stay below the target level of 1g/kg fuel, even when the combustion chamber is fully-conditioned. Also, both of CCD layers derived from blends containing PBA additive exhibit a significant increase in EINO_x during the conditioning sweep; this occurs at 9 hours of engine run-time for the D10+PBA layer and 4.5 hours for the CARBOB+10%EtOH+PBA CCD accumulation. This suggests that despite the slower average rate of deposition at this point in the growth process, there is a localized escalation of deposit growth somewhere in the chamber, which causes the precipitous jump.

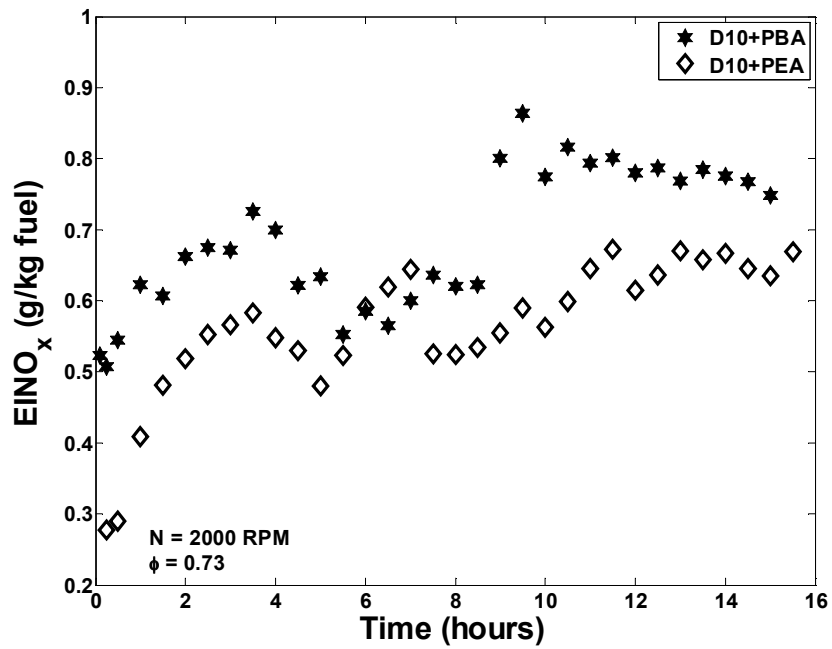


Figure 12.11 - Emissions index for NO_x (EINO_x) species in the exhaust as deposits accumulate in-cylinder; from the D10+PBA and D10+PEA tests

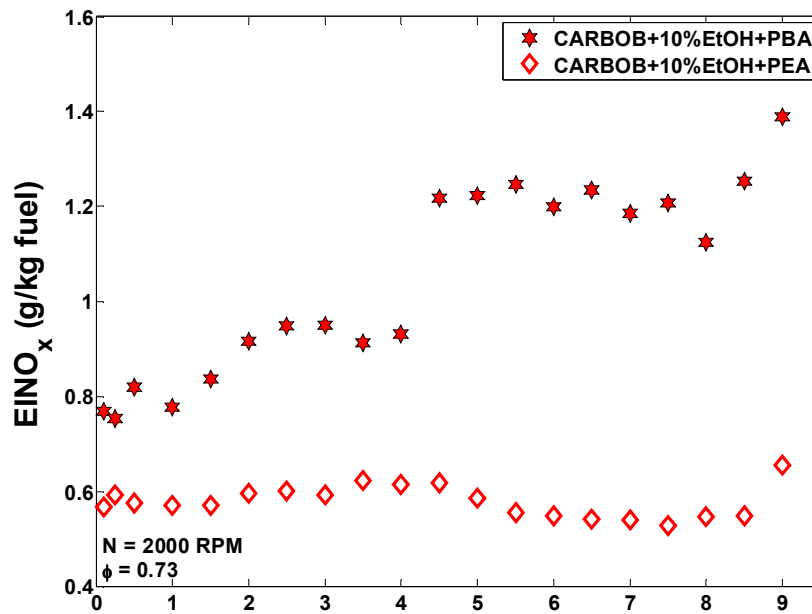


Figure 12.12 - Emissions index of NO_x (EINO_x) in the exhaust as the CCD layer builds for the CARBOB+10%EtOH+PBA and CARBOB+10%EtOH+PEA fuels

The emissions index of hydrocarbon species (EIHC) displayed in Figure 12.13 and Figure 12.14 shows a similar trend for several of the deposit layers as was presented in Chapter 11. All of the curves have an initial drop in EIHC that is anticipated when the initial deposit layer builds, combustion advances and in-cylinder temperatures increase to bolster combustion efficiencies and drive down hydrocarbon emissions. What is not as intuitive (and was shown for both the unadditized fuels in Chapter 11) is that with the D10+PBA, D10+PEA and CARBOB+10%EtOH+PBA deposit layers, there is a slight increase in EIHC following the initial drop-off. The only exception to this trend is the CARBOB+10%EtOH+PEA conditioning sweep, which decreases over the entirety of the accumulation process.

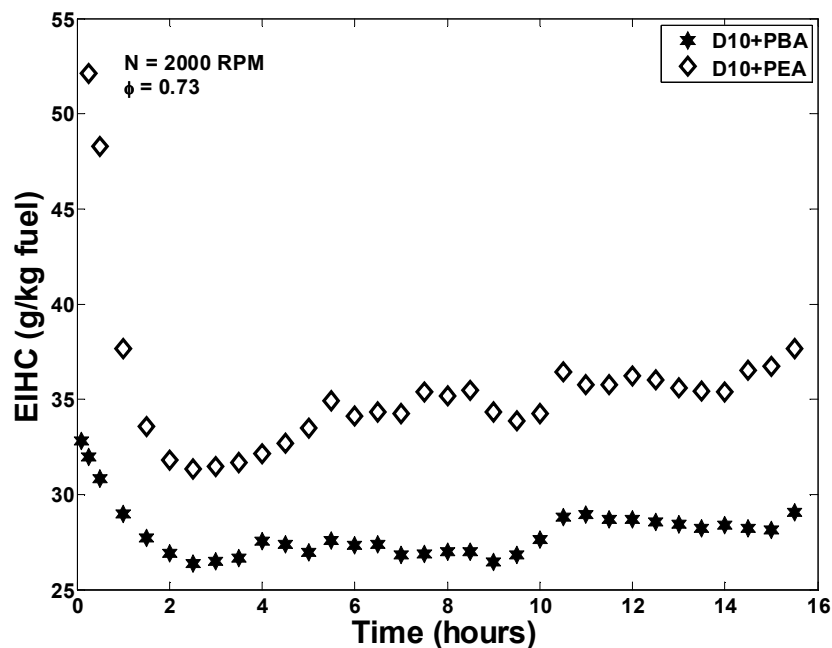


Figure 12.13 - D10+PBA and D10+PEA evolution of the emissions index of hydrocarbon species as the deposit layer accumulates

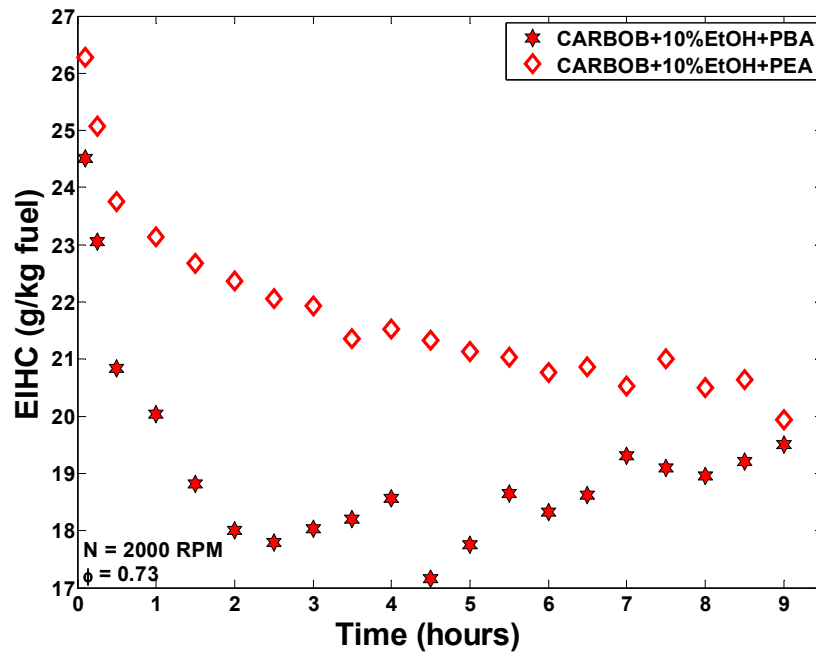


Figure 12.14 - CARBOB+10%EtOH+PBA and CARBOB+10%EtOH+PEA hydrocarbon emissions index (EIHC) as the CCD builds over a conditioning sweep

One possible explanation for this observation lies in the CCD's coverage of the piston. As shown in this chapter, the CARBOB+10%EtOH+PEA deposit layer was the only CCD accumulation to leave a significant portion of the piston bowl uncovered and clean. Because the injected fuel spray impinges on the bowl of the piston it is possible to surmise that if this area is coated with a rough, porous layer of deposits some of the fuel might become trapped in the layer's pores and outgassed later in the cycle. This would result in higher levels of hydrocarbon emissions, despite the competing effects, from more advanced combustion phasing and higher temperatures that act to lower EIHC. Chapter 11 dealt with this same phenomenon, but given the clean piston bowl results of the CARBOB+10%EtOH+PEA layer, the fuel entrainment theory is further strengthened.

12.4 Changes in Heat Flux at the Wall Surface and CCD Layer Interface

After exploring more holistic in-situ phenomena in the previous section, this portion of the chapter will deal with deposit growth localized on the coaxial heat flux probe, located above the “squish” region of the piston (location 1). Both the PBA conditioning runs are shown in Figure 12.15 and Figure 12.16, for D10+PBA and CARBOB+10%EtOH+PBA, respectively. Heat flux evolves in a different manner for each of these blends. Initially, the D10+PBA layer induces a very sharp drop in heat flux, between the clean state and 1 hour of operation, followed by a gradual decrease until the end of the conditioning sweep. On the other hand, the layer that results from the CARBOB+10%EtOH+PBA fuel initially causes a gradual decrease in heat flux, followed by a sharp plummet as the chamber approaches the equilibrium state.

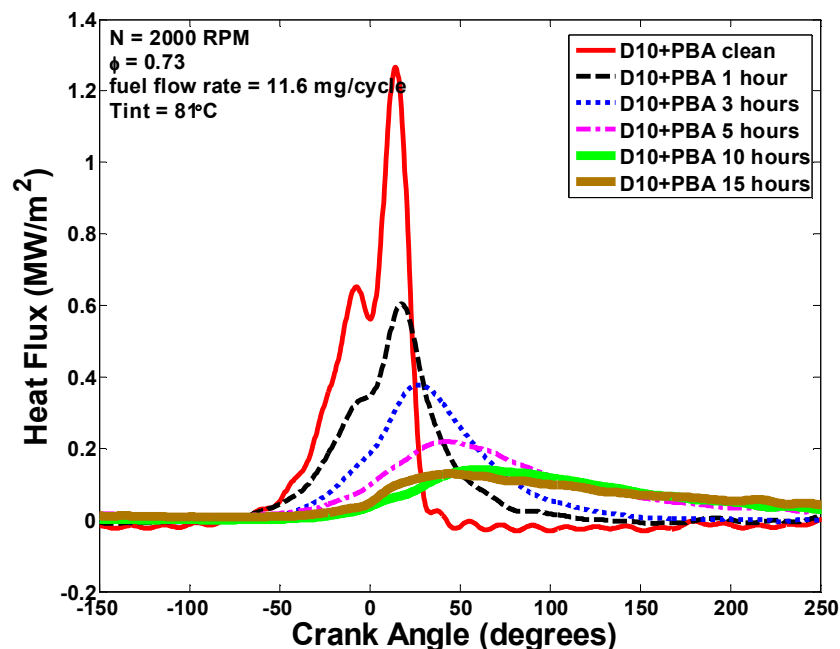


Figure 12.15 - D10+PBA head probe location 1 heat flux change during deposit buildup

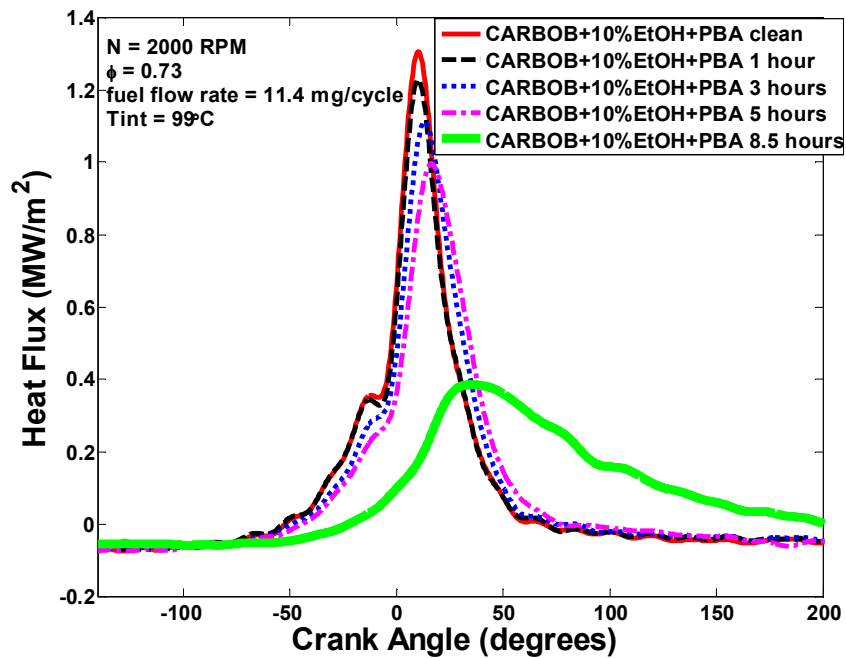


Figure 12.16 - CARBOB+10%EtOH+PBA change in heat flux at probe location 1 during deposit accumulation

As shown in Chapter 11, at the same location in the combustion chamber, deposits can accumulate at vastly different rates based on the underlying chemical composition of the refinery stream fuel run in the engine. This is also the case in the previous two figures, for the PBA dosed D10 and CARBOB+10%EtOH blends. It was also noted in Chapter 11 that the changes observed for the heat flux probes are not necessarily synchronized with the variation of the combustion event over the course of the conditioning sweep. Based on the fact that CARBOB+10%EtOH+PBA does not have much CA50 change from 5 hours to 8.5 hours of engine operation (about 0.3 CAD difference), the large decrease in heat flux shown through the probe, in Figure 12.16, is not indicative of the rate of overall cylinder deposition, which is much more gradual, as shown by the CA50 in Figure 12.10.

The heat flux trends for the PEA dosed fuels are illustrated in Figure 12.17 and Figure 12.18. The probe in location 1 experiences similar deposit development during the end of the conditioning sweep; the heat flux is nearly the same from 10 to 15 hours with the D10+PEA, and from 5 to 8.5 hours with the CARBOB+10%EtOH+PEA. The initial stages of growth appear dissimilar, as D10+PEA has little change in heat flux from the “clean” to the 1 hour point, but CARBOB+10%EtOH+PEA has a stark drop between these same two points in time. Based on the results of this section, it is expected that the deposit accumulation process for a specific region of the cylinder head will depend on the additive package present in the fuel being run, and that this process will not necessarily follow what is occurring in the rest of the combustion chamber.

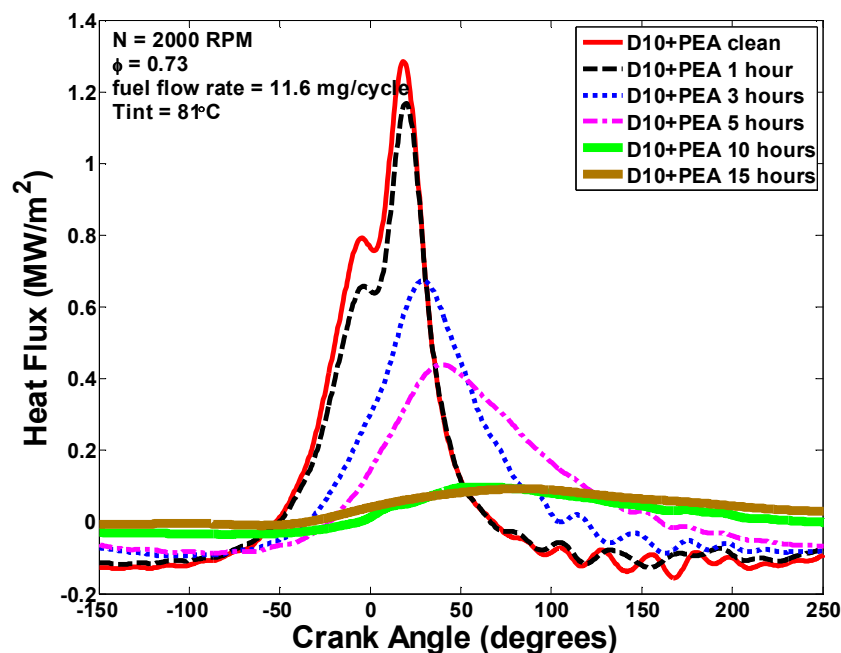


Figure 12.17 - Heat flux evolution during deposit buildup for D10+PEA at head probe location 1

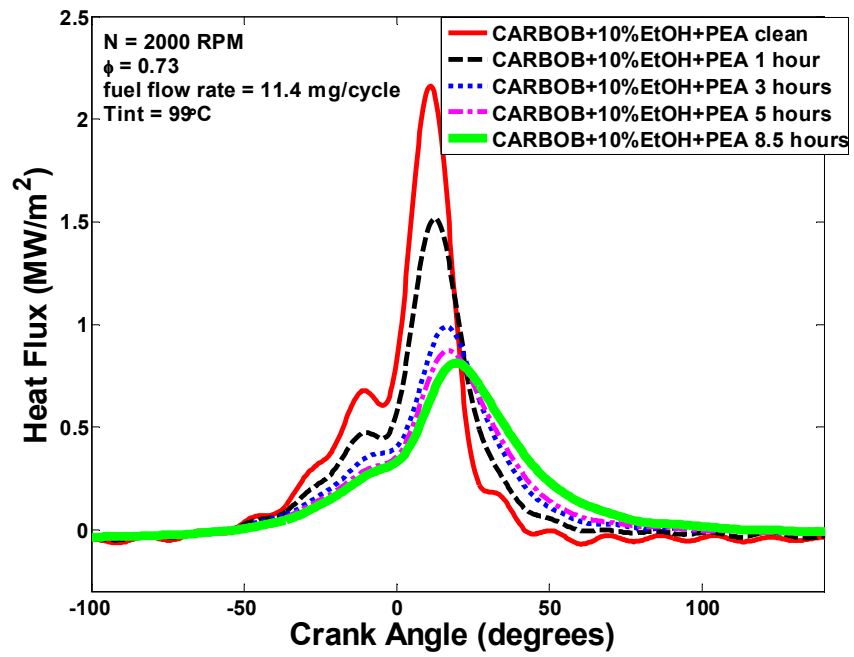


Figure 12.18 - Heat flux evolution during deposit buildup for CARBOB+10%EtOH+PEA at head probe location 1

CHAPTER 13

A Study of the Properties of HCCI Deposits for Refinery Stream Fuels

13.1 Introduction

This chapter examines the properties of deposits formed by the two base fuel types and additive packages detailed in the previous two chapters. Previously the CCD layer was only considered from a holistic, high-level standpoint, where the CCD layer was an averaged coating over the cylinder acting on the combustion event. In reality, the morphology of the layer is quite complex, and the formation of its structure can be sensitive to the variation between fuels of dissimilar chemical composition or even different additive packages. Studying some of the layer's detailed properties will aid in determining whether specific layer structures are important for the overall HCCI combustion process, in an attempt to bridge the study of CCD growth, examined in Chapters 11 and 12, with the study of CCD's impact on engine performance, which will be looked at in Chapter 14. The deposit samples were extracted from the flat portion of the piston bowl, as illustrated in Figure 13.1. The decision to take deposits from this region was one of necessity. One condition sweep only creates a small mass of deposition, and it was imperative to have a sufficient mass in order to complete the tests detailed throughout the rest of this chapter. This requirement dictated that samples

come from an area where growth was thickest, for all the fuels and additive packages run through conditioning sweeps.

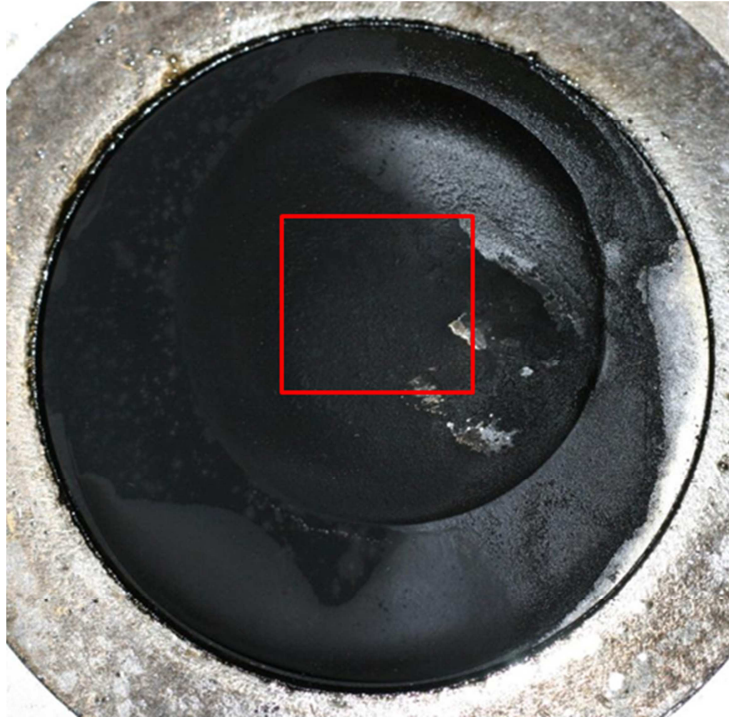


Figure 13.1 - General area over which deposits were collected for ex-situ analysis

13.2 Qualitative Microscopic Imaging

Two different types of electron microbeam imaging techniques were employed in the characterization of deposit morphology, which allowed for the examination of deposits at two different length scales. SEM was used to capture images of piston flakes and study the macroscopic features of various CCD layers. The TEM was used to view small pieces of deposits at the nanometer level, in order to investigate structures and to provide a foundation for X-ray diffraction work, presented later in this chapter.

13.2.1 Scanning Electron Microscopy (SEM)

Deposit samples resulting from the unadditized D10 and CARBOB+10%EtOH fuels are shown in Figure 13.2. The images are shown at two different magnifications because some of the features between the two samples do not exist at exactly the same length scales. However, there are common features in the form of cracks or fissures, which are highlighted in both images by circles. Both deposit flakes are also moderately porous in structure at this microscopic scale, as shown by void areas inside the boundaries of the samples. While the features are not the same size, there are some fundamental, morphological similarities between the deposits formed by the unadditized refinery stream fuels.

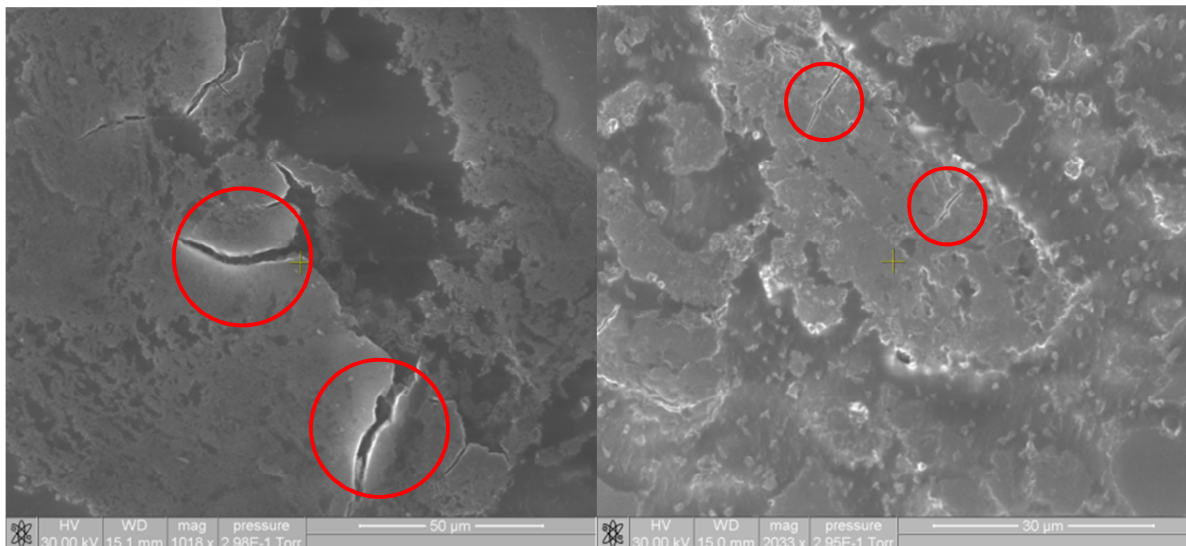


Figure 13.2 - Deposits from the D10 base fuel on the left side (1000 times magnification) and CARBOB+10%EtOH on the right side image (2000 times magnification) with fissure type structures in the flakes

Much like the deposits created by the unadditized fuels, there are likenesses between the deposits formed from the two PBA dosed fuel blends. Again, these features are found at different characteristic dimensions. Figure 13.3 shows the two samples at the same magnification. Both these flakes appear to have a more smooth texture than the base fuel derived deposits, although there are still some craggy surface features in the case of the D10+PBA deposit sample. The CARBOB+PBA+10%EtOH derived deposit samples have some rough features on its surface as well, though they are smaller and do not cover as much surface area as what is on the D10+PBA specimen. These flakes appear to be more robust in structure, as they lack the deep fissures and pockets found in the base fuel deposit samples. This could be due to disparities in the formation mechanism between the deposits from refinery stream fuels with no additive package and those created from fuel dosed with a PBA package, which has been known in some cases to promote in-cylinder deposit growth. Recall from the background information in Chapter 1 that the deposits derived from fuel are constituted of partially unburned hydrocarbon species that condense on the walls, whereas additive based deposits are a solidified form of the additive itself. This accounts for the morphological variation between the deposits formed by the base fuels and those shown in Figure 13.3.

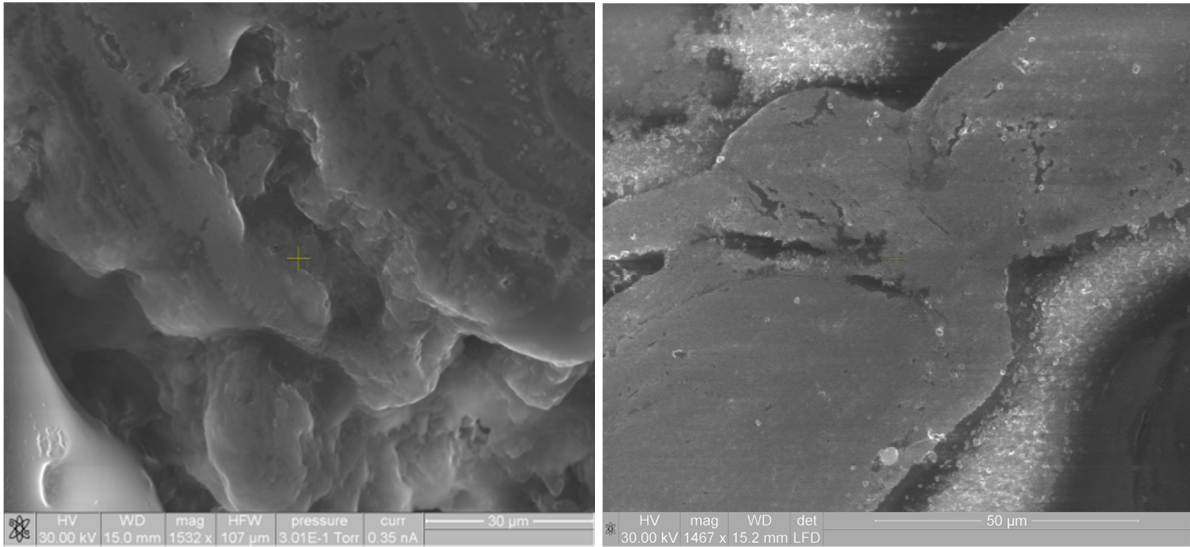


Figure 13.3 - D10+PBA derived deposits on the left image (1500 times magnification) and CARBOB+10%EtOH deposits on the right side (1500 times magnification)

The final set of images, in Figure 13.4, show the deposits created by the pair of fuels containing the PEA additive package. Both samples have the appearance of rocky outcroppings of growth across the deposit sample's surface. As with the other pairs of images, the features on these flakes are not the same size. In this case, the features of deposits from the CARBOB+10%EtOH+PEA are larger than those of the D10+PEA (the CARBOB is shown at 1500 times magnification while the D10 is at 2500 times magnification). The PEA derived deposits are similar to the PBA samples in that all four are robust flakes that do not display the more tenuous fissure structures present in the base fuel deposits. It can be surmised from these sets of images that accumulation of the CCD layer in an HCCI engine is impacted by the additive package present in the refinery stream fuel that is run. The chemical components of the fuel

itself seem to play a larger role in the development of a characteristic size of deposit morphological features, rather than the form factor itself.

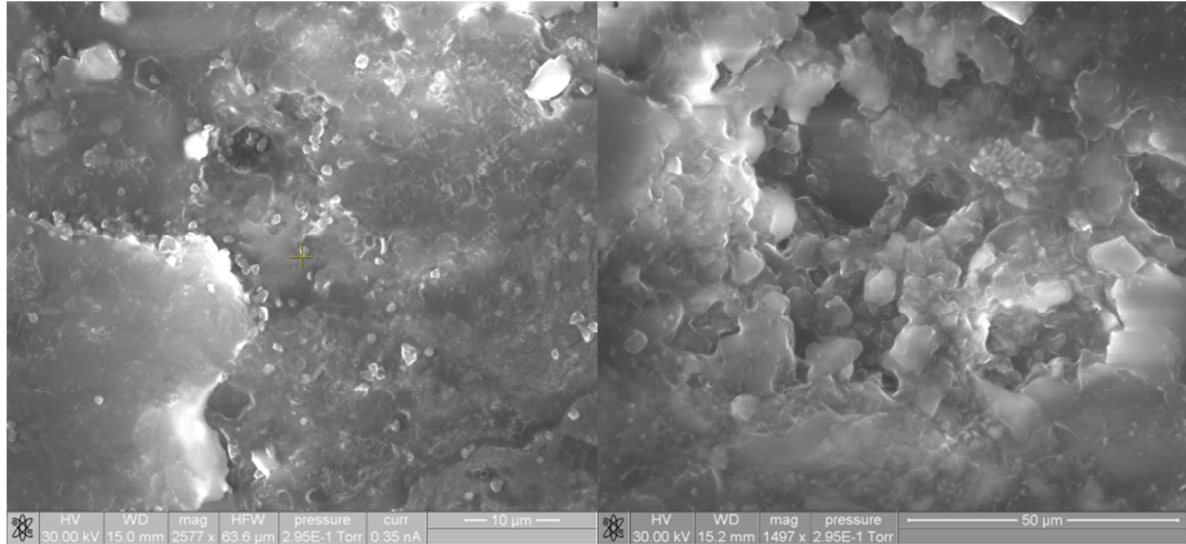


Figure 13.4 - Deposits samples from PEA additized fuels; D10 on the left (2500 times magnification) and CARBOB+10%EtOH on the right (1500 times magnification)

13.2.2 Transmission Electron Microscopy (TEM)

Once a sample of deposit flakes was affixed to the copper TEM grid and inserted into the column for examination, several locations on an individual flake pieces were photographed in order to identify potentially interesting features. The deposit samples appeared to be predominantly amorphous carbon, which concurs with previous findings in SI engines [117]. One such example of this is found in Figure 13.5, a piece of a flake from the CCD layer of D10+PBA.

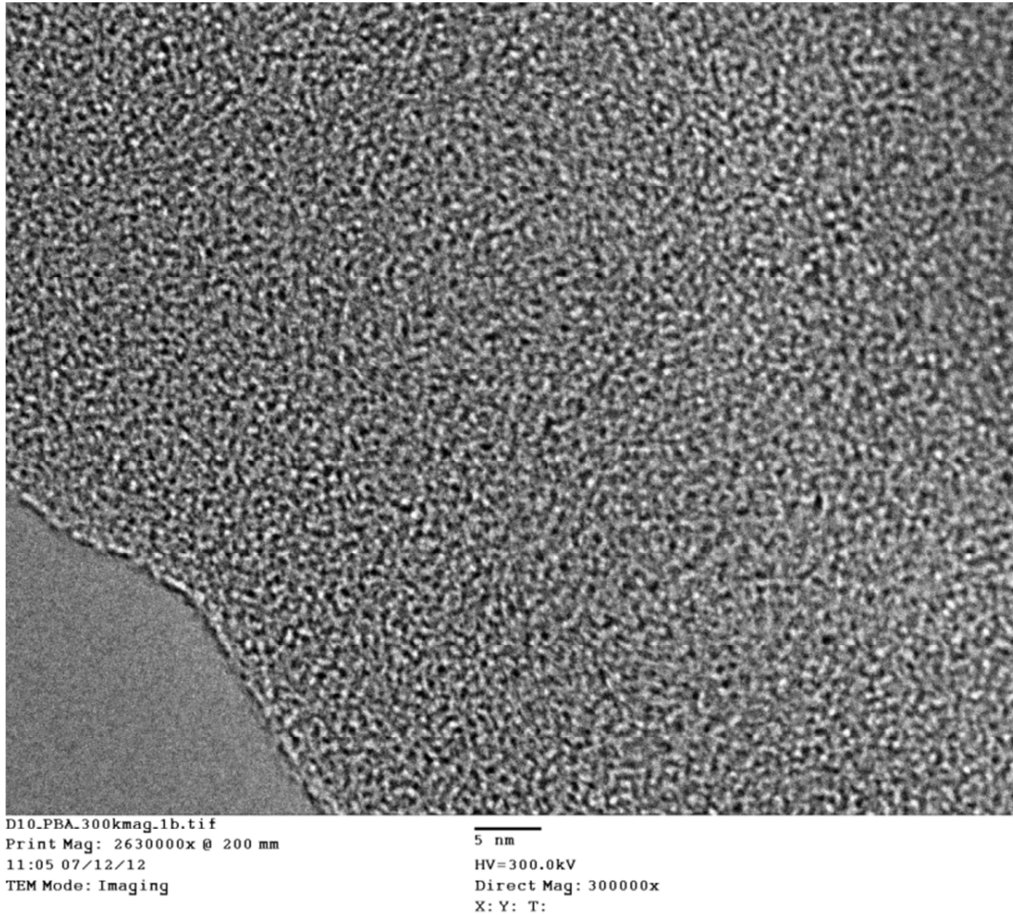


Figure 13.5 - Deposit sample from D10+PBA (at 300k magnification) showing features of amorphous carbon

One of the great advantages of TEM imaging is its ability to readily qualify the nature of a porous medium. The void space in the image above is visible as darker spots, while the solid volume is the lighter regions. From Figure 13.5 it is apparent that the extracted deposit sample is extremely porous. There is a more rigorous quantification of this void fraction, or porosity, in a later section.

One interesting discovery revealed during the TEM analysis was the presence of soot-like structures in some of the deposit samples. Whereas the vast majority of the

engine deposits studied take on a form similar to Figure 13.5, which is to be expected, there were a couple of imaged locations from the D10 base fuel and CARBOB+10%EtOH+PBA deposits that assumed a different form factor. For reference, examples of soot particles from diesel exhaust are presented in Figure 13.6. Notice how their structure differs from the HCCI engine deposits presented in Figure 13.5. Soot is characterized by more organized, sheet-like swirls rather than the more amorphous features of most engine deposits, which do not have any discernible pattern at the nanometer scale.

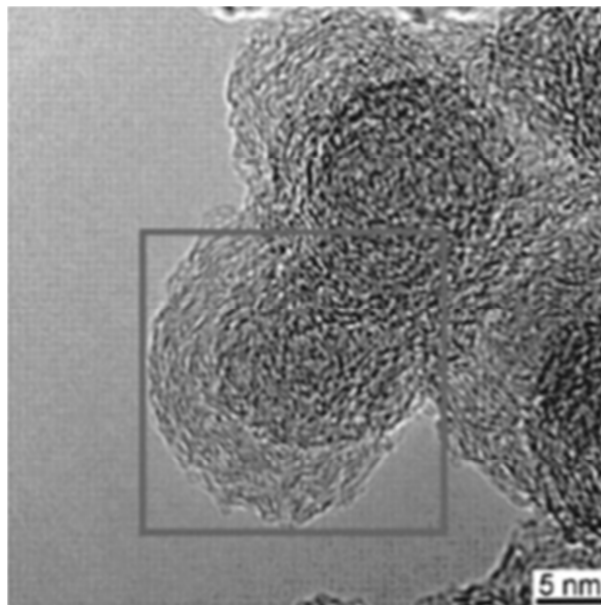


Figure 13.6 - An example of soot particles taken from diesel exhaust [172]

A deposit flake produced from the D10 base fuel is shown in Figure 13.7, within a pair of thinner (lighter in color), protruding regions, highlighted in the picture by circles, there are the hints of a more organized form of carbon, which is indicative of the presence of soot structures. It is also important to note that the length scales

associated with these swirling structures are the same between Figure 13.6 and Figure 13.7, another suggestion of the relationship between these patterns.

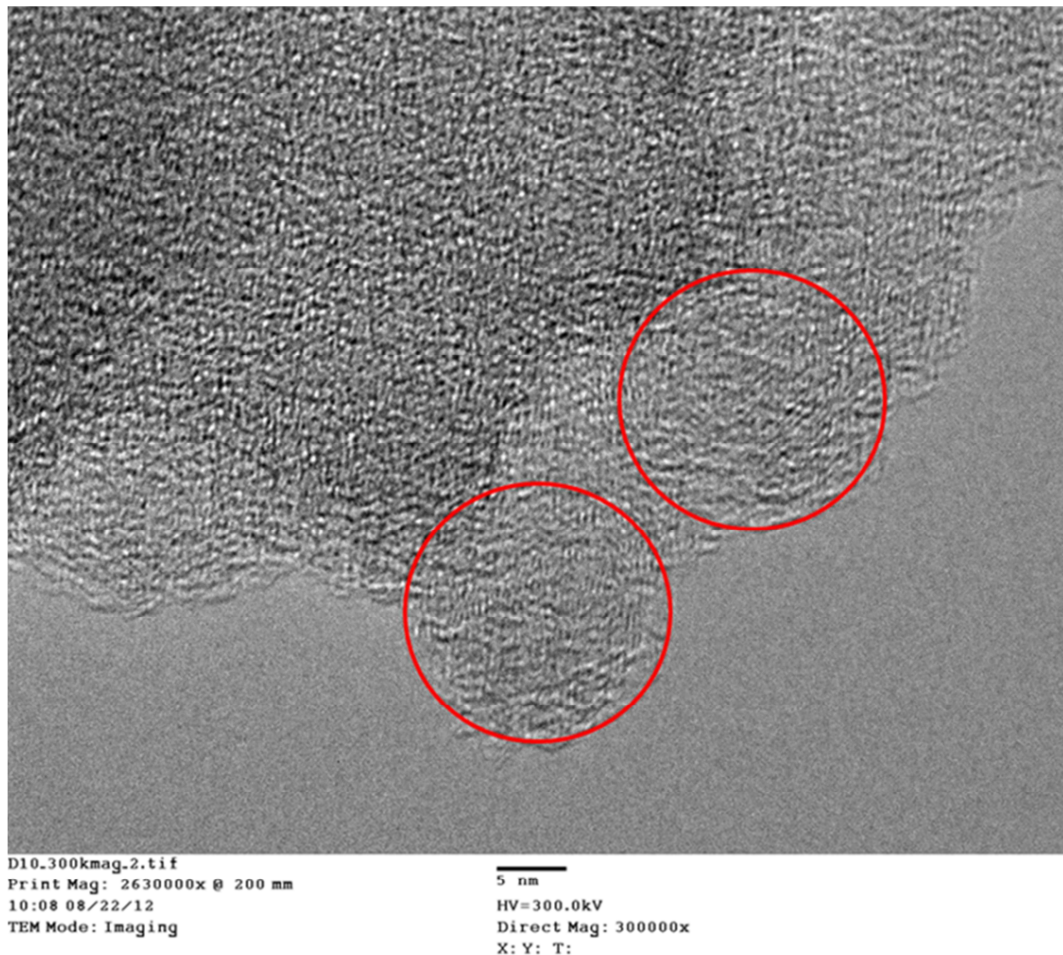


Figure 13.7 - Deposit flake from the CCD layer formed by D10 base fuel with soot features marked by circles, 300k magnification

The sample of CCD from CARBOB+10%EtOH+PBA, shown in Figure 13.8, also has a thinner region in contrast to a thicker portion, similar to Figure 13.7, that has the more typical, unorganized structure of engine deposits. Again, some of the subtle, soot-

like features, highlighted by the circles in the photograph, exist at dimensions similar to the previous two figures.

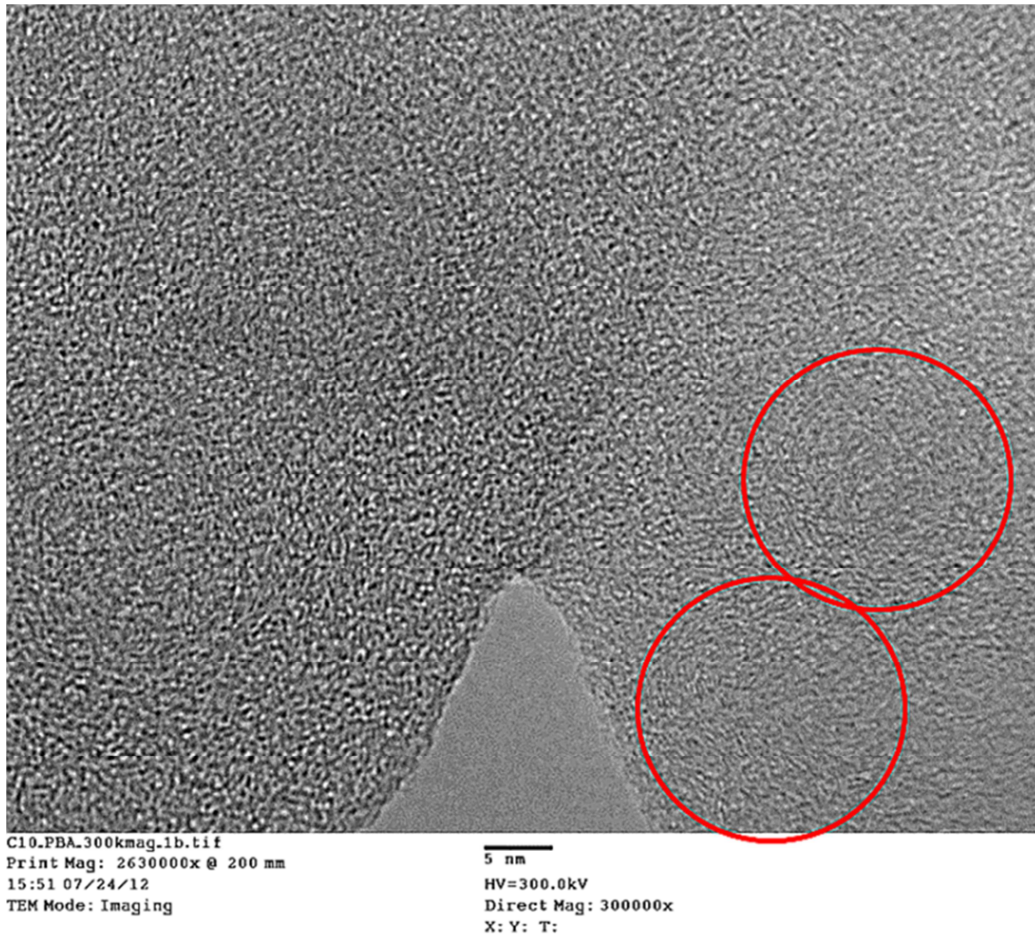


Figure 13.8 - CARBOB+10%EtOH+PBA derived deposit flake showing some signs of soot-like behavior as marked with circles; 300k magnification

These results were unexpected when TEM analysis first commenced, as previous microscopic work of CCD in SI engines did not detect the presence of sooting. However, soot and particulate emissions *have* previously been observed in SI gasoline operation when direct-injection strategies, which resulted in stratified fuel and air

mixtures, were employed [173-176]. The experimental HCCI setup described in this document also utilizes direct injection, albeit at very early timings during the intake stroke (333 bTDC) in order to minimize the equivalence ratio stratification of the in-cylinder charge. Hence, it is possible that some of the soot structures in the CCD layer are caused by the delivery strategy of the fuel or are the result of potentially richer zones of fuel, contributing to partially unburned hydrocarbons condensing on the combustion chamber walls.

Another more likely source of the swirling soot structures in the layer is the accumulation process itself. In a seminal study conducted by Daly et al. [33] that was mentioned in the background material of Chapter 1, a mechanism for the formation of deposits in gasoline engines consisting of a two stage process was proposed. This mechanism is illustrated in Figure 13.9.

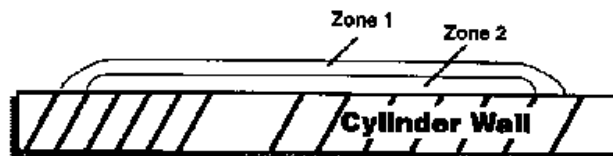


Figure 13.9 - Proposed mechanism for in-cylinder CCD formation [33]

The first layer is Zone 2, which is the initial part of CCD accumulation that occurs when the engine is fired with a clean metal piston and cylinder head. This is the more robust portion of the layer that closely resembles lacquer, and requires a fair amount of effort to remove by hand once the engine is disassembled. The Zone 1 layer is the principal location from which sample flakes were extracted for ex-situ analysis. Zone 1

growth corresponds to the point in the accumulation cycle where the overall rate of CCD buildup slows as the surface temperature of the layer increases and begins to approach the equilibrium point. This portion of the CCD growth is more “soot-like” [33] and has a more powdery texture than Zone 2 growth. Ultimately, the thickness of the Zone 1 region is related to the chemical components of the fuel run in the engine, which is responsible for forming the deposits. CCD growth from the D10 base fuel and CARBOB+10%EtOH+PBA, as discussed in Chapters 11 and 12, has some of the thickest overall levels of deposition in the piston bowl, and induces the most combustion phasing advance of the baseline point during the conditioning sweep. Therefore, it is reasonable to estimate that the Zone 1 accumulation of these fuels is most substantial in the piston bowl, where deposit samples were collected. Thus, the samples display soot-like structures, as shown in Figure 13.7 and Figure 13.8. Furthermore, higher thicknesses and more advanced combustion phasing result in hotter surface temperatures of the CCD layer, and this promotes the growth of these more crumbled and powdery deposits on the surface. It appears that even with a direct injection fuelling strategy that attempts to mitigate any stratification of the incoming charge, it is possible for soot to occur and condense on the walls of the combustion chamber. This phenomenon is driven by fuel composition and additive packages that promote the most in-cylinder growth.

13.3 Spectroscopic Results

We have seen a number of the physical comparisons and contrasts between CCD layers formed from refinery stream fuels with differing chemical components and

additive packages, but the question of how the composition of these layers might vary and what impact this variation might have on combustion still remains. The spectroscopic results detailed in the next section of this chapter attempt to address these issues, using both XEDS and XPS to provide a “bulk” scan of the deposit samples cold-mounted in epoxy and a 10 nm detailed surface scan, respectively.

13.3.1 X-Ray Energy Dispersive Spectroscopy (XEDS)

XEDS tests are run using a spot beam focus for several locations in a given image. For one deposit specimen within an epoxy mount, the elemental composition of the sample was extremely consistent over these differing locations, with major elements like carbon and oxygen varying by at most 2%, in terms of atomic percentage. Thus the bulk deposit elemental composition, at least for the piston bowl deposits extracted for these samples, appeared to be fairly homogeneous.

Several example spectra for all the deposit samples from the D10 fuels are shown in Figure 13.10, Figure 13.11 and Figure 13.12. The major components, carbon and oxygen, are common throughout all the samples. In addition there are trace amounts of other elements that have previously been detected in SI engine deposits, as discussed in Chapter 1. The spectra images for the CARBOB+10%EtOH deposits are not shown because from a qualitative standpoint, they look extremely similar to the D10 deposit spectra. All the XEDS results, from all the spectra pictured, as well as those that are not, are summarized in Table 13.1.

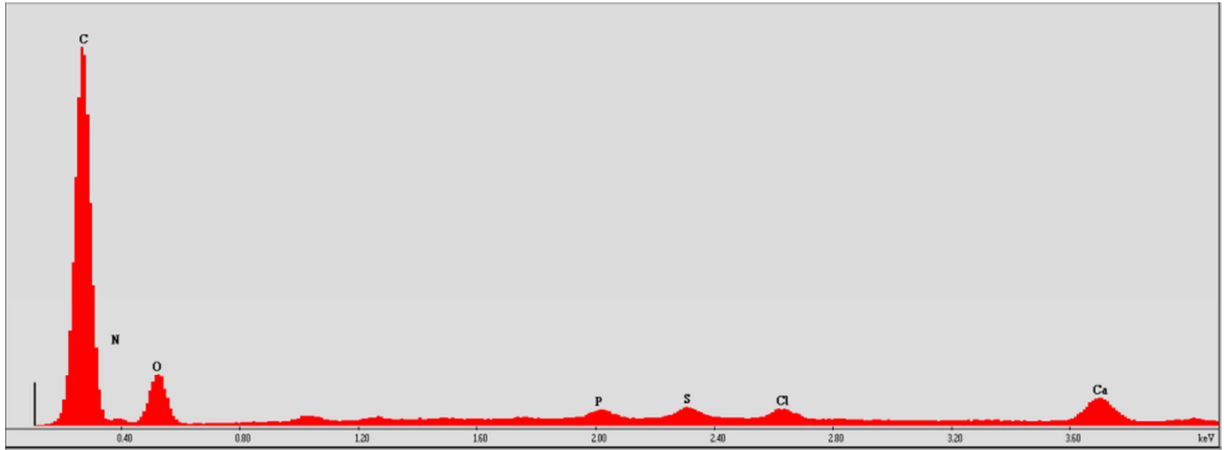


Figure 13.10 - D10 derived deposit XEDS spectrum

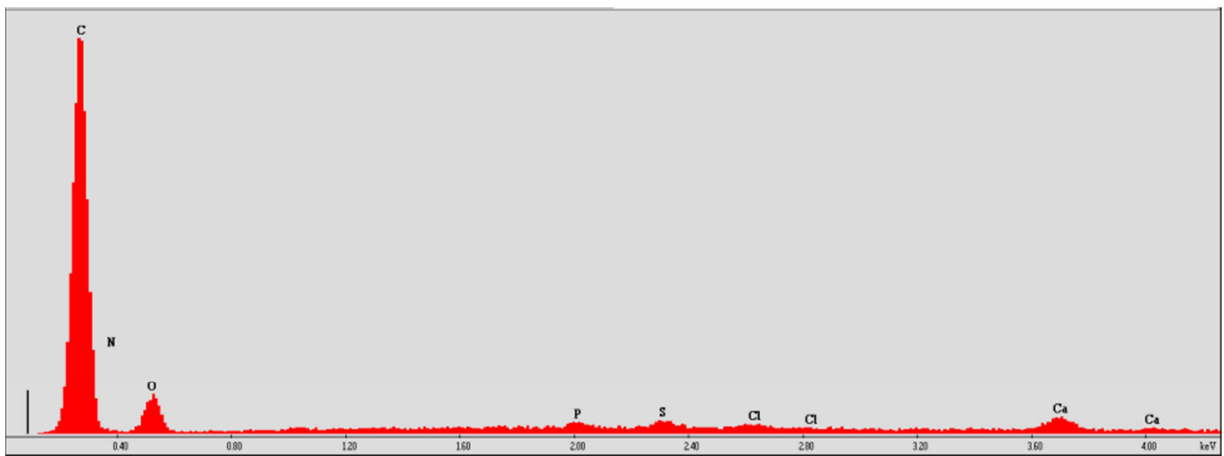


Figure 13.11 - D10+PBA derived deposit XEDS spectrum

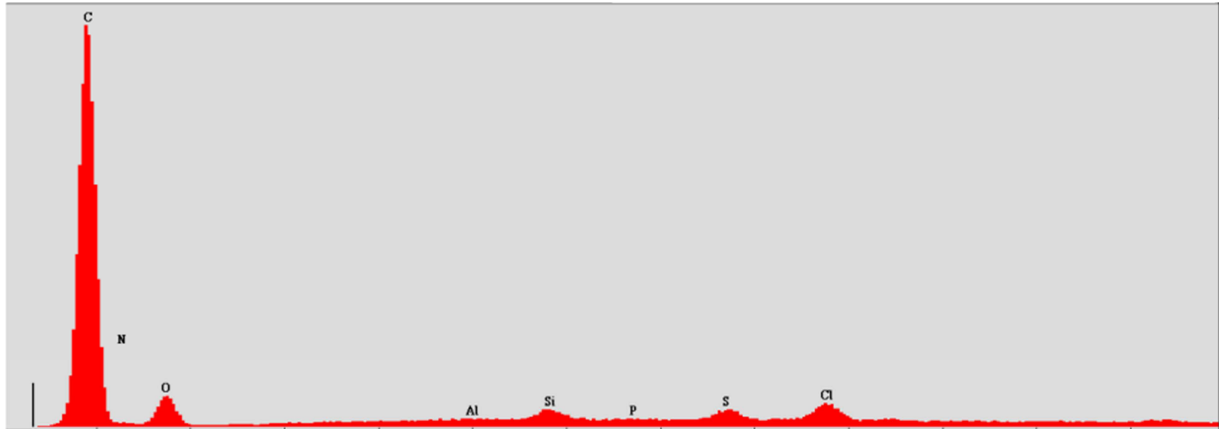


Figure 13.12 - D10+PEA derived deposit XEDS spectrum

Table 13.1 - Summary of XEDS composition results with C:O ratio included

	Atomic Percentages (%)								C+O	C:O
	C	O	N	S	P	Ca	Cl	Other		
D10	74.42	17.90	6.24	0.29	0.23	0.66	0.26	0.0	92.32	4.16
C10*	79.92	14.47	3.05	0.63	0.39	1.24	0.31	0.0	94.39	5.52
D10+PBA	81.09	15.08	2.86	0.22	0.19	0.43	0.13	0.0	96.17	5.38
C10+PBA*	84.65	12.20	1.63	0.38	0.0	0.47	0.67	0.0	96.85	6.94
D10+PEA	83.43	11.52	3.98	0.27	0.01	0.0	0.43	0.35	94.95	7.24
C10+PEA*	79.09	15.43	1.45	0.83	0.52	1.83	0.30	0.55	94.52	5.13

*CARBOB+10%EtOH is abbreviated here as C10, not to be confused with the C10 fuel discussed in Chapters 5-9

While there is some variation of elemental components between fuels and additives, overall their constituents appear quite similar, particularly when considering the atomic percentages of carbon and oxygen versus the balance (shown in the second to last column of the table). In fact, because the compositional differences are so small, it would be difficult to assess distinctive trends because no “standard” sample was used to apply correction factors (see Chapter 3 for more detail about ZAF correction). One important conclusion to take away from this analysis is that the bulk compositions of the deposits, regardless of the fuel or additive from which they are derived, have similar

components in similar proportions. The bulk composition is also insensitive to the equilibrium thickness of the layer and the morphology of the CCD, as these characteristics varied greatly among the deposit samples tested.

13.3.2 X-Ray Photoelectron Spectroscopy (XPS)

While the results from the XEDS provide quantitative intra-specimen variation of composition, because there was no Z (atomic number) correction applied to the samples, the results cannot confidently be compared to one another on an absolute basis. They provide only an approximation of the differences in chemical makeup. XEDS is affected by the composition of the sample in question, as the interaction volume between the electron and the specimen is related to the atomic numbers of the elements being scanned. Because XPS does not depend on the interaction of electrons between the deposit sample and the beam as XEDS does, it is possible to obtain a quantifiable chemical composition for the sample using XPS, though these results are limited to the initial 10 nm of the sample, as the softer XPS beam cannot penetrate further. In this section, two kinds of plots are shown for deposit samples created from both base fuel types and additive packages. The first plot is the core scan, which provides a spectrum of elements similar to the spectra in the previous section. This is used to gain some basic insight into the overall composition of elements in the samples. The second type of plot is a carbon scan, where the 1s electron peak for carbon is isolated and studied, to determine the molecular constituents in the surface of the deposit sample. As discussed in Chapter 3, a 4-peak model is used to fit four molecular

peaks to the carbon scan for molecular quantification, and the specific molecules corresponding to the peak energy levels is looked up in a XPS handbook [126].

Figure 13.13 and Figure 13.14 contain the XPS results for deposit samples from both of the base fuels. Notice that the ratio of C to O in both cases is extremely similar, as shown in Figure 13.13, and the location of the peaks for the carbon scan is also nearly the same. The overall shape of the carbon scans for the deposits resulting from the unadditized fuels have some similar, distinct features. There is a main peak at 284 eV (near that of pure carbon) and a smaller peak, or bump, at roughly 281.5 eV. Moreover, the locations of the four peaks in the fit for each deposit sample in Figure 13.14 are remarkably close. This suggests that the surface composition of the two deposit samples, despite originating from fuels with different chemical composition, shares many traits. We know from Chapter 11 that fuel composition plays a significant role in the overall CCD accumulation process, growth rate and overall equilibrium thickness. However, the chemical composition of the layer itself is insensitive to variations in the chemical components of refinery stream fuels. The next few pages of plots are presented in the same fashion as Figure 13.13 and Figure 13.14, and investigate if CCD's chemical structure is affected by the additive package in the fuel from which the deposits are derived. Figure 13.15 and Figure 13.16 contain XPS results for the deposit samples created by the two PBA dosed fuels, while Figure 13.17 and Figure 13.18 have the XPS data for the fuels with the PEA additive package.

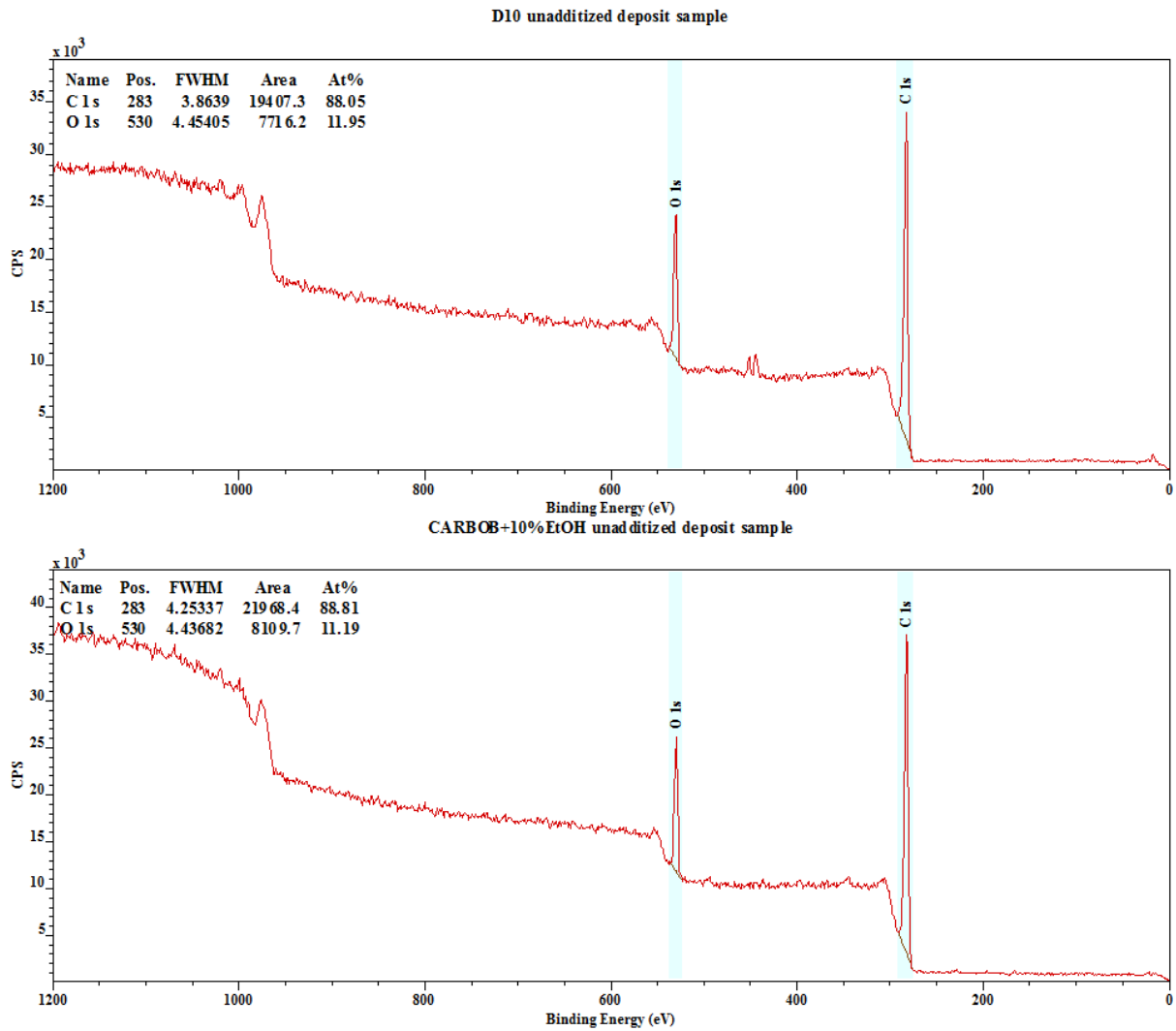


Figure 13.13 - Spectra for the unadditized D10 and CARBOB+10%EtOH deposit samples scanned by XPS (D10 on the top, CARBOB on the bottom); here the dominant elements, C and O, are highlighted

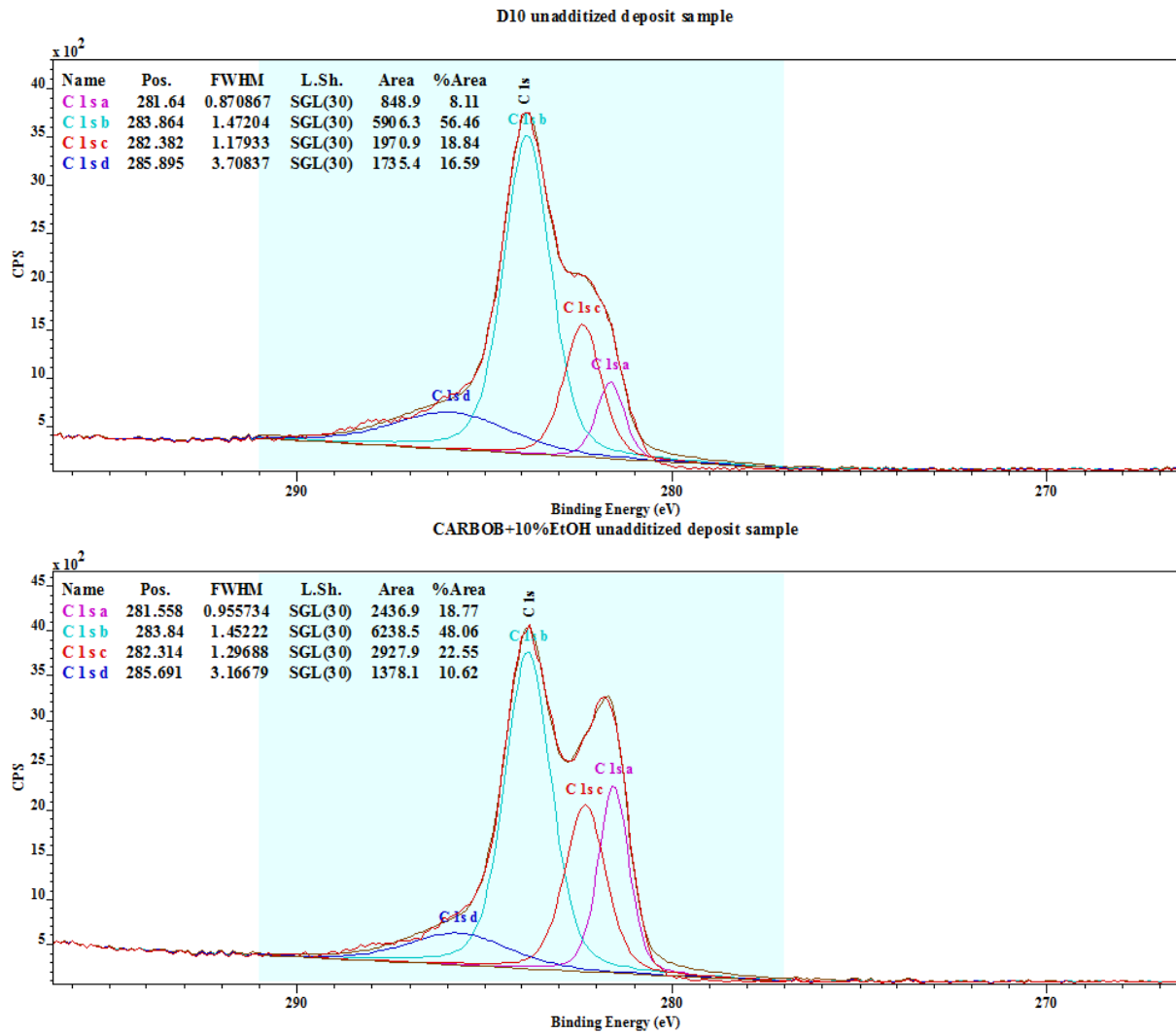


Figure 13.14 - Carbon scan for the unadditized D10 and CARBOB+10%EtOH deposits (D10 on the top, CARBOB on the bottom)

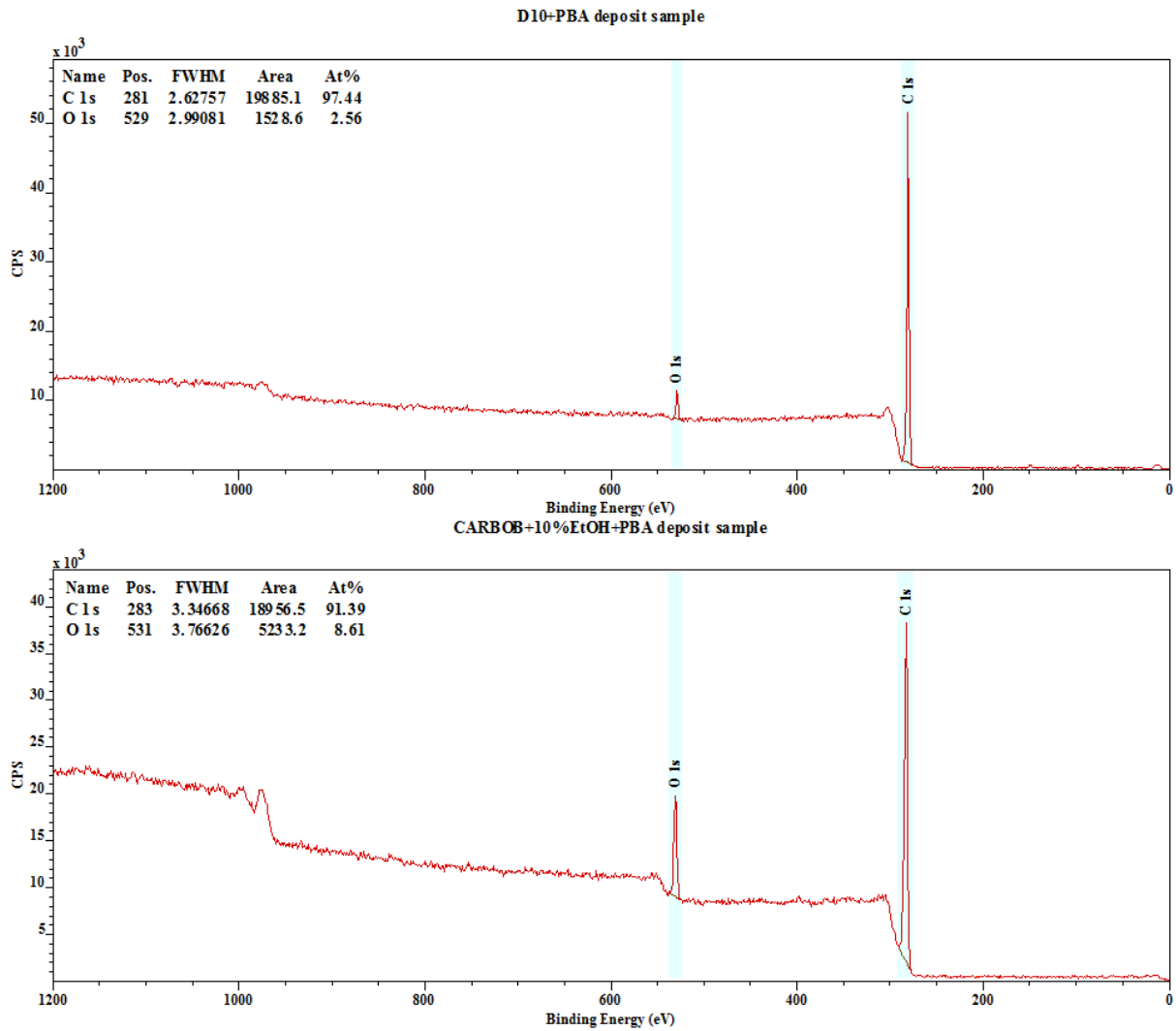


Figure 13.15 - Core scan for deposits from both base fuel types dosed with a PBA additive package; carbon and oxygen peaks are highlighted along with atomic composition (D10+PBA on the top, CARBOB+PBA on the bottom)

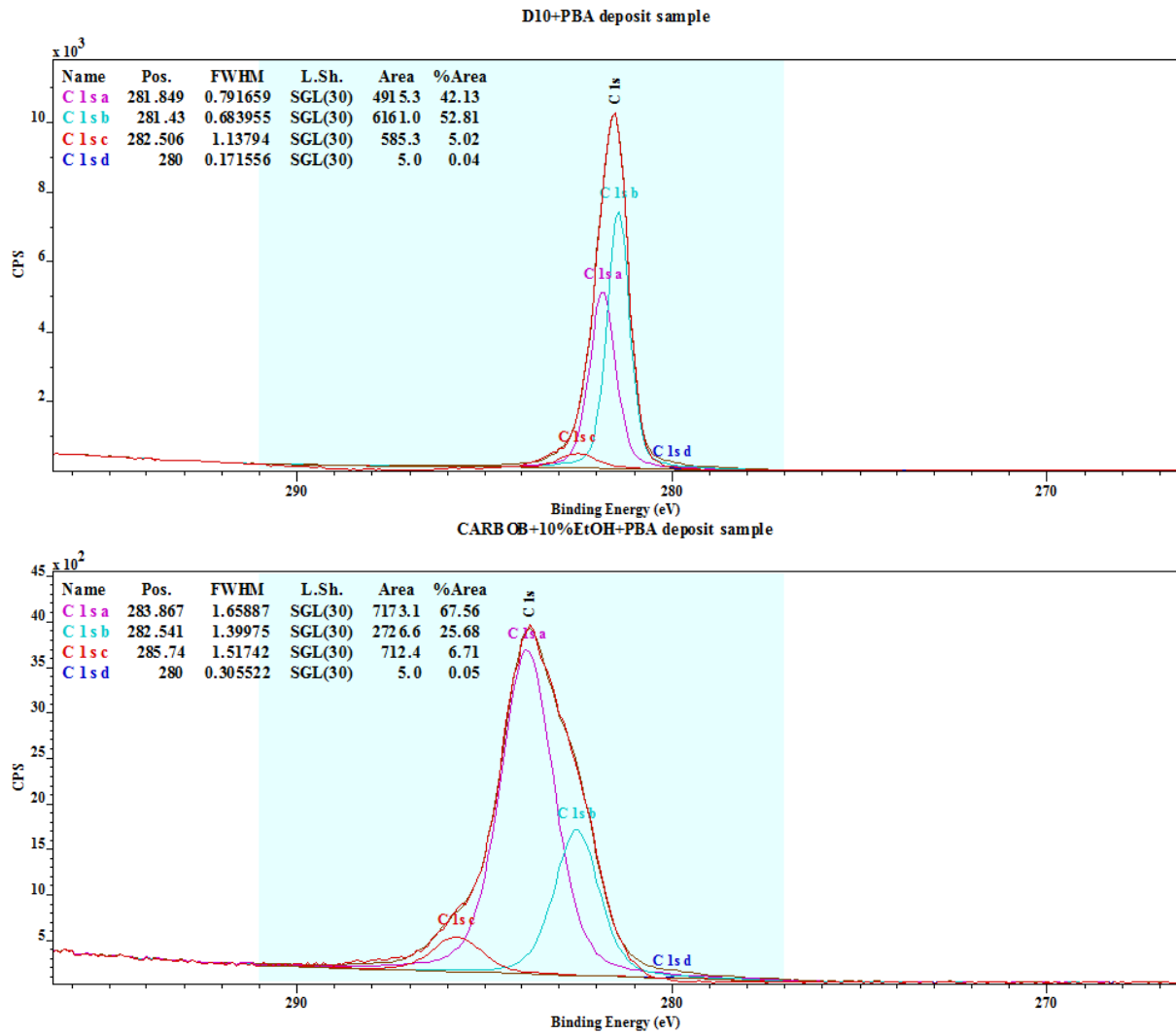


Figure 13.16 - Carbon scan for deposits samples from both fuel types dosed with the PBA additive package (D10 on the top, CARBOB on the bottom)

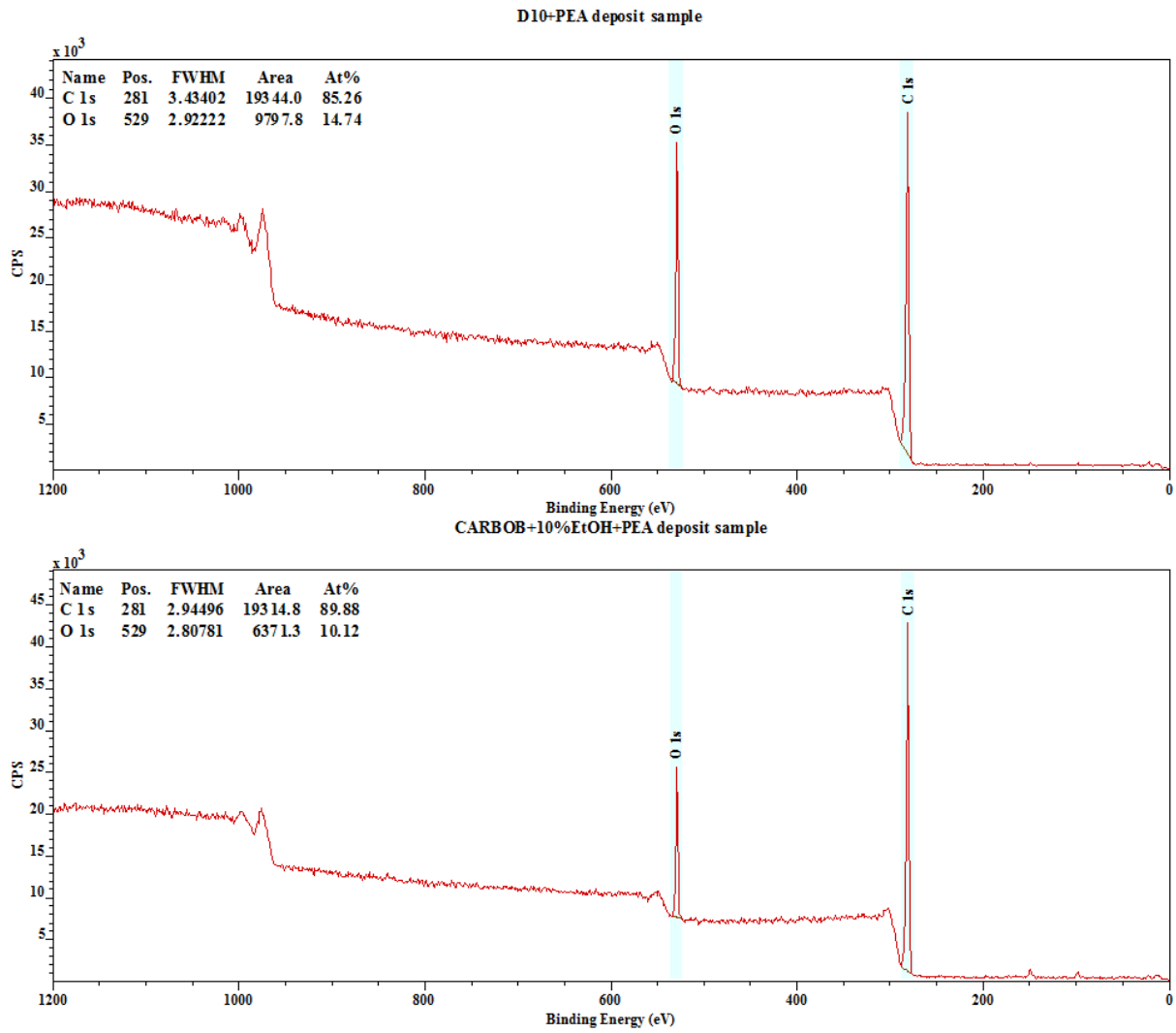


Figure 13.17 - PEA additized deposit samples core scan with carbon and oxygen peaks highlighted (D10 on the top and CARBOB on the bottom)

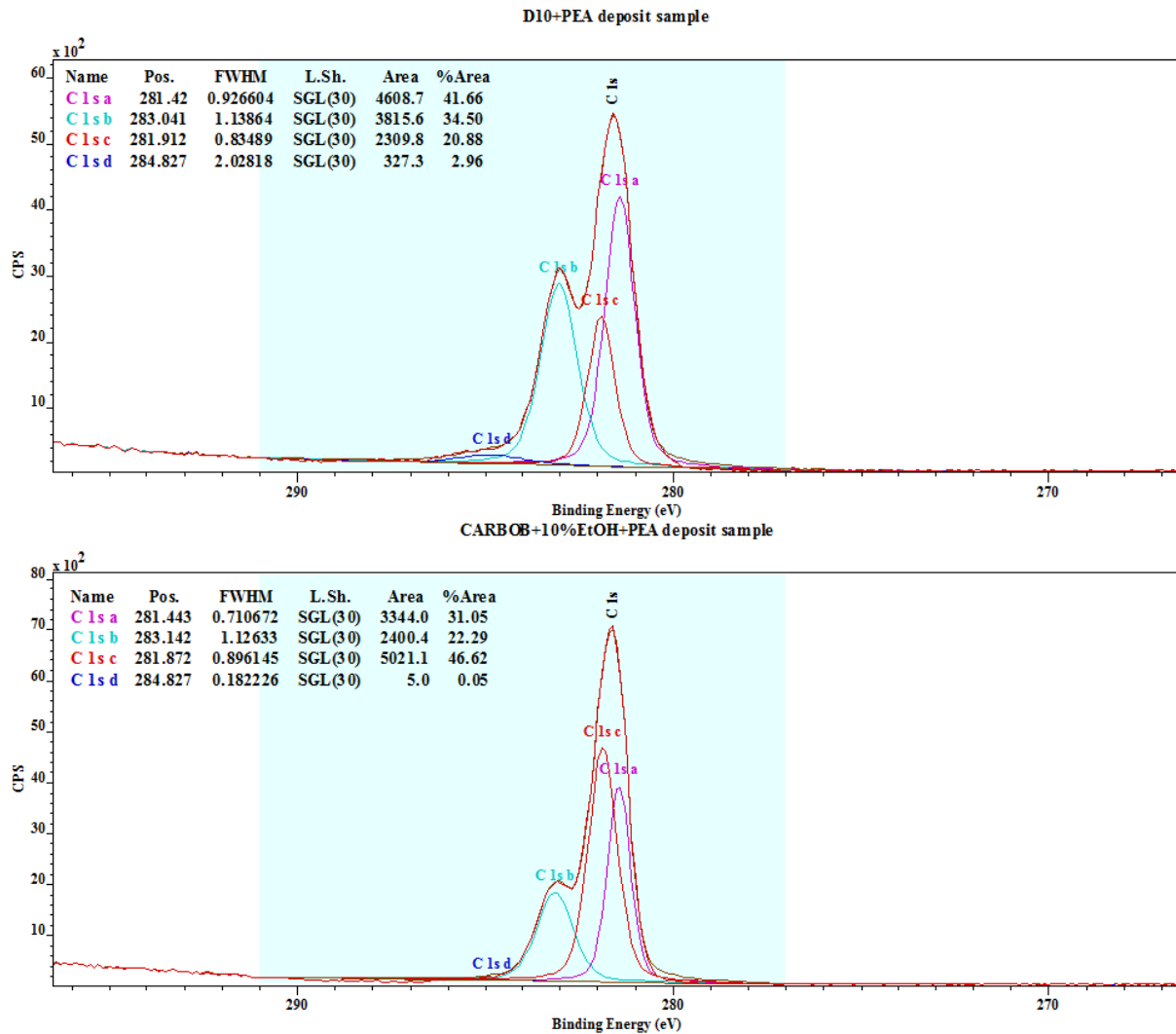


Figure 13.18 - Carbon scan for deposit samples from PEA additized fuels (D10 on the top, CARBOB on the bottom)

For the carbon scans in Figure 13.16 and Figure 13.18, there is similarity in the overall shape of the red, experimental curves within one additive package. Both of the carbon scans of deposits derived from fuel dosed with PBA look like one large peak (albeit they are offset from one another), and the scans of deposits created by fuel dosed with the PEA package have one main peak at about 281.5 eV, as well as one

more minor peak at approximately 283.5 eV. It does appear that the basic form of the carbon scan is highly dependent on the additive package in the fuel from which the deposits were derived (or the lack thereof) rather than the constituents of the base refinery stream fuel, as the samples from the same additive have similar molecular compositions. This result is in agreement with the study in section 13.2.1, where a number of CCD flakes' surfaces were imaged using an SEM. The surface morphology of the flakes studied shows more sensitivity to the additive package used than to the composition of the refinery stream fuel blend. The results from the XPS figures are summarized below in Table 13.2 and Table 13.3. The second table translates the 4 peak fits, using the XPS handbook mentioned, to list the specific types of molecules and the relative percentage of each, in these deposit samples. The carbides in the first column correspond to methyl groups (CH_3), as well as other small hydrocarbon molecules, like CH and CH_2 . These simple hydrocarbon molecules are almost certainly portions of a side chain of a more complex, underlying hydrocarbon structure, as carbides this simple and not bonded to some larger molecule would have evaporated and never had the chance to condense on the combustion chamber walls. The XPS scan will, however, only detect composition on the surface of a sample, so if these more complex molecules are located deeper in the specimen's bulk, they will not be captured by the results of the XPS scan.

Table 13.2 - Carbon to oxygen ratios for all tested deposit samples from XPS analysis

Fuel Derived Deposit Type	Carbon At%	Oxygen At%	C:O Ratio
D10 base fuel	88.05	11.95	7.37
CARBOB+10%EtOH base fuel	88.81	11.19	7.94
D10+PBA	97.44	2.56	38.06
CARBOB+10%EtOH+PBA	91.39	8.61	10.61
D10+PEA	85.26	14.74	5.78
CARBOB+10%EtOH+PEA	89.88	10.12	8.88

Table 13.3 - Summary of the molecular structure for all the deposit samples tested with XPS; molecules given as a % area from the 4-peak analysis of the carbon scans

Deposit Sample Type	Molecular Compound % Area from Carbon Scan		
	Carbide	Elemental C	C with N/S/Cl
D10	26.95	56.46	16.59
CARBOB+10%EtOH	41.32	48.06	10.62
D10+PBA	100	0	0
CARBOB+10%EtOH+PBA	25.73	67.56	6.71
D10+PEA	97.04	2.96	0
CARBOB+10%EtOH+PEA	99.95	0	0.05

In general, the ratio of the atomic percentage of carbon to oxygen is higher for the surface scan with XPS than the bulk sample XEDS results of Table 13.1. Also, of note is that while the samples as analyzed by XPS contain some oxygen, the estimation of molecular composition at the surface, in Table 13.3, shows that the surface composition of all the deposits is primarily elemental carbon and simple hydrocarbon structures. This may occur because the more complex molecules containing carbon and oxygen bonds are present within the bulk of the sample, but not the surface. This finding concurs with the previously discussed SI, two zone formation mechanism, as more complex carbon based molecules are able to condense on the relatively colder

metal walls during initial CCD growth. The layer's increasing thickness and surface temperature allows for better combustion of these unburned species, such that only more simple carbides and small hydrocarbon molecules are able to build onto the CCD layer closer to the equilibrium condition.

13.4 X-Ray Diffractometry

The final methodology used to characterize the structure of the deposit samples, examined in this chapter, is X-ray diffraction tests that use the small-angle X-ray scattering (SAXS) techniques detailed, in Chapter 3. This technique allows for the determination of porosity, the fraction of void volume to solid volume, as well as for the evaluation of the characteristic dimensions of the substance's pores. The fundamental quantities measured by the SAXS instrument are scattering curves of intensity versus the scattering angle. Generally, this angle is converted into a quantity known as the scattering vector, \mathbf{q} , detailed in Chapter 3, which is inversely proportional to the wavelength of the X-ray beam used to irradiate the sample (hence the units of \mathbf{q} are given as \AA^{-1}). Other methods to quantify porosity and characteristic pore dimension exist, however due to the lack of deposit mass created with the conditioning sweeps discussed in Chapters 11 and 12, these were not viable options.

An initial test for the validity of the SAXS method was performed using a deposit sample from an older piston, run in a different single-cylinder HCCI engine at the University of Michigan. This piston had a sufficient amount of sample that could be extracted in order to perform a nitrogen gas sorption test, to determine a characteristic pore length. The results of this test determined that the pore width is 24 nm, and

measuring three different locations of a flake using SAXS and the method outlined in Chapter 3 resulted in a pore width of 23.55 ± 0.11 nm. There is good agreement between the gas sorption test and the SAXS method, which was encouraging going forward with the characterization of deposit samples using diffractometry.

The following two figures show the scattering curves for the deposit samples from the D10 blends (in Figure 13.19) and from the CARBOB+10%EtOH blends (in Figure 13.20). The largest differences in these scattering curves exist at lower values of the scattering vector, which correspond to higher scattering angles from smaller pore features. For the D10 blends of fuel, both the additized deposit samples deviate noticeably from the deposits of the base fuel at the low q values.

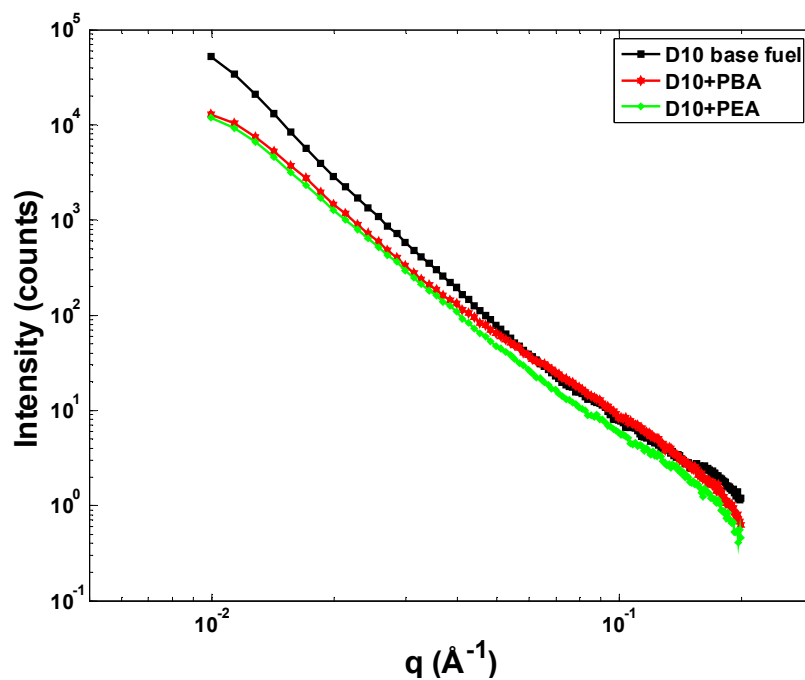


Figure 13.19 - Scattering curves for deposits derived from D10 blends showing the collected intensity against the scattering vector q

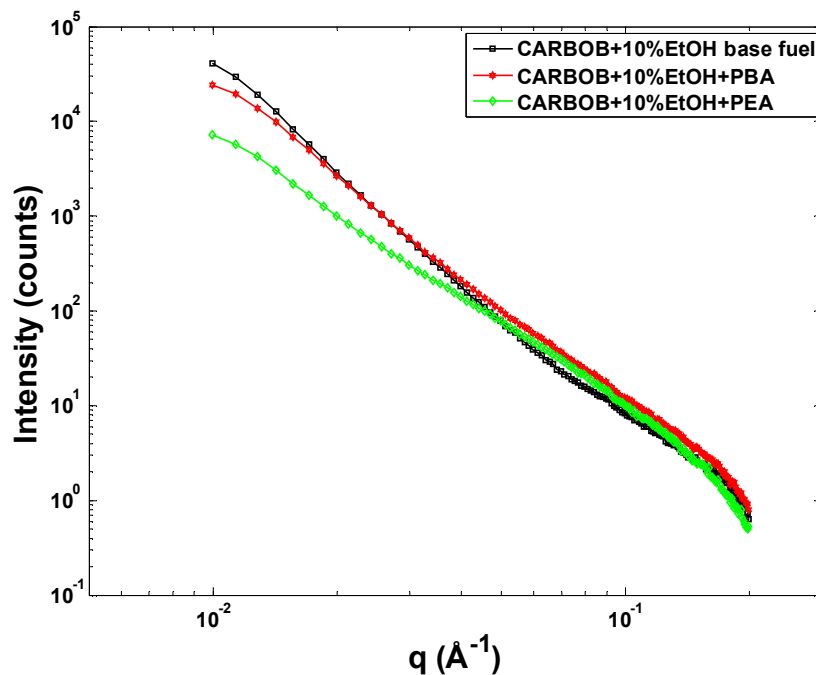


Figure 13.20 - CARBOB+10%EtOH deposit sample scattering curves with intensity plotted against the scattering vector q

In the case of the CARBOB+10%EtOH deposits, both the PBA and PEA deposit samples display differences from the base fuel sample, however there is far more divergence in the case of the PEA sample. In fact, the deviation of the CARBOB+10%EtOH+PEA sample from the base CARBOB deposits is slightly larger at the lowest q values than the deviation of the D10+PEA deposits from the base D10 deposits. This will be further examined once the properties of the deposits are enumerated.

From the scattering curve data, the characteristic function $\gamma(r)$ can be created using the equations outlined in Chapter 3. As a reminder, the best way to visualize the data in Figure 13.21 and Figure 13.22 is to consider the value on the y-axis as the

probability that a given particle volume (a pore in this case) shifted by a distance r intersects the translated volume.

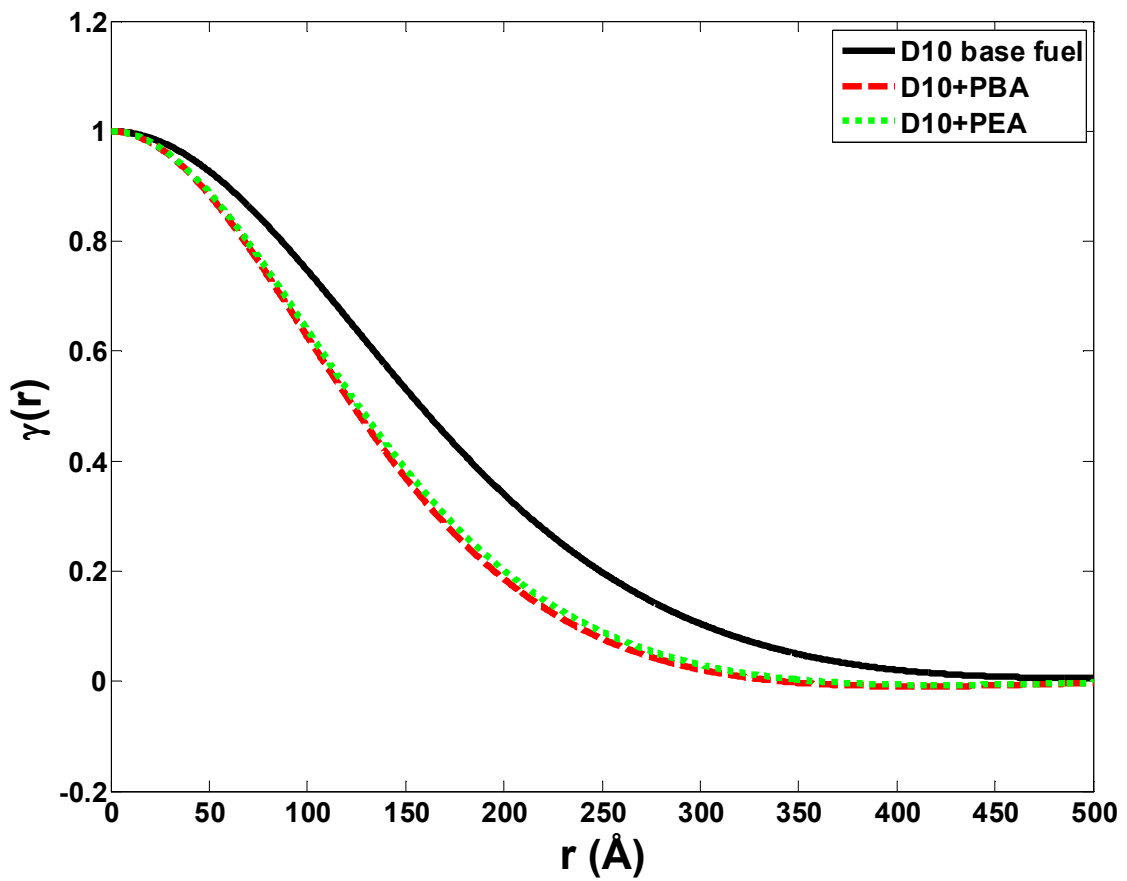


Figure 13.21 - Characteristic function for the D10 deposit samples against the translation length r , measured in angstroms

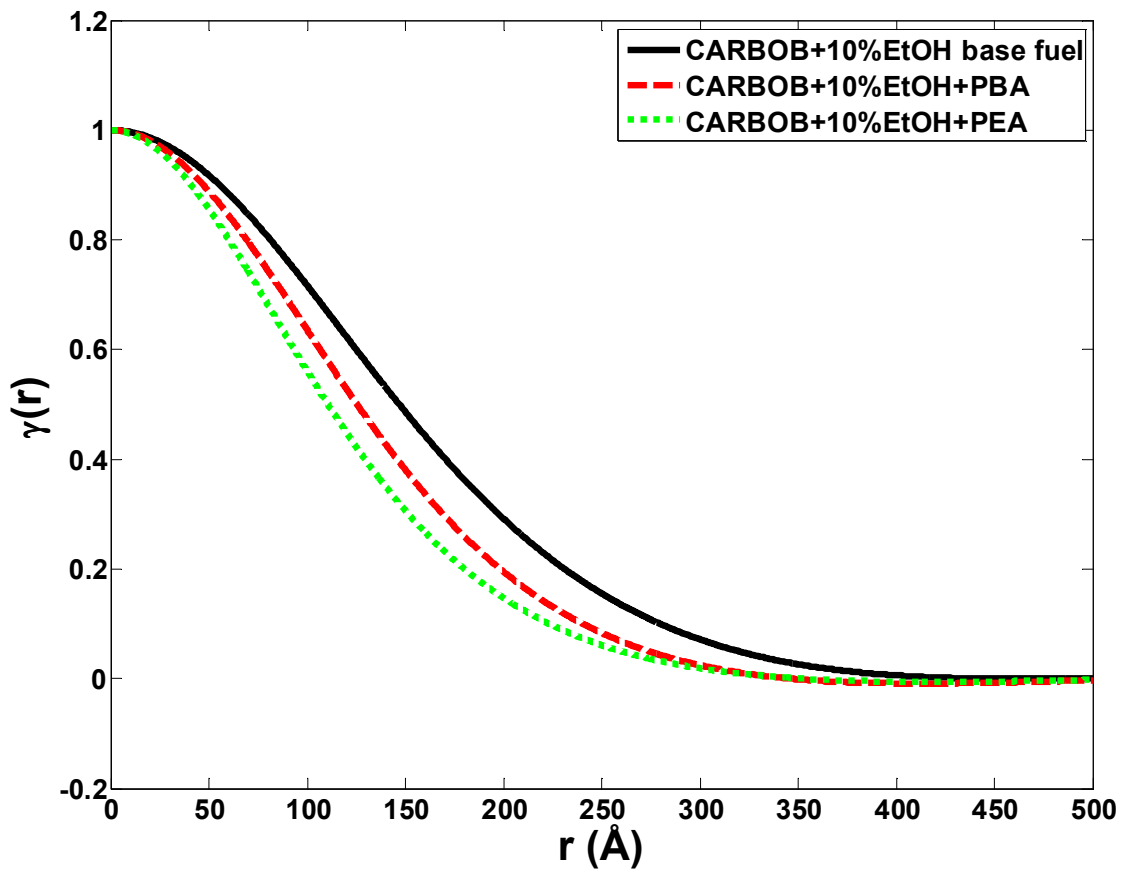


Figure 13.22 - Characteristic function for the CARBOB+10%EtOH deposit samples against the translation length r , measured in angstroms

The story of these plots is similar to the trends shown in the scattering curves, which is to be expected given the dependence of $\gamma(r)$ on the data in the scattering curve. The curves for the deposit samples of additized fuel lay nearly on top of one another for the D10 deposit samples, but are better differentiated from one another with the CARBOB deposits. Again, the additive packages appear to have a significant impact on the fundamental structure of the deposits regardless of which base fuel they are blended into.

Once the characteristic function plots, which make no assumption regarding the underlying form of pores in the tested samples, are calculated, some form factor must be used to determine specific attributes of the samples. Originally, it was suspected that a spherical approximation would be sufficient to estimate the dimensions of pore size for the HCCI engine deposits. However, after viewing the TEM results, such as those shown in Figure 13.5, it was determined that this approach was not the most accurate way to capture the porous structure of the flakes, as they do not conform to the spherical estimation. Therefore, the model proposed in Chapter 3, which agrees well with nitrogen sorption results for RD3-87 deposits, was utilized. Some of the salient pieces of data for the deposit samples discussed in this chapter are highlighted in Table 13.4. The uncertainties here are due to precision, as all these quantities were averaged over three different sampling locations for each deposit sample examined in the SAXS device.

Table 13.4 - SAXS results summary for all tested deposit samples

	Pore Width (nm)	Porosity (%)	S_v (m²/cm³)
D10 base fuel	27.28±0.60	56.34±0.53	83.98±3.9
D10+PBA	21.36±0.04	52.03±0.46	258.18±50
D10+PEA	21.63±1.48	51.01±2.37	211.69±46
CARBOB+10%EtOH base fuel	24.72±0.44	55.25±0.20	102.86±9.4
CARBOB+10%EtOH+PBA	21.91±0.26	52.75±0.45	211.85±5.1
CARBOB+10%EtOH+PEA	18.87±1.02	45.61±1.87	545.96±57

This table offers keen insight into the nature of these deposits. The first important piece of information to interpret is the characteristic pore width of these deposit samples. In previously published work on SI engine deposits, the pore width is

roughly an order of magnitude smaller [117], although this SI research actually mixed together extracted deposits from both the cylinder and piston top. The samples in the work of this chapter were extracted from the piston only.

Another major finding is that the porosity of deposits from the additized fuels is relatively lower than those of the base fuels with no additive. It is possible that additive molecules which have not completely decomposed during the combustion process are filling some of the pore structures during deposit accumulation, and reducing effective porosity of the CCD layer [37]. However, were this the sole explanation however, we would expect that the deposits from fuels with the PBA additive package would possess smaller porosity, as the PBA structure breaks down less readily than the PEA backbone. But, as shown in Table 13.4, the opposite is true, with PBA deposit porosities higher than those of the PEA deposit samples. This could be attributable to the relatively small area over which deposits were collected; other locations might experience different “pore filling” behavior between the two additive packages.

The last finding from the data in Table 13.4 is in the last column, which contains the surface area per unit volume, S_v . This quantity can be thought of as a quantification of roughness, as a larger surface area per unit volume corresponds to a sample that is far from being a smooth, homogeneous surface, and more akin to something with a jagged structure. The additive packages have a significant impact on this surface roughness, particularly in the case of the CARBOB with PEA additive. These deposits were the most distinctive from what was shown in the photographs in Chapter 12, and this difference is confirmed by the SAXS findings. In summary, the partial

decomposition of the additive molecules and the subsequent deposition on the CCD layer has a quantifiable influence on the physical structure of the surface.

13.5 Thermal Diffusivity Studies

The final section of this chapter explores the properties of the cylinder head deposits via the coaxial heat flux probes, mounted flush with the combustion chamber wall. While the measurements of peak temperature phase delay (which are necessary for the diffusivity calculation) were taken in-situ with the engine firing, in contrast to the more static tests of the previous sections, the thicknesses on the probe deposits had to be collected ex-situ with the probes removed from the engine. Thermal diffusivity (α) is an important property of the deposit layer, as it provides a way to characterize the thermal conductivity of a substance relative to its bulk heat capacitance. A deposit layer of lower α will insulate the chamber more effectively, as heat propagates more slowly through the deposit material. This is physically detected by the heat flux probes as the difference in delay in the crank angle location of the peak temperature, between the “dirty” probe and the “clean” probe.

Figure 13.23 shows the calculated thermal diffusivities for a number of thickness measurements taken on both heat flux probes, for each fuel. General trends are drawn as dashed lines for each heat flux probe, as they were not the same in the case of the thinner deposit layers. The difference between the two probes could be due to the phenomenon discussed in Chapter 11, in which there were instances of deposit “speckling” on heat flux probe 2 in or around the measuring junction that impact temperature readings. Another factor in the discrepancy may be that the structure of

the deposits is different between locations 1 and 2. This conjecture is reasonable, since the geometry of the piston is vastly dissimilar at each of the probe locations (one in the “squish” region, one in the “anti-squish”), and the interaction of fuel and the metal surfaces could therefore vary between positions.

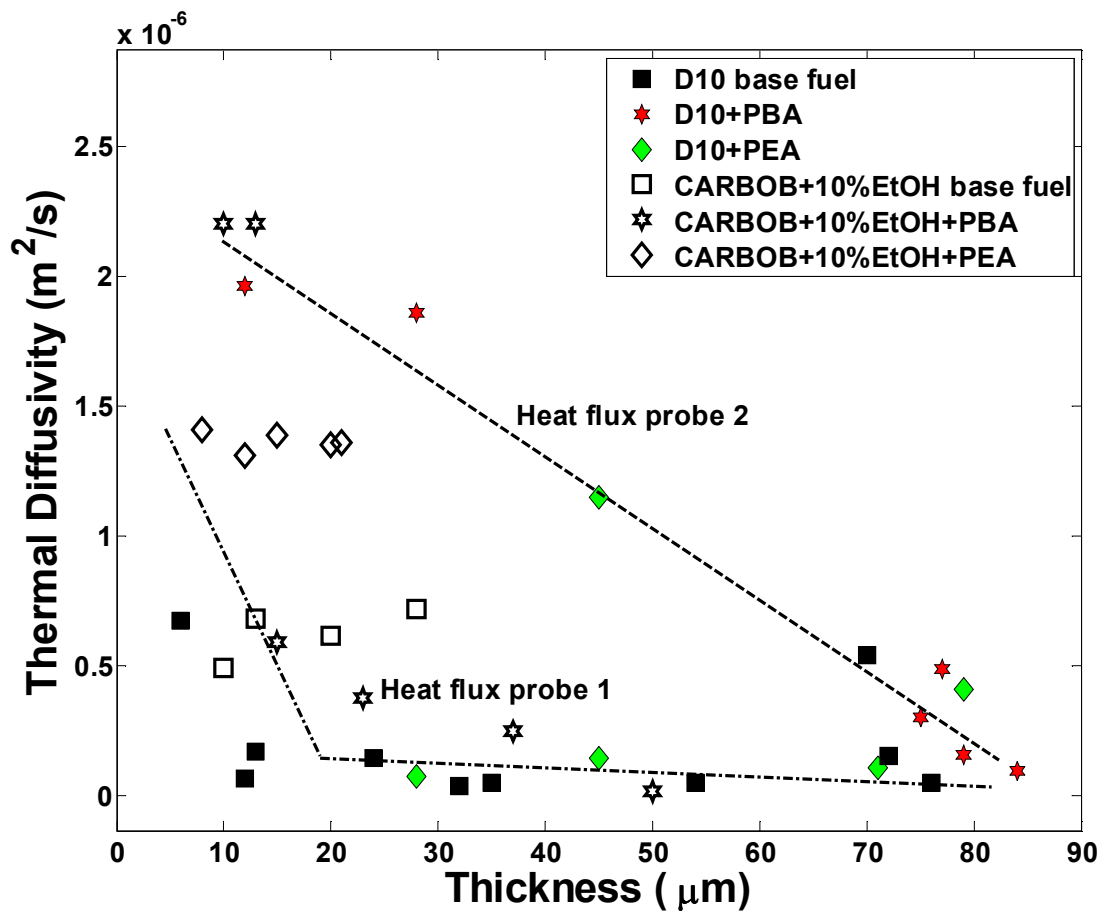


Figure 13.23 - Thermal diffusivity for deposits samples of all tested fuels against thickness measured on the coaxial heat flux probe

At high enough thicknesses, which are only found with deposits from the D10 blends, the thermal diffusivity values for the two probes begin to converge regardless of

the additive package used. Even at lower thicknesses, where there is more divergence between the two probes, the thermal diffusivity of the layer generally increases no matter what fuel or additive package is used.

This broaches another important topic regarding the nature of CCD in HCCI engines; the thermal diffusivity of the layer on the cylinder head is relatively insensitive to the refinery stream fuel or additive used to produce the deposition. Rather, the thickness of the deposits is the most important factor in determining the primary impact of the CCD layer upon HCCI combustion. Extending this argument, it is logical to conclude that the global cylinder-wide HCCI combustion event is impacted more by the thermal characteristics of the CCD layer than by any specific compositional properties. This has been observed throughout this chapter as well as Chapters 11 and 12. To further investigate this hypothesis, a simple linear regression was performed against the fully-conditioned CA50 using the total deposit thickness over the entire piston (adding all the deposit thicknesses in the maps of Chapters 11 and 12), as well as a total thickness of the periphery (to accentuate the importance of growth in the lowest clearance volume portion of the piston, on the “ring” that surrounds the bowl) and the intake air temperature (as this contributes to the overall charge temperature and combustion phasing as well, and was changed in order to compensate for the differences in the auto-ignition kinetics of the two base fuels). The measured equilibrium CA50 values displayed in Figure 13.24 are calculated as averages of the CA50 over the last 3 hours of engine run time, once the combustion advance had stopped and either reached an asymptote, or begun to oscillate about an average value (burn-off and rebuilding of deposits at the fully-conditioned state). The regression formula is shown in Equation

13.1, where TT is the total thickness of deposits over the entire piston, PT is the total thickness of periphery locations, and T_{int} is the baseline intake air temperature used for a fuel during a conditioning sweep.

$$CA50 = aTT + bPT + cT_{int} + d \quad (13.1)$$

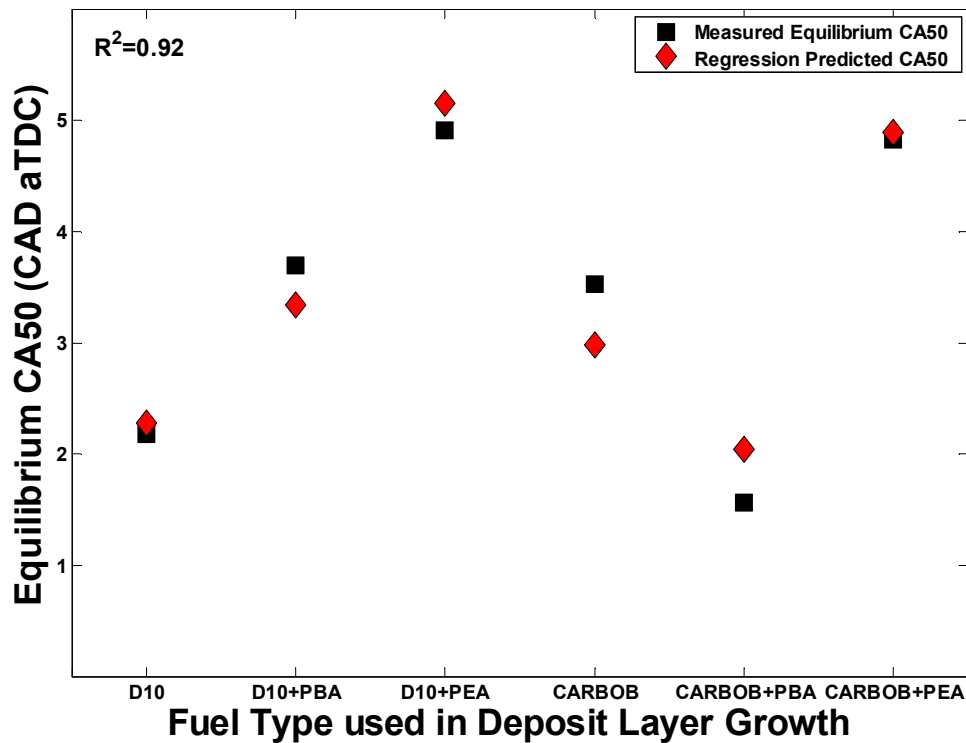


Figure 13.24 - Fully-conditioned CA50 for deposit layers from all test blends in Chapters 11 and 12 as compared to a correlation using intake temperature and deposit layer thickness

Notice that the regression does not use any terms that involve chemical composition of the deposit layer or any kind of chemical structure terms. As shown by

the high strength of the regression in Figure 13.24 ($R^2 = 0.92$), this simple correlation is able to capture the impact of the CCD layer on the equilibrium HCCI combustion phasing, for a given fuel. Again, the intake air temperature term arises as a consequence of the specific procedures used in these experiments, as the two base fuels were run at different intake air temperatures to offset dissimilarities in auto-ignition chemical kinetics (and naturally, this change in intake temperature impacts charge temperature and combustion phasing). Looking at either fuel by itself and the resulting CCD it created, the fully-conditioned CA50 is almost exclusively a function of deposit thickness.

To reiterate, HCCI combustion phasing was most significantly impacted by the amount of deposits that accumulated in-cylinder for each base fuel with and without additive packages. Looking at various results from this chapter, chemical composition is often similar between two layers created from the same additive package, or from the base fuels. However, two layers that are chemically alike, such as those that result from the D10 and CARBOB+10%EtOH base fuels, affect the combustion event differently. Ultimately, the HCCI process is extremely sensitive to combustion phasing, and in turn, this phasing is dramatically influenced by charge temperature. The temperature of the incoming charge of fuel and air is directly affected by charge heating from the CCD layer, and in the case of these experiments, also by the baseline reference intake air temperature needed to combust a given fuel. Thus, the most important impact of the chemical components of refinery stream fuels and additive packages is their influence on the rate of growth, and the equilibrium thickness of the deposits they induce, rather than the compositional type of layer they create. The

engine itself does not possess any form of hysteresis; it cannot distinguish how the combustion chamber arrived at a certain state of conditioning, but merely reacts to how this layer insulates the chamber and provides charge heating during the intake stroke, by limiting heat loss to the walls. This effect is primarily a function of the CCD layer's thickness.

CHAPTER 14

Impact of a Fully-Conditioned Piston and Cylinder Head on HCCI Combustion

14.1 Introduction

As demonstrated in previous chapters, the growth of a CCD layer has a significant impact on the HCCI combustion event. Recalling that the HCCI combustion event can be envisioned as “controlled knocking”, any phenomenon that affects the incoming charge temperature and pressure will ultimately play a substantial role in HCCI combustion and engine operation. In order to explore these issues, this chapter will investigate the changes in engine operating performance generated by CCD layers formed by the two base refinery stream fuels, D10 and CARBOB+10%EtOH, as well as by both of these blends in combination with a PBA and PEA additive package.

14.2 Variation of Charge Temperature to Offset CCD Growth

As mentioned in Chapter 10, once a conditioning sweep is completed for a given fuel (i.e. the CCD layer had reached a point of equilibrium growth), several other experiments are run on the engine to assess the impact of the deposit layer on engine operation. Intake air temperature sweeps were run in the same manner as was detailed

in Chapter 5, in an effort to tie some of the research on deposits back to previous work concerning refinery stream fuels' impact on HCCI combustion, independent from deposits. These tests are all run at a constant coolant temperature of 95°C.

14.2.1 Intake Air Temperature Adjustment

Once the combustion chamber of the engine was fully-conditioned for each fuel blend tested, a sweep of intake air temperature was performed to assess how different CCD layers might impact the combustion event, for a range of intake charge temperatures. Figure 14.1 shows the CA50 for all the fuel blends in a conditioned chamber, over the sweep of intake air temperature. Here, the relative location for each CA50 curve correlates well with the overall amount of deposition the fuel blend creates. For instance, the D10 base fuel has the thickest amount of deposits and has the most advance in the baseline CA50, as shown in Chapter 11, compared to the other D10 blends containing additive packages. In the case of the CARBOB+10%EtOH fuels, the deposits from fuel dosed with the PBA additive package had the most CA50 advancement at the reference condition. Both of these have the lowest CA50 for a given intake air temperature, as shown by the plots in Figure 14.1. Both of the CCD layers from D10 blended with PBA and PEA additive packages have a similar impact on combustion phasing at similar intake air temperatures, while in the case of the CARBOB blend they are separated by about 4 CAD. In this instance, the effect of the additive packages on engine performance with a fully-conditioned combustion chamber is dependent on the chemical composition of the base fuel it was blended into. As shown by the results outlined in Chapters 11 and 12, this is due in large part to the manner in

which the deposits are distributed throughout the chamber, as a fuel and additive package that results in more deposits in the “squish” region of the chamber ultimately has more advance in combustion phasing at the baseline, and a lower CA50 for these intake air temperature sweeps.

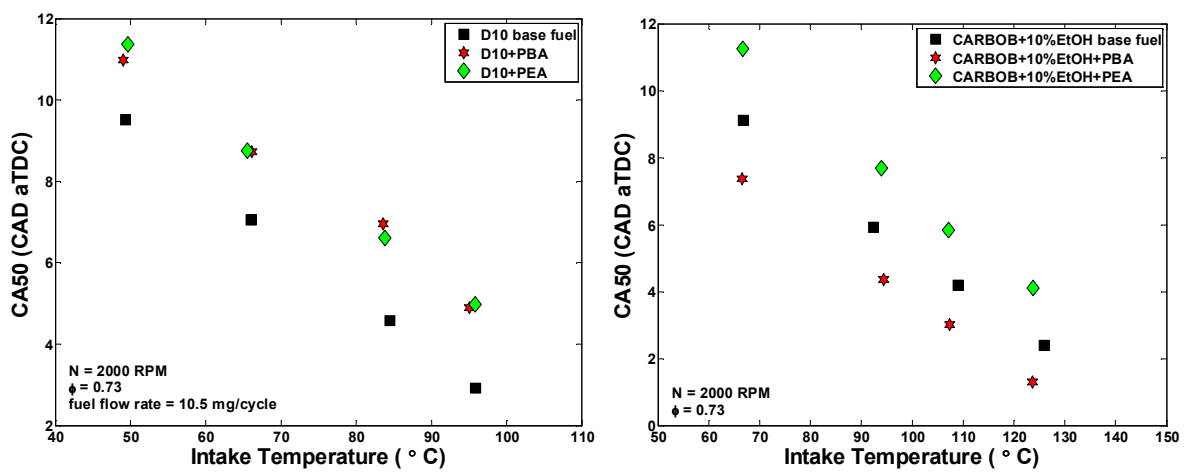


Figure 14.1 - CA50 combustion phasing over a sweep of intake air temperature for all the test fuels and additive packages; D10 blends are on the left and CARBOB+10%EtOH blends are on the right

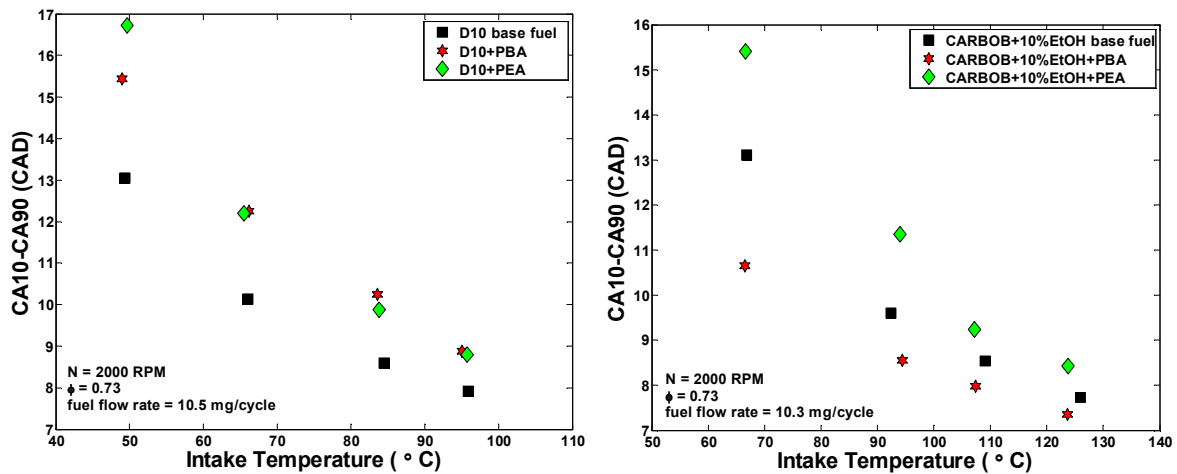


Figure 14.2 - Burn length (CA10-CA90) for all the test fuels over a sweep of intake air temperature; D10 blends are on the left and CARBOB+10%EtOH on the right

The CA10-CA90 burn duration for all of the test fuels and additive packages is plotted in Figure 14.2. The burn lengths converge at higher charge temperatures and diverge as charge temperatures and CA50 retard. In more advanced cases at higher intake air temperatures, the HCCI combustion event happens over a relatively short span (~8-9 CAD), and the differences in the engine response, between conditioned chambers for these refinery stream fuels and additive packages, becomes muddled. It appears that there is more potential for impact from the CCD layers at the lower charge temperatures that correspond to more retarded combustion phasing and more instability in the combustion event (longer burn durations), where the divergence occurs.

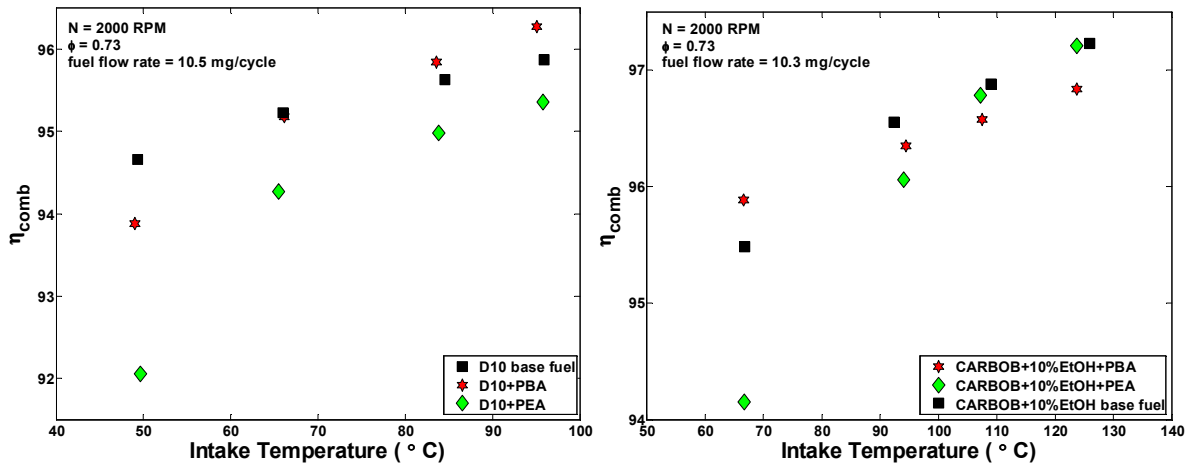


Figure 14.3 - Combustion efficiency for the test fuels run in a fully-conditioned combustion chamber with D10 blends on the left and CARBOB+10%EtOH on the right

A further investigation of this is presented in Figure 14.3, in which combustion efficiency is graphed against the intake air temperature. Among the CARBOB blends, there is a significant drop-off in combustion efficiency for the blend with PEA additive at the lowest intake air temperature, while efficiencies are relatively similar throughout the rest of the tested range of temperatures. This same sort of drop in efficiency is present with the PEA dosed D10 fuel, however, the spread between the curves stays relatively constant throughout the sweep of intake air temperature. This observation suggests that the less robust, thinner deposit layer shown with both base fuel types in Chapter 12, has a more incomplete and slightly less stable combustion event at lower charge temperatures in comparison to the other charge temperature sweeps conducted. Again, because the shape of all the curves is similar for most of the temperature range, it appears that the impacts and differences between layers (i.e. any secondary effects that might be present) assert themselves at lower charge temperatures and longer burn

durations. The spread between D10 blends throughout the range is likely attributable to the fact that there is more variation in how much the CCD layer advances the baseline condition for the base fuel and additive packages, than with CARBOB+10%EtOH.

14.2.2 Coolant Temperature Adjustment

Another method for impacting the thermal environment of the combustion chamber, and thus influence HCCI combustion phasing, is to alter the coolant temperature. This reduces the temperature at the walls of the cylinder and increases heat transfer from the gas to walls, effectively cooling the charge temperature. The result is a retardation of combustion phasing similar to that caused by decreasing intake air temperature. Recall that each of these runs were performed at constant intake air temperature, equivalent to that of the baseline condition (81°C for the D10 blends and 99°C for the CARBOB+10%EtOH blends).

Figure 14.4 shows the CA50 for all the tested fuels and additive packages over a sweep of coolant temperature. The overall trends are quite similar to what was shown by the intake air temperature sweeps, albeit in the instance of coolant temperature they take place over a smaller range. This result agrees with previous studies that demonstrates the phasing of the HCCI combustion process is more sensitive to coolant temperature than to intake air temperature for the unoxygenated, unadditized test fuel RD3-87 [5]. As with the intake temperature sweeps, the relative location of these curves is strongly tied to the results from Chapters 11 and 12 as well as Figure 13.24 that characterized how much advancement of baseline CA50 is induced by the CCD layer formed by each test fuel and additive package. Notice that in Figure 14.4 the base

D10 fuel and CARBOB+10%EtOH+PBA are still at the most advanced CA50 for a given intake air temperature. As demonstrated by the burn lengths in Figure 14.5, there is still divergent behavior between the different fuels and their respective additized blends, as coolant temperatures are dropped, causing more retarded combustion phasing. In particular, the PEA dosed blends begin to diverge more at the lowest temperatures, which correspond to the most unstable HCCI combustion event.

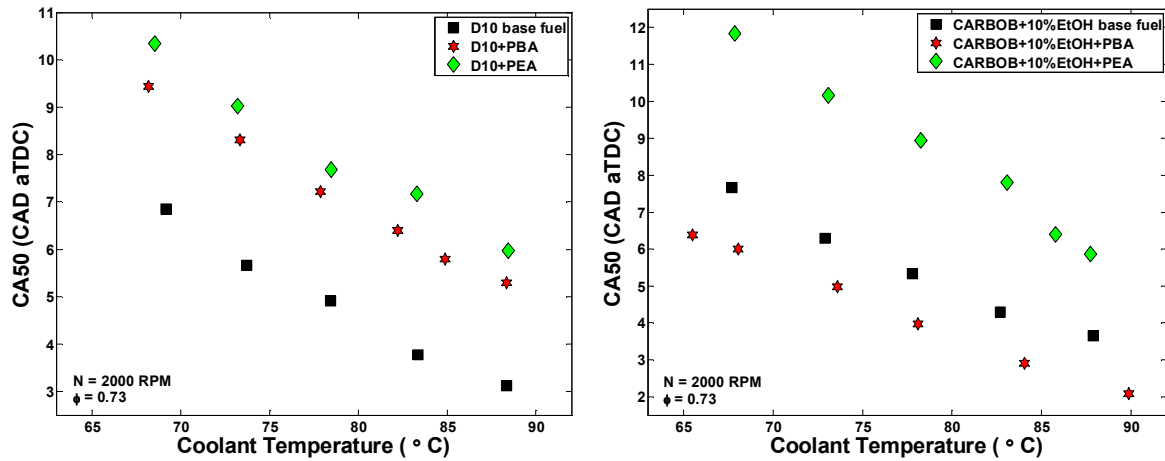


Figure 14.4 - CA50 combustion phasing for a sweep of coolant temperature in a fully-conditioned combustion chamber for all fuels and additive packages

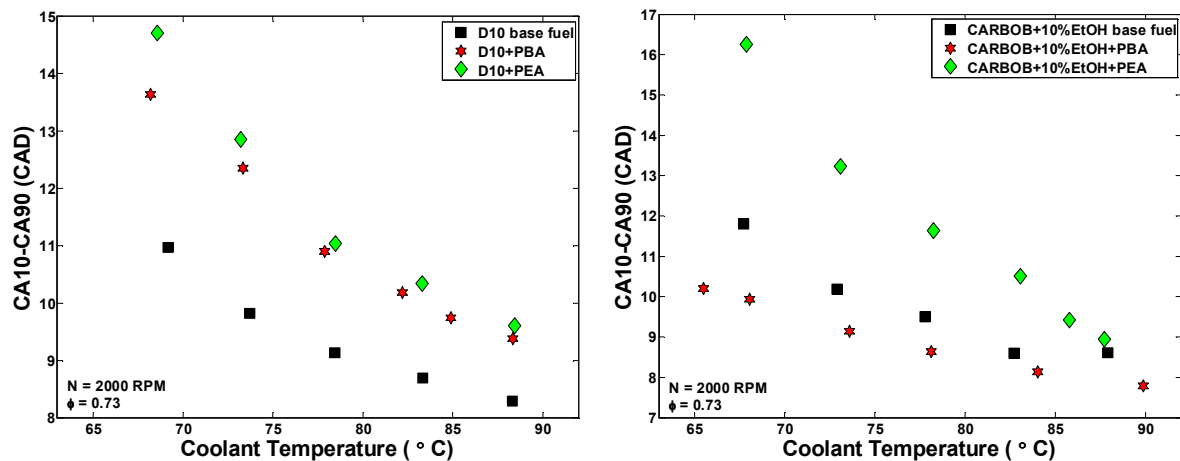


Figure 14.5 - Burn durations from CA10-CA90 over a sweep of coolant temperature in the fully-conditioned combustion chamber for all test fuel blends

Figure 14.6 is similar to Figure 14.3 in that both show combustion efficiency, in this case over a sweep of coolant temperature. As before, the overall location of the curves is tied to the overall levels of deposition in the fully-conditioned combustion chamber (higher CCD and more insulation results in higher combustion efficiency). Also, the blends dosed with PEA additive begin to significantly drop off at the lowest coolant temperatures.

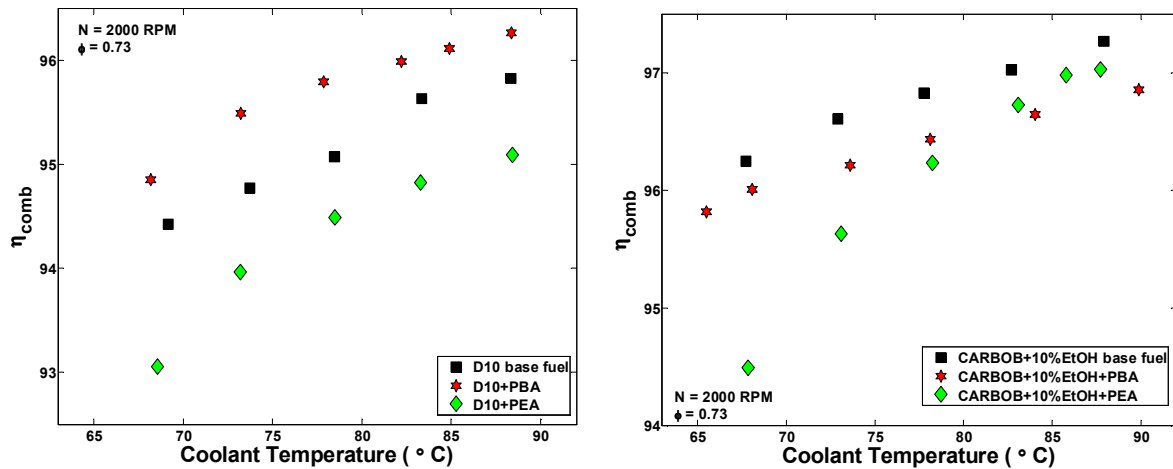


Figure 14.6 - Coolant temperature sweeps and the resulting combustion efficiencies in a conditioned combustion chamber

In both the case of the intake air temperature sweeps and the coolant temperature sweeps there is a direct connection between the results and the results of previous chapter. Recall that the deposits created with each base fuel type in combination with PEA had the lowest overall porosities. In general, a lower porosity means there is less volume of air trapped in the pores. Therefore it is logical to assume that the thermal conductivity of these layers is relatively higher than that of others, as air has a much lower conductivity than carbon (roughly an order of magnitude lower), the primary component in the solid volume of the CCD layer. With the higher thermal conductivity of PEA CCD layers, there is more heat transfer from the gas to the walls, leading to a cooler charge, and potentially a greater impact on combustion phasing and combustion efficiency. This effect is visible at the lowest charge temperatures, and is more pronounced in the CARBOB+10%EtOH+PEA fuel blend, which shows a larger drop-off in efficiency at low intake and coolant temperatures, due to its relatively lower

porosity and an estimably higher thermal conductivity than D10+PEA (approximate 45.6% compared with 51.0% porosity).

Also notice that for Figure 14.3 and Figure 14.6 the combustion efficiency curves do not follow the same trend as the CA50. The relative location of the CA50 curves against intake temperature and coolant temperature was primarily driven by how much the CCD layer advanced the combustion phasing of the baseline point. With combustion efficiency, the nature of the layer itself may play a role in the HCCI combustion process, as the highest efficiencies do not necessarily correspond to CCD layers with the highest thickness or most phasing advance. In general, the combustion efficiencies of deposits derived from blends containing PBA do not follow the same trends shown by other CCD layer tests, as the combustion efficiency does not correspond well to the equilibrium CA50. It is important to note that any effects specific to a certain type of layer morphology or structure are relatively minor, as shifting any of these PBA curves by 0.5% or less would be sufficient to line up all the curves according to the trend in CA50.

One other instance in which the impact of different layers is noticeable is the specific fuel consumption of the engine, shown in Figure 14.7. The differences are relatively small, however the CCD layers formed from the unadditized fuels have slightly more favorable (lower) ISFC over the coolant sweep, particularly at the lowest coolant temperatures. Combustion efficiency decreases as coolant temperature is reduced and combustion phasing retards, so ISFC should increase (the engine does not produce as much indicated power for the same fuel input), as occurs with both the PEA layers. The slight decrease for both the base fuels and CARBOB+10%EtOH+PBA layers across the

coolant sweep suggests that the increase in charge density, due to reduced coolant temperatures, is sufficient to overcome the loss of combustion efficiency. The influence of charge density competes with the location of combustion phasing, as a charge that is too cool will lose some indicated power due to a more retarded combustion phasing location, which may be the case for the PEA curves.

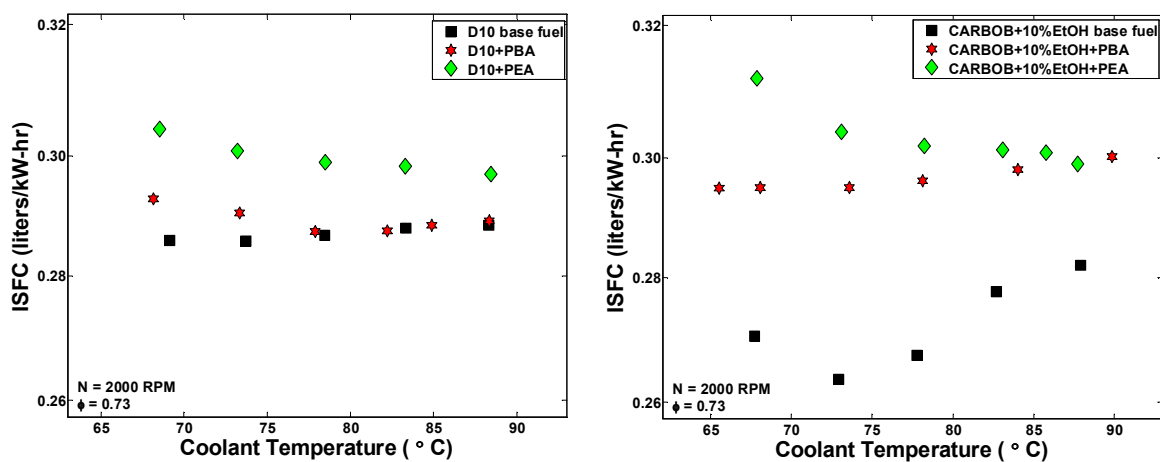


Figure 14.7 - ISFC against coolant temperature for the conditioned combustion chambers with D10 on the left and CARBOB+10%EtOH on the right

14.3 Impact of an Equilibrated CCD Layer on the HCCI Operating Range

As with the first set of combustion studies in Chapter 5, a limits sweep over engine speed was conducted for each fuel once the CCD equilibrium was achieved. This was performed so that the operating limits of a “dirty” combustion chamber could be compared to those of a “clean” chamber. As discussed in the background of Chapter 1, the expectation is that because the CCD layer has such a prolific effect on HCCI combustion at all operating conditions, the presence of a fully developed layer

should have an impact on the range of HCCI operation. Specifically, it is expected that the deposit layer will shift the operating map down [5], making it important to quantify how much different refinery stream fuels and additive packages would influence this shift. One important point to note, emphasized previously, is that the combustion chamber can never be “clean”, since deposits begin forming when fuel is injected and the engine starts firing. Hence, the “clean” limits maps presented in Figure 14.7 and Figure 14.8 are taken from previous D10 and CARBOB+10%EtOH experiments, run in combustion cylinders where deposit growth was minimized (e.g. the engine limits sweep was done at a point in time when only some growth had occurred, and the rate at which it was building was gradual enough that the effects of the deposits could be decoupled from the effects of the fuel chemical components). Essentially, if we could hit our established reference condition for a given fuel (as explained in Chapter 5), then the combustion chamber was considered to be in a “clean” state, and data could be collected. This obviously varies from the conditioned state for the fuel blends, in which the baseline point could not be reached at the reference intake air temperature and fuelling rate.

Figure 14.8 and Figure 14.9 display the limits of HCCI operability, based on the constraints detailed in Chapter 5, for all the blends of D10 and CARBOB+10%EtOH respectively. These are also compared against the clean limits, shown as blue circles, in order to reference the shift of the operating maps with the presence of an equilibrium deposit layer.

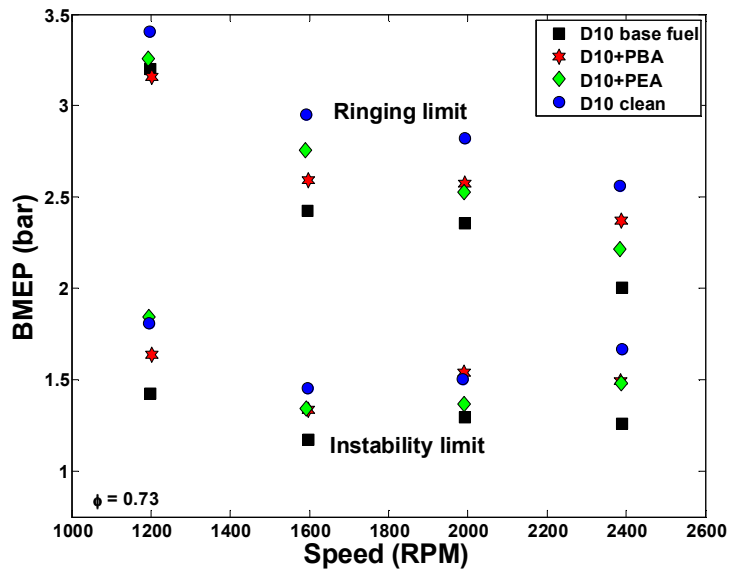


Figure 14.8 - HCCI limits of operability for all the CCD layers formed with D10 fuel blends compared to the limits test where the deposit chamber was not fully-conditioned

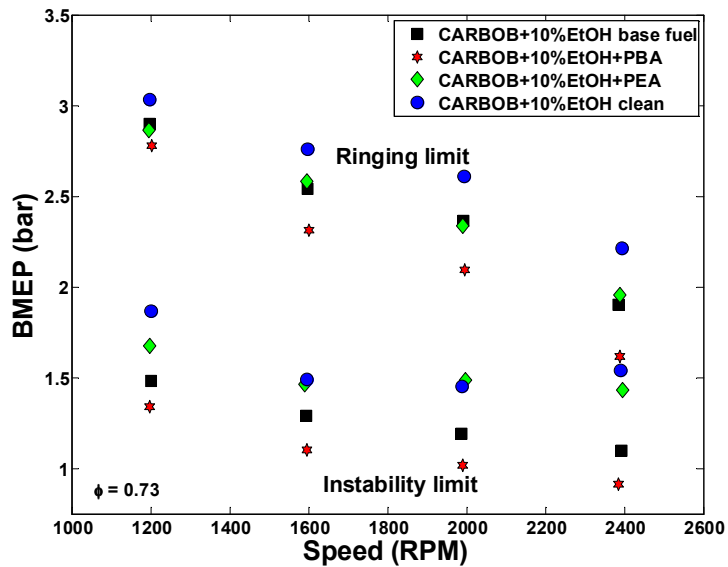


Figure 14.9 - Comparison of the operating limits for the CARBOB+10%EtOH blends with a fully-conditioned combustion chamber and the "clean" case

In all cases, the fully-conditioned chamber shifts the operating map down by a non-negligible amount given the experimental uncertainty in BMEP (on the order of ± 0.05 bar). What is inconsistent among the blends is the overall magnitude of this shift, and the effect that the two additive packages have upon the operating range. In the case of D10, a fuel with high aromatics, generally considered a “dirty” fuel in terms of the deposit growth it causes, the deposit layer that results from the unadditized blend has the most downward movement in its limits of operation. The base D10 blend had lower HLLs and LLLs across the speed range, consistent with the results of Chapters 11 and 12. Recall that the base D10 fuel has the largest change in its baseline point from a clean metal chamber to the fully-conditioned state, because it has the highest amount of CCD growth. Because of the larger mass of deposits, the expectation is that more heating of the incoming charge will occur during compression, creating the ability to run at lower loads, and the inability to reach higher loads before excessive knocking occurs. In the case of CARBOB+10%EtOH, it is the PBA additized fuel blend that alters the operating map most substantially, which is consistent with findings from previous chapters (this blend had the thickest deposits of all the CARBOB+10%EtOH samples tested). As stated previously, the unadditized D10 and CARBOB+PBA+10%EtOH create the thickest overall deposition between the two base fuel blends and the most significant advance of combustion phasing at the baseline condition, at the equilibrium thickness. It appears that deposit thickness and the consequent charge heating is correlated with the determination of how the limits of operability can be translated for the engine when the combustion chamber is conditioned with CCD.

This point is further examined in Figure 14.10 and Figure 14.11, which both show an operating map area normalized with that of RD3-87 (similar to the procedure outlined in Chapter 7) and a quantification of the overlap of the operating range areas for the conditioned chambers and that of their respective clean limits sweeps. The overlap plots are a convenient way to provide a numerical value for the relative amount a CCD layer induces a shift in the operability limits; a lower value indicates less overlap due to a more significant shift. In the right half of Figure 14.10 and Figure 14.11 the D10 base fuel and CARBOB+10%EtOH+PBA have the lowest overlap values. This indicates that their respective CCD layers and the resulting operating maps have the most displacement from the “clean” operating ranges, which confirms the observations of Figure 14.8 and Figure 14.9. Again, it appears that the additive packages have different effects when blended into refinery stream fuels of dissimilar chemical composition.

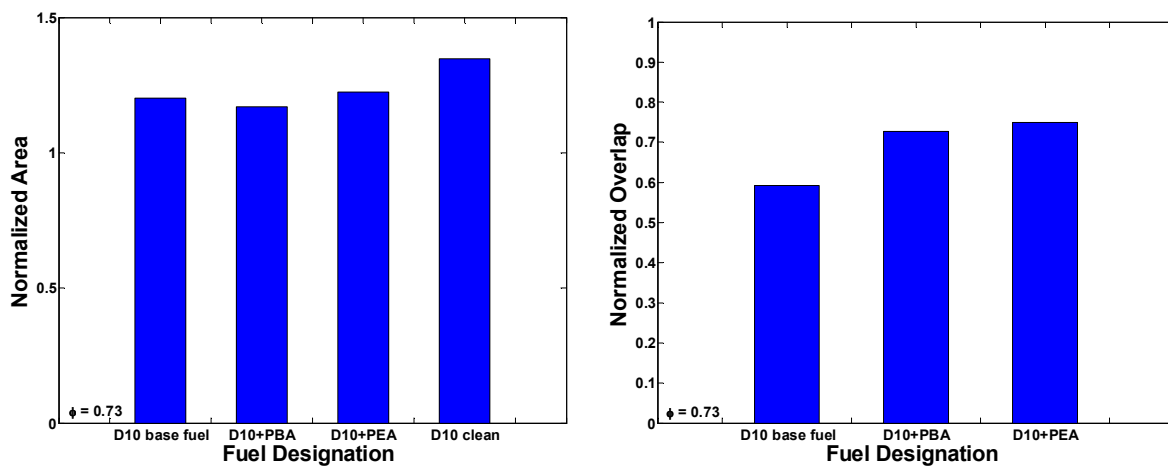


Figure 14.10 - HCCI operating map areas for D10 blends normalized to RD3-87 on the left and the amount that conditioned operating maps overlap with the “clean” range on the left

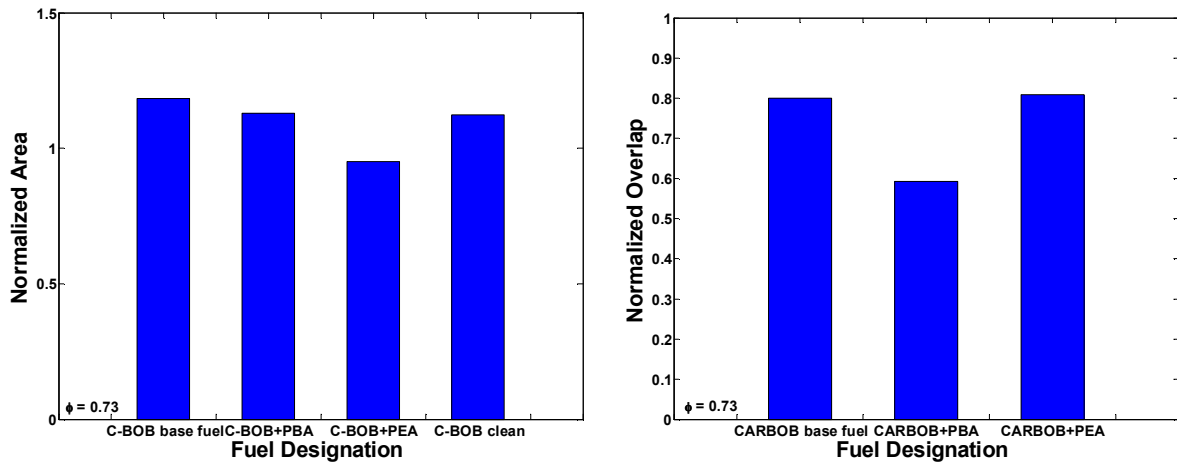


Figure 14.11 - CARBOB+10%EtOH normalized operating areas on the left and overlap areas on the right; note that the fuel designation has been shortened for space considerations

In addition to the shift that a fully-conditioned combustion chamber imparts on the HCCI operating map, there is also a change in the size of the area over the sweep of speed. This variation is shown by the length of the bars in the left-hand portion of the previous two figures. In the case of the D10 blends, the “clean” instance has the largest overall operating area over the sweep of speed, while in the case of the CARBOB+10%EtOH blends it is the fully-conditioned unadditized blend that has the most sizeable area of operating range, by a slim margin. It appears that this occurrence is the result of the shape of its HCCI operating limit, shown in Figure 14.9. The low load limit continually decreases with speed, so there is little decrease between the upper and lower load limits through the speed range. A similar phenomenon also presents with the PBA dosed CARBOB blend, which results in a slightly larger operating area

compared to the non-conditioned combustion chamber running CARBOB+10%EtOH. The behavior of these blends at the LLL for higher engine speeds of 2000 and 240 RPM is dissimilar to that of the other operating maps, shown in both Figure 14.8 and Figure 14.9, and is worth further examination. Also, the smallest operating range areas are the result of different additive packages for the two fuel blends; the D10+PBA and CARBOB+10%EtOH+PEA had the least overall area for their operating maps.

In an attempt to gain deeper insight into the behavior of the combustion process at high and low load limits, we apply some of the analytical heat release techniques utilized in Chapter 7. In Figure 14.12 the combustion phasing given by CA50 is plotted for the LLL and HLLs of the D10 and CARBOB+10%EtOH blends (low load limits on the upper left portion of the plots and high load limits on the lower right). Overall, combustion phasing is less sensitive to changes in load at the LLL than at the HLL, as illustrated by comparing the relatively tight cluster of operating points in the upper left for the instability limit and the wide spread of ringing intensity constrained points in the bottom right. This figure also highlights a component of the combustion process for the shape of the CARBOB+10%EtOH+PBA and CARBOB+10%EtOH fully-conditioned operating maps, at the LLL. As shown by the group of open squares and open stars at the top of the figure, these fuels operate at some of the most advanced CA50 values for the group of operating points, even though they are run among the lowest of engine loads. It appears that when these fuel blends are run in the fully-conditioned combustion chamber they receive a substantial benefit from the charge heating effect of the CCD layer at the LLL, particularly as speed is increased.

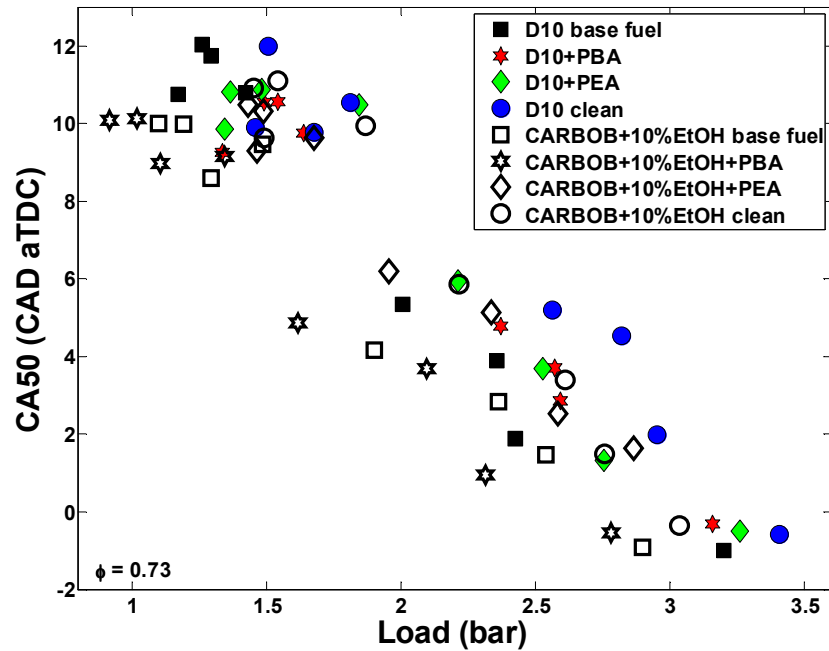


Figure 14.12 - CA50 of the load limits for the D10 and CARBOB+10%EtOH blends shown against engine load (BMEP)

Figure 14.13 is a slightly different representation of the HCCI combustion event at the limits, for all the fuels tested, which plots the CA10-CA90 burn duration against engine load. In the case of burn duration, there is a substantially decreased sensitivity for burn length as load is increased, at the HLL, as opposed to changes in CA50 at the HLL. However, looking at the burn lengths for the LLL points, there does not appear to be an appreciable difference in the spread of points in Figure 14.13 and the spread of points in Figure 14.12. As stated in Chapter 7, the burn length at the LLL changes more with smaller steps in engine load, for all the unadditized fuels with a relatively clean combustion chamber. This suggests that the effect of the CCD layer on burn length at the LLL differs from the effects due to changing fuel composition, discussed previously. While having a fully-conditioned CCD layer in the combustion chamber shifts the LLLs

to lower magnitudes, the burn durations at the new instability limits remains relatively similar. To reiterate, differences in the chemical composition of a refinery stream fuel leads to dissimilar burn lengths at the LLL with small changes of engine load. A “dirty” combustion chamber can run at loads as much as 0.5 bar lower than its clean counterpart, but have a similar combustion event in terms of CA10-CA90 burn duration.

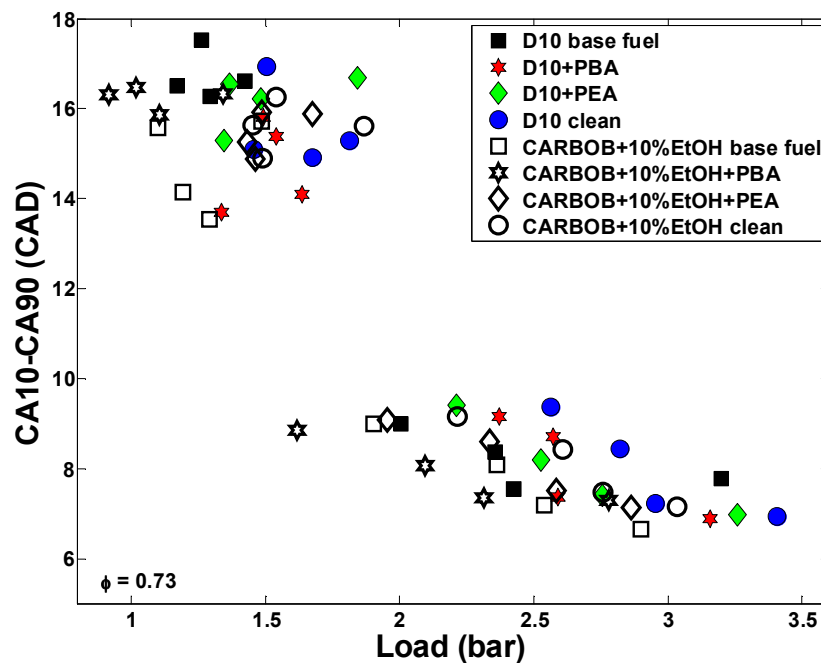


Figure 14.13 - CA10-90 burn duration at the limits against engine load (BMEP) for the both the D10 and CARBOB+10%EtOH blends

One other trend to observe regarding the LLLs is the combustion efficiency of the fuels over the sweep of speed during the operability limits test, shown on both sides of Figure 14.14. On the CARBOB side of the plot (the right side) as speed increases and reaches 2000 and 2400 RPM at the LLL, the combustion efficiencies for the conditioned chamber, caused when using PBA and PEA additized fuels, equal or surpass those of

the “clean” limits and a fully-conditioned chamber from CARBOB+10%EtOH base fuel. A similar phenomenon is present with the D10 fuel, on the left side of Figure 14.14, for the same two additized blends. The combustion efficiency for the D10+PBA exceeds that of the base D10 and “clean” D10 tests at 2000 RPM, and both D10+PBA and D10+PEA equal or surpass the efficiency of the “clean” D10 at 2400 RPM. However, in the case of D10+PBA and D10+PEA there is a lower increase in combustion efficiency from the lowest to highest speed at the LLL than was shown for the CARBOB blends dosed with the same additive packages (a difference of roughly 1% increase versus 1.5%).

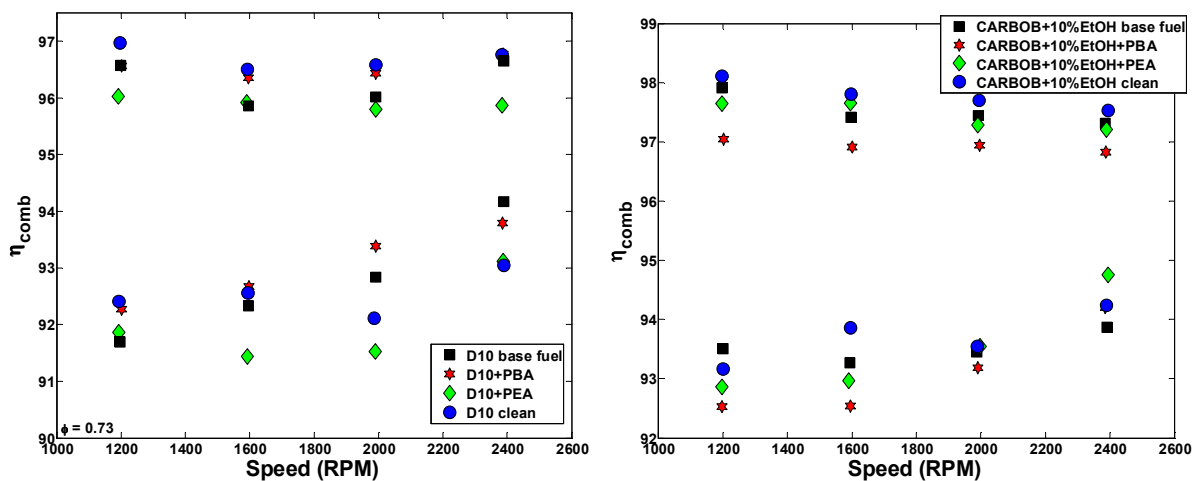


Figure 14.14 - Combustion efficiency of the D10 and CARBOB+10%EtOH blends for the operating limits sweep against speed; D10 blends are pictured on the left, CARBOB blends are on the right

Figure 14.8 and Figure 14.9, show that the relative shift of the HCCI operating maps is related to how much each CCD layer advances the phasing of the baseline

point, however this sort of clear distinction with combustion efficiency through the speed sweep is not apparent in Figure 14.14. A similar observation was made about the combustion efficiencies of the intake air and coolant temperature sweeps in previous sections. There are potential secondary effects from each CCD layer that impact combustion efficiency (outgassing or catalytic reactions on the surface), and these differences are most noticeable at the LLL, where there is more unstable combustion and the possibility for these effects to have a larger influence on the combustion event. However, in light of the relatively small changes in combustion efficiency, (at most a spread of 2% at any given speed) these effects are a minor influence on the overall HCCI combustion process.

CHAPTER 15

Conclusions and Contributions to Internal Combustion Engine Research

15.1 Introduction

This chapter is a summary of the major discoveries of the work presented in previous sections of this dissertation. It will also highlight the contributions to combustion science and automotive engineering made in each phase of this work, as well as discuss possible areas for future research among the chief topics of this project.

15.2 Scientific Contributions

There are a number of original scientific contributions that stem from the systematic experimental investigations pursued in this research program. The overarching goal was to characterize the interplay between gasoline fuel properties, HCCI combustion and deposit formation, while also taking into account additive packages. The experimental program was designed to enable insight into the combustion effects first, followed by the study of deposit formation, an exploration of the impact of deposits on combustion and finally the detailed characterization of physical and chemical properties of CCD. In the end, each phase of work produced unique

scientific contributions. Most importantly, it is possible to establish links between different stages of research, and correlate fuel properties with certain aspects of HCCI combustion behavior and/or deposit formation.

The relevance of the research effort was established through the selection of the fuel matrix, as the fuels and additive packages used are similar to what consumers in the United States use in their cars. Previous studies have tackled fundamental, chemical kinetics problems by using single component fuels and surrogates, but ultimately a fuel such as iso-octane or toluene will not be available for use in any HCCI technology developed for the mass market. Thus, to assess the manner in which the variability of commercial gasoline impacts combustion in an HCCI engine, it was necessary to undertake the efforts described in this document. Moreover, it was discovered that the variation in the properties of refinery stream gasoline has a tangible effect on specific fuel consumption and the limits of operability, which in turn has a profound impact on estimates of vehicle level fuel economy. The research also offered insight into which components of refinery streams, chiefly aromatics and ethanol content, have the most significant influence on the HCCI engine system, operating under realistic conditions. The major contributions can be summarized as follows:

15.2.1 Fuels and HCCI Combustion

The first major discovery was that the chemical composition of the refinery stream fuels has a significant impact on the rate of intake air temperature compensation required to keep combustion phasing constant over a sweep of fuelling rates. In particular, this rate increases for fuels of increasing olefinic content and decreases with

fuels that contain more aromatics. This has important implications for the control of HCCI engines, as the dominant chemical components of a refinery stream fuel will determine how much charge preparation is needed, at different points in the operating map, to ensure stable and consistent combustion. The overall intake temperature level required to obtain optimum HCCI combustion phasing varies by as much as 45 degrees Kelvin, depending on fuel composition. The detailed, quantitative characterization of HCCI combustion behavior provides direct guidance for future work aiming to develop robust HCCI strategies.

The chemical constituents of the fuel also influence the fuel consumption of the HCCI engine beyond the direct impact of the fuel's lower heating value. Because fuels of different compositions require different charge temperatures to operate in a similar manner in an HCCI engine, the impact of heat transfer on thermodynamic processes leads to tangible differences in cycle efficiency, and consequently, specific fuel consumption. In particular, denser fuels that can run at lower charge temperatures will be ideal. Interestingly, the combustion efficiency is consistent over the entire range of fuels.

The benefits to fuel economy from the HCCI mode, over a comparable SI engine, depend on the ability to run in an HCCI combustion regime over a large range of conditions. The findings in this work quantify the impact of fuel composition on the overall size of the HCCI operating map. The operability range was investigated both in terms of achievable load range and variations of the combustion features across the load range. The fuels with high aromatic content (~37%) demonstrate an impressive increase in operability range. This was due, at least in part, to the auto-ignition

resistance of aromatic molecules allowing for higher load limits, as well as robust operation over a wider range of engine loads.

Finally, insights were captured in a new correlation which accounts for major chemical components in commercially available gasoline, such as the percent of aromatic and olefin compounds by volume. The current research standard used to quantify the behavior of a fuel in an HCCI engine, the Octane Index, was originally developed using fuel surrogates, and is formulated using only the RON and MON of the fuel. However, this shows that the original OI is not able to adequately predict the auto-ignition behavior in an HCCI engine. Therefore, a new correlation which better reflects how a refinery stream fuel will operate was developed.

15.2.2 Fuels and Deposit Formation

The impact of a refinery stream fuel's chemical composition on the rate of deposit growth in the HCCI engine was explored through systematic, chamber conditioning tests. The equilibrium CCD thickness was shown to be on the order of 250 μm for a highly aromatic fuel, which is three to five times more than the CCD of a low aromatic fuel, with high saturates. The impacts of full conditioning, i.e. building the equilibrium CCD thickness in the chamber, lead to a dramatic acceleration of the HCCI burn rates, namely a 12 degree advancement of CA50 from a "clean" to a fully-conditioned chamber, in the worst case. The entire HCCI operating map is shifted down; this shift is directly tied to the overall thickness of deposits in the combustion chamber. Therefore, engine controls engineers must be prepared to handle the variability of fuels and additives, in order to deal with variations over the life of the vehicle.

The ability of the additive package in a given fuel to alter the development of in-cylinder deposits was studied using conditioning tests. These experiments lead to surprising discoveries. For example, a PBA additive package actually increases the deposit growth versus when the same fuel with no additive is used. In contrast, the PEA additive reduces the equilibrium thickness and exposes bare metal in the center of the piston bowl. This equilibrium was reached much faster than in other cases. The first ever investigation of the physical and chemical properties of HCCI deposits revealed that the CCD's morphological and compositional structure depends more on the additive package than the fuel composition run in the engine.

The chemical composition of various deposit samples, extracted from a fully-conditioned layer at the equilibrium, was found to be dominated by simple hydrocarbon molecules and elemental carbon. The samples have similar chemical components irrespective of fuel constituents and additives, which demonstrates that the molecular composition of the surface is relatively insensitive to the fuel or additive package used in the engine. For engine developers, mitigation of deposit growth will hinge on choosing fuels and additives that do not contain excessive amounts of deposit precursors, however they will not have to excessively concern themselves with the structure of resulting deposits.

In summary, the challenges presented by variability in refinery stream fuel must factor into the design of HCCI engines and development of control strategies. The original contributions of the work presented here, provide a comprehensive set of insights about and guidance for planning and executing future HCCI engine development. Significant robustness or adaptability need to be built into practical HCCI

engine system design and control, in order to develop a viable product for the diverse U.S. and global marketplace.

15.3 Conclusions

Major findings and conclusions are presented in order of their appearance in the dissertation document. A list of the primary conclusions of the fuels and combustion work discussed Chapters 6-9 is presented first, followed by the deposits studies of Chapters 11-14.

15.3.1 Summary of Refinery Stream Fuels and Combustion Work

The intake air temperature required to maintain constant combustion phasing at the reference condition, across the 10% ethanol fuel matrix, varies between 53°C and 103°C. The slope of the intake temperature compensation, plotted as a function of fuelling rate, changes appreciably with alterations in fuel properties. A reduced slope for some fuels indicates that less change is required when preparing the intake charge through a sweep of fuelling rates, and in a practical application this could potentially allow for easier control. Fuel composition introduces unique ignition characteristics, and variation in RON and MON alone cannot explain the differences observed. A change in S at a given RON is accompanied by an increase of aromatic or olefinic content, but the behavior over a load sweep is altered by the compounds used. Adding more aromatics to increase S results in less temperature compensation being required to maintain constant phasing (less sensitivity to load). The opposite effect was observed for

increasing S by increasing the content of olefins. Every fuel displays different, specific fuel consumption characteristics that are not due solely to differences in LHV. In general, when considering ISFC on a volumetric basis, the denser aromatic fuels have better indicated specific fuel consumption. Combustion efficiency and burn duration are almost constant across the matrix of fuels tested, as long as combustion phasing does not change. Therefore, the spread in specific indicated fuel consumption, beyond what is an expected result due to LHV variations, is attributed to thermodynamic effects that impact the fuels' indicated thermal efficiency. Large variations of intake air temperature in the HCCI engine, with the re-induction of residual, lead to differences in heat transfer and gas exchange, which in turn affect IMEP. Physical properties of the fuels can influence the in-cylinder thermodynamic state as well. When combustion phasing and injected fuel energy are matched for a variety of refinery stream fuels, it is possible to achieve comparable combustion events i.e. similar burn durations. This is likely the result of rapidly progressing combustion, with a CA10-CA90 interval of only 9 CAD at the reference condition for each fuel. The relative impact of changes due to kinetics is thus diminished. This is fortuitous for HCCI engine control schemes, as attention can be focused on thermal effects that dictate combustion phasing. However, different levels of intake air temperature and variation over a range of loads will be required in case of drastic changes in fuel composition.

The variation in properties and composition of gasoline fuels, blended from different refinery streams, is sufficient to induce dissimilarity in the LLLs and HLLs between fuels. Fuels with high aromatic content (>35%) have larger operating ranges than fuels with high olefin content. The sensitivity of a fuel plays a role in range

determination as well, as in most cases fuels of increased sensitivity operate over a wider range of loads, across the speed sweep. Highly aromatic fuels exhibit greater change in the location of CA50 combustion phasing going, from the LLL to the HLL throughout the speed range, than highly olefinic fuels. The behavior of the HCCI combustion event at the low and high limits has some distinct characteristics for each refinery stream fuel in the test matrix. The differences in composition impact the overall engine loads that are achievable at the imposed constraints of this experimentation, but exert different effects on the combustion process depending on which operability limit is considered. At the LLL, the fuels are phased nearly the same (similar CA50), though burn durations (CA10-CA90) vary from one fuel to another. At the HLL, combustion phasing changes at each speed among the test fuels, though the burn durations are similar.

The refinery stream blends tested with a higher content of ethanol (20% by volume) have a much lower range of reference intake air temperatures (52°C to 60°C), than those with a lower (10% by volume) ethanol content (53°C to 87°C). Fuels of higher ethanol content also have compensated load curves that lay closer to one another as opposed to 10% ethanol fuels. In essence, the fuels containing increased levels of ethanol operated over a narrower range of intake air temperature compensation for the sweep of fuelling rate. A change in S at a given RON is accompanied by an increase of aromatic or olefin content, but the behavior over a load sweep is quite different depending on the fuel composition used. Adding more aromatics to increase S necessitates a lower rate of intake air temperature compensation to maintain constant phasing (less sensitivity to load) when the fuel was

10% ethanol by volume. The opposite effect was observed for increasing S by increasing the olefin content with 10% ethanol content. With the 20% ethanol fuels, there was no difference between adding more olefins or adding more aromatics; as long as S increases, the rate of intake air temperature compensation required decreases over the sweep of load. Regardless of ethanol content or other variations in the chemical composition of the test fuels, when combustion phasing and injected energy into the cylinder are matched for each fuel at the baseline, combustion efficiency and burn duration were similar. This implies that fuels of different composition can undergo a remarkably similar HCCI combustion processes, if the combustion phasing and available fuel energy remain constant. Because of the reduced heating values for fuels containing the extra ethanol, the 20% ethanol blends have higher specific fuel consumption values than those of the 10% ethanol blends, which is a chief disadvantage of ethanol addition. The additional ethanol blended into the refinery stream fuels changed the location of the operational limits for HCCI combustion. The HLL benefits from the ethanol addition at nearly every speed point, for all four 20% ethanol fuels that were tested. Behavior at the LLL varies depending on the changes in composition caused by going from a 10% blend to a 20% blend. Increased ethanol content, in general, increases the overall size of the HCCI operating map. The amount that combustion phasing changes over a range of engine speed, from the LLL to HLL is “smoothed” by the inclusion of additional ethanol. In other words, the ΔCA_{50} going from the LLL to HLL stayed more constant (flatter slope) across the speed range for the higher ethanol fuel blends. When a sweep of intake air temperature is run, the spread of CA₅₀ combustion phasing is reduced when using fuels of higher ethanol content.

One common theme throughout all the experiments, presented in this study, is that the inclusion of additional ethanol in refinery stream blends serves to negate some of the other chemical variation (e.g. aromatics and olefins) that exist among the blends, due to the single-stage ignition characteristics of the ethanol counterbalancing other auto-ignition kinetics. Conversely, reducing ethanol levels in refinery stream fuels enhances these same variations and their impact on HCCI combustion.

An experimental study of intake air temperature sweeps was conducted for seventeen fuels with varying chemical properties, including 0%, 10%, 20% and 100% ethanol fuels, as well as blends that feature high aromatics or high olefins. Fifteen fuels from the matrix were blended using refinery stream gasoline with varying chemical composition, in terms of the volumetric percentage of aromatics, olefins and saturates. One of the fuels, RD3-87, was a non-oxygenated 87 ON fuel, and the last test fuel was 100% ethanol. A comparison study was done using the original Kalghatgi OI model, the Shibata-Urushihara model and a newly modified OI model. The measured CA50, RON, MON and S of the fuels are regressed to find K for each intake temperature point. The dependence of CA50 on OI was studied for each of these models, with the fuels data collected from the UM engine setup. This examination showed that the behaviors of pump grade gasoline caused by high aromatic and high ethanol content is not captured successfully using the original OI correlation. A modified CA50 and OI model was developed that emphasizes the importance of aromatic and ethanol content in refinery stream fuels, and statistical analysis was repeated with the new correlation. Using this correlation, the relationship between the OI of the fuels and the combustion phasing becomes much stronger for the refinery stream fuels, particularly at lower intake air

temperature conditions. Also, the outlier fuels, with high aromatic and high ethanol content, have better agreement with the new OI model than with the original OI correlation. One further comparison was conducted by using the UM fuels engine data in the Shibata-Urushihara model. The SU model is similar to the modified OI model, and uses compositional terms strengthen the correlation. The SU model worked well at high intake temperature conditions, but the correlation deteriorated at low intake temperatures. Lastly, the relation between the new OI rating and net heat release rates was considered. The modified OI was found to correlate well with the maximum net heat release rate. As OI increases, the heat release rate peak becomes more retarded. Given the definitions of RON and OI, this is intuitive, but the advantage of using the modified OI model is the ability to better distinguish between refinery stream fuels that have similar RON and S values. This may prove to be a useful tool in future controls strategies for HCCI engines.

15.3.2 Summary of Fuels and Deposits Work

The chemical composition of fuel has a significant impact on the presence of deposits in the HCCI engine. Specifically, the D10 fuel has a sizeable volumetric percentage of aromatic compounds (~37%), and as in the case of SI combustion, this seems to be a contributing factor to a higher thickness measurement of deposits. While the fuel with a higher aromatic content has a thicker CCD layer overall, the CCD layer produced from CARBOB+10%EtOH on the piston is thicker in some regions than the layer produced by the D10. The combination of differing physical properties, direct injection and piston geometry all play a role in how the deposition is distributed in-

cylinder. The combustion phasing change that occurs when D10, the higher aromatic fuel, is run is larger than what is shown for the CARBOB+10%EtOH blend, going from “clean” to a fully-conditioned combustion chamber state. The time it took for the D10 to reach an equilibrium level of deposits was more than twice as long as for the CARBOB+10%EtOH, however the CARBOB blend builds an initial layer at a faster rate than D10. Both fuels show a somewhat unexpected trend with EIHC. It was anticipated that as the CCD accumulated and combustion phasing advanced EIHC would be reduced as the result of higher combustion efficiencies and higher in-cylinder temperatures. However, after an initial drop, there is a slight increase in EIHC, suggesting that once enough deposits accumulate, a small amount of the directly injected fuel impinging on the layer may be trapped in the layer’s pores and later outgassed, leading to increased EIHC levels. The growth of deposits on the cylinder head heat flux probes is not as gradual a process for D10 as it is for the CARBOB blend. D10 has more overall deposit growth on the coaxial heat flux probes. Unlike the change in surface temperature and heat flux, the advance of D10 NHRR peaks is steady throughout the conditioning sweep. Conversely, the evolution of CARBOB+10%EtOH NHRR is less gradual than what is shown on the probes. This suggests that composition and the properties of the fuels play a role in the rate of deposit growth in different regions of the cylinder (piston or head). Deposits on the piston influence the overall combustion event (CA50 and NHRRs) more significantly than cylinder head deposits. For the D10 fuel, when there is an apparent thinning of deposits on the head, NHRR still advances. The opposite was shown for the CARBOB

blend, as deposits appeared to grow steadily on the head while the peak of NHRR is retarding.

Just as refinery stream fuel composition impacts deposit growth rates and the deposit accumulation process, so does the additive package mixed into the fuel. The PBA additive package is less effective in the prevention of deposit accumulation compared with the PEA additive. When dosed in the CARBOB+10%EtOH fuel, the PBA additive results in more in-cylinder deposition than the unadditized fuel. As shown in Chapter 11, there is a slight increase in EIHC that occurs while the CCD layer heads towards the asymptotic equilibrium condition. In further examination, the argument for the adsorption and outgassing of fuel from the CCD layer in the bowl is bolstered by the CARBOB+10%EtOH+PEA results, as the absence of deposit coverage in the bowl does not display an increase in EIHC, as engine run time elapses. Each additive has a different impact on the progression of deposit growth on the cylinder head probes, as determined from an inspection of the changes in heat flux with engine operation time.

SEM imaging confirms that the morphology of CCD flakes is similar when comparing samples that are derived from the same additive package (or lack), but exhibits noticeable variation between deposit samples from different fuel additives. This suggests that the morphology at the macroscopic level is not strongly dependent on the composition of the pump gasoline blends tested. This phenomenon is due to the insensitivity of fundamental steps in the deposit formation process to the fuel used in the engine. The chemical constituents of refinery stream fuels has a greater impact on the overall rates of deposit growth and the eventual equilibrium thickness that is reached in an HCCI engine. TEM analysis of deposit samples demonstrates that HCCI engine

deposits are predominantly amorphous carbon. There are a few notable exceptions in the case of the thickest accumulations which potentially have the highest surface layer temperatures. In these cases, some soot-like structures are shown at the same length scales as what has been reported for diesel exhaust, a common place to find soot particles. Soot particles are undesirable if they matriculate into the exhaust, as this introduces an emissions challenge that is often regarded as already solved by the HCCI mode of combustion. Two forms of elemental quantification were utilized to study the deposit samples, XEDS for a bulk scan and XPS for a surface scan. The XEDS spectra, which provided an approximate comparison of composition between samples, indicates that there are no discernible trends with the composition of refinery stream fuels or additive packages. This is likely due to the CCD formation process which operates independent of the fuel run in the engine. It also indicates that while the additive package can have an effect on the morphological features of the layer, it does not significantly impact the layer's bulk composition. XPS analysis revealed that the additive package present in the fuel changed the distribution of molecules surrounding carbon atoms in the CCD layer's surface. However, the overwhelming majority of the deposit samples analyzed were composed of carbides and elemental carbon. The XPS surface composition results, which consist of similar types of molecules for the deposit samples, confirm this formation mechanism proposition. Small-angle X-ray scattering studies showed that there is more variation of porosity and surface area to volume ratio between deposits from different additive packages than deposits from different base fuels. It is encouraging that this is in agreement with the morphological results provided by the SEM analysis, as SAXS is ultimately quantifying a physical property of the CCD

layer that should appear in the microscopic imaging. Furthermore, the porosity of the additive-based deposits are slightly lower than the deposit samples from unadditized fuel, likely due to partially decomposed additive molecules filling the void volume, during deposit accumulation. Thermal diffusivity characterization confirms that the principal steps in the deposit formation process occur independently from the refinery stream fuel or additive run in the engine. The thermal diffusivity is largely a function only of thickness, and not sensitive to the fuel or additive used to create the deposits.

HCCI operability is impacted substantially when the combustion chamber is fully-conditioned, i.e. has reached the equilibrium state of deposit growth. Intake air and coolant temperature sweeps reveal that the resulting phasing of the HCCI combustion event is strongly tied to the overall amount of CCD growth and CA50 advancement at the baseline operating point. The combustion phasing can be retarded using less alteration of the coolant temperature than to the intake air temperature, in the case of all the layers, which agrees with previous University of Michigan tests conducted using the test fuel RD3-87. While the predominant impact of the CCD layer is related to its thickness, there are indications that at certain operating conditions, structural variations between layers may assert themselves as secondary effects on the combustion event. While the differences in CA50 among the conditioned chambers is consistent throughout the range of temperature, there is a divergence of CA10-CA90 and combustion efficiency at low intake air temperatures and low coolant temperatures, most noticeably for the PEA conditioned chambers. Based on the lower porosities of these layers, found in Chapter 13, this divergence could be due to the higher thermal conductivity of PEA derived layers, leading to more heat loss to the walls. This effect

becomes relatively more important for operation near the instability limit (lower charge temperatures). HCCI operating maps are influenced by a “dirty” combustion cylinder, predominantly by shifting the maps to lower engine loads. This vertical shift is correlated to the change in the baseline CA50 in all test cases, and that CA50 phasing change arises as a consequence of deposit accumulation. More deposit growth and higher charge temperatures at the baseline condition result in more shift of the operating map. The area of the operating range also changes depending on what type of layer is present in-cylinder. While the ranges for the PEA based CCD layers are smaller than the “clean” operating range, there is no obvious trend with the other areas. While the impact of layers with different structures is felt most actively at the instability limit, where wall effects play a larger role (e.g. late burn, oxidation events), they are still secondary to the influence of thermal properties. Some secondary effects of the CCD layer are apparent from the combustion efficiencies at the LLL over the speed sweep, because these are not tied as strongly to the layer thickness as the operating map shifts.

15.4 Suggestions for Continuing Efforts

One area in this research effort where there is opportunity for further work, is in establishing a clearer connection between the ex-situ deposit studies and the in-situ engine results. More rigorously defined properties of the CCD layer, such as thermal conductivity, would be instrumental in strengthening some of the explanations provided in this work which are, at this juncture, conjecture and hypotheses. An experimental modulated intensity laboratory furnace was created by a former University of Michigan

PhD student, Dr. Mark Hoffman, which has the capability to assess the thermal diffusivity and thermal conductivity of heat flux probes coated with deposits. More non-destructive methods for the study of deposits would expand the understanding of the structure of deposit layers over a larger area of the combustion chamber. Atomic force microscopy (AFM) is an attractive option for the future characterization of physical properties of the CCD layer, although an instrument that has a housing or fixture of the proper dimensions to mount a piston or our coaxial heat flux probes would need to be located. Another potential method for measuring layer thickness more accurately than our Dualscope would be the use of a digital microscope, which can use its focal plane length to determine how close a specimen is to the lens against a reference distance, providing useful thickness measurements. This would require having some manner of moveable cart apparatus, as the microscope can only be put into place when the cylinder head is removed and the deposit layer exposed.

REFERENCES

1. Hoffman, M., *Characterization of Combustion Chamber Deposits Formed During Homogeneous Charge Compression Ignition and the Impact of a Thermal Barrier Coating on Deposit Accumulation and HCCI Operability*, in *Mechanical Engineering2012*, University of Michigan: Ann Arbor. p. 165.
2. *Annual Energy Outlook 2012 with Projections to 2035*. Department of Energy/Energy Information Administration, 2012.
3. Najt, P.M., F., D.E., *Compression-Ignited Homogeneous Charge Combustion*. SAE Paper 830264, 1983.
4. Epping, K., Aceves, S., Bechtold, R., Dec, J., *The Potential of HCCI Combustion for High Efficiency and Low Emissions*. SAE Paper 2002-01-1923, 2002.
5. Guralp, O., *The Effect of Combustion Chamber Deposits on Heat Transfer and Combustion in a Homogeneous Charge Compression Ignition Engine*, in *Mechanical Engineering2008*, University of Michigan: Ann Arbor. p. 273.
6. Sjoberg, M., Dec, J.E., *An Investigation of the Relationship Between Measured Intake Temperature, BDC Temperature, and Combustion Phasing for Premixed and DI HCCI Engines*. SAE Paper 2004-01-1900, 2004.
7. Guralp, O., Filipi, Z., Kuo, T., Najt, P., Rask, R., *Characterizing the Effects of Combustion Chamber Deposits on a Gasoline HCCI Engine*. SAE Paper 2006-01-3277, 2006.
8. Leppard, W.R., *The Chemical Origin of Fuel Octane Sensitivity*. SAE Paper 902137, 1990.
9. Wilk, R.D., Cernansky, N.P., Cohen, R.S., *The Oxidation of Propane at Low and Transition Temperatures*. *Combustion Science Technology*, 1986. **49**: p. 41-78.
10. Dec, J.E., Sjoberg, M., *Isolation the Effects of Fuel Chemistry on Combustion Phasing in an HCCI Engine and the Potential of Fuel Stratifications for Ignition Control*. SAE Paper 2004-01-0557, 2004.
11. Spilners I.J. and Hedenburg, J.F., *Effect of Fuel and Lubricant Composition on Engine Deposit Formation*. *Chemistry of Engine Combustion Deposits*, ed. L. Ebert1985, New York, NY: Plenum Press. 289-302.
12. Ebert, L.B., *Reductive Chemistry of Aromatic Hydrocarbon Molecules*. *Chemistry of Engine Combustion Deposits*, ed. L.B. Ebert1985, New York, NY: Plenum Press. 303-376.
13. Kalghati, G., *Deposits in Gasoline Engines - A Literature Review*. SAE Paper 902105, 1990.
14. Cheng, S.S., *A Micrographic Study of Deposit Formation Processes in a Combustion Chamber*. SAE Paper 962008, 1996.

15. Cheng, S.S., *The Impacts of Engine Operations Conditions and Fuel Compositions on the Formation of Combustion Chamber Deposits*. SAE Paper 2000-01-2025, 2000.
16. Bittner J.D., F., S.M., Howard, J.B. and Longwell, J.P., *Deposit Formation by Diffusion of Flame Intermediates to a Cold Surface*. Chemistry of Engine Combustion Deposits, ed. L.B. Ebert1985, New York, NY: Plenum Press. 227-243.
17. Price, R.J., Spink, C. D., Morley, C., *Prediction of Combustion Chamber Deposit Growth in SI Engines*. SAE Paper 972835, 1997.
18. Newby, W., *Emphasises the effects of boiling point on deposit formation*. SAE Transactions, 1958. **66**: p. 294.
19. Price, R.J., Wilkinson, J. P. T., Jones, D. A. J., Morley, C., *A Laboratory Simulation and Mechanism for the Fuel Dependence of SI Combustion Chamber Deposit Formation*. SAE Paper 952445, 1995.
20. Shore, L.B., Ockert, K.F., *Radiotracer Study Points Way to Make Clean-Burning Gasoline*. SAE Journal, 1957. **65**: p. 18.
21. Shore, L.B., Ockert, K.F., *Combustion-Chamber Deposits--a Radiotracer study*. SAE Transactions, 1958. **66**: p. 285.
22. Kelemen, S.R., Siskin, M., Avery, N.L., Rose, K.D., *Gasoline Type and Engine Effects on Equilibrium Combustion Chamber Deposits (CCD)*. SAE Paper 2001-01-3583, 2001.
23. Myers, P.S., Uyehara, O.A., DeYoung, R., *Fuel composition and vaporization effects on combustion chamber deposits*, in Report No. DOE/CS/50020--11981, U.S. Department of Energy.
24. Lauer, J.L., Frier, P.J., *Some Properties of Carbonaceous Deposits Accumulated in Internal Combustion Engines*. Combustion and Flame, 1960. **4**: p. 107.
25. Uehara T., T.Y., Hoshi H., Shiratani K. and Okada M., *Study on Combustion Chamber Deposit Formation Mechanism - Influence of Fuel Components and Gasoline Detergents*. SAE Paper 971722, 1997.
26. Ebert, L.B., *Chemistry of Engine Combustion Deposits: Literature Review*. Chemistry of Engine Combustion Deposits, ed. L.B. Ebert1985, New York, NY: Plenum Press. 3-18.
27. Edwards, J.C., Choate, P.J., *Average Molecular Structure of Gasoline Engine Combustion Chamber Deposits Obtained by Solid State ¹³C, ³¹P and ¹H Nuclear Magnetic Reasonance Spectroscopy*. SAE Paper 932811, 1993.
28. Kelemen, S.R., Siskin, M., Homan H.S., Pugnire R.J., Solum, M.S., *Fuel, lubricant and additive effects on combustion chamber deposits*. SAE Paper 982715, 1998.
29. Siegl, W.O., Zinbo, M., *On the Chemical Composition and Origin of Engine Deposits*. Chemistry of Engine Combustion Deposits, ed. L.B. Ebert1985, New York, NY: Plenum Press. 53-70.
30. Moore, S.M., Sabourin, E.T., Yeh, S.W., *The Effects of Engine Operating Temperature on CCD Surface Chemistry and Morphology*, in *Technische Akademie Esslingen 1st International Colloquium*1997: Technische Akademie Esslingen.

31. Cheng, S.S., Kim, C., *Effect of Engine Operations Parameters on Engine Combustion Chamber Deposits*. SAE Paper 902108, 1990.
32. DeGregoria, A., *Modelling the Effect of Engine Deposit of Octane Requirements*. Chemistry of Engine Combustion Deposits, ed. L.B. Ebert 1985, New York, NY: Plenum Press. 213-226.
33. Daly, D.T., Fog, D.A., Bannon, S.A., Harold, S.M., *Mechanism of Combustion Chamber Deposit Formation*. SAE Paper 941889, 1994.
34. Takei, Y., Uehara, T., Hoshi, H., Okada, M., *Effects of gasoline and gasoline detergents on combustion chamber deposit formation*. SAE Paper 941893 (1994), 1994.
35. Tupa, R.C., Dorer, C.J., Miller, C.O., *Gasoline and diesel fuel additives for performance/distribution/quality - II*. SAE Paper 861179, 1986.
36. Sturgis, B.M. *Additives in petroleum fuels - a decade of progress*. in ACS symposium on a Decade of Progress in Petroleum Technology. 1961.
37. Zerda, T.W., Yuan, X., Moore, S.M., *Effects of fuel additives on the microstructure of combustion engine deposits*. Carbon 2001, 2000. **39**: p. 1589-1597.
38. Adams, K.M., Baker, R.E., *Effects of combustion chamber deposits location and composition*, in *Chemistry of Engine Combustion Chamber Deposits*, L.B. Ebert, Editor 1985, Plenum Press. p. 19-37.
39. Keller, C.T., Corkwell, K.C., *Honda Generators Used to Evaluate Fuels and Additive Effects on Combustion Chamber Deposits*. SAE Paper 940347, 1994.
40. Keller, H., Shimkoski, D.A. in *Proceedings of the CRC Workshop on Combustion Chamber Deposits*. 1993. Orlando.
41. Megnin, M.K., Choate, P.J., *Combustion Chamber Deposit Measurement Technique*. SAE Paper 940346, 1994.
42. Nagao, M., Kaneko, T., Omata, T., Iwamoto, S., Ohmori, H., Matsuno, S., *Mechanism of combustion chamber deposit interference and effects of gasoline additives on CCD formation*. SAE Paper 950741, 1995.
43. Cornetti, G., Liguori, V., Amendola, L., *Power loss due to combustion chamber deposits*. Journal of Automotive Engineering, 1971: p. 8-14.
44. Duckworth, J.B., *Effects of Combustion Chamber Deposits on Octane Requirement and Engine Power Output*. SAE Quarterly Transactions, 1951. **5**: p. 577-583.
45. Dumont, L.F., *Possible mechanisms by which combustion chamber deposits accumulate and influence knock*. SAE Quarterly Transactions, 1951. **5**: p. 565-576.
46. Benson, J.D., *Some factors which affect octane requirement increase*. SAE Paper 750932, 1975.
47. Fuentes-Afflick, P. in *Proceedings of the CRC Workshop on Combustion Chamber Deposits*. 1993. Orlando.
48. Niles, H.T., McConnell, R.J., Roberts, M.A., Saillant, R., *Establishment of ORI characteristics as a function of selected fuels and engine families*. SAE Paper 750451, 1975.
49. Nishiwaki, K., Muhammad, H., *The Determination of Thermal Properties of Engine Combustion Chamber Deposits*. SAE Paper 2000-01-1215, 2000.

50. Peyla, R.J., *Motor Gasoline and Deposit Control Additives - A Challenge for the 90s*, Paper No. FL-91-118, in *NPRA National Fuels and Lubricants Meeting 1991*: Houston.
51. Saillant, R.B., Pedrys, F.J., Kidder, H.E., *More data on ORI variables*. SAE Paper 760196, 1976.
52. Kalghati, G., *Combustion chamber deposits in spark-ignition engines: A literature review*. SAE Paper 952443 (1995), 1995.
53. Bussovansky, S., Heywood, J.B., Keck, J.C., *Predicting the effects of air and coolant temperature, deposits, spark timing and speed on knock in spark ignition engines*. SAE Paper 922324, 1992.
54. Bitting, W.H., Firmstone, G.P., Keller, C.T., *Effects of combustion chamber deposits on tailpipe emissions*. SAE Paper 940345, 1994.
55. Gagliardi, J.C., *The effects of fuel anti-knock compounds and deposits on exhaust emissions*. SAE Paper 670128, 1967.
56. Harpster, M.O., Matas, S.E., Fry, J.H., Litzinger, T.A., *An experimental study of fuel composition and combustion chamber deposit effects on emissions from a spark ignition engine*. SAE Paper 950740, 1995.
57. Huls, T.A., Nickol, H.A., *Influence of engine variables on exhaust oxides of nitrogen concentrations from a multicylinder engine*. SAE Paper 670482, 1967.
58. Studzinski, W.M., Liiva, P.M., Choate, P.J., Acker, W.P., Smooke, M., Brezinsky, K., Litzinger, T., Bower, S., *A Computational and Experimental Study of Combustion Chamber Deposit Effects on NOx Emissions*. SAE Paper 932815, 1993.
59. Leikkanen, H.E., Beckman, E.W., *The effect of leaded and unleaded gasolines on exhaust emissions as influenced by combustion chamber deposits*. SAE Paper 710843, 1971.
60. Pahnke, A.J., Conte, J.F., *Effect of combustion chamber deposits and driving conditions on vehicle exhaust emissions*. SAE Paper 690017, 1969.
61. Myers, J.P., Alkidas, A.C., *Effects of combustion-chamber surface temperature on the exhaust emissions of a single-cylinder spark-ignition engine*. SAE Paper 780642, 1978.
62. Russ, S.G., Kaiser, E.W., Siegl, W.O., Podsiadlik, D.H., Barrett, K.M., *Compression ratio and coolant temperature effects on HC emissions from a spark-ignition engine*. SAE Paper 950163, 1995.
63. Wentworth, J.T., *Effect of combustion chamber surface temperature on exhaust hydrocarbon concentration*. SAE Paper 710587, 1971.
64. Spink, C.D., Barraud, P.G., Morris, G.E.L., *A critical road test evaluation of two high-performance gasoline additive packages in a fleet of modern European and Japanese vehicles*. SAE Paper 912393, 1991.
65. Graiff, L.B., *Some new aspects of deposit effects on engine octane requirement increase and fuel economy*. SAE Paper 790938, 1979.
66. Kalghatgi, G.T., McDonald, C.R., Hopwood, A.B., *An experimental study of combustion chamber deposits and their effects in a spark-ignition engine*. SAE Paper 950680, 1995.

67. Nakamura, Y., Yonekawa, Y., Okamoto, N., *The effects of combustion chamber deposits on octane requirement increase and fuel economy*, in *Chemistry of Engine Combustion Deposits*, L.B. Ebert, Editor 1985, Plenum Press. p. 199-211.
68. Tsutsumi, Y., Nomura, K., Nakamura, N., *Effect of mirror-finished combustion chamber on heat loss*. SAE Paper 902141, 1990.
69. Yonekawa, Y., Kokubo, K., Nakamura, Y., Okamoto, N., *The study of combustion chamber deposits (part 5): The role of combustion chamber deposits in fuel economy*. J. Japan Petroleum Institute, 1982. **25**: p. 177-182.
70. Anderson, C.L., Wood, B.S., *Gasification of Porous Combustion Chamber Deposits in a Spark Ignition Engine*. Sae Paper 931032, 1993.
71. Guralp, O., Hoffman, M., Filipi, Z., Assanis, D., Kuo, T., Najt, P. and Rask, R., *Thermal Characterization of Combustion Chamber Deposits on the HCCI Engine Piston and Cylinder Head Using Instantaneous Temperature Measurements*. SAE Paper 2009-01-0668, 2009.
72. Chang, J., *Thermal Characterization and Heat Transfer Study of a Gasoline Homogeneous Charge Compression Ignition Engine Via Measurements of Instantaneous Wall Temperature and Heat Flux in the Combustion Chamber*, in *Mechanical Engineering2004*, University of Michigan: Ann Arbor.
73. Hopwood, A.B., Chynoweth, S., Kalghatgi, G.T., *A Technique to Measure Thermal Diffusivity and Thickness of Combustion Chamber Deposits In-Situ*. SAE Paper 982590, 1998.
74. Tree, D.R., Wiczynski, P.D., Yonushonis, T.M., *Experimental Results on the Effect of Piston Surface Roughness and Porosity on Diesel Engine Combustion*. SAE Paper 960036, 1996.
75. Tree, D.R., Oren, D.C., Yonushonis, T.M., *Experimental Measurements on the Effect of Insulated Pistons on Engine Performance and Heat Transfer*. SAE Paper 960317, 1996.
76. Angelos, J.P., Andreae, M.M., Green, W.H., Cheng, W.K., Kenney, T., Xu, Y., *Effects of Variations in Market Gasoline Properties on HCCI Load Limits*. SAE Paper 2007-01-1859, 2007.
77. Mingfa Yao, Z.Z., Haifeng Liu, *Progress and recent trends in homogeneous charge compression ignition (HCCI) engines*. *Progress in Energy and Combustion Science*, 2009. **35**: p. 398-437.
78. Farrell, J.T., Bunting, B.G., *Fuel Composition Effects at Constant RON and MON in an HCCI Engine Operated with Negative Valve Overlap*. SAE Paper 2006-01-3275, 2006.
79. L. Starck, B.L., L. Forti, N. Jeuland, *Impact of fuel characteristics on HCCI combustion: Performances and emissions*. *Fuel*, 2010. **89**: p. 3069-3077.
80. Aceves, S.M., Flowers, D., Martinez-Frias, J., Espinosa-Loza, F., Pitz, W.J., Dibble, R., *Fuel and Additive Characterization for HCCI Combustion*. SAE Paper 2003-01-1814, 2003.
81. Amann, M., Ryan, T.W., Kono, N., *HCCI Fuels Evaluations-Gasoline Boiling Range Fuels*. SAE paper 2005-01-3727, 2005.
82. Bunting, B.G., Crawford, R.W., Wolf, L.R., Xu, Y., *The Relationships of Diesel Fuel Properties, Chemistry, and HCCI Engine Performance as Determined by Principal Components Analysis*. SAE paper 2007-01-4059, 2007.

83. Bunting, B.G., Eaton, S.J., Crawford, R.W., *Performance Evaluation and Optimization of Diesel Fuel Properties and Chemistry in an HCCI Engine*. SAE Paper 2009-01-2645, 2009.
84. Shen, Y., King, E., Pfahl, U., Krile, R.T., Slone, E., Orban, J.E., Wright, K., *Fuel Chemistry Impacts on Gasoline HCCI Combustion with Negative Valve Overlap and Direct Injection*. SAE Paper 2007-01-4105, 2007.
85. Shibata, G., Oyama, K., Urushihara, T., Nakano, T., *The Effect of Fuel Properties on Low and High Temperature Heat Release and Resulting Performance of an HCCI Engine*. SAE paper 2004-01-0553, 2004.
86. Shibata, G., Oyama, K., Urushihara, T., Nakano, T., *Correlation of Low Temperature Heat Release With Fuel Composition and HCCI Engine Combustion*. SAE Paper 2005-01-0138, 2005.
87. Shibata, G., Urushihara, T., *Auto-Ignition Characteristics of Hydrocarbons and Development of HCCI Fuel Index*. SAE Paper 2007-01-0220, 2007.
88. Shibata, G., Urushihara, T., *Stabilizations of High Temperature Heat Release CA50 and Combustion Period against Engine Load with Dosage of Toluene in Fuel*. SAE Paper 2010-01-0575, 2010.
89. Xie, H., Wei, Z., He, B., Zhao, H., *Comparison of HCCI Combustion Respectively Fueled with Gasoline, Ethanol and Methanol through the Trapped Residual Gas Strategy*. SAE Paper 2006-01-0635, 2006.
90. Kalghatgi, G.T., Head, R.A., *The Available and Required Autoignition Quality of Gasoline-Like Fuels in HCCI Engines at High Temperatures*. SAE paper 2004-01-1969, 2004.
91. Vanhove, G., Petit, G. Minetti, R., *Experimental study of the kinetic interactions in the low-temperature autoignition of hydrocarbon binary mixtures and a surrogate fuel*. Combustion and Flame, 2006. **145**: p. 521-532.
92. Tanaka, S., Ayala, F., Keck, J., Heywood, J.B., *Two-stage ignition in HCCI combustion and HCCI control by fuels and additives*. Combustion and Flame, 2002. **132**: p. 219-239.
93. Mittal, G., Sung, C., *Homogeneous charge compression ignition of binary fuel blends*. Combustion and Flame, 2008. **155**: p. 431-439.
94. Yang, J., *Expanding the Operating Range of Homogeneous Charge Compression Ignition-Spark Ignition Dual-Mode Engines in the Homogeneous Charge Compression Ignition Mode*. International Journal of Engine Research, 2005. **6**(279).
95. Ortiz-Soto, E., Assanis, D., Babajimopoulos, A., *A comprehensive engine to drive-cycle modelling framework for the fuel economy assessment of advanced engine and combustion technologies*. International Journal of Engine Research, 2011. **12**.
96. Szybist, J., Nafziger, E., Weall, A. *Load Expansion of Stoichiometric HCCI Using Spark Assist and Hydraulic Valve Actuation*. in *Directions in Engine-Efficiency and Emissions Research Conference*. 2010. Detroit.
97. Yun, H., Wermuth, N., Najt, P., *Extending the High Load Operation Limits of a Naturally-Aspirated Gasoline HCCI Combustion Engine*. SAE Paper 2010-01-0847, 2010.

98. Hyvonen, J., Haraldsson, G., Johansson, B., *Supercharging HCCI to Extend the Operating Range in a Multi-Cylinder VCR-HCCI Engine*. SAE Paper 2003-01-3214, 2003.
99. Kuboyama, T., Moriyoshi, Y., Hatamura, K., Takanashi, H., Urata, Y., Yamada, T., *Extension of Operating Range of a Multi-Cylinder Gasoline HCCI Engine using the Blowdown Supercharging System*. SAE Paper 2011-01-0896, 2011.
100. Yun, H., Wermuth, N., Najt, P., *High Load HCCI Operation Using Different Valving Strategies in a Naturally-Aspirated Gasoline HCCI Engine*. SAE Paper 2011-01-0899, 2011.
101. Handford, D.I., Checkel, M.D., *Extending the Load Range of a Natural Gas HCCI Engine using Direct Injected Pilot Charge and External EGR*. SAE Paper 2009-01-1884, 2009.
102. Dec, J.E., Yang, Y., Dronniou, N., *Boosted HCCI - Controlling Pressure-Rise Rates for Performance Improvements using Partial Fuel Stratification with Conventional Gasoline*. SAE Paper 2011-01-0897, 2011.
103. Sjoberg, M., Dec, J.E., *Potential of Thermal Stratification and Combustion Retard for Reducing Pressure-Rise Rates in HCCI Engines, Based on Multi-Zone Modeling and Experiments*. SAE Paper 2005-01-0113, 2005.
104. Sjoberg, M., Dec, J.E., *Influence of EGR Quality and Unmixedness on the High-Load Limits of HCCI Engines*. SAE Paper 2009-01-0666, 2009.
105. Bower, S.L., Litzinger, T.A., Frottier, V., *The effects of fuel composition and engine deposits on emissions from a spark ignition engine*. SAE Paper 932707, 1993.
106. Chapman, J.L., Williamson, J., Preston, W.H., *Deposits in internal combustion engines*. *Deposition from Combustion Gases*, ed. J. A.R.1989, Bristol, UK: IOP Publishing Ltd. 113-127.
107. Kalghatgi, G., *Deposits in Gasoline Engines - A Literature Review*. SAE Paper 902105, 1990.
108. Uehara, T., Takei, Y., Hoshi, H., Shiratani, K., Okada, M., *Study on Combustion Chamber Deposit Formation Mechanism - Influence of Fuel Components and Gasoline Detergents*. SAE Paper 971722, 1997.
109. Nikanjam, M., Boom R., *The Effects of Fuels and Engines on Intake Valve and Combustion Chamber Deposits*. SAE Paper 962028, 1996.
110. Jackson, M.M., Pocinki, S.B., *Effects of fuel and additives on combustion chamber deposits*. SAE Paper 941890 (1994), 1994.
111. Cheng, S.S., *A Physical Mechanism for Deposit Formation in a Combustion Chamber*. SAE Paper 941892, 1994.
112. Matsushima, J., *Development of a high speed piston surface temperature measurement apparatus for application to steady-state and transient heat release and exhaust gas analysis in a single-cylinder spark-ignition engine*, in *Mechanical Engineering2002*, University of Michigan: Ann Arbor.
113. Overbye, V.D., Bennethum, J.E., Uyehara, O.A., Myers, P.S., *Unsteady Heat Transfer in Engines*. SAE Transactions, 1961: p. 461-494.
114. Woschni, G., *A Universally Applicable Equation for the Instantaneous Heat Transfer in Engines*. SAE Transactions, 1961. **69**: p. 461-494.

115. Fischer. *Eddy current method according to DIN EN ISO 2360*. MPOR Coating Thickness Test Instruments 2007.
116. Goldstein, J.I., Newbury, Dale E., Echlin, P., Joy, D.C., Fiori, C., Lifshin, E., *Scanning Electron Microscopy and X-Ray Microanalysis*1981, New York: Plenum Press.
117. Zerda, T.W., Yuan, X., Moore, S.M., Leon y Leon, C.A., *Surface area, pore size distribution and microstructure of combustion engine deposits*. Carbon 1999, 1999. **37**: p. 1999-2009.
118. Pantea, D., Darmstadt, H., Kaliaguine, S., Summchen, L., Roy, C., *Electrical Conductivity of Thermal Carbon Blacks-Influence of Surface Chemistry*. International Carbon Journal, 2001. **39**(8): p. 1147-1158.
119. Chescoe, D., Goodhew, P.J., *The operation of the transmission electron microscope*1984, New York: Oxford University Press.
120. Fuchs, E., Oppolzer, H., Rehme, H., *Particle Beam Microanalysis*1990, Weinheim: VCH.
121. Riemer, L., *Transmission Electron Microscopy: Physics of Image Formation and Microanalysis*. Second ed. Springer Series in Optical Sciences, ed. H.K.V. Lotsch1989, Berlin: Springer-Verlag.
122. Spilners, J.S., Hedenberg, J.F., Spohn, C.R., *Evaluation of Engine Deposits in a Modified Single-Cylinder Engine Test*. Chemistry of Engine Combustion Deposits, ed. L. Ebert1985, New York, NY: Plenum Press. 277-288.
123. Guinat, E., *Engine Deposits and the Determination of their Origin by Atomic Emission Spectrometry*. Chemistry of Engine Combustion Deposits, ed. L. Ebert1985, New York, NY: Plenum Press. 273-276.
124. Garratt-Reed, A.J., Bell, D.C., *Energy-Dispersive X-Ray Analysis in the Electron Microscope*. Royal Microscopy Society Microscopy Handbooks, ed. M. Rainforth2003, Oxford: BIOS Scientific Publishers Limited.
125. Briggs, D., *Surface analysis of polymers by XPS and static SIMS*. Cambridge Solid State Science Series, ed. D.R. Clarke, Suresh, S., Ward, I.M.1998, Cambridge: Cambridge University Press.
126. Moulder, J.F., Stickle, W.F., Sobol, P.E., Bomben, K.D., *Handbook of X-ray Photoelectron Spectroscopy*, ed. J. Chastain1992, Eden Prairie: Perkin-Elmer Corporation.
127. Feigin, L.A., Svergun, D.I., *Structure Analysis by Small-Angle X-Ray and Neutron Scattering*, ed. G.W. Taylor1987, New York: Plenum Press.
128. Guinier, A., Fournet, G., *Small Angle Scattering of X-Rays*1955, New York: John Wiley & Sons, Inc.
129. Sinha, S.K., *Small-Angle Scattering from Porous Materials*, in *Methods in the Physics of Porous Media*, P. Wong, Editor 1999, Academic Press. p. 223-262.
130. Glatter, O., *Data Treatment*, in *Small Angle X-ray Scattering*, O. Glatter, Kratky, O., Editor 1982, Academic Press.
131. Porod, G., *General Theory*, in *Small Angle X-ray Scattering*, O. Glatter, Kratky, O., Editor 1982, Academic Press.
132. Radlinski, A.P., Mastalerz, M., Hinde, A.L., Hainbuchner, M., Rauch, H., Baron, M., Lin, J.S., Fan, L., Thiyagarajan, P., *Application of SAXS and SANS in*

- evaluation of porosity, pore size distribution and surface area of coal.* Coal Geology, 2004. **59**: p. 245-271.
133. Kraus, M., *Fundamental Building Blocks of Nanoporous Networks from Ultra-Small-Angle X-Ray Scattering (USAXS) and Small-Angle X-Ray Scattering (SAXS) Experiments*, 2010, University of Missouri.
 134. Fairen-Jimenez, D., Carrasco-Marin, F., Djurado, D., Bley, F., Ehrburger-Dolle, F., Moreno-Castilla, C., *Surface Area and Microporosity of Carbon Aerogels from Gas Adsorption and Small- and Wide-Angle X-ray Scattering Measurements.* Journal of Physical Chemistry B, 2006. **110**: p. 8681-8688.
 135. Bruker. *Nanostar Small-Angle X-Ray Scattering Solutions*. 2010; Available from: http://www.bruker-axs.com/fileadmin/user_upload/PDF_2010/NANOSTAR_DOC-B88-EXS011_low.pdf.
 136. Bale, H.D., Carlson, M.L., Kalliat, M., Kwak, C.Y., Schmidt, P.W., *Small-Angle X-Ray Scattering of the Submicroscopic Porosity of Some Low-Rank Coals*, in *The Chemistry of Low-Rank Coals* 1984: Washington, DC.
 137. Gille, W., *Characteristics of the SAS correlation function of long cylinders with oval right section.* Journal of Applied Crystallography, 2010.
 138. Gille, W., Enke, D. Janowski, F., *Order distance estimation in porous glasses via transformed correlation function of small-angle scattering.* Journal of Porous Materials, 2001. **8**(2): p. 111-117.
 139. Gille, W., Enke, D. Janowski, F., *Stereological macropore analysis of a controlled pore glass by use of small-angle scattering.* Journal of Porous Materials, 2001. **8**(3): p. 179-191.
 140. Kistler. *Crank Angle Encoder*. 2005; Available from: http://www.kistler.com/mediaaccess/2613B_000-366e-06.05.pdf.
 141. Kistler. *6125C_000-695e-10.11*. 2011; Available from: <http://www.kistler.com/mediaaccess/000-695e-10.11.pdf>.
 142. Kistler. *4007B_000-614e-09.09*. 2009; Available from: http://www.kistler.com/mediaaccess/4007BA5F_000-614e-09.09.pdf.
 143. Kistler. *4043A_000-003e-10.09*. 2009; Available from: <http://www.kistler.com/mediaaccess/000-003e-10.09.pdf>.
 144. Omega. *Thermocouples - An Introduction*. Omega Engineering Technical Reference; Available from: <http://www.omega.com/thermocouples.html>.
 145. *Model 213 Piston Flow Meter (Frequency)*. Max Machinery, 2012; Available from: http://www.maxmachinery.com/sites/default/files/213_Frequency.pdf.
 146. *Model FT2 Gas Mass Flow Meter & Temperature Transmitter*. Fox Thermal Instruments, 2012; Available from: <http://www.foxthermalinstruments.com/pdf/ft2/FT2%20Datasheet.pdf>.
 147. Interface. *Model SM S-Type Load Cell*. 2005; Available from: http://www.interfaceforce.com/documents/SM_46.pdf.
 148. Bosch. *Lambda Sensor LSU 4.9*. 2011; Available from: <http://www.bosch-motorsport.de/pdf/sensors/lambda/lisu49.pdf>.
 149. *CO/CO₂ Analyzer AIA-72X Series Instruction Manual*, Horiba, Ltd., 2007.
 150. *NO/NO_x Analyser CLA-720MA Instruction Manual*. Horiba, Ltd., 2007.
 151. *O₂ Analyzer MPA-720 Instruction Manual*. Horiba, Ltd., 2007.
 152. *THC Analyzer FIA-725A Instruction Manual*. Horiba, Ltd., 2007.

153. AVL, *Indiset 642 Hardware Product Guide*, 2008.
154. NI PCI-6220. National Instruments, 2012; Available from: <http://sine.ni.com/nips/cds/print/p/lang/en/nid/14130>.
155. Chang, J., Filipi, Z., Assanis, D., Kuo, T., Najt, P., Rask, R., *Characterizing the thermal sensitivity of a gasoline homogeneous charge compression ignition engine with measurements of instantaneous wall temperature and heat flux*. IMechE, 2005. **6**: p. 289-309.
156. Stivender, D.L., *Development of a Fuel-Based Mass Emission Measurement Procedure*. SAE Paper 710604, 1971.
157. Kalghatgi, G., Risberg, P., Angstorm, H., *A Method of Defining Ignition Quality of Fuels in HCCI Engines*. SAE Paper 2003-01-1816, 2003.
158. Kalghatgi, G.T., *Auto-Ignition Quality of Practical Fuels and Implications for Fuel Requirements of Future SI and HCCI Engines*. SAE Paper 2005-01-0239, 2005.
159. Brezinsky, K., *The High-Temperature Oxidation of Aromatic Hydrocarbons*. Combustion Science Technology, 1986. **12**.
160. Eng, J.A., *Kinetics of HCCI Combustion*, in *Homogeneous Charge Compression Ignition (HCCI) Engines: Key Research and Development Issues*, F. Zhao, Asmus, T.W., Assanis, D.N., Dec, J.E., Eng, J.A., Najt, P.M., Editor 2003, Society of Automotive Engineers: Warrendale.
161. Ray, D.J.e.a., *Low Temperature Oxidation of 2-Butene in the Gas Phase*. Journal of American Chemical Society, 1968. **90**.
162. McCallum, L. *Pawlenty signs bill increasing ethanol content in gasoline*. 2005; Available from: http://news.minnesota.publicradio.org/features/2005/05/10_ap_ethanol/.
163. Lacey, J.S., Sathasivam, S.R., Filipi, Z.S., Peyla, R.J., Cannella, W.J., Fuentes-Afflick, P.A. *Impact of Refinery Stream Gasoline Property Variation on Load Sensitivity of the HCCI Combustion*. in *Proceedings of the ASME 2012 Internal Combustion Engine Division Spring Technical Conference 2012*. Torino, Piemonte, Italy.
164. Sjoberg, M., Dec, J.E., *Ethanol Autoignition Characteristics and HCCI Performance for Wide Ranges of Engine Speed, Load and Boost*. SAE International Journal of Engines 2010-01-0338, 2010.
165. Sjoberg, M., Dec, J.E., *Smoothing HCCI Heat Release with Vaporization-Cooling-Induced Thermal Stratifications using Ethanol*. SAE Paper 2011-01-1760, 2011.
166. Kalghatgi, G., *Fuel Anti-Knock Quality - Part I. Engine Studies*. SAE Technical paper 2001-01-3584, 2001.
167. Kalghatgi, G., Risberg, P., Hans-Erik Angstorm, *A method of defining ignition quality of fuels in HCCI engines*. SAE technical paper 2003-01-1816, 2003.
168. Kalghatgi, G., *Auto-Ignition Quality of Practical Fuels and Implications for Fuel Requirements of Future SI and HCCI Engines*. SAE Technical paper 2005-01-0239, 2005.
169. Kalghatgi, G. and R.A. Head, *Combustion limits and efficiency in a homogeneous charge compression ignition engine*. International Journal of Engine Research, 2005. **7**: p. 22.
170. Glassman, *Combustion*. 3rd edition ed1998: Academic Press.

171. Kalghatgi, G.T., *Combustion Chamber Deposit Flaking and Startability Problems in Three Different Engines*. SAE 2003-01-3187, 2003.
172. Lee, K., Zhu, J. Ciatti, S., Yozgatligil, A., *Sizes, Graphitic Structures and Fractal Geometry of Light-Duty Diesel Engine Particulates*. SAE 2003-01-3169, 2003.
173. Cole, R.L., Poola, R.B., Sekar, R., *Exhaust Emissions of a Vehicle with a Gasoline Direct-Injection Engine*. SAE Paper 982605, 1998.
174. Kaiser, E.W., Siegl, W.O., Brehob, D.D., Haghgoeie, M., *Engine-out Emissions from a Direct-Injection Spark-Ignition (DISI) Engine*. SAE Paper 1999-01-1529, 1999.
175. Maricq, M.M., Podsiadlik, D.H., Brehob, D.D., Haghgoeie, M., *Particulate Emissions from a Direct-Injection Spark-Ignition (DISI) Engine*. SAE Paper 1999-01-1530, 1999.
176. Di Iorio, S., Lazzaro, M., Paolo, S., Vaglieco, B.M., *Particle Size Distributions from a DI High Performance SI Engine Fuelled with Gasoline-Ethanol Blended Fuels*. SAE Paper 2011-24-0211, 2011.